# FEM Analysis of an Ultra High Temperature Ceramic Matrix Composite Thruster for Upper Stage Application

Tamim Doozandeh 5029236

**TU**Delft

# FEM Analysis of an Ultra High Temperature Ceramic Matrix Composite Thruster for Upper Stage Application

by

| Student Name | Student Number |
|---|---|
| Tamim Doozandeh | 5029236 |

Supervisor: Dr B.V.S Jyoti and Dr Prakhar
Date: Wednesday 11th September, 2024

Cover: Thesis Figure

**TU**Delft

# Preface

I am deeply grateful to my advisors, Dr. B.V.S Jyoti and Dr. Prakhar Jindal, for their invaluable guidance and encouragement throughout this research. I also thank Professor Chritos Kassapoglou, Professor Sergio Turtletaub, Professor Daniel Peeters, Professor Barry Zandbergen, and Professor Angelo Cervone for the knowledge and expertise they provided whenever I had questions. I also extend my thanks to my colleagues who assisted me throughout this thesis; Andrea Battegazzore, Lorenz Viethen, Maximilian Pfohl, and Iason Krinis. Special thanks to my family, whose unwavering support made this work possible.

This thesis represents not only the culmination of my academic journey, but also my passion for space and what lays beyond.

*Tamim Doozandeh*
*Delft, September 2024*

# Contents

# List of Tables

# List of Figures

# Nomenclature

## Abbreviations

| Abbreviation | Definition |
|---|---|
| UHTCMC | Ultra High Temperature Ceramic Matrix Composite |
| UHTC | Ultra High Temperature Ceramic |
| CMC | Ceramic Matrix Composites |
| FEA | Finite Element Analysis |
| CFD | Computational Fluid Dynamics |
| FEM | Finite Element Method |
| HAN | Hydroxylammonium Nitrate |
| ADN | Ammonium Dinitramid |
| NDE | Non-Destructive evaluation |
| CTE | Coefficient of Thermal Expansion |
| FSS | Free Shock Separation |
| RSS | Restricted Shock Separation |
| CoPreD | Composite Pre-Design Tool |
| LRE | Liquid Rocket Engines |
| SRM | Solid Rocket Motor |
| NDE | Non-Destructive Evaluation |
| FCGR | Fatigue Crack Growth Rate |
| CTE | Coefficient of Thermal Expansion |
| C | Celsius |
| k | Kelvin |

## Symbols

| Symbol | Definition | Unit |
|---|---|---|
| $\Delta V$ | Delta V | $[ms^{-1}]$ |
| $V_e$ | Exhaust Velocity | $[ms^{-1}]$ |
| $m_0$ | Initial mass | [kg] |
| $m_f$ | Final mass | [kg] |
| $\Delta V$ | Delta-V | $[ms^{-1}]$ |
| $I_\rho$ | Volumetric Specific Impulse | $[s]$ |
| $I_{sp}$ | Propellant Specific Impulse | $[s]$ |
| $I_{ssp}$ | System Specific Impulse | $[s]$ |
| $I_t$ | Total Impulse | $[Ns]$ |
| $w$ | Exhaust Velocity | $[ms^{-1}]$ |
| $g_0$ | Gravitational Acceleration on the surface | $[ms^{-2}]$ |
| $W_p$ | Propellant Weight | $[N]$ |
| $M_{ps}$ | Propulsion System Mass | $[kg]$ |
| $M_p$ | Propellant Mass | $[kg]$ |
| $t_a$ | Rocket Operation Time | $[s]$ |
| $\dot{m}_p$ | Propellant mass flow rate | $[kgs^{-1}]$ |
| $F$ | Force | $[N]$ |
| $K$ | Stiffness | $[Nm^{-1}]$ |
| $X$ | Deflection | $[m]$ |

| Symbol | Definition | Unit |
| --- | --- | --- |
| $T$ | Temperature | $K$ |
| $\dot{q}$ | Heat flux | $Wm^{-2}$ |
| $\lambda$ | Thermal Conductivity | $Wm^{-1}K^{-1}$ |
| $\sigma$ | Boltzman Constant | $Wm^{-2}K^{-1}$ |
| $\epsilon$ | Emmisivity | - |
| $L$ | Length | $m$ |
| $r$ | radius | $m$ |
| $p$ | Pressure | $Pa$ |
| $a$ | inner radius | $m$ |
| $b$ | outer radius | $m$ |
| $\alpha$ | CTE | $K^{-1}$ |
| $E$ | Young's Modulus | $Pa$ |
| $\delta_T$ | Thermal Delfection | $m$ |
| $\sigma_T$ | Thermal Stress | $Pa$ |
| $I$ | Second moment of area | $m^4$ |
| $\delta_3 point$ | 3 point bending deflection | $m$ |
| $h$ | Convection coefficent | $Wm^{-2}K-1$ |
| $C$ | Bartz Constant | - |
| $c_p$ | Specific Heat | $Jkg^{-1}K^{-1}$ |
| $\mu$ | Viscosity Coefficient | $Pas$ |
| $d_t$ | Throat area | $m$ |
| $Pr$ | Prandtl Number | - |
| $\dot{m}$ | Mass flow | $kgs^{-1}$ |
| $A_t$ | Throat Area | $m^2$ |
| $r_c$ | Radius of curvature | $m$ |
| $A$ | Local Area | $m^2$ |
| $T_w$ | Wall Temperature | $K$ |
| $T_o$ | Chamber Temperature | $K$ |
| $k$ | Specific Heat | $Jkg^{-1}K^{-1}$ |
| $Ma$ | Local Mach Number | - |
| $p_e$ | Exit Pressure | $Pa$ |
| $p_a$ | Ambient Pressure | $Pa$ |
| $A_e$ | Exit Area | $m^2$ |
| $R$ | Specific Gas Constant | $Jkg^{-1}K^{-1}$ |
| $T_c$ | Chamber Temperature | $K$ |
| $\gamma$ | Specific Heat Ration | - |
| $m_{sc}$ | Spacecraft Mass | $kg$ |
| $N_{pulses}$ | number of Pulses | - |

# Executive Summary

Ultra-high Temperature Ceramic Matrix Composite (UHTCMC) is a material designed to be extremely durable and exhibit highly favourable properties. It combines the benefits of Ultra-High Temperature Ceramics (UHTC) and Ceramic Matrix Composites (CMC) and represents a relatively new development in material science. With the rapid growth of the space industry and the increasing demand for propulsion systems, creating a thruster out of UHTCMC material could significantly extend thruster operational life.

This research aims to structurally investigate a 100 N bi-propellant thruster made entirely from a custom composition of 65 vol% ZrB2-20 vol% SiC and 35 vol% chopped short 6mm carbon fibres. The study seeks to answer the following questions: What are the expected loads and boundary conditions for such a thruster? What stresses and temperatures will it experience? What is the optimum thruster thickness? What are the long-term effects of operation on the thruster? To address these questions, research papers were reviewed, and ANSYS R2 2023 was utilized for simulations. Tutorials on effective modelling, meshing, and software settings were found on the ANSYS website. Additionally, professors and colleagues were consulted to fill knowledge gaps and provide guidance.

The findings indicate that the thruster's nozzle section thickness can be reduced to a minimum of 2 mm, based on manufacturing limitations. The thickness decreases linearly from 4 mm at the flange to 2 mm at the beginning of the nozzle's convergent section. The peak stress in the nozzle, 133 MPa, occurs 2.16 seconds after the start of thrusting, while the peak stress near the flange increases continuously during prolonged thrusting. After 10 seconds of operation, the highest temperature recorded is 1643 K at the nozzle throat, with a peak stress of 302 MPa occurring on the outer surface near the flange's curved section, 10 to 14 mm along the thruster. Thermal expansion results in a 0.51% increase in length and a 0.11 mm increase in radius at the beginning of the convergent section after 10 seconds of operation. Although the stresses never exceed the flexural strength limit, with a 20% margin, it remains important to identify when and where the margin is lowest to determine the most critical damage mechanisms.

Between 0 and 0.59 seconds of operation, thermal stress cracks, ablation, and erosion are the most critical factors, occurring near the nozzle throat in the inner convergent section. From 0.59 to 3.68 seconds of continuous operation, thermal stress cycling is likely to cause failure in the region 10 to 15 mm inside the thruster, near the flange. Operations longer than 3.68 seconds pose a significant risk of failure at the curved section connecting the flange to the chamber body, likely due to stress concentrations. The longer the thruster operates continuously, the fewer cycles it can withstand. Given UHTCMC's inherent durability, no additional coating was used, as research indicates minimal erosion or ablation under more severe and extended operational conditions with similar UHTCMCs.

Propulsion functions such as attitude control, limited orbit correction, and station-keeping are feasible for this thruster, as they require short pulses of thrust, typically less than 0.59 seconds. More intensive operations, such as orbit corrections, station-keeping, and light drag makeup, which involve thrust pulses between 0.59 and 3.68 seconds, will place additional strain on the inner thruster near the flange. However, extremely intensive thrusting operations requiring continuous pulses longer than 3.68 seconds, such as re-entry, extensive drag makeup, or evasive manoeuvres, are not well-suited for this thruster due to the significant impact on its cycle life.

Overall, the use of UHTCMCs in thrusters designed for short pulse durations focused on attitude control and limited orbit maintenance is highly advantageous. The ability to maintain thruster performance over extended periods makes this material particularly suitable for long-term low Earth orbit missions. The specific thruster design discussed in this thesis should be tested to confirm its structural capabilities, with particular attention to the stresses at the flange section. If the actual stresses at the flange are

lower than anticipated, the thruster may perform better than expected, especially during more intensive propulsion functions.

# 1

# Introduction

This chapter will aim to introduce the thesis paper and the motivations behind the topic. The chapter will start with the background and necessary motivation for the thesis in section 1.1. Then the objectives and requirements will be stated in section 1.2. Afterwards, the scope and limitation, section 1.3, of the thesis will be discussed to bring the focus to specific topics in the field in question. Finally, the outline for the entire thesis and flow of information will be denoted in section 1.4.

## 1.1. Background and motivation

As there is a great number of smallsats being launched every year, with nearly 95% of all spacecraft launched in 2022 being under 600 kilograms [55] and an increasing trend expected in the year 2024 [11], the need to perform in-orbit manoeuvers or other such in space manoeuvres and activities necessitates an adequate propulsion system to facilitate such diverse operations. Such operations will be done using in-space propulsion systems, of which there are 3 types; chemical, electrical, and non-propellant based. [36]

Due to the more performant thrust-to-weight ratio of chemical propulsion systems, they are chosen as the focus of this thesis. There are also additional benefits that come with choosing chemical propulsion systems due to the extensive history of using them in space applications. During space operations, the thrusters are expected to run at very high temperatures and pressures, this has caused research to be done into materials that exhibit excellent thermal shock resistance and can operate under extreme temperatures and pressures more effectively. The type of material is chosen to be Ultra High-Temperature Ceramic Matrix Composites (UHTCMCs), exhibiting very favourable physical properties for use in thruster manufacturing. Additionally, given the new trend of using green propellants, this new type of material will have to be done in combination with environmentally friendly propellants, signifying a significant step forward in sustainable and effective space exploration.

As such, it is important to perform a Finite Element Analysis (FEA) to capture and documents any design flaws, stress concentrations, and excessive deformation and implement any adjustments where necessary. Such a step is necessary to verify the loads experienced by the thruster wall, in addition to validating the nozzle from a structural standpoint. The FEA step is done before fully committing to manufacturing and creating a nozzle for a test fire, as without it, any faults found during testing would result in a very long and expensive iteration in the design to be done.

## 1.2. Objectives and requirements

The goal of an FEA analysis is to determine the viability of the design before committing to the expensive and time-consuming task of actual manufacturing and testing of the rocket thruster. Therefore, there are some goals and outcomes that are to be achieved by the FEA analysis. These goals are outlined below.

- **Determine the location of Stress Concentration:** it is important to know where stress concentrations occur and why they occur

- **Determine Strain and Deflection:** It is important to know to what extent deflection occurs
- **Safety factor:** It is important to know if there is sufficient margin in the design to withstand the loads
- **Damage and Crack formation:** It is important to characterize what the causes of cracks are, what influences their growth rate, and what can be done to reduce them and prevent critical failure
- **Determine any changes to the thickness of nozzle walls:** If the stress exceeds the yield strength of the material, the thickness of the walls may have to change to meet the design loads and required safety margins.

## 1.3. Scope and limitation

Given that FEA is a very broad field and there are many ways of approaching a problem, the scope of the analysis will be limited. In a later chapter, the tools that will be used for the analysis will be discussed and motivated. The scope of the research done during the literature review and therefore the entire thesis are stated below.

- The operating range of the thruster is from 100 to 1000 km in altitude
- 3D CFD results will be imported from a colleague performing the analysis, while this report will use analytical equations as a basis for verifying the received 3D CFD results.
- The thruster design has already been made and the only factor that can be changed is the thickness of the thruster walls
- The wall material is limited to a specific UHTCMC composed of a mixture of ZrB2- 20 vol% SiC, the Ultra High-Temperature Ceramic (UHTC), with 35 vol% chopped 6mm carbon fibres, this will be described in further detail in later sections, and a green propellant combination of kerosene as the fuel and hydrogen peroxide as the oxidizer.
- The thermal expansion and contraction of the nozzle due to being manufactured on earth and then taken to space is assumed to be within the margin of precision of the manufacturing process.

## 1.4. Report Outline

The report outline is given below in chronological order. Starting first from the literature review where the basic knowledge of rocket staging, and propellants are given before then going into the state-of-the-art research that occurs in the realm of 3D FEA analysis for rocket thrusters, chapter 2. Once the literature review has been done, the work plan for what steps will be taken and what specific methods will be used to answer the research question will be outlined in chapter 3. The UHTCMC material will be covered in detail in this chapter. Then, it is expected that the inputs to the FEA are going to be the thermal and pressure loads obtained from CFD results. The 3D CFD, which will be used in simulations, will be done by a colleague and imported to be used in the 3D FEA. These will be covered in chapter 4. After the CFD has been covered, the 3D FEA can then start and the process and specific details that are to be outlined for the solution will be covered in detail, including the creation of the custom mesh and model in the FEA software, all also covered in chapter 4. Afterwards, the results will be discussed in chapter 5. Followed finally by the conclusion and recommendation, chapter 6.

# 2

# Literature Review

The literature review section will aim to build a basis for knowledge and the state of the art from which this thesis will be built. Essential thruster and propellant knowledge will be covered in section 2.1. Next, the state of the art in thruster FEA is covered in section 2.2. The research gap is then discussed in section 2.3, followed by the derived research question in section 2.4.

## 2.1. Basic Knowledge

Rocket staging is a common practice in the aerospace industry. During a launch, to increase the effectiveness of a rocket, the dead structural weight is discarded in stages. This effectively increases the initial to final mass ratio, thereby increasing the Delta-V delivered by the rocket, represented via the equation below. [21]

$$\Delta V = V_e ln(\frac{m_o}{m_f})$$
(2.1)

As can be seen in Equation 2.1, reducing the final mass by jettisoning dead weight, increases the delivered Delta-V given that all other variables are constant. Therefore, when a certain section is jettisoned the remaining rocket is called the upper stage, which is also usually accompanied by a thruster to propel the stage forward. It must also thus be said that there are two general categories of upper-stage thrusters; orbital and interplanetary. The distinction is made based on the area in which the application is done. Orbital refers to any application which is maintained within the sphere of influence of the Earth, while interplanetary encompasses high orbit transfers or interplanetary trajectories. The aforementioned can be considered a high Delta-V application, while orbital upper stages can be considered a low Delta-V application. Manoeuvres and applications that are done within the sphere of influence of the earth can include the following; attitude adjustments, orbit manoeuvring, orbit control, station keeping, etc.

As the market for small satellites increases in demand, the need for effective and small thrusters will only continue to grow. Small form factor propulsion systems with good mass and volume properties constrained by small sat mass and dimensions will grow increasingly popular. The design and manufacturing of such propulsion systems can be expected to be very time-consuming and costly, requiring the need to apply computational methods such as CFD and FEA to assess the theoretical performance of a rocket thruster and identify and localised areas of stresses or deformation that need to be addressed before actual hot fire testing.

The analysis of a rocket engine depends on the type of engine that the analysis is performed on. There are three main categories of thrusters in space propulsion, listed below. [36]

- *Chemical*: such as mono-propellant or bi-propellant, solid rocket motors, and hybrid rocket thruster systems
- *Electrical*: which uses electric fields to accelerate ions and generate thrust
- *Propellant-less*: propulsion systems such as those that use solar sailing technology

Of all the technologies mentioned above, a focus is placed on chemical-based propulsion systems due to the high thrust-to-weight ratios and ability to perform high-thrust manoeuvres compared to other propulsion types. Additionally, The 4 main advantages of chemical systems are as follows: [36]

- Extensive Flight Heritage, they have been used in a multitude of flight applications
- Extensive Component System, chemical systems are widely used and can be customized to specific applications
- Cold Start Qualified, thrusters can be qualified for many cold starts
- Extensive safety and handling standards

The subsequent sections of literature review will aim to focus on chemical propulsion systems' limited operations within the sphere of influence of the Earth. The literature study will focus heavily on material properties, combustion effects, and consequences, in addition to damage mitigation or life cycle improvement methods. Common materials used in nozzles, and constituents, concerning propellant choice (and therefore the combustion) will also be covered.

Since the thesis places a focus on bi-propellant chemical propulsion systems, many metrics can be used to define the performance of such a system. A comprehensive list of such performance parameters used for performance is given below[82].

- Propellant Specific Impulse: expressed in seconds and is the total impulse over the propellant weight.

$$I_{sp} = \frac{w}{g_0} = \frac{I}{W_p} \quad (2.2)$$

- System Specific Impulse: defined as the impulse delivered by the propulsion system weight

$$I_{ssp} = \frac{I}{M_{ps}g_0} \quad (2.3)$$

- Total Impulse: defined as the total change in momentum delivered by the rocket system.

$$I_{tot} = Ft_a = M_p w \quad (2.4)$$

- Thrust: The force generated by the thruster

$$F = \dot{m}_p w \quad (2.5)$$

- Thruster Mass: this refers to the dry mass of the propulsion system
- Thruster Volume: This refers to the volume the thruster occupies when integrated into a spacecraft

Thruster mass is an especially useful metric in this case as given the ability to adjust the thickness of the thruster walls, it is highly advantageous to minimize mass as much as possible. As expected, minimizing mass can increase the thrust-to-weight ratio, thereby increasing the performance of the thruster. Additionally, reducing thruster volume via the adjustment of wall thickness also allows for easier fitment into a spacecraft.

## 2.1.1. Green Propellants

Traditional propellants such as Hydrazine are dangerous to handle, thus research into alternative propellants such as ionic liquids, electrolysed water, and hydrogen peroxide is being done. Some ionic liquid formations such as ammonium dinitramide (ADN) and Hydroxylammonium Nitrate (HAN) can offer higher specific impulse and performance compared to hydrazine mono-propellants. There are also developments in high-concentration hydrogen peroxides as an oxidizer in bi-propellant systems with alcohol as the fuel. Green propellants, as these alternative fuels are called, have many considerations as listed below. These are compiled from a NASA source.[36]

- **Improved Safety Classification:** Greener propellants tend to be less reactive and toxic, this makes the regulations easier to meet for these propellants.

- **Safety and Handling:** As the propellants do not need to be stored at extreme temperatures, they need fewer valve seats for power. This improved handling also allows accelerated launch operations, since many operations would then be able to be done in parallel, like fuelling. However, it must be noted that safety and handling standards will depend specifically on the propellant used and may differ slightly, even if all fall under the green propellant umbrella.
- **Immature Component System:** While development has been done on a component level, it is still lacking on a whole system level where multiple components are integrated.

The above considerations also align with other NASA sources of information that state the advantages of green propellant as; improved safety, higher specific impulse, and lower turnaround times.[51] Though the higher specific impulse comment is expected to be limited to specific combinations and mixtures of green propellants as mentioned previously using ADN and HAN. Since the green propellant used by the 100-N class thruster is made to operate using $H_2O_2$, the advantages and disadvantages of the green propellants will be provided below. Hydrogen Peroxide is chosen since the thruster is made by SolvGe, which primarily focuses on the usage of hydrogen peroxide in thruster applications.[64]

**Table 2.1:** Advantages and Disadvantages of $H_2O_2$ [15]

| Advantage | Disadvantage |
| --- | --- |
| Non-Toxic | Still requires certain safety standards when handling |
| Commercially Available and cheap | Incompatible with Titanium |
| Can be used as an oxidizer in bi-propellant and as a mono-propellant | Low Isp performance as a mono-propellant |
| Low Decomposition temperature of less than 1000°C | High self decomposition ratio |
| Cold start capable | |
| Can be manufactured on-site, by companies such as SolvGE | |

The driving force for green propellants research can also be attributed to traditional propellants such as hydrazine being limited in the future. [15] This further urges development into these fuels for use shortly. This does mean that there is still a lot of room for development to be made in this field with continuous research into storability, performance in mono and bi-propellant configurations, material compatibility, and commercial availability.

## 2.1.2. Finite Element Analysis
Finite element methods are used to obtain approximate solutions to real-world scenarios. The basics of such a method are to take the structure and divide it into subsequent nodes and elements that can then be characterized using local and global matrices to solve. Such a method can be used in electromagnetic analysis, structural analysis, and thermal analysis among many more.[24]
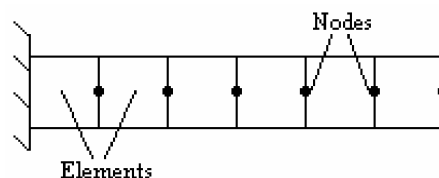


**Figure 2.1:** An example of a beam structure being divided into elements and nodes [24]

The essential elements and knowledge of solving a finite element problem are obtained from the Linear modelling course given in TU Delft.[46] When it comes to solving a structural model using finite elements, 6 steps must be followed. This is to ensure that the solution is correct and representative of the use case in question. The 6 steps are outlined below:

1. **Idealize**: Determine how to best represent the model using the element type that is available to you, This would take into account the type of analysis you are aiming to perform based on the loads and boundary conditions you expect to occur

2. **Discretize**: This refers to meshing the problem. At this stage, the initial mesh is used to determine the general deformation of the solution.

3. **Loads and Boundary Conditions**: In addition to applying loads and boundary conditions at this step, It must be noted the simplified nature of the loads that may be applied in the software vs what they are in practice. An example would be a constant load applied on the surface of an object, wherein in reality it may vary every so slightly across the surface.

4. **Mesh Convergence**: This step is directly related to the number of nodes and elements chosen to divide the model into. The reason it matters is that although simulating with millions of elements would yield the best result, it would be computationally too expensive. Thus, a balance between computation time and solution accuracy would need to be met.

5. **Verification**: At this stage, the last 4 steps need to be checked again to ensure that all decisions made to reach the converged solution are sufficient and represent the real-world scenario closely enough.

6. **Validation**: Real-world results are used to check whether the results of the simulation are correct, this can only be done however if real-world data exists. If it is unavailable, expectation can be placed whether the simulation is expected to over or underestimate the resultant loads or deflections.

Another consideration that is seen for FEA problems is the decisions made on the model level. This pertains to decisions on whether to include non-linearities in the model or to use linear or quadratic element types when creating the model mesh. First, it is important to understand the difference between linear versus quadratic element types and what such a decision would mean to the model. Linear elements are essentially linear shape functions that represent the deflection between two nodes as a linear varying function. Quadratic functions, however, use a higher-order polynomial to interpolate the deflection between the nodes. It can be seen in Figure 2.2 that linear elements are limited in best-representing deflection given the first-order polynomial used to interpolate between points. Quadratic elements however can best match the true deflection due to the higher-order interpolation used. However, as the number of elements increases, the solution becomes closer to the true solution and matches the quadratic solution.
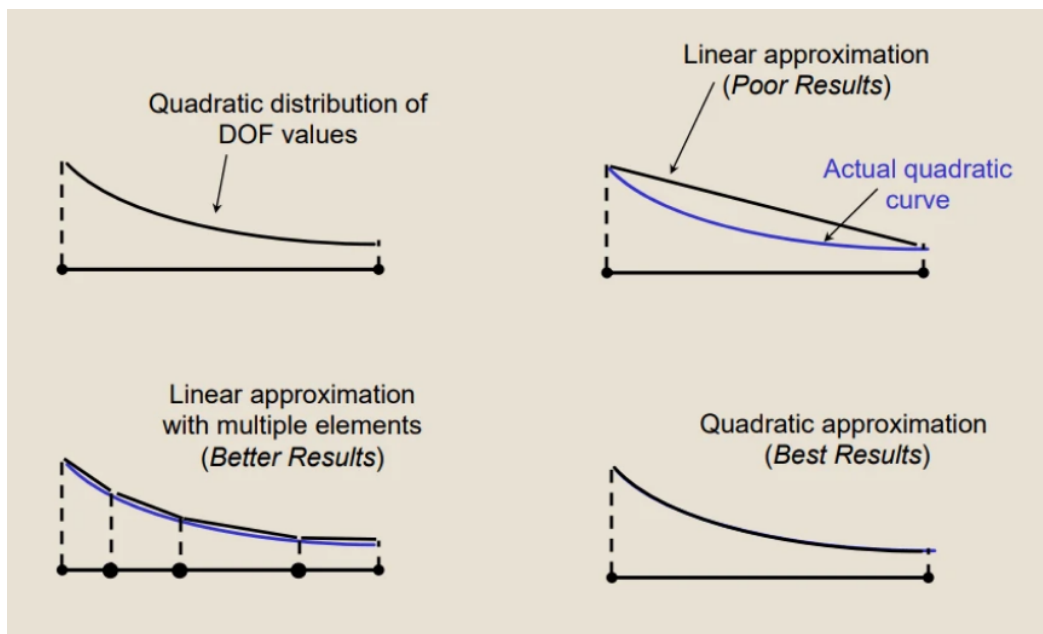


**Figure 2.2:** A figure showing the limitations of linear elements as well as the advantages of quadratic elements when it comes to best approximating deflection behaviour[72]

This, in combination with the element shapes chosen, would require a balancing act to be achieved between hexahedral or tetrahedral elements as well as whether they are linear or quadratic.[72] The recommendation of using seconds order elements when possible and preferring Hexahedral linear elements was also seen in other sources. [77] Overall, the consensus is to use second-order elements to minimize sensitivity to element distortion, obtain more accurate stress distributions, represent curved edges and surfaces accurately, and get better results, all at the cost of being more expensive to run computationally. Given the complex curved shape found in thrusters, it is expected that quadratic elements will be highly preferred. Additionally, there is the option to use both, hexahedral and tetrahedral elements in FEA software such as ANSYS when creating a mesh.
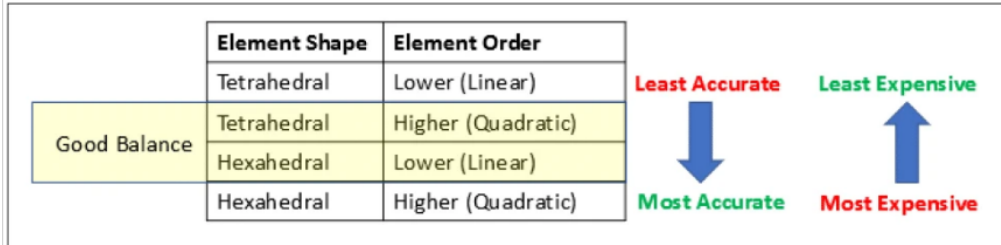


**Figure 2.3:** This shows the considerations that can be made when choosing elements shapes and order for the best balance of speed and accuracy[72]

Another consideration is whether to run linear or non-linear FEA. To explain the difference between the two, the following equation will be used:

$$(F)_{vec} = [K]_{mat} \cdot (X)_{vec} \tag{2.6}$$

The above equation can be called a global stiffness matrix for an FEM problem. (F) is the force vector, [K] the global stiffness matrix, and (X) the displacement vector for each node corresponding to each node in the stiffness matrix. A linear analysis means that the (X) vector does not affect the stiffness matrix or force vector, while a non-linear FEA affects them. There are three main considerations as to why a model would be considered non-linear, as listed below and obtained from the same source[73].

- Geometric Non-Linearity, implemented when the deformations are large enough to affect the orientation of the loads that are being applied. They are also considered alongside stress stiffening of the structure, causing the structure to weaken.
- Contact Non-Linearity that occurs due to changes that occur in the contact surfaces of the structure. An example would be friction between contacting surfaces where a surface can slide on another. This is especially relevant when choosing the types of contacts in a nozzle. ANSYS classifies bonded and no separation contacts as linear and rough, and frictional and frictionless contacts as nonlinear.
- Material Non-linearity is when the loading of the materials causes them to exceed the linear regime, past the yield point, and into the plastic region. Such effects in the plastic region are inherently non-linear.

From the above, it can be seen that there may be a situation that arises that requires the use of a non-linear analysis to determine the stresses and deformations in a structure. Given that the upper stage nozzle in this thesis is made of material with a higher stiffness than traditional thruster material, and the fact that the thruster is most likely going to be used for small bursts up to a maximum of 5 (or potentially 10) seconds, the thruster would most likely have to be designed to not enter the plastic region during operations to retain its shape and material properties. Therefore, given that the problem would likely be fully contained in the elastic region and be designed with minimal deformation in mind to maintain performance, the problem would most likely be classed as a linear problem.

Element types used in the analysis are also of great consideration when solving a finite element problem. Given that the software to be used is going to be ANSYS, the user manual can be used to find exactly what the element types are called and what their characteristics are for steady-state thermal and

structural analysis. Below are the quadratic Solid226, or Hex20 elements, that are most likely to be used during finite element modelling. The element is also capable of coupled-field structural-thermal analysis for static, full harmonic, and full transient analysis types. [18]
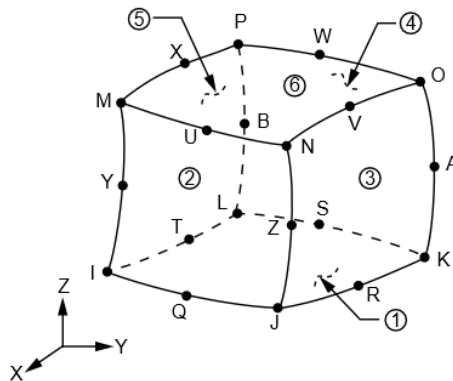


**Figure 2.4:** Notice the middle nodes on the edges that show that this element is not linear, but quadratic.[18]

## 2.2. State-of-the-Art research

Although green propellants can be said to be relatively new in the space industry, there are still many developments made. One development uses hydrogen peroxide and ethanol propellant combination in a bi-propellant micro rocket engine, which is made by the Mechatronic, Austria and the Space Propulsion branch of the Austrian Research Center.[15] The same paper also states an interesting observation of the thrust-to-weight, $\frac{T}{w}$, which decreases as the size of the thruster decreases contrary to the cubic/square law. This was attributed to the phenomena and limitations of current technology that become more present as the rocket is scaled down; technology limitations and increased viscous flow effects. Technology limitations can be applied to manufacturing the walls, where there is still excess unused material left and the inability for small pumps to sufficiently increase chamber pressures. As for viscous flows, as the nozzle size decreases, the Reynolds number tends to decrease as well. Below a Reynolds number of 10000 for small thrusters, discharge ratios increase, harming the rocket's performance. This effect can also be compounded when taking into account boundary layer growth and its significance when the nozzle is miniaturized.[15]

### 2.2.1. Loads Found in Nozzles

Rocket engines operate under two main categories; transient and steady state. Transient operations are related to start-up and shutdown procedures where pressure is still building up or the rocket is rapidly cooling down, respectively. Steady-state operations refer to when the conditions in the nozzle are constant, or in practice remain within the limits to be considered constant. Describing the definitive loads found in a nozzle and their exact causes was seen to be difficult, as there are still many investigations ongoing into the different causes of certain loads and phenomena in nozzles. A study by NASA on failure mechanisms implicitly identified that thermal and mechanical loads act on a nozzle. [62] This was also in line with another article that discusses failure mechanisms on the nozzle, with the addition of identifying mechanical vibration originating from internal and external sources. [12] Other sources stated that exhaust nozzles are exposed to the highest shear stresses, pressure and heat fluxes in a chemically aggressive environment. [57][33] While no sources have explicitly identified loads that are steady and transient in their entirety, this was still an important factor to consider, ensuring that no steady loads are missed and that no transient loads are included in the rocket nozzle analysis.

Rocket nozzle loads can be split into 3 main types that are of importance; thermal, pressure, and vibrational. Additionally, since a rocket can operate under transient and steady-state conditions, these loads can vary in intensity and severity. The loads experienced by a nozzle are listed as such:

- **Thermal**

    – Steady State

* Thermal loads from steady-state combustion of the propellants
* Thermal radiation and/or convection of the nozzle outer wall into the environment
* Radiative heating from external sources such as the sun or the other spacecraft components in proximity to the nozzle into the nozzle outer wall and components

– Transient

* Thermal temperature variations that occur during start-up and shut-down procedures where thermal gradients are high and thermal shocks are prevalent [39]
* During Startup, the thermal gradients are likely to be the highest. Especially when the spacecraft is on the "cold" side of the orbit in space.

- **Pressure**

– Steady State

* Pressure applied on the nozzle inner walls due to combustion processes. Based on exit conditions and expansion ratio, there could be under-expansion, ideal-expansion or over-expansion occurring.

– Transient

* During pressure build-up at start-up, the flow may not yet be fully attached to the boundaries, thereby introducing phenomena such as side loads which can cause failure. [6]
* During start-up transient ignition overpressure could occur which results from large pressure disturbances occurring [60]
* Shocks during start-up and shut down [8]

- **Vibrational**

– Steady State

* Engine combustion can have some vibration loads that are generated from internal and external sources, with random and sinusoidal being most dominant and severe in a steady state. [8]
* Resonance may occur based on the natural frequency of the structure material and operating oscillation frequency

– Transient

* Unstable combustion, turbo pump rotor imbalance, loosening of mechanical components, and damage to mechanical systems may induce vibration loads [84]
* In the case that there is a thrust vector control unit or a throttle, vibrations may be induced when such operations are performed due to the movement of mechanical components

It must be noted that for vibration loads, specifically the random type which originates from combustion processes, fluid flow and turbulence, are not fully characterized due to their inherent complexity. This essentially means a FEM of the rocket could not simply be taken, and the loads applied, thereby limiting sch analysis to real-world fire tests for representative and practical data.[8] A further step taken to identify steady state loads was studying other research done on thermally and statically coupled analysis on rocket nozzle walls. This was done to see what types of loads are used as inputs for a rocket FEA as well as the additional considerations taken by each researcher on applying the loads. One coupled thermo-structural analysis determined the material temperature profile using position-dependent as well as constant heat flux coefficients, this was then used to calculate the stresses using temperature-dependant material properties.[67] A similar analysis on the thermo-structural response of a composite nozzle employed the use of spatial line function of the temperature and pressure along the nozzle wall with temperature-independent material properties to calculate the stresses.[30] A further study investigating composite ablative liners used temperature-dependent liner properties and applied a temperature distribution, obtained from 2D analysis, and pressure distribution, calculated using a function, along the wall for FEM calculations on a 3D Nozzle.[34] A further study on a 122 mm nozzle applied the total temperature and pressure loads calculated from CFD into the FEA as input loads. It

must be stated that an actual test for validation of operational conditions was used to determine the boundary conditions for the CFD.[71] The aforementioned study is especially important as it demonstrates the use of a test to validate CFD results. Given that the thruster used in the thesis is based on an existing one with different materials and propellants, the characteristics of the CFD results can still be validated, although carefully and to a limited extent given the changing propellants and wall properties. A thesis is also found on 3D fluid structural interaction using the fluid results of convection and pressure at the channel walls of nozzle coolant to calculate the loads using ANSYS.[24]

**Table 2.2:** Summary of Nozzle FEM analysis Papers

| Source | Inputs | Outputs |
|---|---|---|
| 3D FEM Nozzle[58] | <ul><li>Static Pressure using the ideal gas</li><li>Temperature using the ideal gas</li><li>Analytical ideal gas validated to within 6% using CFD</li></ul> | <ul><li>Thermal and Force Stresses</li><li>Total Deflection</li><li>Thickness determined based on total deflection and yield stress</li></ul> |
| 2D FEM[67] | <ul><li>Temperature dependant materials</li><li>Pressure, heat transfer coefficient, and temperature from quasi 1D isentropic flow</li></ul> | <ul><li>Transient Thermal analysis with flow temp as ambient and convection along walls</li><li>Equivalent von Mises Stress</li></ul> |
| 3D FEM Coolant Channel[24] | <ul><li>Convection and Pressure from ANSYS CFX using k-$\omega$ SST</li><li>Bulk Temperature and heat transfer coefficients From Thermal Analysis</li></ul> | <ul><li>Total Deformation</li></ul> |
| 2D FEM[71] | <ul><li>Temperature and Pressure from ANSYS CFD (k-$\omega$ SST model)</li><li>Experimental Data from test fire (used for validation of CFD)</li><li>Nozzle 2D model</li></ul> | <ul><li>Equivalent von Mises Stress</li><li>Used stress to check the variation of stress with insulator thickness</li></ul> |
| 2D FEM [30] | <ul><li>temperature-independent material</li><li>Spatial line functions of Temperature and pressure from experimental data</li><li>Convection to air for exposed surfaces</li></ul> | <ul><li>Thermal temperature in wall</li><li>Axial, radial and hoop Stress</li></ul> |
| 2D FEM [59] | <ul><li>Pressure and Convection data as tabular inputs</li><li>Temperature Dependent Material Properties</li></ul> | <ul><li>Von-Mises, X and Y Stress</li><li>Temperature Distribution with transient analysis</li></ul> |

**Table 2.2 continued from previous page**

| Source | Inputs | Outputs |
|---|---|---|
| 2D and 3D FEM [34] | <ul><li>Analytical convective Heat-transfer coefficient along the wall</li><li>Analytical pressure along the wall</li><li>Temperature-dependent structural properties</li><li>Combustion temperatures on the inner wall</li></ul> | <ul><li>Von-Mises, shear, and hoop Stress in the scarfed nozzle</li><li>Radial Displacement at nozzle tip</li></ul> |
| 3D FEM [79] | <ul><li>Pressure, convection and flow gas temperature data</li><li>Temperature-dependent material properties of multiple materials, since thruster is made of many of them stuck together</li></ul> | <ul><li>Nozzle Temperature Contour</li><li>Radial, axial, hoop, and interlaminar Stress</li><li>Axial stress over time</li><li>Reliability and sensitivity analysis</li></ul> |
| 3D FEM[25] | <ul><li>Pressure and Thermal Loads</li><li>Temperature Dependent Material Properties</li><li>Thermophysical properties of methane for flow and heat transfer</li></ul> | <ul><li>Stress and Strain</li><li>Temperature Distribution</li><li>Cyclic loading thermo-mechanical response</li></ul> |

From the above papers and studies, the consensus was that pressure loads and temperature distribution along the nozzle inside the wall are to be applied. Furthermore, it is best to have temperature-dependent material properties to take into account material performance at varying locations in the nozzle, given the large temperature difference expected to be seen in the chamber compared to the nozzle exit. 3D-based studies have been seen to perform CFD analysis and then transfer loads of temperature, pressure, and convection to then perform the FEM analysis. CFD results have also been seen to be validated using real-world testing results of the nozzle under analysis. The aforementioned can be especially useful when investigating the properties of different nozzle materials whilst using representative nozzle loads. A final remark is that to perform the steady state FEA of a thruster, then the CFD would in turn have to be in a steady state.

Transient loading is seen as especially dangerous for nozzles. It is stated that the main reason for rocket engine failure is buckling caused by the presence of side loads.[9] Such phenomena occur for over-expanded nozzles during start-up and shutdown transients, in stages where the ambient pressure is higher than the exit pressure. Such over-expansion of the flow is seen as critical. The higher ambient pressure may rush in upstream of the nozzle along the walls causing flow separation and recirculating zones.[63] This sideloads phenomenon is also expected to occur due to the transition phase between free shock separation (FSS) to restricted shock separation (RSS) and vice versa. The aforementioned phenomena are also dependent on the pressure ratio of the chamber to ambient pressure.[60]Additionally, a thesis states potential other sources of these phenomena of side loads including; tilted separation line, pressure pulsations in separation and re-circulation regions, and aeroelastic coupling. For the tilted side load theory, the flow separation that occurs may be asymmetric which can cause a force to act around the nozzle gambling point, thus generating a side load. [40] This tilted separation line which occurs under free shock conditions occurs when the separation is asymmetric, this is displayed visually in Figure 2.5.
Ignition overpressure is another transient phenomenon that occurs during start-up and is well-established in solid rocket motors (SRMs). The presence of ignition overpressure generates high pressure loads on

the nozzle as to well as the added effect of influencing the ignition process itself. A study also found peak and frequency loads generated during the start-up transient due to the interaction between ignition overpressures and generated vortex rings.[60] One final observation for transient loading refers to the thermal gradients seen in nozzles. As can be expected, the thermal gradients are highest during start-up where the further away parts of the nozzle are still coldest, this, in turn, causes the highest thermal stresses.[39]
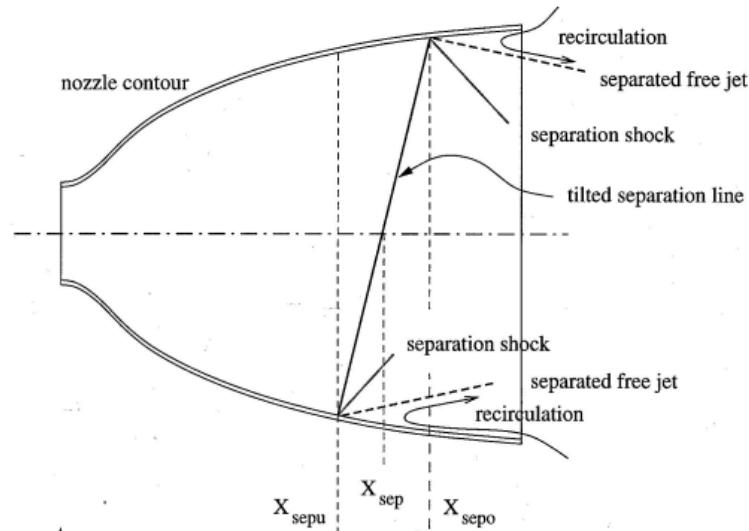


**Figure 2.5:** Asymmetric and tilted separation line, causing a moment around the throat[40]

As can be inferred, for steady-state operations, transient phenomena must not be captured. This is, although it is determined that transient phenomena such as side loads are one of the main factors that cause rocket engine failures. Since the thesis is also only focused on steady-state rocket operations and the subsequent loads and environment experienced during nominal operations, the CFD and FEA must capture appropriate loads for a steady-state analysis.

## 2.2.2. Nozzle Materials
A paper by NASA on erosion resistance and failure mechanisms of several nozzle materials in a small solid-propellant rocket engine stated the following nozzle materials commonly used; Refractory metals, Graphites, Cermets and Ceramics, and composite material.[62] Another paper on the analysis of composite De-Laval nozzles suitable for rocket application identified similar material types with the addition of refractory compounds and specifically reinforced plastics.[7]Another paper on the Characterization of novel ceramic composites for rocket nozzles in high-temperature harsh environments, identified refractory metal carbides separately as well.[33]

The aforementioned paper also states that Ultra-High-Temperature Ceramic (UHTC) are a recent development in aerospace. Such developments are attributed to the increased importance of high-temperature capable material and good oxidation resistance properties. However, due to the catastrophic failures observed by this material in high enthalpy flows, implementing Carbon or Silicon Carbide fibres in UHTCs is being investigated. This new material that contains fibres is called Ultra-High-Temperature Ceramic Matrix Composite (UHTCMC). The development of UHTCMCs is also part of the Horizon 2020 European $C^3HARME$ project, focusing on near zero-erosion rocket nozzles. When UHTCMCs were tested, they demonstrated much better performance compared to graphite nozzles.[33] Though the properties of the UHTCMC differed based on the fibre length, sintering conditions, and material porosity. The exact effect of such differences will be covered in the next subsection when discussing the effect of loads on nozzle material about specific material properties where applicable.

Given that the $C^3HARME$ project has dived greatly into UHTCMC, specifically ones with ZrB2 and SiC, a lot of information was gathered from respective reports. A report titled Introduction to H2O2O project $C^3HARME$ [56], found favourable results when manufacturing UHTCMC for ZrB2 enriched matrices. Hot press and spark plasma sintering techniques were used for the consolidation of the material. Additionally, the use of conventional powder processing methods to produce short-fire reinforced composites resulted in fully dense and crack-free material. It was also found that controlling temperature and dwell times has a direct effect on the fibre and matrix interface bonding. It was also mentioned why SiC is incorporated into the ceramic matrix, with benefits for densification, oxidation resistance, and fibre and matrix adhesion observed for the final material. Given the unique properties of UHTCMC, a Python-based tool called the Composite Pre-Design Tool (CoPreD) was also developed by the $C^3HARME$ to predict the mechanical and thermal properties of the composites being made as the specific constituents are being varied.[20] The program uses analytical equations to predict composite behaviour from constituent properties, however, the predictions made by the tool are not accurate enough to make concrete decisions on specific UHTCMC material compositions. The reasoning is that UHTCMCs are still relatively new and already-developed micromodels for composites are insufficient to capture behaviour at a microstructural level, this is further exacerbated with an increasing number of constituents. The usage of test data to validate the model was also stated, and it was explicitly said that the CoPreD tool can be used to determine if a fibre coating will be needed to yield crack deflection at the matrix and fibre interface.[20]

### 2.2.3. UHTCMC material behaviour and properties

To understand the complexity of UHTCMCs, It is first necessary to understand that there are many ways of manufacturing them. Such methods can be found in the literature, and the consensus is that the material properties are heavily dependent on the processing method and form of reinforcement decided upon when creating the UHTCMC.[38]
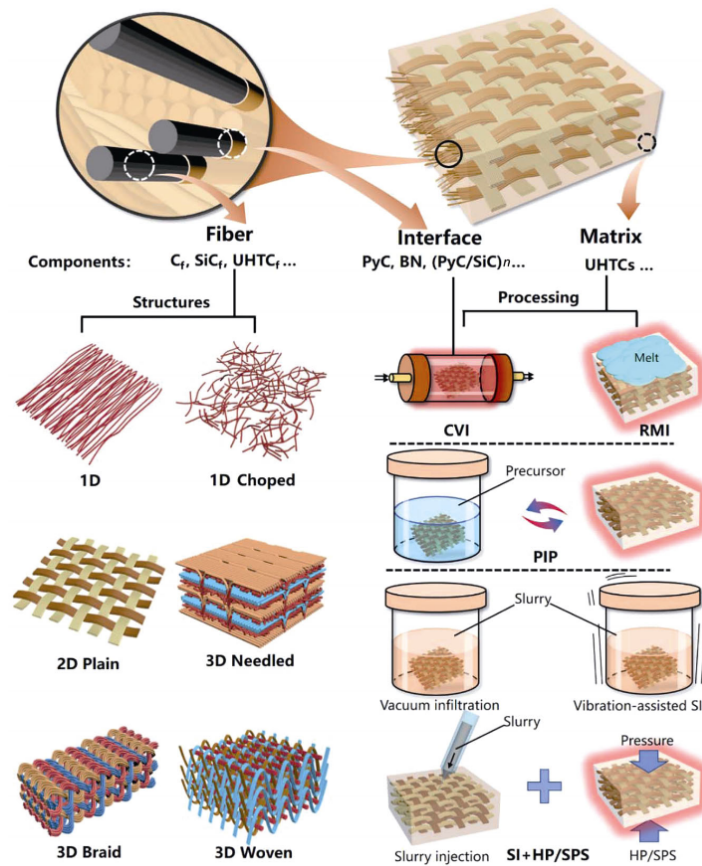


**Figure 2.6:** A diagram showing the different combinations and processes that go into making UHTCMCs[38]

It must also be understood that the purpose of UHTCMCs was to combine the advantages of CMCs and UHTCs whilst at the same time removing unfavourable material properties.[85]

| Material | Processing | Density (g·cm⁻³) | Open porosity (%) | Flexural strength (MPa) | Elastic modulus (GPa) | Ablation method | Temperature (°C) Flame | Surface | Ablation time (s) | Heat flux (MW·m⁻²) | Ablation rate | Ref. |
|---|---|---|---|---|---|---|---|---|---|---|---|---|
| 3D-$C_f$/C–TaC | CVI | 5.48 | 5 | 196.8 | | | | | | | | [214] |
| 3D-$C_f$/ZrB₂–SiC | SI+HP | 2.93 | 3.7 | 169±12 | | | | | | | | [176] |
| 1D-$C_f$/ZrB₂–SiC | SI+HP | 3.8 | 10 | 320±10 | | | | | | | | [250] |
| 1D-$C_f$/ZrB₂–SiC | SI+SPS | 4.0 | 5 | 260±20 | | | | | | | | |
| 2.5D-$C_f$/HfB₂–C | Slurry injection + CVI | 3.2±0.16 | 16 | 121.4±18.3 | 28.3±3.2 | | | | | | | [196] |
| 2D-$C_f$/ZrB₂–SiC | SI+PIP | 3.2 | 6 | 491±44 | 220±9 | | | | | | | [229] |
| 3D-$C_f$/ZrB₂–SiC | Vibration-assisted SI+HP | 4.10 | 2.6 | 204±18 | | | | | | | | [176] |
| 2.5D-$C_f$/C–ZrC–SiC | CLVD | | | | | OAT | ~3000 | | 60 | 4.18 | 1210 mg·s⁻¹ 1160 μm·s⁻¹ | [258] |
| 2D-$C_f$/C–HfB₂ | PIP+CVI | 1.77–1.84 | | | | OAT | | ~2150 | 90 | 4.18 | 2.75 g·m⁻²·s⁻¹ 3.14 μm·s⁻¹ | [211] |
| 2D-$C_f$/ZrB₂–SiC | SI+PIP | 2.15 | ~8.6 | | | Plasma torch | | 2500 | 300 | | 3.07 g·m⁻²·s⁻¹ 1.05 μm·s⁻¹ | [259] |
| 3D-$C_f$/C–SiC–ZrC | PIP | 1.94 | 8.5 | | | Plasma torch | | 2300 | 60 | | 0.56 mg·s⁻¹ 16.33 μm·s⁻¹ | [260] |
| 3D-$C_f$/ZrC–SiC | PIP | 2.11 | 15 | 136.0±13.1 | 31.8±2.6 | OAT | ~3000 | | 40 | 4.2 | 8.8±0.4 mg·s⁻¹ 23±1 μm·s⁻¹ | [230] |
| 3D-$C_f$/ZrC–SiC | PIP | 2.13 | 18 | 142.4±17.5 | 19.2±2.9 | OAT | 3000 | | 80 | 4.2 | 11.7 mg·s⁻¹ 31.8 μm·s⁻¹ | [231] |
| 3D-$C_f$/HfC–SiC | PIP | 3.18±0.04 | 13.2±0.4 | | | Plasma wind tunnel | | 1706–2454 | 600 | | 0.87 mg·s⁻¹ 0.067 μm·s⁻¹ | [232] |
| 3D-$C_f$/ZrC–SiC | PIP | 2.18 | 4.9 | 749±15 | 141±12 | | | | | | | [233] |
| 3D-$C_f$/ZrC–SiC | RMI | 2.64 | 3.5 | | | Plasma torch | | ~1890 | 60 | 4.02 | 6.97 mg·s⁻¹ 0.29 μm·s⁻¹ | [239] |
| 3D-$C_f$/ZrC–SiC | RMI | 2.52 | 1.7 | 380 | 61 | | | | | | | [209] |
| 3D-$C_f$/SiC–ZrC–TiC | RMI | 3.25 | 9.7 | | | OAT | | 2500 | 60 | | 0.008 mg·s⁻¹ 0.000 μm·s⁻¹ | [219] |
| 3D-$C_f$/C–SiC–ZrC | RMI | 2.42 | 5.0 | 143.5±11.2 | 13.4±3.3 | OAT | | ~2400 | 60 | 4.18 | 1.21±0.33 mg·s⁻¹ 5.90±0.90 μm·s | [240] |

**Figure 2.7:** A table compiling different UHTCMC materials and how their processing and composition affects material properties.[38]

In Figure 2.7, take note of the empty cell values, showing that data is missing and still needs to be gathered for the many different combinations. This is in stark contrast to UHTCs where there is much more information on material behaviour because it has been researched for longer. UHTCs have much more detailed research found on elastic modulus, different material compositions, as well as details into the material property relations to temperature and factors such as milling time.[65] UHTC material properties for ZrB2-SiC and their varying compositions have been researched in papers such as Mechanical properties of sintered ZrB2 –SiC ceramics [83], Microstructure and properties of ZrB2–SiC and HfB 2–SiC composites fabricated by spark plasma sintering (SPS) using TaSi 2 as sintering aid [16], and a thesis [65], Mechanical Properties And Thermal Residual Stresses Of ZrB2-SiC Ceramic Composites For Hypersonic Vehicle Applications Ceramic Composites For Hypersonic Vehicle Applications. As the UHTCMC material is to be used in a thruster in space with temperatures that may vary from near 0 Kelvin to 2500 Kelvin, the material properties are also expected to change. Most sources for UHTCMC, however, do not cover such material strength concerning changes in the temperature environment and the data can be inconsistent as the material manufacturing affects its properties. The general trends of UHTC can be potentially used to extrapolate material properties to higher temperatures, given the lack of sufficient test data on the specific UHTCMC that will be used in the thruster. Below are figures showing the temperature dependence of material strength against temperature for ZrB2-based composites.[75] The paper states that the tensile strength of the UHTC is much lower compared to compressive

and flexural as seen in Figure 2.8, therefore making it the critical parameter for failure evaluation.
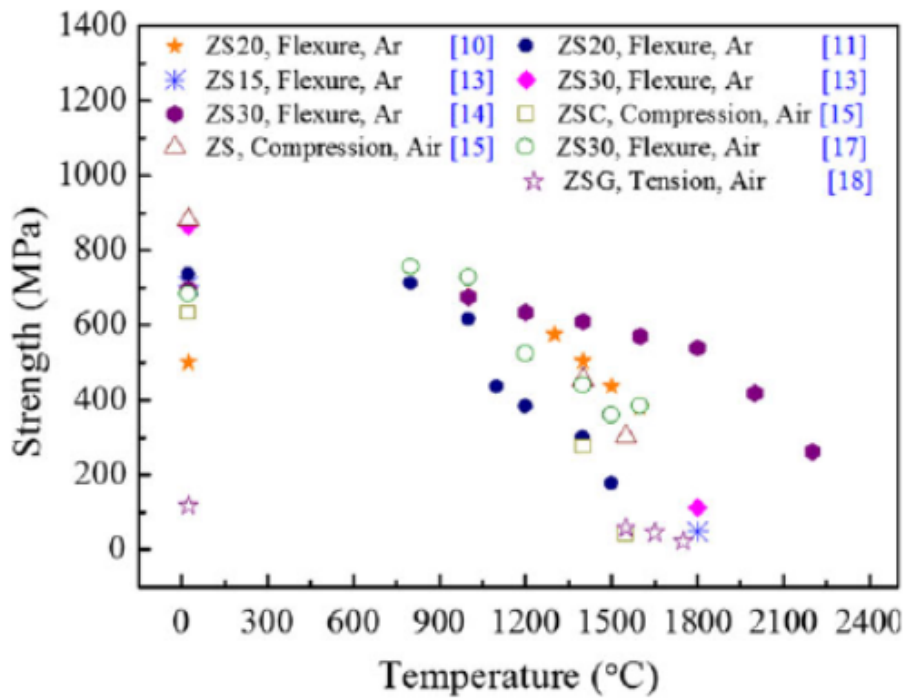


**Figure 2.8:** ZrB2-based composites strength variation with temperature[75]

The aforementioned paper then went on to further test the UHTC sample in tensile loads at different temperatures, as seen below in Figure 2.9.
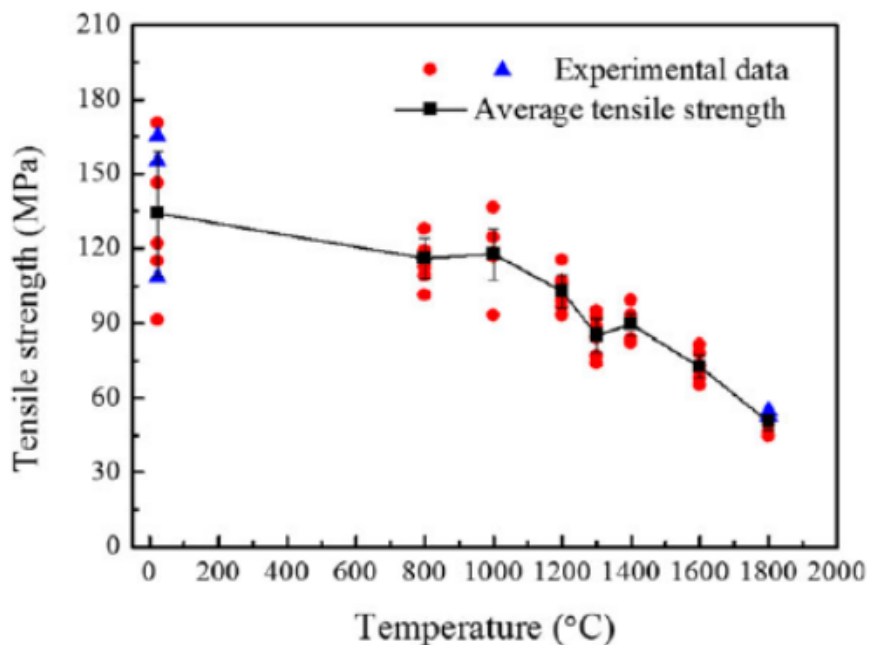


**Figure 2.9:** Tensile strength variation with temperature of ZrB2-SiC-graphite composite [75]

Including the above figures, The paper titles: ZrB2-SiC Based Ultra High-Temperature Ceramic Com-

posites: Mechanical Performance and Measurement and Design of Mechanical Performance and Measurement and Design of Thermal Residual Stresses for Hypersonic Vehicle Applications Thermal Residual Stresses for Hypersonic Vehicle Applications[66], delves into detail regarding the following material aspects of UHTCs: ablation rate versus time ad heat flux, thermal conductivity and specific heat capacity versus temperature, flexural, compressive, and Young's modulus versus temperature. The paper also looks into varying properties due to SiC volume fraction like similar aforementioned papers.

Overall, it is determined that the below list are just some of the factors that affect UHTCMCs properties derived from the UHTCs used and carbon fibre reinforcement when manufactured.

- The fraction of ZrB2 to SiC
- The porosity of the material
- The carbon fibre orientation, length, and fraction used
- The manufacturing method (and therefore factors such as sintering temperature, time, and pressure come into effect)
- SiC particle Size
- Material Purity

The above factors will have to be taken into account when determining how to extrapolate the material properties of a UHTCMC from its constituents, given the lack of information. A paper investigating the addition of short fibres to hot pressed ZrB2-SiC showed that the addition of the fibres increased the fracture toughness by 54.3%, from 4.25 $MPam^{\frac{1}{2}}$ to 6.56 $MPam^{\frac{1}{2}}$, while decreasing the flexural strength by 11% to 445 MPa from 502 MPa.[81] However it must be stated that in this case, no porosity was found, and it was determined to not affect the mechanical properties. To implement a specific UHTCMC material into the software, the material properties expected to be of use are as follows; Young's Modulus (with Poisson ratio, bulk modulus, or shear modulus), Coefficient of Thermal Expansion, thermal conductivity, and tensile yield strength, all preferably versus temperature. Given that there is the possibility that all the desired data may not be available and that the UHTC data is plentiful, assumptions can be made to facilitate extrapolating data such as fracture toughness and material behaviour over a range of temperatures. This will however come at the expense of not being able to represent the material exactly to the real material.

## 2.2.4. Damage and Degradation Mechanisms

It is established that loads on the nozzle can have many effects. A main concern of these loads is the damage that can occur to the thruster due to stresses, thermal gradients, and vibrations. Cyclic loading, repeated thermal exposure, intrinsic material properties such as CTE, thruster design, and specific material composition are all factors that combined with loadings can cause different types of failures to occur in thrusters. This section will aim to outline all damage mechanisms and motivate the factors affecting them. A list of the different mechanisms and effects that will be covered is given below.

- **Thermal (Thermal Shocks and gradients):** This mechanism deals with the effect of material properties and thermal effects on the damage that can occur
- **Vibrational:** This mechanism can be prevalent in steady-state conditions with constant vibrations. It covers effects that concern fatigue cycling and several loadings.
- **Erosion, Ablation, and Oxidation:** These effects while distant are combined since they occur at the same time in most nozzles due to the fluid flow, specific propellant composition, wall and propellant combination, etc.

### Thermal

As can be expected, different loads can have different amounts of damage caused to the thruster over certain durations of time. One study on Propulsion tests on ultra-high-temperature ceramic matrix composites for reusable rocket nozzles attributed the presence of sharp corners at the convergent section of the nozzle to the formation of microcracks under loading.[57] Another study, On the thermal shock resistance and mechanical properties of novel unidirectional UHTCMCs for extreme environments, stated that when there is a mismatch in the coefficient of thermal expansion (CTE), there is the possibility of

micro cracks and macro cracks to occur. Such effects are especially prevalent in composites that apply a 0 and 90-degree fibre cross-ply architecture. The cracks still have a likelihood to occur in composites that use a unidirectional fibre layout, with the cracks forming perpendicular to longitudinal fibres. An additional cause of cracks is also attributed to differential shrinkage between the matrix and fibre and during densification. [85] The thermal expansion mismatch between fibre and matrix, causing cracks to form inside the identified matrix when cooled, was also corroborated in another paper on UHTCMC. It was also suggested that such cracks can be partially mitigated by controlling the cooling process.[56] Such crack formation, element shape and expansion of material is very important to consider when taking into account the high range of operational temperatures that a thruster may have to operate in, especially in the vacuum of space with temperatures reaching as low as 2.725 Kelvin.[35] A paper on Selection, processing, properties and applications of ultra-high temperature ceramic matrix composites, UHTCMCs – a review, also found stated similar concerns for CTE of UHTCMCs. When comparing Ultra High-Temperature Ceramic (UHTC) materials to UHTCMCs, the lower CTE is due to the presence of carbon fibres. Additionally, CTE is stated to depend more on the matrix and the material porosity, with large differences in CTE between the fibres and UHTC matrix yielding residual stresses.[5]

A paper on the Mechanical behaviour of carbon fibre reinforced TaC/SiC and ZrC/SiC composites up to 2100°C states cracks being found when testing at temperatures of 1500 to 2100 Celsius in the case of ZC20, attributed to the high ceramic matrix strain. TC20 showed only blisters occurring due to the formation of gaseous species such as SiO. The differences between ZC20 and TC20 results are the lower melting point of ZrC and the fibre and matrix interface strength being weaker due to the higher porosity of the ZC20. Another interesting observation is that the porosity of the ZC20 increased with high-temperature testing, most likely due to the evaporation of SiC. [74] A closer look is taken at the nozzle specifically, and the effect of loads on the material. As mentioned previously, thermal stresses in a nozzle can arise due to the large temperature difference in the chamber and the nozzle exit. Such thermal stresses cause cracking and severe erosion locally at cracked regions, this is especially prevalent during the startup transients where the nozzle exit is still at a much lower temperature compared to the chamber, hence the largest observed thermal stresses.[39] Such large thermal stresses that occur are expected to be smaller, using simplified analysis, when occurring in smaller thrusters.[7]

### Vibrational
The thruster will be subject to a certain vibrational loads during operations, whether the operations are steady or transient. A study on Experimental characterization of fatigue life of $ZrB_2 - SiC$ based ultra-high-temperature ceramic matrix composites showed favourable long fibre-based UHTCMC behaviour when under vibrational load.[50]
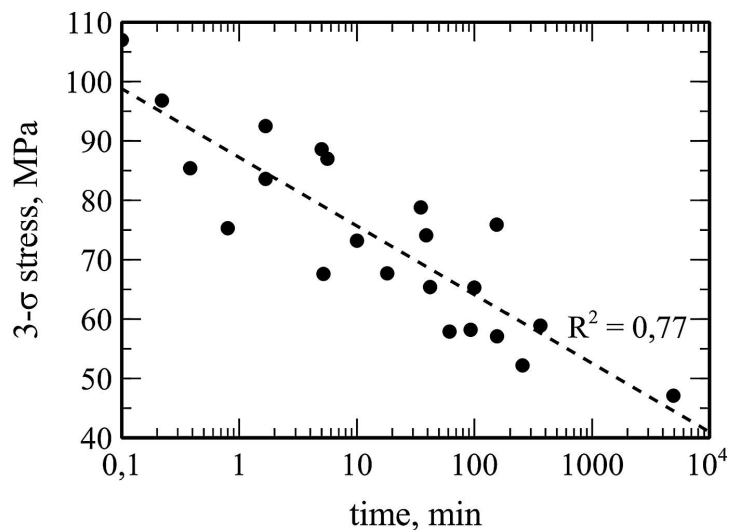


**Figure 2.10:** Fatigue life, measured in time before failure for short fibres UHTCMC [50]

UHTCMCs with short fibres broke under continuous loading, the material no longer showed a reso-

nance peak between 100 and 1000 Hz. Long-fibre UHTCMC performed much better in fatigue testing. A sine dwell test was instead performed on the long fibres, to demonstrate its fatigue performance. The paper concludes that it is possible to define the fatigue life concerning time or the number of cycles. The aforementioned paper recommended testing at high temperatures to capture performance at operational conditions.[50] The graphs below show the correlations that were found for short and long fibres, Figure 2.10 and Figure 2.11 respectively.
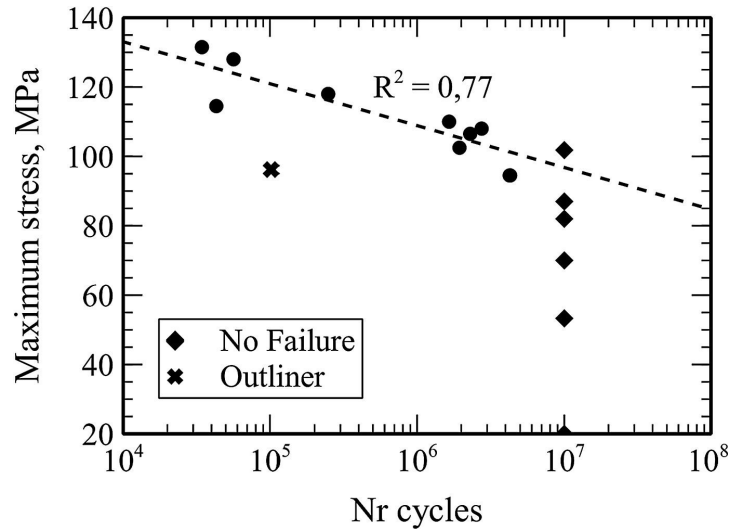


**Figure 2.11:** Fatigue life measured in cycles before failure for long fibres UHTCMC[50]

### Erosion, Ablation, and Oxidation:
First, a description of each of the mechanisms is given below. These can be used to obtain a better understanding of the information and sources compiled.

- *Ablation:* This is a chemical process of material being removed from the inner surfaces of the thruster due to the high temperatures experienced.
- *Erosion:* This is a mechanical process where the material is wearing away due to the impact of internal fluid flow and combustion material with the walls.
- *Oxidation:* This refers to chemical compounds reacting and forming oxides. Such oxides can be deposited on the inner walls of the thruster

A consequence of high nozzle loads is erosion, thermal gradient formation and as a result thermal shock in the radial direction with tensile stresses in the longitudinal direction. A less porous UHTCMC made by hot pressing under repeated thermal shocks leads to lateral cracks, leading to stress concentrations at sharp edges. An interesting observation for testing a UHTCMC made of $ZrB_2/SiC$ is a decrease in nozzle throat diameter, thereby increasing inner wall pressure. This was due to the oxidation process of the material. The deposition of a $ZrO_2$–$SiO_2$ coating layer formed during this process is attributed to the decrease in throat diameter. It must be noted that this layer was not chemically bonded to the surface and was removed during a polishing procedure. The throat diameter decrease was from 9.6 mm to 9.4 for SPS-2 and 9.6 mm to 9.2 for HP-2. However, HP-3 had no measurable difference observed, Additionally, a $SiO_2$ liquid layer that was formed was displaced downstream of the nozzle by the gas towards the divergent section. Repeated testing leads to the liquid oxide layer forming and protecting the divergent nozzle section from further oxidation.[57] This paper was the only one found observing a decrease in nozzle throat diameter, as opposed to other papers either observing no measurable difference or an increase.
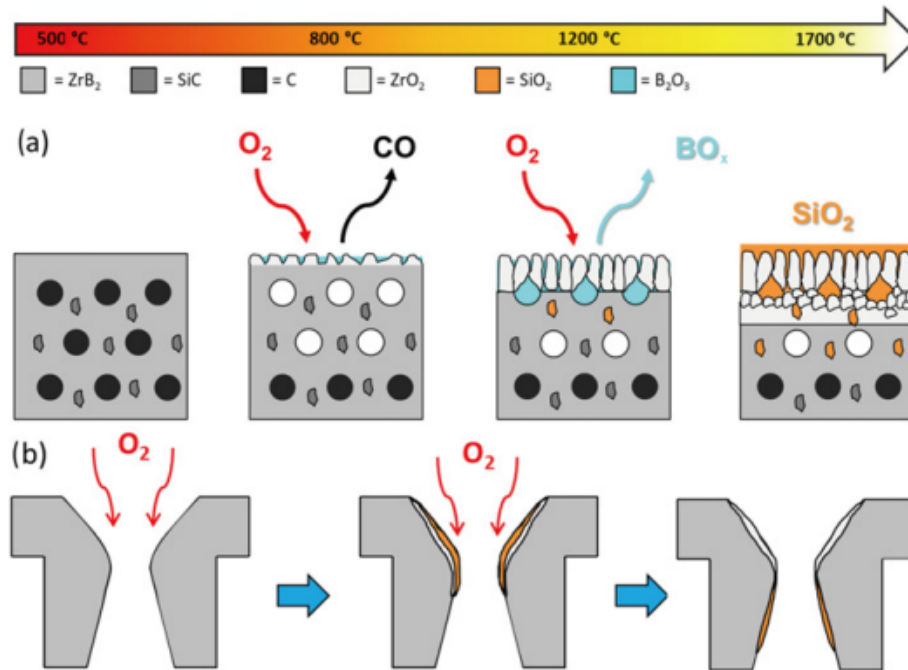
**Figure 2.12:** Diagram showing the flow and formation of liquid $SiO_2$ to the divergent section, creating the protective oxide layer [12]

A paper additionally states the mechanisms by which rocket nozzles sustain damage; oxidation/vaporisation of nozzle wall material, surface ablation, entrained solid or liquid particles removing wall material, and erosion.[37] All the above conditions can occur during both the steady and transient states of the thruster operation and further reaffirm that these phenomena are paramount to understanding thruster damage that occurs. When looking at the chamber specifically, it is seen that blanching of the chamber liner could occur due to the reaction of oxidizer-rich gases and cryogenic droplets in LREs. This occurs in copper alloy linings, with the corrosion causing the liner to become flaky. The combustion chamber is also weakened as it is cyclically loaded due to hydrogen embrittlement, fatigue, creep, oxidation, and free radical OH attacks. Such effects fail in the longitudinal direction.[12]

A paper, investigating the aero-thermal chemical response of UHTCMC [54], states that the worst-case ablation environment for UHTCMC is at maximum heat flux and lowest pressure. Since this research was for the $C^3HARME$ project, the extreme flux and pressure cases were defined as follows: maximum heat flux of 1988 $kW/m^2$ and maximum pressure of 65 $kPa$. It must be noted that this combination of heat flux and pressure does not however need to be sustained by the material simultaneously. The paper also states that there is a transition from passive to active oxidation for UHTCMCs using SiC fibres at the lowest pressures.

Research called An Experimental Investigation Into Aspects of Erosion in Rocket Motor Tail Nozzles [37] showed many interesting conclusions discussing damage patterns, the extent of damage and the factors affecting them. The points to take away from the paper are listed below.

- Even distribution of solid particles in the gas stream results in even nozzle erosion, with grooving occurring in the event of particle concentrations in certain angular positions
- Impact angle on the nozzle wall affects damage. Ductile material gets more damaged at shallow angles of attack, this indicates shear forces playing a role. Brittle material gets damaged at high angles of impact by cracking, crazing and spalling.
- Increasing particle speed and decreasing particle size increases damage, with evidence showing particle concentration affects particle velocity and hence erosion.
- Erosion damage increases with wall surface temperature. This is attributed to higher temperatures and reduced mechanical strength of the wall material.

Other sources also suggested a relation between particle size and angle of impact to the damage observed.[12] Additionally, there was also a correlation found between temperature and molar mass of the species on ablation. The paper on Experimental analysis of SiC-based refractory concrete in hybrid rocket nozzles states that an increase in static temperature increases ablation additionally so does an increase in oxidizer molar mass.[57] Furthermore it was also mentioned that the ablation rate at the throat depends on parameters such as gas flow temperature, flow velocity, surface roughness and oxidizer molar fraction, though it was not feasible to relate these parameters adequately to each other to determine when ablation starts.[10] Another consideration for erosion is the presence of cracks already in the material. As cracks already in the material promote higher erosion locally at the crack.[39]

UHTCMC fibre length and porosity also play are role in erosion resistance. A study on this determined that out of 3 total samples, one of the long fibre samples survived with no erosion damage. Long fibre UHTCMC chamber inserts had visible oxidation during operation while short fibres were subjected to fatal structural cracks, although no change in throat diameter was seen. The short fibres' poor performance was due to the faulty sintering process which caused too little porosity and hence the material behaved like a brittle ceramic.[33] This paper also shows the importance of ensuring careful watching over the manufacturing process and ensuring sufficient porosity is present for adequate thermal shock resistance and not just for erosion.

Other factors intrinsic to the propellants and operating conditions also affect the ablation and erosion observed in the nozzle. The throat ablation rate was found to be highly dependent on chamber pressure and propellant mixture ratio. With a higher propellant mixture ratio, higher static temperatures occur, which can not only increase ablation as discussed previously but also activate ablation to occur earlier. Being above or below the stoichiometric ratio can explain the trends seen in the chamber pressure ratio with other parameters such as mass flux and the characteristic velocity. Furthermore, ablation is also observed to have a linear relation with chamber pressure for hybrid and solid rocket motors. A positive correlation between combustion time and throat ablation is also seen. [10] About combustion times, for UHTCMC with overall operating times up to 30 seconds, no measurable erosion or failure was encountered.[57]

A final effect to be discussed is the asymmetric ablation of a nozzle. A paper observed such asymmetry and reported the following; that such asymmetry may be due to gravitational effects, but that needs to be confirmed via testing. The paper tested three nozzles HERA 17, HERA 18, and HERA 20, SiC-based refractory micro concrete nozzles, with varying stoichiometric conditions and combustion durations. It was found that asymmetric ablation may cause gas flow separation in HERA 17, a phenomenon usually observed when the atmospheric pressure is 2.5 to 4 times greater than the exit pressure. The jet separation implies the formation of a tangential thermal gradient, which is hypothesised to lead to longitudinal cracks appearing. Circumferential cracks on the other hand depend on stresses generated during combustion or assembly. The addition of short metallic fibres is also determined to improve durability for the SiC-based microcrete.[10]

### Other Considerations

As cracks can already be present in the nozzle at manufacturing and the fact that nozzle wall thickness can be varied in the thruster design for this thesis, it was expected that a relation between crack growth and nozzle thickness could be present. A paper was found investigating this for 304 stainless steel where specimen thickness was plotted against fatigue crack growth rate (FCGR), and it was found that the growth rate increased with specimen thickness.[41] Since this is material dependent, UHTCMCs will need to be investigated experimentally for such behaviour.

### Effects on Thruster Performance

It was discussed what the different damage mechanisms are and what are the variables that affect them. This section will now aim to describe the consequences of having damage to the thruster performance. The table below is given to present this logically.

**Table 2.3:** Damage mechanism and its effects on thruster performance

| Damage | Consequence |
|---|---|
| Throat Ablation | • Increase in throat diameter, decrease in pressure curve, decrease in thrust, decrease venturi pressure [84][10]<br>• Decrease life cycle if ablation is severe<br>• Re circulation zones and instabilities in case of gas separation due to asymmetric ablation [10] |
| Thermal Stress Cracks | • Cause areas of increased localised erosion [39]<br>• Decrease the viable life cycle of thruster |
| Chamber Liner Blanching | • Decrease load carrying and heat transfer ability [12] as a result, expected to decrease its life cycle |
| Erosion | • Decrease chamber pressure affecting thrust and specific impulse [57]<br>• Decrease life cycle if erosion is severe |
| Delamination between overlapped layers[56] | • Decrease in the life cycle of thruster<br>• Decrease in material properties and performance |
| Oxidation | • Can reduce nozzle throat area given oxide deposition in the throat with specific material combinations in UHTCMC. [57] |

## 2.2.5. How to protect nozzles

There are two main methods of protecting a nozzle, or reducing the damage that it has to sustain; applying a protective coating/film or altering the operating conditions the nozzle operates. Each one of these methods has its benefits, specific methods to apply them, and the most ideal situation to use them in. Protective coatings and such methods will first be discussed before moving on to altering the operating conditions of the thruster.

One of the methods of protecting a nozzle is using a less reactive protective thin layer atop the nozzle wall itself. A paper on Experimental analysis of SiC-based refractory concrete in hybrid rocket nozzles, suggests using chemical vapour deposition to create a layer of thermoset ablative material, one which is more resistant to ablation.[10] Another paper suggests using protective coatings to reduce the issues of damage to unprotected combustion chamber liners to reduce cyclic fatigue.[12] The aforementioned paper also states the importance of damage evaluation and detecting defects and flaws during the manufacturing and assembly of a rocket. It was suggested to use Non-Destructive Evaluation (NDE) techniques to detect such faults in material during the manufacturing process. Below is a summary of all the NDE techniques mentioned.

**Table 2.4:** Summary of NDE methods[12]

| Method | Description |
|---|---|
| Penetrating Dye | Used to check for surface cracks and make them more visible. |

**Table 2.4 continued from previous page**

| Method | Description |
| --- | --- |
| Eddy-current probe | By checking for changes in conductivity, cracks below the surface can be detected. |
| Ultrasonic Shear waves | Used to look for deeper cracks in the material by listening to characteristic echoes. |
| Radiographic Testing | X-ray, gamma rays or neutrons are shot through the material and detected on the other side with a detector. Bright spots or shadows indicate flaws in the material. |
| X-ray computed tomography | Useful for geometry characterization of local damage in rocket motor cases made of composite material |
| Thermographic Test | Detects subsurface defects by variation in heat flow, causing localised hot/cold regions. |
| Shearography | Holographic techniques are used to identify regions of very fine relative strain or displacement by making use of reflections of the material surface and a specialised camera. |
| Acoustic emission Monitoring | Small microphones are used to detect sound emissions from the hardware throughout a loading cycle. Cracks and flaws make noise, and their position can be determined by triangulation. |

As seen in Table 2.4, many methods can be used, however, not all of these methods can be applied in all situations and some have limitations. Large enclosed structures are difficult to perform NDEs on. Ultrasonic techniques may need large supports in place, and acoustic emission monitoring has difficulty in event spatial location. The surface roughness of the material can affect reflectivity and emissivity, affecting techniques dependent on heat for flaw detection. Finally, ultrasonic, X-ray, and eddy current techniques may require components to be disassembled.[12] It must be said that if the tests are performed at every step of the manufacturing process on a component level, then this may prevent the need for disassembling the components. However, this can prove costly, additionally, once a test is performed on the entire system, it would expect to need to be disassembled for inspection anyway for damage analysis. It must be further noted that control of the manufacturing process itself is also imperative to the material characteristics. An example is the sintering process, fibre integrity can be compromised, causing short-fibre UHTCMC to behave in a brittle manner.[33]

Looking at coating techniques and materials, due to the good material properties and reaction resistance of UHTCMC [68], the methods used to apply coatings of different types of UHTCMC will be covered. The methods that will be stated can apply to the following UHTCMC materials; $ZrC$, $ZrB_2$, $HfC$, and $HfB_2$. This can be especially useful if it is seen that erosion is severe in the Nozzle despite it already being made of UHTCMC, requiring perhaps a layer of different UHTCMC composition to act as a protective shield. Therefore, it would be necessary to know the options available to apply such a coating and if there are any limitations. These methods are shown in Table 2.5

**Table 2.5:** methods to apply UHTCMC coatings[68]

| Method | Description |
| --- | --- |
| Chemical Vapour Deposition (CVD) | A precursor in vapour-phase reacts with a surface substrate to form the protective coating ($ZrC$, $ZrB_2$, $HfC$, $HfB_2$) |
| Physical Vapour Deposition (PVD) | Process involves using electrolysis-induced vaporisation of substances which then condense onto a substrate. The target acts as a cathode, where a reaction occurs with the gas molecules.($ZrC$, $HfB_2$) |

**Table 2.5 continued from previous page**

| Method | Description |
|---|---|
| Reactive melt infiltration | Molten Metal is infused into a ceramic substrate. The ceramic would have to be heated to above the metal melting point, for the metal to flow in and fill the preform pores.($ZrC$, $HfC$) |
| Magnetron sputtering | Better than CVD for $HfC$ due to low deposition temperature, easier, more adaptable, ideally suited or multi-layer coatings. ($ZrC$, $HfC$) |
| Plasma Spraying | Process gases are ionised forming a plasma plume reaching high enough temperatures to melt the UHTCMC powdered materials and "spray" them at varying velocities onto the surface inducing varying properties. ($HfC$ ) |

Another method of protecting the thruster would reconstitute a redesign focused on smoothing out any sharp edges. As a study fond microcracks occurring due to sharp angles in a thruster prototype[57], this suggests designing thrusters while keeping in mind smooth corner to avoid localised stress concentrations. This method is most likely inapplicable to the thesis thruster as the design is fixed, and such drastic design change would only occur as a last resort if applying a coating or film is simply not enough of a protective measure or the stresses are too high . A different approach to protecting the thruster is altering the combustion and propellant mixtures used. Since it was determined that erosion rates can depend on the oxidising species, chamber pressure, combustion time, and chamber temperature, the exact operating conditions of the rocket can be altered to reduce the stress.[10] This is expected to however come with performance drawbacks, as a reduction in chamber pressure or adjustment to the fuel mixture ratio can result in less thrust being developed, thereby decreasing the thrust-to-weight-ratio-given no other design alterations.

## 2.3. The Research Gap

The literature review of UHTCMC material and their subsequent usage and modelling in a thruster environment showed that research in this specific area is either not performed to such an extent due to the relatively new nature of the UHTCMC material, or the research is still not made publicly available on the subject. Until further strides are made in characterizing the performance and manufacturing of UHTCMC with varying parameters, the behaviour of the material cannot be described with the confidence that is seen when using traditional materials such as Silica carbide, etc. It must be said that the research being done is very promising, especially when it comes to the $C^3HARME$ project. Though the research there is more focused on placing samples in the exhaust plumes to characterize performance at high heat fluxes and low pressures, the results are still promising and loads can be seen as comparable in certain situations.

Additionally, not much has been covered on how to adequately capture all the "necessary" material properties in different FEA software. The closest paper found on how to capture all the material properties is the CoPreD model, which was unable to be validated for specific cases of UHTCMC because of a lack of test data. It was also stated that information on the microstructure of UHTCMC is not well-researched in the literature.[20] This would inherently limit the extent of reliable numerical methods that can be applied to simulate the material, given the lack of understanding of certain material structure behaviour. This material modelling gap is crucial for FEA analysis, as such the methods used to represent the material will also have their advantages and drawbacks in capturing certain material behaviour. A paper was not seen that provides specifics of the FEA setting or software used to construct a nozzle made of UHTCMC and proceed to find deflections and stress concentrations. Traditional materials have plenty of FEA papers found, capturing the data adequately, but with the new class of UHTCMC, this gap in research will have to be dealt with with great caution to ensure the simulation results are comparable with the real world. Finally, given the unique composition of the UHTCMC ZrB2 and SiC combination with ideally no but practically little porosity, the erosion, oxidation, and other damage and degradation mechanisms will need to be investigated too.

## 2.4. Research Question and sub questions

With this, the research questions will be devised based on the literature study results. The research question and sub-questions will be given here below.

---

**Research Question 1: What are the loads experienced by the thruster under nominal operations?**

1.1 What are the thermal loads and boundary conditions experienced by the thruster?

1.2 What are the structural loads and boundary conditions experienced by the thruster?

1.3 What are the expected use cases for the 100 N thruster and their corresponding extreme operating conditions?

---

**Research Question 2: What are the 3D FEA steady state analysis results of the 100-N Thruster?**

2.1 What are the temperatures and stresses experienced by a UHTCMC thruster, and where are they most severe?

2.2 What are the deflections experienced by the UHTCMC thrusters, and what are their effects?

2.3 What is the optimum thickness for the UHTCMC thruster?

---

**Research Question 3: What steps can be taken to reduce the loads and stresses experienced by the nozzle over time if required?**

3.1 What is the cause and effect of the UHTCMC thruster degradation from a qualitative perspective?

3.2 Should there be preventative measures taken to protect the thruster from damage over operational life due to erosion, thermal damage, or more?

3.3 How can damage effect be related to prolonged operation affect the thruster system?

---

Given the limitations and results found during the literature study, these questions will be aimed to be answered. The questions are aimed to answer questions related to the required knowledge when making a finite element analysis, the output results desired of the analysis, and the long-term behaviour of a thruster design. Such questions can be deemed crucial given that the thrusters are aimed to be made of a UHTCMC material which its composition and specific mixture properties is not found in literature.

# 3

# Work Plan

The methodology that will be employed during the duration of the thesis will be outlined in this chapter. This chapter covers 4 aspects of approaching finite element analysis of a UHTCMC nozzle. Starting with managing time, the resources and information available in section 3.1. Then the material properties inputted to ANSYS will be covered in section 3.2. Afterwards, the methodology used to approach the FEA and how to select the most optimum model thickness is denoted in section 3.3. Finally, the methodology for post-processing analysis will be outlined in section 3.4.

## 3.1. Information, Resource, and Time Management

Given the limited time for the thesis, adequate time management is imperative. This is also combined with utilising the available resources to the most capacity to maximise the results of the thesis. The resources that are available during this thesis are as follows, but not limited to; advice and information from professors, state-of-the-art research papers, thesis reports of similar work, ANSYS tutorials and user guides, and ANSYS forums for debugging.

As was mentioned, ANSYS tutorials, user guides and forums will be used. This is because ANSYS 2023R2 was chosen as the software to use for the analysis done in the thesis. The reasons for using ANSYS 2023R2 are listed below.

- The CFD results and analysis that will be used as input loads are done in ANSYS 2023R2, this ensures data compatibility and smooth importing and reading files experience when opening the data generated on a different machine.
- ANSYS 2023R2 is available with no restriction to the number of elements or nodes from default to all TU Delft students. This makes it easy to set up and start since the installation manuals and experienced ANSYS users are highly likely to be found among students and professors.
- Data and results transferability from thermal to structural modules, and high availability of varying modules and guides. The entire analysis of thermal and structural can be done with ease within the ANSYS 2023R2 software, with very detailed and prevalent user guides on all available modules. This also includes recommended steps to take for common analysis at times.

Another important factor to take into account is the time management throughout the thesis. More importantly, how to most effectively use the available time that would otherwise be spent waiting on results or responses from colleagues. To ensure highly effective time usage, the following guideline is used:

- Keep a schedule using Google Calendar or similar software to ensure important dates and milestones are saved
- During long simulations, user guides and a review of the simulation settings can be looked over to ensure everything is running as intended. This would occur even after the pre-run checks.
- When waiting for results from colleagues such as CFD and materials input, verification procedures for what to do with the data and how to handle it will be thoroughly investigated and documented.
- As contacting professors for guidance may take a long time and their time is limited, establish a list of questions to ask and a clear agenda before attending the meetings to maximize the output.

- To minimize time wasted on dead-ends and potentially too complex methodologies that are being tested without knowing so, the processes will be run by professors and colleagues to obtain feedback. This feedback can point out complexity concerns, thereby causing a rethinking of the methodology approach to fit within the thesis milestone time frames

It must be noted that running ideas and methodologies by supervisors and colleagues will not be done immediately, but after enough research has been done to form a solid basis of understanding as to what is expected. The main role of obtaining external feedback here is to show other avenues that have not yet been explored or to point towards unforeseen complexity and issues with the process chosen. With all this in mind, the next section on material properties and how to check that it behaves properly with the expected loads will be discussed.

## 3.2. Material

This section will cover the material properties of the material that the thruster will be made of and how they were derived. Since the material properties for the custom UHTCMC were not found in its entirety online, the individual constituents' material properties were complied with and used to estimate the UHTCMC material properties, found in Table 3.1. The UHTCMC of ZrB2-20vol% SiC and 35 vol% short chopped carbon fibres is split into two: ZrB2-20vol% SiC and short chopped carbon fibres. They will have their material prompters over a range of temperatures derived in subsection 3.2.1 and subsection 3.2.2 respectively. Afterwards, the UHTCMC material properties, which combine the properties of its constituent, will be described in subsection 3.2.3.

**Table 3.1:** The individual constituents of the UHTCMC

| Volume Fraction | Material |
|---|---|
| 0.65 | ZrB2- 20vol%SiC |
| 0.35 | 6mm Chopped Carbon Fibre |

### 3.2.1. ZrB2-20vol% SiC Material Properties

ZrB2- 20vol%SiC with short carbon fibre and its properties were not directly found over a range of temperatures. The individual constituents of the UHTCMC can however have their material properties found. ZrB2-20vol% SiC has been thoroughly investigated in literature and therefore had plenty of data points to be found and documented. The main reason this approach is preferred is that the UHTCMC material properties always focus on material strength, fracture toughness and Young's modulus. Finding a paper that listed all the material properties throughout a large range of temperatures was not found for UHTCMC, but was much more prevalent for UHTCs.

**Table 3.2:** Compilation of all ZrB2-20%vol SiC material properties over a range of temperatures

| Temperature $C$ | Young's Modulus $GPa$ | CTE $10^{-6}K^{-1}$ | Thermal Conductivity $Wm-1K-1$ | Specific Heat $Jkg^{-1}K^{-1}$ | Fracture Strength $MPa$ | Source |
|---|---|---|---|---|---|---|
| RT | - | - | - | - | 445 | [81] |
| RT | 474 | - | - | - | 463 | [83][65] |
| RT | 458.8 | - | 43.28 | - | - | [16] |
| RT | - | - | - | - | 558.27 | [65] |
| RT | - | - | - | - | 329.3 | [65] |
| RT | - | - | - | - | 523.71 | [65] |
| RT | - | - | - | - | 540.66 | [65] |
| RT | - | - | - | - | 552.31 | [65] |
| RT | 473.5 | - | - | - | - | [66] |
| RT | 506 | - | - | - | 487 | [44] |
| RT | 504 | - | - | - | 546 | [86] |
| RT | - | - | 89.53 | - | - | [27] |
| RT | - | - | 99.2 | - | - | [27] |

**Table 3.2 continued from previous page**

| Temperature C | Young's Modulus GPa | CTE $10^{-6}K^{-1}$ | Thermal Conductivity $Wm-1K-1$ | Specific Heat $Jkg^{-1}K^{-1}$ | Fracture Strength $MPa$ | Source |
|---|---|---|---|---|---|---|
| RT | - | - | 131 | 560 | - | [43] |
| RT | - | - | 87 | - | 404 | [43] |
| RT | - | - | 89.5 | 448 | - | [43] |
| RT | - | - | 88.53 | - | - | [43] |
| RT | 480 | 6.5 | - | - | 523 | [76] |
| RT | 431* | - | - | - | 578.4* | [66] |
| RT | - | - | 67.6 | - | - | [76] |
| 150 | - | - | - | 563 | - | [26] |
| 200 | 497* | - | - | - | - | [86] |
| 200 | - | - | - | 599 | - | [26] |
| 200 | - | - | 85 | - | - | [42] |
| 200 | - | - | 64.5 | - | - | [76] |
| 250 | - | 6.21 | 100* | 635 | - | [26] |
| 300 | - | - | - | 645 | - | [26] |
| 400 | 492* | - | - | - | - | [86] |
| 400 | - | - | 77.5* | - | - | [43] |
| 400 | - | - | 62.1 | - | - | [76] |
| 500 | - | 6.45 | 92* | - | - | [26] |
| 600 | 485* | - | - | - | - | [86] |
| 600 | - | - | 72.5* | - | - | [43] |
| 600 | - | - | 60.8 | - | - | [76] |
| 750 | - | 6.64 | 86* | - | - | [26] |
| 800 | 476* | - | - | - | - | [86] |
| 800 | - | - | 68* | - | - | [43] |
| 1000 | 462* | - | - | - | 677 | [86] |
| 1000 | - | 6.84 | 75* | - | - | [26] |
| 1000 | - | - | 74.79 | - | - | [27] |
| 1000 | - | - | 79 | - | - | [27] |
| 1000 | - | - | 66* | - | - | [43] |
| 1000 | - | 7.02 | 55.9 | - | - | [76] |
| 1200 | - | - | 63.5* | - | - | [43] |
| 1250 | - | 7.04 | 75* | - | - | [26] |
| 1300 | 443.5 | - | - | - | - | [86] |
| 1300 | - | - | - | - | 605* | [86] |
| 1400 | - | - | - | - | 546 | [86] |
| 1400 | - | - | 62 | - | - | [43] |
| 1500 | - | - | - | - | 500 | [86] |
| 1500 | - | 7.18 | 75* | - | - | [26] |
| 1600 | - | - | - | - | 460 | [86] |
| 1750 | - | - | 65* | - | - | [26] |
| 2000 | - | - | 66* | - | - | [26] |

From Table 3.2 above, the material properties of ZrB2 were compiled. Density was only taken at room temperature with values 5500 and 5720 taken from [81] and [66] respectively. Poisson ratio was also

taken only at room temperature with values 0.138, 0.125, and 0.144, all taken from [86], [76], and [66] respectively. One of the main considerations about this compiled data is that most papers gave the results as a table and the results had to be estimated based on the coarse graph provided, an asterisk marks such numbers. Additionally, while more sources can be found for the ZrB2 with 20% vol SiC, some sources show data points which have extremely high variability for what is to be expected for such a material. Therefore, these numbers were ignored. This can be done since the material itself can be manufactured in a multitude of ways and there are many factors which can affect the material qualities, from the grain size of the constituents to the sintering or hot pressing process, to the porosity of the material. The table attempts to avoid such numbers with high variability and only captures numbers that are within acceptable ranges of the material.

The stiffness of the UHTC will be calculated more intensively. All of the asterisk-labelled stiffness values come from a singular source. Then, to account for the decrease in stiffness over time, the rate of decrease will be determined using values marked with an asterisk from the paper high-temperature bending strength, internal friction and stiffness of ZrB2–20 vol% SiC ceramics [86]. The CTE was simply averaged at all temperatures, and the temperatures of 250 and 500 were used to linearly extrapolate and estimate the room temperature CTE to smooth out the curve. The thermal conductivity will only be averaged at each temperature value. Although the graph produced due to this would be erratic, it still shows a downward decreasing trend of a lower thermal conductivity with temperatures. A relation was not opted to be used here since there is a lot of data and factors that can easily affect the material properties, with grain size and porosity expected to be the greatest factors. Density and Poisson ratio are kept constant with temperature, this is a major assumption that is made since there is not much data found on the material's Poisson ratio behaviour with temperatures. Specific heat capacity of the material uses the theoretical values of specific heat of the material found in heat conduction mechanisms in hot pressed ZrB2 and ZrB2–SiC composites, [43]. The theoretical values will be used to determine the rate of change of specific heat at higher temperatures and to fill out data points that are left empty. This is similar to the Young's Modulus process, but instead of the relation and rate of change of specific heat with temperature being obtained from experimental results, they are obtained from theory, hence why they were also omitted from Table 3.2. Finally, the fracture strength will be averaged at each temperature. An additional data point at 2500 degrees Celsius is also added to ensure that material properties are captured in this temperature region. The properties at this temperature were linearly extrapolated using the last two obtained data points for the property. Although the material is not expected to get to 2500 C, capturing the material properties in this region is done in case this is seen to occur during simulations, otherwise, ANSYS would assume constant material properties after 2000 degrees, which is not expected to be true in practice.

**Table 3.3:** Determined ZrB2 - 20 vol% SiC material properties. Density and Poisson Ratio are independent of temperature at 5610 $kgm^{-3}$ and 0.136 respectively.

| Temperature $C$ | Young's Modulus $GPa$ | CTE $10^{-6}K^{-1}$ | Thermal Conductivity $Wm-1K-1$ | Specific Heat $Jkg^{-1}K^{-1}$ | Fracture Strength $MPa$ |
|---|---|---|---|---|---|
| RT | 475.3 | 5.99 | 86.955 | 470.7 | 504.2 |
| 150 | - | - | - | 563 | - |
| 200 | 468.3 | - | 74.75 | 599 | - |
| 250 | - | 6.21 | 100 | 635 | - |
| 300 | - | - | - | 645 | - |
| 400 | 463.3 | - | 69.8 | 665 | - |
| 500 | - | 6.45 | 92 | 680 | - |
| 600 | 456.3 | - | 66.65 | 692 | - |
| 750 | - | 6.64 | 86 | 710 | - |
| 800 | 447.3 | - | 68 | 716 | - |
| 1000 | 433.3 | 6.93 | 70.138 | 740 | 677 |
| 1200 | - | - | 63.5 | 764 | - |
| 1250 | - | 7.04 | 75 | 770 | - |
| 1300 | 414.8 | - | - | 776 | 605 |

**Table 3.3 continued from previous page**

| Temperature C | Young's Modulus GPa | CTE $10^{-6}K^{-1}$ | Thermal Conductivity $Wm-1K-1$ | Specific Heat $Jkg^{-1}K^{-1}$ | Fracture Strength $MPa$ |
|---|---|---|---|---|---|
| 1400 | - | - | 62 | 788 | 546 |
| 1500 | - | 7.18 | 75 | 800 | 500 |
| 1600 | - | - | - | 812 | 460 |
| 1750 | - | - | 65 | 830 | - |
| 2000 | - | - | 66 | 860 | - |
| 2500 | 340.8 | 7.74 | 68 | 920 | 100 |

The next step was to compile the properties of the short-chopped carbon fibre to be used in the fraction of 35 % by volume.

## 3.2.2. Chopped Carbon Fibre Material Properties

The chopped carbon fibre properties, unlike the ZrB2-20vol% SiC, proved more difficult to find data points for. Therefore, a different approach was taken. Similar carbon fibres and their material property behaviour would be used to estimate the chopped carbon fibre material properties over a range of temperatures. This method is much more prevalent in the carbon fibre material properties. It must be noted that the chopped carbon fibre is PAN-based and is expected to have low thermal conductivity since the final UHTCMC is expected to have a low thermal conductivity, hence similar chopped carbon fibres which exhibit the same low thermal properties will also be used. All the data will be extrapolated from similar chopped PAN-based carbon fibres, where material behaviour over a range of temperatures is known. First, the material properties of the chopped 6mm carbon fibres that are known, which are listed below [14]:

- Young's modulus of 230 GPa
- Density of 1700 $kgm^{-3}$
- Tensile Strength of 3500 MPa
- Filament Diameter of 7 $\mu m$
- Length of 6 $mm$

The material properties of CTE, thermal conductivity, Poisson ratio and specific heat will be estimated. Fracture Strength will be estimated, as only the fracture strength of the final material will be estimated using an analytical equation.

### Chopped Carbon Fibre Thermal conductivity relation

Thermal properties of PANEX33 and TC20, PAN-based fibres, have their material properties for thermal conductivity extrapolated from thermal properties of carbon fibres at very high temperature, [49]. It will be assumed that thermal conductivity progresses linearly with temperature, thus only two points were obtained for each of the materials. PANEX33 was chosen for the version that is treated at, 2500K since more data points for it were seen over a broader range. TC20 was chosen as "as received" since it was the shallowest and least thermal conducting carbon fibre. This way, the most, and least thermally conducting PAN-based fibres will have their slope estimated from these two points, averaged and the slope used to estimate how the carbon fibre to be used in combination with the UHTC will behave. The slope estimated from taking PANEX33 at 2500K and TC20 as received is 0.01615. To obtain the intercept, an important assumption will be made, and that is the thermal conductivity of the specific chopped carbon fibres. Since it was not mentioned what the thermal conductivity is before, it will be assumed to be on the lower side of carbon fibres, as the UHTCMC material aims to have low thermal conductivity. For this, a similar PAN-based carbon fibre was found, which had a similar Young's Modulus. The specific fibre in question is TR06U PAN24t 6mm long chopped fibres with a fibre diameter of 7 $\mu m$ manufactured by Mitsubishi Chemical Group. The Young's Modulus is 224 GPa, the density is 1810 $kgm^{-3}$ and the thermal conductivity is 7 $Wm^{-1}K^{-1}$. [29] Using this value of thermal conductivity as the chopped carbon fibres thermal conductivity at room temperature and the slope of the linear relation obtained from extrapolation, a linear relation is formulated for the thermal conductivity of the chopped carbon fibres with temperature.

$$Thermal_{conductivity} = 0.01615 \cdot T + 2.233406417 \tag{3.1}$$

The temperature used in this equation is measured in Kelvin. Another assumption made here is that this relation holds from room temperature until 2500 C. Such an assumption may not hold at very high temperatures where other phenomena may affect this relation. With the relation for thermal conductivity determined, the combined UHTCMC material properties can be extrapolated for thermal conductivity by using both these data sets for the UHTC and chopped carbon fibres.

### Coefficient of Thermal Expansion Carbon Fibers

Carbon Fibres have their coefficient of thermal expansion defined in the longitudinal and transversal directions separately. A paper was found that measured the specific CTE of different carbon fibres from a temperature range of 300K to 2500K, The specific CTE formula is given below:

$$\alpha_s = \frac{\beta(T) - \beta(T_0)}{\beta(T_0)} \tag{3.2}$$

Equation 3.2 was calculated at each tested temperature and presented in a graph in per cent to show how the specific CTE developed with temperature. The paper also provided a polynomial coefficient for the best-fit curve for the transverse and longitudinal specific CTEs. Panex33 treated at 2500K was chosen yet again since the data is available to a temperature of 2500K. [47]

**Table 3.4:** Panex33 treated at 2500k specific CTEs polynomial coefficients with respect to direction [47]

| Direction | $a_4$ | $a_3$ | $a_2$ | $a_1$ | $a_0$ |
|---|---|---|---|---|---|
| Transverse | - | -5.201E-11 | 1.874E-07 | 6.221E-04 | -2.368E-01 |
| Longitudinal | 2.808E-14 | -1.671E-10 | 4.070E-07 | -2.978E-04 | 5.506E-02 |

Table 3.4 is used to determine the specific CTE at each temperature denoted in Table 3.3. With the specific CTEs obtained, they will then have to be converted to the CTEs in units per Kelvin from percentages, for this the following equation is used.

$$CTE_T = \frac{\alpha_s \cdot 100}{(T - 300)} \tag{3.3}$$

With this formula, the room temperature CTE will have to be assumed to be the same as the CTE at 150 degrees. The actual CTE will then be calculated as the average of the longitudinal and transverse CTEs.

### Young's Modulus Carbon Fiber

A paper was found that investigated the degradation in the Young's modulus of PAN-based carbon fibres as a ratio of the original measured Young's modulus at room temperature. This rate of degradation will be used to determine how the thesis-specific PAN-based chopped 6 mm carbon fibre will degrade over a range of temperatures.

**Table 3.5:** Young's Modulus degradation over temperature[53]

| Temperature C | $\frac{E}{E_0}$ |
|---|---|
| 24 | 1.00 |
| 1000 | 0.985 |
| 1200 | 0.977 |
| 1400 | 0.957 |
| 1600 | 0.916 |
| 1800 | 0.818 |
| 2000 | 0.695 |

Table 3.5 is extended further to 2500 degrees Celsius by linearly extrapolating using the 1800 and 2000 degrees data points. It must be noted that 24 degrees Celsius was taken as room temperature and

essentially comparable to 22 degrees Celsius. This is because, as mentioned previously, many papers take temperatures ranging from 20 to 25 degrees Celsius as the standard for room temperature. The degradation for PAN-based fibres at 2500 degrees is 0.3875.

### Specific Heat Carbon Fiber

The specific heat of the carbon fibres is extrapolated from those measured for PANEX33 treated at 2500K. This was done because of the many more data points that were present in the graphs seen in the literature. Although there are many data points, the actual values still had to be estimated from the graphs as they were not stated explicitly. The below table shows the extrapolated data points.

**Table 3.6:** Graphically estimated specific heat of PANEX33 treated at 2500K[48]

| Temperature K | Estimated Specific Heat |
|---|---|
| RT | 750 |
| 500 | 1200 |
| 750 | 1500 |
| 1000 | 1750 |
| 1500 | 2100 |
| 2000 | 2250 |
| 2250 | 2200 |

The data points in Table 3.6 were used to linearly interpolate between points for the desired temperature values for the carbon fibre. Additionally, an extra point at 2500 degrees Celsius is also interpolated linearly by using the last two temperature data points; 2000 and 2250 degrees Kelvin.

### Carbon Fibre Material Properties concerning temperature

All the previously extracted data will be used to estimate the material properties of the chopped carbon fibre using the room temperature properties as the basis.

**Table 3.7:** Determined Chopped 6mm Carbon fibre material properties. Density and Poisson Ratio are independent of temperature at 1700 $kgm^{-3}$ and 0.27 respectively.

| Temperature $C$ | Young's Modulus $GPa$ | CTE $10^{-6}K^{-1}$ | Thermal Conductivity $Wm-1K-1$ | Specific Heat $Jkg^{-1}K^{-1}$ |
|---|---|---|---|---|
| RT | 230 | 1.92 | 7 | 750 |
| 150 | 2.3E+02 | 1.92 | 9.07 | 1038.22 |
| 200 | 2.29E+02 | 2.42 | 9.87 | 1150.80 |
| 250 | 2.29E+02 | 2.73 | 10.68 | 1233.78 |
| 300 | 2.29E+02 | 2.95 | 11.49 | 1293.78 |
| 400 | 2.29E+02 | 3.28 | 13.10 | 1413.78 |
| 500 | 2.28E+02 | 3.51 | 14.72 | 1528.15 |
| 600 | 2.28E+02 | 3.70 | 16.33 | 1628.15 |
| 750 | 2.27E+02 | 3.91 | 18.76 | 1769.71 |
| 800 | 2.27E+02 | 3.98 | 19.56 | 1804.71 |
| 1000 | 2.27E+02 | 4.17 | 22.79 | 1944.71 |
| 1200 | 2.25E+02 | 4.31 | 26.02 | 2084.71 |
| 1250 | 2.24E+02 | 4.34 | 26.83 | 2108.45 |
| 1300 | 2.22E+02 | 4.37 | 27.64 | 2123.45 |
| 1400 | 2.20E+02 | 4.41 | 29.25 | 2153.45 |
| 1500 | 2.15E+02 | 4.44 | 30.87 | 2183.45 |
| 1600 | 2.11E+02 | 4.47 | 32.48 | 2213.45 |
| 1750 | 1.94E+02 | 4.50 | 34.91 | 2244.37 |
| 2000 | 1.60E+02 | 4.53 | 38.94 | 2194.37 |

**Table 3.7 continued from previous page**

| Temperature C | Young's Modulus GPa | CTE $10^{-6}K^{-1}$ | Thermal Conductivity $Wm{-}1K{-}1$ | Specific Heat $Jkg^{-1}K^{-1}$ |
|---|---|---|---|---|
| 2500 | 8.91E+01 | 4.55 | 47.02 | 2094.37 |

From Table 3.7 it can be seen that the Poisson Ratio was also included. This Poisson ratio was estimated based on a source stating the various axial positions of different carbon fibres, which varied from 0.26 to 0.28. The fibre types were 38/III, WS/2/3, and Safril each with 0.27, 0.26 and 0.28 axial Poisson ratios respectively.[22] 0.27 was taken as an average between them, and this was assumed to be independent of temperature, as temperature-dependent data was not able to be found reliably.

### 3.2.3. UHTCMC properties

With the individual components of the UHTCMC, the UHTC and the short carbon fibre material properties all compiled, they can then be used to compute the material properties of the UHTCMC concerning temperature. The CTE, thermal conductivity, density, Poisson ratio and specific heat were estimated by taking the average of the upper and lower bound of the individual material properties using the rule of mixtures. The upper and lower bound rules of mixture formulas are given below.

$$P_{upper} = V_M * P_M + V_f * P_f \tag{3.4}$$

$$P_{lower} = (\frac{V_M}{P_M} + \frac{V_f}{P_f})^{-1} \tag{3.5}$$

$$P = \frac{P_{upper} + P_{lower}}{2} \tag{3.6}$$

$P$ denotes the material property that is being estimated and $V$ denotes the volume fraction. The subscripts $M$ and $f$ denote the matrix (UHTC) and fibre, respectively. For Young's modulus and Fracture Strength, analytical equations are used. This is because the rule of mixtures is not expected to apply very well for short randomly oriented carbon fibres. Although the UHTCMC material is theoretically perfectly isotropic, there may be additional complications that arise due to the inherent bias that may be present for the short fibre orientation. Two papers were found that gave analytical means of estimating the stiffness of the short-fibre UHTCMC. The first method, from Analysis of the Mechanical Properties in Short Carbon Fibre-toughened ZrB2-SiC Ultra-high Temperature Ceramic [80], provides the following analytical equation:

$$E = E_m(1 - V_f) + V_f \int_0^{\frac{\pi}{2}} (\cos\theta^2 - \nu\sin\theta^2)E_f \cos\theta^2 d\theta \tag{3.7}$$

With $E_m$ and $E_f$ denoting the matrix and fibre stiffness respectively. $V_f$ denoting the fibre fraction, and $\nu$ is the matrix Poisson ratio. Given that the Poisson ratio is 0.136, Equation 3.7 can be simplified to the below equation.

$$E = E_m - V_f(E_m - 0.562E_f) \tag{3.8}$$

A porosity factor can also be added using the below equation.

$$E = E_0(1 - 1.9P + 0.9P^2) \tag{3.9}$$

Equation 3.9 implements porosity as a percentage, P. This would give an elasticity assuming perfectly distributed fibre over the whole material, thus it also assumes a perfectly isotropic material that behaves the same in all directions. The same source also provides an equation to be able to calculate the UHTCMC material strength. This equation is given below.

$$\sigma_{max} = (\sigma_m)_{max}(1 - V_f) + V_f \int_0^{\frac{\pi}{2}} (\epsilon_{max}\cos\theta^2 - \epsilon_{max}\nu\sin\theta^2)E_f \cos\theta^2 d\theta \tag{3.10}$$

$$(\sigma_f)_{\epsilon_{max}} = E_f \frac{(\sigma_m)_{max}}{E_m}$$

$$\sigma_{max} = (\sigma_m)_{max}(1 - V_f(1 - 0.562\frac{E_f}{E_m})) \tag{3.11}$$

The next source, The stiffness of short and randomly distributed fibre composites [61], also provides two analytical equations to estimate the stiffness of such a composite with short randomly distributed carbon fields. The first equation is based on the simple rule of mixtures with the addition of the coefficient $\eta_e$, selected to be 0.375. The equation for the simple rule of mixtures with this formulation is given below.

$$E_c = E_m + \frac{(\eta_e E_f - E_m)M_f}{\frac{\rho_f}{\rho_m} + (1 - \frac{\rho_f}{\rho_m})M_f} \tag{3.12}$$

In Equation 3.12, $\rho$ denotes the densities, and $E$ denotes the stiffness. $M_f$ describes the fibre mass fraction and the subscript $f$ and $m$ refer to the fibre and matrix respectively. The next equation provided is the Christensen equation, given below, which is also derived from the simple rule of mixture but is more rigorous in its analysis of the micromechanics.

$$E_{2D} = \frac{E_f}{3}U_f + \frac{1 - U_f}{3}E_m + \frac{19}{27}(\frac{E_f(1 + U_f) + E_m(1 - U_f)}{E_f(1 - U_f) + E_m(1 + U_f)})E_m \tag{3.13}$$

Equation 3.13 combines the geometric averaging techniques and quasi-isotropic models to obtain the formula. In the equation, $U_f$ refers to the fibre volume fraction. Using all three stiffness equations with the same numbers using the room temperature extrapolated data for the carbon fibre and UHTC, a decision can be reached on which equation to use for obtaining the UHTCMC material properties. The input data is as follows:

- Porosity = 3%
- $E_m = 475.3\ GPa$
- $E_f = 230\ GPa$
- Fibre Volume Fraction = 0.35
- $\rho_m = 5610\ kgm^{-3}$
- $\rho_f = 1700\ kgm^{-3}$

**Table 3.8:** Young's Modulus Estimated from different equations

| Equation(s) | Young's Modulus $GPa$ |
| --- | --- |
| Equation 3.8 and Equation 3.9 | 334.33 |
| Equation 3.13 | 391.71 |
| Equation 3.12 | 352.31 |

In Table 3.8, it can be seen that the first source, which specifically pertains to UHTCMC material property estimations, with the addition of including a porosity factor yields the smallest stiffness value. It is interesting to note that both sources and all three equations yield nearly similar results within an acceptable margin, although Equation 3.12 and Equation 3.13 mainly deal with a matrix that has a lower stiffness than the fibre. Since UHTCMC material properties are lower than what is expected from ideal conditions, the first source will be used with the addition of a 20 % margin lower stiffness to account for imperfect manufacturing consistency for the UHTCMC. Thus yielding a room temperature stiffness of 267.5 $GPa$ for the UHTCMC of ZrB2 - 20vol% SiC with 35 vol% short random fibres.

For the strength of the material, the same paper which provides the preferred equation to estimated stiffness, is used, Equation 3.11. The material strength in this case will not have an additional safety factor placed onto it, as it is very well in line with the expected fracture strength of the specific

UHTCMC. Thus the final material properties of the UHTCMC that will be inputted into ANSYS are displayed below.

**Table 3.9:** Determined ZrB2 20 vol% SiC with 35% vol short random fibres material properties. Density and Poisson Ratio are independent of temperature at 3674.77 $kgm^{-3}$ and 0.17 respectively.

| Temperature $C$ | Young's Modulus $GPa$ | CTE $10^{-6}K^{-1}$ | Thermal Conductivity $Wm-1K-1$ | Specific Heat $Jkg^{-1}K-1$ | Fracture Strength $MPa$ |
|---|---|---|---|---|---|
| RT | 267.47 | 4.00 | 38.18 | 554.83 | 375.78 |
| 150 | - | - | - | 699.86 | - |
| 200 | 263.94 | - | 37.35 | 755.96 | - |
| 250 | - | 4.64 | 47.10 | 804.75 | - |
| 300 | - | - | - | 827.19 | - |
| 400 | 261.38 | - | 38.86 | 871.70 | - |
| 500 | - | 5.21 | 48.69 | 910.40 | - |
| 600 | 257.84 | - | 40.56 | 943.00 | - |
| 750 | - | 5.51 | 50.30 | 989.58 | - |
| 800 | 253.32 | - | 43.74 | 1002.34 | - |
| 1000 | 246.34 | 5.80 | 47.09 | 1053.25 | 509.72 |
| 1200 | - | - | 46.30 | 1103.96 | - |
| 1250 | - | 5.94 | 52.10 | 1114.20 | - |
| 1300 | 236.65 | - | - | 1122.58 | 457.10 |
| 1400 | - | - | 47.54 | 1139.33 | - |
| 1500 | - | 6.06 | 54.77 | 1156.08 | - |
| 1600 | - | - | - | 1172.84 | - |
| 1750 | - | - | 52.20 | 1194.95 | - |
| 2000 | - | - | 54.81 | 1209.78 | - |
| 2500 | 180.52 | 6.42 | 59.74 | 1237.84 | 70.1 |

When looking a Table 3.9, there are many gaps in values for the temperature-related properties. To resolve this, except for the Density and Poisson ratio, the material properties with no data points for specific temperatures will be linearly interpolated between the points. An interesting observation here is that the fracture strength of the material becomes the highest at a temperature of 1000 degrees Celsius. This is because the ZrB2 with 20 vol% SiC also exhibits similar behaviour as reported by other pieces of literature cited in Table 3.2. A paper using long continuous fibre UHTCMCs also found a similar trend of increasing flexural strength with temperature from room temperature to 1500 degrees Celsius.[85] Regarding the actual values of strength, a UHTCMC of ZrB2 + 10 vol% SiC with 40 vol% short random carbon fibre has a room temperature flexural strength of 135 MPa [50], another paper states the flexural strength of ZrB2 + 20 vol% SiC with 20 vol% short random carbon fibre to be 445 MPa.[81] A previously mentioned source, Analysis of the Mechanical Properties in Short Carbon Fibre-toughened ZrB2-SiC Ultra-high Temperature Ceramic, which was used to obtain the flexural strength formula was made by the same authors that found the flexural strength of 445 MPa just mentioned. Equation 3.10, taken from the mentioned paper, actually yields a fracture strength of 452 MPa, a difference of 1.6%. [80] It must therefore be noted that the equation for fracture strength is much preferred to be used rather than taking a guess based on similar materials since it was also corroborated by the same authors that made the material. Other sources, while also giving the material strength, will have small variations in the raw material used which can add up to drastically different material properties under the same UHTCMC name. A simple example that may cause such discrepancy is that the lower flexural strength UHTCMC uses milled and highly conductive carbon fibres, while the higher flexural strength UHTCMC uses chopped fibres. Thus, this demonstrates that UHTCMC material properties are heavily dependent on the exact properties of the raw mixture used, from the length of the short carbon fibres to the method of preparation and specific settings used in SPS. Given all these complexities, a source which has both made the material and created a formula to describe the flexural strength of that same material is preferred as the scientists would have an unparalleled understanding of the exact microstructure and manufacturing of that specific UHTCMC sample.

## 3.3. FEA

The decision was made to use ANSYS FEA software to perform the entire thesis numerical simulations. This decision was made since the 3D CFD is to be done using fluent, after which the results will be imported to ANSYS static thermal and structural analysis. Given the versatility of ANSYS to apply such varying analysis types and the ease of use when it comes to transferring and importing data from one computer to another, it was chosen as the preferred software. The version that will be used is ANSYS 2023 R2, with access to all accompanying documentation for the aforementioned version. The sources used to determine how to apply loads, take into consideration contacts and attachment points, meshing, convergence, and verification procedures, all taken mainly from research reports and published papers. Another source of information that can be especially useful is the course material for FEM courses given at TU Delft. Any missing information will be taken from secondary sources such as ANSYS official video tutorials and forum and discussion pages.
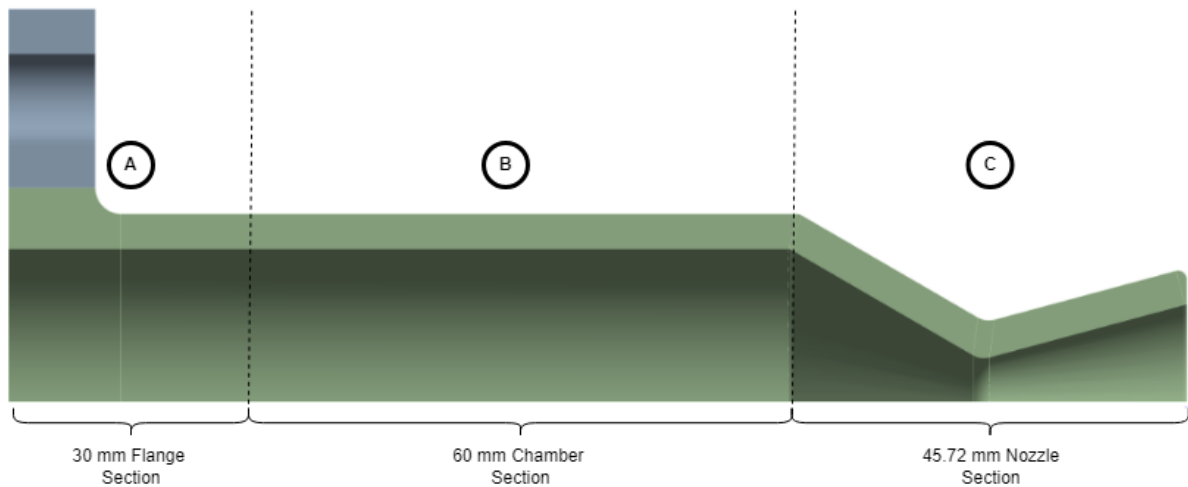


**Figure 3.1:** Section Naming Scheme

Figure 3.1 splits the thruster into sections to facilitate discussions later when referring to certain phenomena that are observed. Distances along the axial position are also included. These can be used to identify the results from one area when plotted against axial positions. In later chapters, area A will be split from areas B and C given the different complexities exhibited by these two different sections. This will be seen later in chapter 5.

Given that the 3D CFD will be given as input. A pipeline for information flow can already be designed based on desired outcomes. Given the requirements and design points that are free to be changed, the following process flow is outlined:

1. **Material Properties**: The custom UHTCMC material properties will be placed into the ANSYS program with temperature-dependent material properties.
2. **Geometry**: The geometry of the thruster and the parameters that are allowed to vary for optimization will be made. It is important to note that 2 different 3D models will be made. as listed below:

   - A simple model that allows for varying 3 regions of thickness in the thruster.
   - A complex model that builds upon the 3 regions of thickness model, but in addition a steel back plate and bolts are also modelled to better represent thruster attachments to a structure.

3. **Meshing**: The geometry will be meshed with quadratic Solid226 elements, with a maximum element size of 1.5 mm, and the minimum element size will be determined based on an accuracy to computational cost trade-off given that many design points will have to be analysed.

4. **Boundary and Loading Conditions**: The supports and attachment points of the entire thruster structure will be outlined, in addition to the operating environment. The thermal and structural boundary conditions are stated below, with assumptions made:

   - Thermal Boundary and Loads
     - Convection, on the inside of the nozzle, can be obtained from CFD and verified using the Bartz equation [3].
     - Radiation outwards to the environment
     - Convection outwards to air ambient temperature
   - Structural Boundary and Loads
     - Thermal stresses due to thruster temperature profile
     - Pressure from propellant and oxidiser reaction flow

5. **Analysis Settings**: The analysis settings in ANSYS will have to be checked to ensure that any complexities are captured by the solution. This can include enabling non-linearities, and therefore large deflections option as an example. If multiple loading steps are present, these will also have to be assessed.

6. **Verification**: The decisions made for loading and thermal expansion will be checked, including whether the loadings have been applied correctly. Simple verification processes, like visual checks, can include testing loadings individually before compounding them to ensure correct behaviour. The final results can also be checked to see fit they align with what is expected to occur from the literature, for example, if the Bartz-derived relation yields similar patterns to what is produced by the CFD.

   - **Mesh Independence**: The solution will then have its mesh size vary to see the effects of a finer mesh on the magnitude of maximum and minimum deflections and stresses. It can also be done to locally refine meshes at high-stress locations to ensure detail is not lost due to coarse meshes or determine if stress singularities are present

7. **Validation**: If experimental or test data is available, it can be used to validate the simulation results within acceptable limits. This however will be limited as it depends on whether this data is provided in the first place or whether a test set-up is made. Qualitative analysis will be used here to determine locations of maximum expected stress and temperatures. Normalised graphs taken from similar FEA studies can also be used and overlayed with the results from the simulations.

8. **Assumptions and Limitations**: Once the analysis has been completed, limitations of the model will have to be discussed to point out any results that deviate too far from what is seen in reality. Since assumptions would have also been made by the time the solution is obtained, the effect of the assumptions will also have to be discussed. This would also have to be done based on test data from a specific thickness thruster if test data is made available.

9. **Final Design**: The final design will be chosen based on minimum mass and not exceeding the material fracture strength.

10. **Final Design Analysis**: A much finer mesh and complex model will be used to generate the final results of the optimum design using the complex model. This will be done such that to ensure enough data points are present for post-processing and discussion of results.

As was previously mentioned, certain assumptions will have to be made and their consequences outlined. One thing to account for is the mesh creation decisions. During the literature study, many videos were found that recommended splitting complex shapes and slicing them to allow for a uniform hexahedral mesh to be made through ANSYS. A shared topology option could then be used to ensure that nodes at the interfaces are shared and that the displacements are transferred directly to the cut body. It must also be noted that Delft Blue, the supercomputer cluster at TU Delft, will be used when feasible to obtain accurate and precise solutions.

It was mentioned previously that a complex model that includes steel back plate and bolts is one of the models used. The complex model is used to see how well the simple model can capture all the necessary stress and temperature concentrations that occur. This would also in turn be a part of the verification processes, this can be used to verify that the stresses in the simple model have similar patterns to the

ones found in the more complex model. An expectation is that since the back of the simple thruster would have to be fixed, this would restrict the deformations in the fixed region, therefore causing stress singularities that are not what would occur in the real world. Therefore, it is expected that the stresses will diverge heavily at the beginning of the thruster chamber, and quickly converge to near identical results well before the convergent section begins. Additionally, regarding the complex model, it is expected that the steel bolts will introduce some additional stiffness at the bolted regions, therefore lightly reducing deflection. Since the steel back plate will be fixed rather than the thruster, the stress singularities seen in the simple model at the beginning of the resulting chamber are expected to be significantly alleviated.

Once the above-mentioned points are taken into account and the areas of deviation have been determined, the areas can be excluded during the optimisation analysis to find the most optimum thruster thickness. An important consideration is that the only way to confidently exclude certain regions from the analysis is to ensure the regions of interest have a good correlation between the simple and complex model. This way a simple model can be used, and only the regions of interest can be scoped with great confidence and be used for comparison to determine which of the many design points and thickness is most optimal.

As mentioned, there are many expected design points to be analysed before the most optimum one is determined. Therefore, reducing computational effort is also something that must be looked into. One consideration is to account for the two axes of symmetry in the nozzle. This can reduce the times of 1 run by 3 to 4 times. Some consideration that has to be made is that since symmetry is used, the mesh generated may have slight differences due to how ANSYS may mesh fully 360-degree rotated parts vs only 90 degrees. Additionally, since the pressure is imported from CFD simulations done on the complete model, there is no guarantee that the pressure and thermal loads are also axisymmetric around 2 axes. Therefore, it is can expected that the asymmetric model will experience some very small deviations from the full model.

Once the final configuration has been chosen as in step 9, the complex model will then be used to determine the stresses, temperatures, and deflections in the final model. A final comment is that ANSYS beta features are enabled throughout this project to access specific functions, such as displaying symmetry in a model or importing CFD results and extrapolating them onto the thruster inner surface in the structural or thermal loading definitions.

## 3.4. Post Processing and Result Analysis

Once the final design has been chosen, the complex model with steel components is used to generate a final model. The stress, temperature, and deflection of the inner and outside the thruster will be plotted to see how these variables develop as we move along from the chamber to the nozzle exit. Regarding erosion, preventive measures to reduce nozzle damage and the thruster performance over time, research questions 3.1 to 3.3, it is expected that these will be done qualitatively. These three subjects have the following considerations when tackling them:

- **Research Question 3.1**: Since the specific UHTCMC combination has not been manufactured before, accurate degradation data will have to be obtained from an actual thruster test. Therefore, for this thesis, it is expected that degradation can be estimated qualitatively by referring to the literature.
- **Research Question 3.2**: The literature study has shown different methods and how to apply certain coatings to thrusters. This can be used to determine which coating would be best suited given the stresses seen. Of course, if a coating is not necessary, it will not be included.
- **Research question 3.3**: Qualitative analysis methods would have to be used that refer to papers that cover the long-term performance of equivalent material to determine how the thrusters would degrade over time. This would have to be done very carefully, as it is expected that the manufacturing methods, porosity, and fibre type would have a great impact on this analysis.

About post-analysis, justification will be given to explain why certain parameters and outputs are used to investigate the thruster. These are provided in the list below.

- $\sigma_{VonMises}$: This stress can be used to directly compare against the flexural strength limit of the material
- *Temperature*: Temperature is such a crucial factor as material properties all depend on it. This means that thermal strain may not directly result in additional stresses if the stiffness degrades faster than the strain develops. Thus temperature contours are essential for a complete analysis.
- *dT/dx*: The temperature gradient can be used as a rough indicator of when the peak stresses may occur and where they may occur. This is because thermal stresses are expected to be the major source of stresses in a thruster, and a larger temperature gradient usually results in higher thermal stresses.
- $\sigma_{axial}$ : Axial stresses can be used to check whether stresses are compressive or tensile, highlighting potential critical zones and why they are critical
- *Strain*: Thermal and Equivalent strain can be used to determine the source of stresses. Essentially differentiating between thermal stresses and mechanical-based ones that may arise from sharp corners for example.
- *StressMargin*: As opposed to the actual stress, the margin of the stress is more important to determine which part of the thruster is close to the fracture limit rather than which part has the highest stress. This distinction is important as fracture strength also varies with temperature, and areas of higher stress are also expected to be at higher temperatures.

# 4

# Modelling and Validation

This chapter will cover the process of creating the thruster model. Such a topic would cover aspects from the model assumptions, the input loads, simulation operational conditions and results processing. It must be noted that this chapter will build the very basis upon which the optimization will be performed to determine the optimum thruster configuration. The chapter will start with the considerations when doing a FEA, section 4.1. Next, the knowledge of how to use ANSYS adequately was verified in section 4.2, using examples and comparing the simulation answers with the analytical ones. Next, the inputs that will be used for the thermo-structural analysis will be discussed in section 4.3. After the inputs are discussed, the actual model used will be covered. Both the simple and complex models used for simulations, why each was created, and the main purposes they serve will be covered in section 4.4. Once the models have been created and results generated and analysed, they will then have to be verified and validated, which will be done in section 4.5 and section 4.6 respectively.

## 4.1. Potential FEA considerations and Errors

Three main factors affect the validity, accuracy, and reliability of the finite element analysis and its results; Modelling Errors. Discretization Errors, and Numerical Errors. These errors are described below [24].

- **Modelling Errors:**

    - *Geometric Errors* which are caused by not knowing specific dimensions, thus needing an assumption to be taken for their value.
    - *Boundary Conditions* chosen can affect the stresses seen in the model and potentially induce large stresses in the regions in proximity of the boundary conditions.

- **Discretization Errors** are related to how many elements are used to discretize the model. If too few elements are used, then the results are not accurate enough, and if too many elements are used, then the computational cost is too much. Elements of poor quality also have to be addressed to avoid large errors.

- **Numerical Errors** include errors that are due to the computer, such as rounding off errors or even the algorithm used to converge to an iterative solution. In the aforementioned case, the algorithm may be unstable, resulting in inaccuracies.

The above-listed reasons can cause inaccuracies and results which are not representative of their real-world counterparts. Such inaccuracies can be mitigated via verification and validation strategies that are implemented to ensure that the obtained results show the model behaving as expected and sustaining the expected amount of loading. Additionally, convergence studies can be done on the meshes and perhaps even time steps for the transient simulations to see the effect of smaller elements or time steps on the final obtained results.

## 4.2. Initial FEA usage Verification

To ensure program understanding is as expected and program behaves as expected based on inputs and everything is set up correctly from the user side to converge to a solution. This also includes the actual

inputting of material properties, although taking them to be mostly temperature-independent at the time to simplify the analytical equations. Because ANSYS verifies the ANSYS code itself, the main goal of this verification is to ensure that the numbers are inputted correctly from the user side and the simulations are set up correctly. A more simplified case of two data points with linear varying material temperature-dependent properties is taken to verify the inputs were done right, rather than the very large range seen in the table. This can serve to solidify the verification better as more analytical solutions are found on the Internet using linearly dependent material properties between two temperatures rather than 3 or more with different material property gradients. The equations used are taken from various sources online [28][45].

## 4.2.1. Steady State Thermal Plate

This case takes an example of a flat plate that experiences a high temperature on one side with just convection, and conduction through the plate, and the exit conditions on the outside of the plate are radiation and convection.
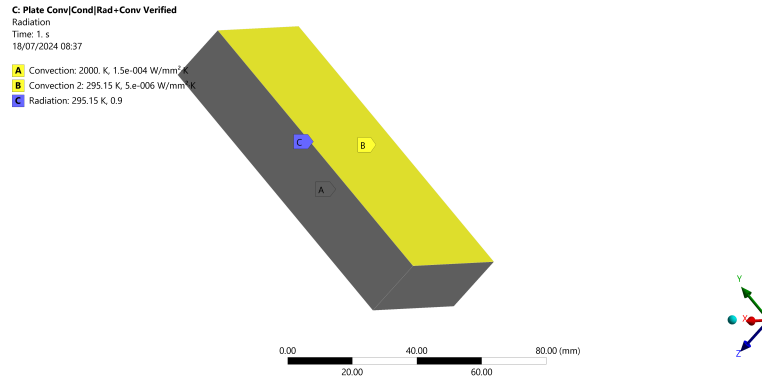


**Figure 4.1:** Thermal Plate Analysis Loading Conditions in ANSYS

Figure 4.1 does not have any loading conditions applied to its sides. Loading condition A is applied on the other side of the plate which is not shown in the figure. The analytical equations for solving this case are given below.

$$T_1 = T_{\infty_1} - \frac{\dot{q}}{k_1} \tag{4.1}$$

$$T_2 = T_1 - \frac{w_{plate} \cdot \dot{q}}{\lambda} \tag{4.2}$$

$$\dot{q} = \sigma\epsilon(T_2^4 - T_{\infty_2}^4) + k_2(T_2 - T_{\infty_2}) \tag{4.3}$$

The above equations Equation 4.1, Equation 4.2 and Equation 4.3 are the basic equations analytical equation which describe how heat passes through the material and what the steady state conditions to have heat balance are. The variables used in the equations are listed below with their values.

- $T_{\infty_1} = 2000$ K
- $T_{\infty_2} = 295.15$ K
- $w_{plate} = 20$ mm
- $\lambda = 30.016 \ Wm-1K-1$
- $\sigma = 5.6 \cdot *10^{-8} \ Wm-2K-1$
- $\epsilon = 0.9$
- $k_1 = 150 \ Wm-2K-1$
- $k_2 = 5 \ Wm-2K-1$

The above equations and constants are rearranged to create an equation, which can be solved numerically to obtain the temperature on either side of the flat plate. These temperatures are also probed in the ANSYS simulations and compared directly. Below are shown the equations for $T_1$ and $T_2$ that can be solved to obtain the temperatures, Equation 4.4 and Equation 4.5 respectively.

$$T_1 = (2000 - \frac{5.67 \cdot 10^{-8} \cdot 0.9 \cdot (x^4 - 295.15^5) + 5 \cdot (x - 295.15)}{150}) -$$
$$(\frac{\frac{20}{1000} \cdot (5.67 \cdot 10^{-8} \cdot 0.9 \cdot (x^4 - 295.15^4) + 5 \cdot (x - 295.15))}{30.016}) - x \tag{4.4}$$

$$T_2 = T_1 + \frac{\frac{20}{1000} \cdot 5.67 \cdot 10^{-8} \cdot 0.9 \cdot (T_1^4 - 295.15^4) + 5 \cdot (T_1 - 295.15)}{30.016} \tag{4.5}$$

## 4.2.2. Steady State Thermal Cylinder

Similarly to the previous flat plate thermal case, the same is repeated for a cylinder where the thin shell assumption does not hold. This can be seen below.
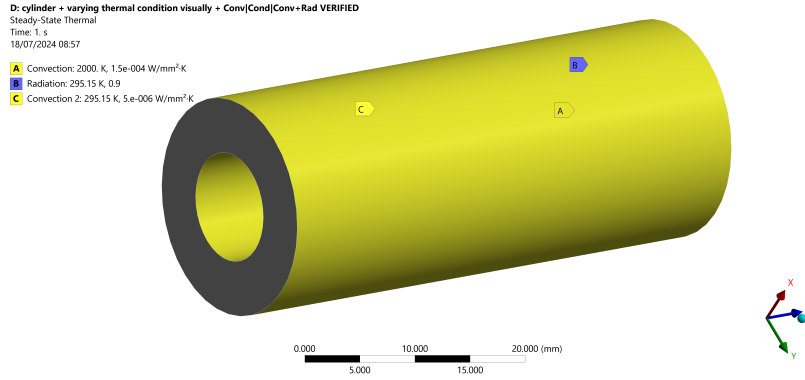


**Figure 4.2:** Thermal Cylinder Analysis Loading Conditions in ANSYS

Figure 4.2 shows loadings conditions B and C on the outside of the surface and loading condition A on the inside. The sides of the cylinder do not have any applied loading conditions in this analysis. Equation 4.1, Equation 4.2 and Equation 4.3 also have small changes made to them to adjust for the change in geometry of the problem at hand. The updated equations are shown below.

$$T_1 = T_{\infty_1} - \frac{\dot{q}}{2\pi r_1 L k_1} \tag{4.6}$$

$$T_2 = T_1 - \frac{\ln(\frac{r_2}{r_1}) \cdot \dot{q}}{2\pi L r_2 \lambda} \tag{4.7}$$

$$\dot{q} = 2\pi L r_2 \sigma \epsilon (T_2^4 - T_{\infty_2}^4) + 2\pi L r_2 k_2 (T_2 - T_{\infty_2}) \tag{4.8}$$

The only difference compared to the flat plate equation is the removal of the width of the plate but the addition of radius 1 and 2, the inner and outer radius of the cylinder. The radii are 5 mm and 10 mm for the inner and outer respectively.

$$T_1 = (2000 - \frac{2 \cdot \pi \cdot \frac{10}{1000} \cdot \frac{50}{1000} \cdot (5.67 \cdot 10^{-8} \cdot 0.9 \cdot (x^4 - 295.15^5) + 5 \cdot (x - 295.15))}{2 \cdot \pi \cdot \frac{5}{1000} \cdot \frac{50}{1000} \cdot 150}) -$$
$$(\frac{\ln(\frac{10}{5}) 2 \cdot \pi \cdot \frac{10}{1000} \cdot \frac{50}{1000} \cdot (5.67 \cdot 10^{-8} \cdot 0.9 \cdot (x^4 - 295.15^4) + 5 \cdot (x - 295.15))}{2 \cdot \pi \cdot \frac{50}{1000} \cdot 30.016}) - x \tag{4.9}$$

$$T_2 = 2000 - \frac{(T_1^4 - 295.15^4) \cdot 2 \cdot \pi \cdot \frac{10}{1000} \cdot \frac{50}{1000} \cdot (5.67 \cdot 10^{-8} \cdot 0.9 + 5 \cdot (T_1 - 295.15))}{150 \cdot 2 \cdot \pi \cdot \frac{5}{1000} \cdot \frac{50}{1000}} \tag{4.10}$$

### 4.2.3. Cylinder Pressure Vessel with symmetry

For this case, symmetry boundary conditions are also used to ensure that the stresses and conditions set in the ANSYS program are done correctly. The pressure vessel uses the thick wall version of the equations to obtain the hoop and axial stresses.[1]
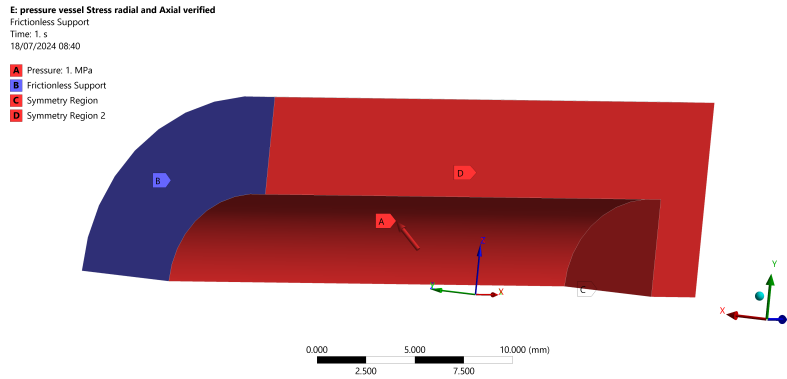


**Figure 4.3:** Cylinder Pressure Vessel Simulation Conditions

Figure 4.3 shows the 2 symmetry planes for the pressure vessel that was tested. Additionally, it also shows the additional consideration that was done of adding frictionless support since this is a half-model pressure vessel that is simplified even further, so a 3 plane of symmetry model.

$$\sigma_\theta = \frac{pa^2(r^2 + b^2)}{r^2(b^2 - a^2)} \tag{4.11}$$

$$\sigma_{ax} = \frac{pa^2}{b^2 - a^2} \tag{4.12}$$

Using Equation 4.12 and Equation 4.11, for a closed hollow cylinder with an inner radius of 5 mm and outer radius of 10 mm that is subject to a pressure of 1 MPa on the inside. This gives an inner and outer stress, in addition to the axial stress. The symbols in the above equation are labelled as follows:

- a = inner radius, 5 mm
- b = outer radius, 10 mm
- r = radial position
- p = pressure load, $1 \, MPa$

### 4.2.4. Constrained Pipe with Varying Temperature and Material Properties

This case has a pipe made of a material with varying Young modulus and thermal expansion coefficient with temperature. The pipe is 2 meters long with a cross-sectional area of 500 $mm^2$. The temperature from one end of the pipe to the other varies by 200 degrees Celsius linearly with distance, from 295.15 Kelvin to 495.15 Kelvin. The specific material properties with temperature are given below for both Young's modulus and the coefficient of thermal expansion.

- Young's Modulus: 294.73 $GPa$ at 295.15 K and 100 $GPa$ at 595.15 K
- CTE: 6.561E-06 $K^{-1}$ at 295.15 K and 1E-06 $K^{-1}$ at 595.15 K
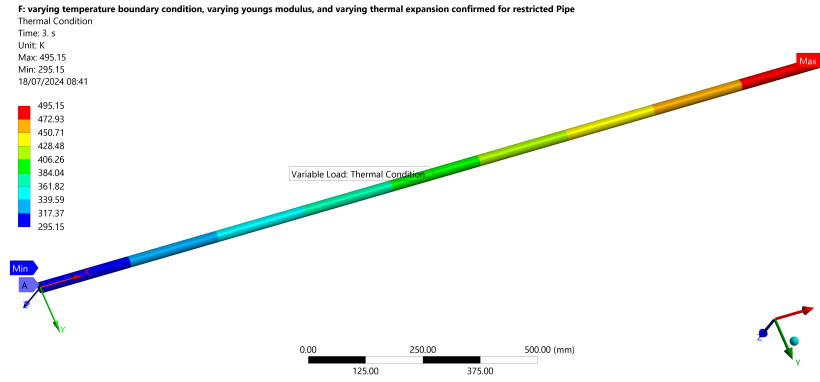
**Figure 4.4:** Constrained Pipe with Varying Temperature boundary conditions applied

Figure 4.4 shows how the applied boundary conditions should look in ANSYS. The equations that will be used to obtain the analytical solution to the stress in the pipe for the above-mentioned case are given below. Starting with the formula for the coefficient of thermal expansion with temperature.

$$\alpha = -1.8537 \cdot 10^{-8} T + 1.2031 \cdot 10^{-5} \tag{4.13}$$

$$E = 10^9 \cdot (-0.6491 \cdot T + 486.312) \tag{4.14}$$

$$\delta_T = \alpha \Delta T dx \tag{4.15}$$

$$\delta_T = \sigma_T \int_0^L \frac{1}{E(x)} dx \tag{4.16}$$

Equation 4.15 [17] is used to calculate the defection using Equation 4.13. Additionally, Equation 4.14 is then taken and the temperature variation of the pipe with distance is substituted in to obtain an E modulus variation with distance along the pipe. Finally, Equation 4.16, which was derived [23], is then used alongside the previously calculated relations and defection to solve for the thermal stress in the pipe.

### 4.2.5. 3-point Bend Test

This is the final check that is performed to see if the material recorded deflection is correct and if the simulation is set up as expected. Euler bending theory is used to check against the situated 3-point bending results. For the simulation, a bar of dimensions 120 mm by 20 mm by 5 mm is used (L x w x h). A load of 100 N was applied to the centre of the beam along a line, and the effective length of the beam after applying the constraints was 100 mm. The analytical equation for 3-point defection calculations is shown below [13] in addition to the moment of area, I.

$$I = \frac{1}{12} wh^3 \tag{4.17}$$

$$\delta_{3point} = \frac{FL^3}{48EI} \tag{4.18}$$

**Figure 4.5:** A look into the constraints placed on the 3-point bend test simulation

Figure 4.5 shows the remote displacements placed on the beam. It must be said that in very proximity to the remote displacement, there is a stress singularity that is expected to occur due to the way the elements are restricte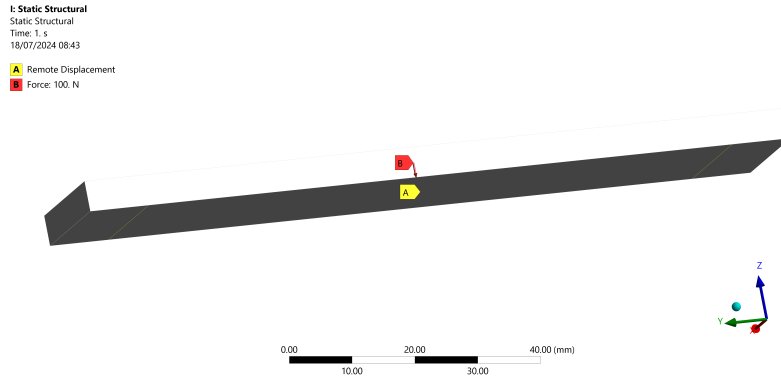d. This will have to be taken into account when interpreting the results. Additionally, something similar occurs when applying a perfect line load. The main idea here is that such loads and constraints cannot be performed in the real world as they are very idealised and perfect, this means that in proximity to these loading conditions, result deviations are expected.

### 4.2.6. Summary of all Verification Procedures

Table 4.1 is provided below to compare all the previous tests made. The primary purpose is to see if the simulations were set up correctly and all inputs accounted for. This is especially important when it comes to transient simulations where long enough simulations need to be done to ensure a steady state is reached since all the aforementioned equations deal with the steady state.

**Table 4.1:** Companions of analytical and Simulation results for the different verification cases

| Test | Probed Value | Analytical | Simulation | Percent Difference |
|------|-------------|-----------|-----------|-------------------|
| Plate Thermal Test | Inside Temperature (K) | 1271.114 | 1271.148 | -0.003096 |
| | Outside Temperature (K) | 1198.264 | 1198.301 | -0.002651 |
| Cylinder Thermal Test | Inside Temperature (K) | 1080.415 | 1080.375 | -0.003700 |
| | Outside Temperature (K) | 1064.449 | 1064.483 | -0.003204 |
| Cylinder Stress Test | Inner Hoop Stress (MPa) | 1.666 | 1.668 | -0.06052 |
| | Outer Hoop Stress (MPa) | 0.666 | 0.666 | -0.09535 |
| | Axial Stress (MPa) | 0.333 | 0.333 | -0.044 |
| Pipe Stress Test | Thermal Stress (MPa) | 91.429 | 91.495 | 0.0725 |
| 3 Point Bend Deflection Test | Deflection (mm) | 0.0339 | 0.0343 | -1.2504 |

The greatest difference is from the 3 points being simulations. Even then the difference is less than 2% making it acceptable. The rest of the simulations show a difference of less than 0.1 %.

## 4.3. Inputs for Thruster FEA

For a thermo-structural finite element analysis, there are two types of main types of loads to be used; thermal loads and structural loads. Each of these loads will be discussed and verified as an additional step to confirm the nature of the load curves applied is as expected.

### 4.3.1. Thermal Loads

The thermal loads on the thruster are of 3 categories; outer surface radiation, outer surface convection and the convection on the inside of the thruster due to the combustion fluid flow. The first two loads,

outer radiation and convection will be taken from the case of the thruster operating on the ground at ambient conditions. This was taken directly from a source seen during the literature review, where convection was defined as 5 $Wm^{-1}K^{-1}$. [67] Looking at the radiation conditions, one of the main considerations to take is the emissivity of the UHTCMC material. The emissivity will be taken as a constant value that does not vary with temperature. A paper, Arc-jet wind tunnel characterization of ultra-high-temperature ceramic matrix composites [32], determined good correlation for a sample UHTCMC that showed an emissivity of 0.85 up to temperatures of 1600K, 0.75 up to 1700K and then decreased to 0.6 and 0.5 for the next 100 K temperature increases. A value of 0.8 is taken, as the paper first assumes 0.75 and then estimates the values for the temperature ranges mentioned previously. Thus, a value of 0.8 is taken as an in-between of 0.75 and 0.85. This in turn tries to balance the high-temperature behaviour of the material and the lower-temperature behaviour. Though there is more bias leaning on the lower temperature region, 0.8 is still taken since the thruster is expected to not exceed 1800K.

The convection on the inside of the thruster is imported from CFD analysis being done by a colleague on the same project. The CFD was done assuming a wall temperature of 1800K, which is assumed to be the maximum experienced by the thruster during operation. It must be said that just because a constant 1800 K temperature constraint is placed during CFD, this does not reflect the actual wall temperatures of the thruster when only taking the convection and radiation thermal loads. The convection was taken from the CFD, and exported into an Excel sheet, and the data was adjusted to take the maximum convection coefficient at each distance from the base of the thruster in steps of 1e-2 mm, 2715 points. This made it easier to import into ANSYS without crashing the workbench due to the high number of pasted cells. The ambient convection temperature was taken as the near wall temperature from the CFD, this was checked using the ANSYS meshing user guide and extremely simplified CFD analysis created and directly compared with what was imported in the thermal simulation. The convection and ambient temperature plots are shown below.
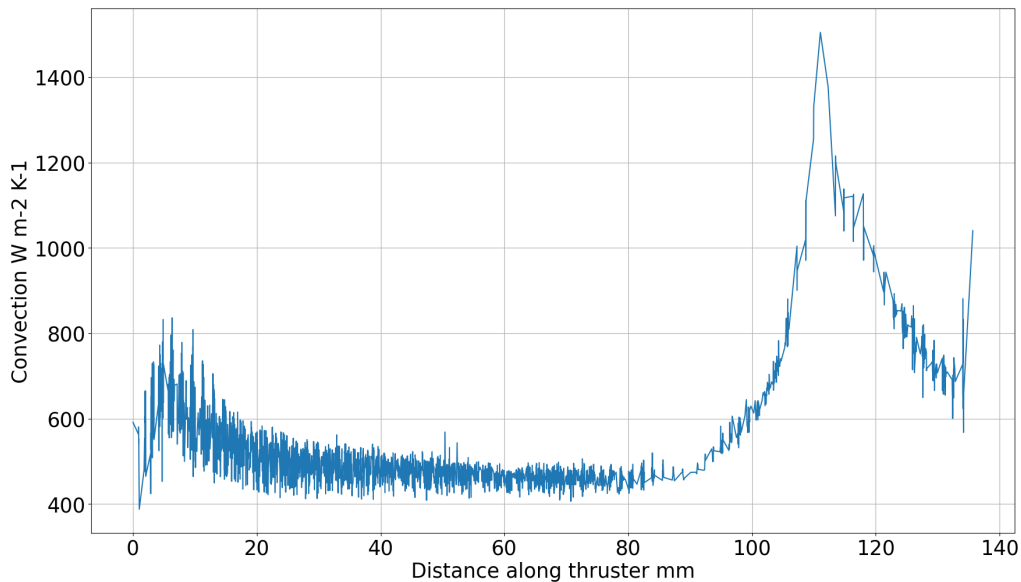


**Figure 4.6:** Convection Coefficient obtained from CFD file and simplified to the nearest 1e-2 mm
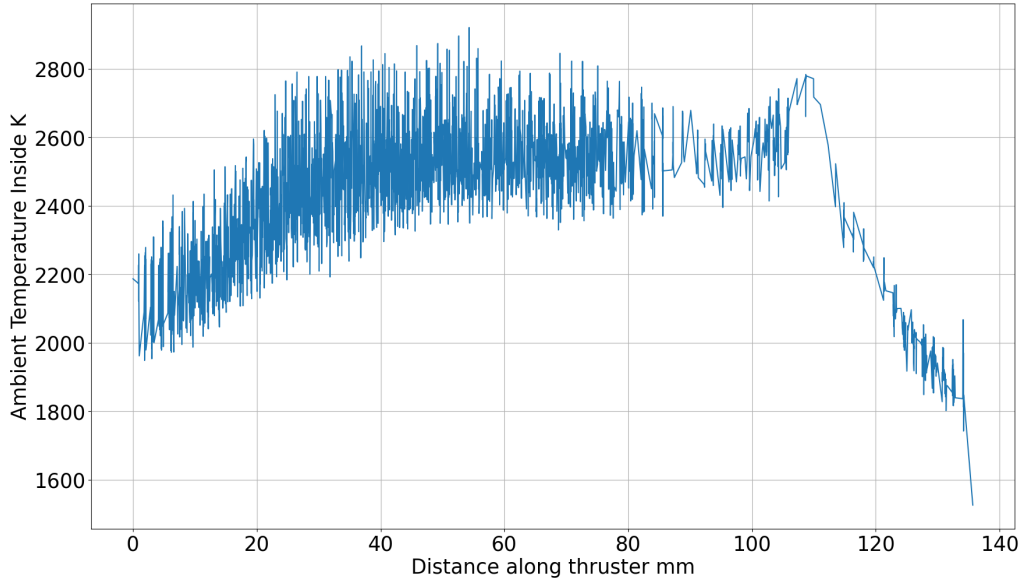
**Figure 4.7:** Near Wall Temperature obtained from CFD file and simplified to the nearest 1e-2 mm

As seen from Figure 4.6 and Figure 4.7, the CFD result shows a maximum convection coefficient of 1500 at the throat and also shows a corresponding near-wall temperature profile for this convection coefficient given a constant wall temperature of 1800K. There is also a small peak at the beginning of the thruster in the chamber. This is expected to be due to the combustion that occurs since the CFD aims to capture the combustion of the fuel and oxidiser, and it occurs at the beginning of the chamber. This also serves to explain the rising ambient near-wall temperature seen in the temperature graph, where the temperature stops rising after around 40 mm. The temperature drop seen in the divergent sections of the conical nozzle also aligns with what is to be expected. While it is a given that these numbers will be used for the simulations, their pattern will still be checked to ensure that the locations of maximum and how the convection coefficient behaves along the axial position of the thruster are as expected. To check this correlation, the Bartz Equation will be used to estimate the convection. Given the higher complexities and mechanisms that the CFD captures, it is not expected that the results will align very well with Bartz. Therefore, Bartz will not be used as a reference for absolute values, but strictly as an indicator for the behaviour of the convection coefficient as the fluid travels along the thruster. The values to be used in the Bartz formula will be obtained from adiabatic CFD simulations under the same conditions, with only the wall being considered adiabatic. The Bartz formula [3][67] used to calculate the heat transfer coefficients is provided below.

$$h = \frac{C}{d_t^{0.2}} \frac{c_p \mu^{0.2}}{Pr^{0.6}} \left(\frac{\dot{m}}{A_t}\right)^{0.8} \left(\frac{d_t}{r_c}\right)^{0.1} \left(\frac{A_t}{A}\right)^{0.9} \sigma_h \tag{4.19}$$

$$\sigma_h = \frac{1}{\left(\frac{T_w}{2T_0}(1 + (k - 0.5)Ma^2) + 0.5\right)^{0.65}(1 + (k - 0.5)Ma^2)^{0.15}} \tag{4.20}$$

In Equation 4.19, h is the convection coefficient, C is set to 0.023 for supersonic flow, $d_t$ is throat diameter, $c_p$ is the specific heat, $\mu$ is the viscosity coefficient, $Pr$ is the Prandtl number, $\dot{m}$ is the mass flux, $A_t$ is the throat area, $r_c$ is the curvature radius of the throat, $A$ is the local area ratio, $T_w$ is the wall temperature, $T_0$ is the chamber temperature, $k$ is the specific heat ratio, and $Ma$ is the local Mach number. It must be noted that preliminary calculations are only done, and in reality, a more iterative approach is expected, such as converging to the final convection coefficient. Since the equation is calculated only once to verify the CFD heat convection in a general sense, the iterative approach is not done. Additionally, this iterative approach requires a lot of time from the CFD side as well which may not be available during the thesis timeframe. The $T_w$ and $T_0$ values chosen are 1800 K and 3100

K respectively. The following values are varying with distance to try to capture the combustion that occurs at the very beginning of the chamber; $k$, $Pr$, and $c_p$.
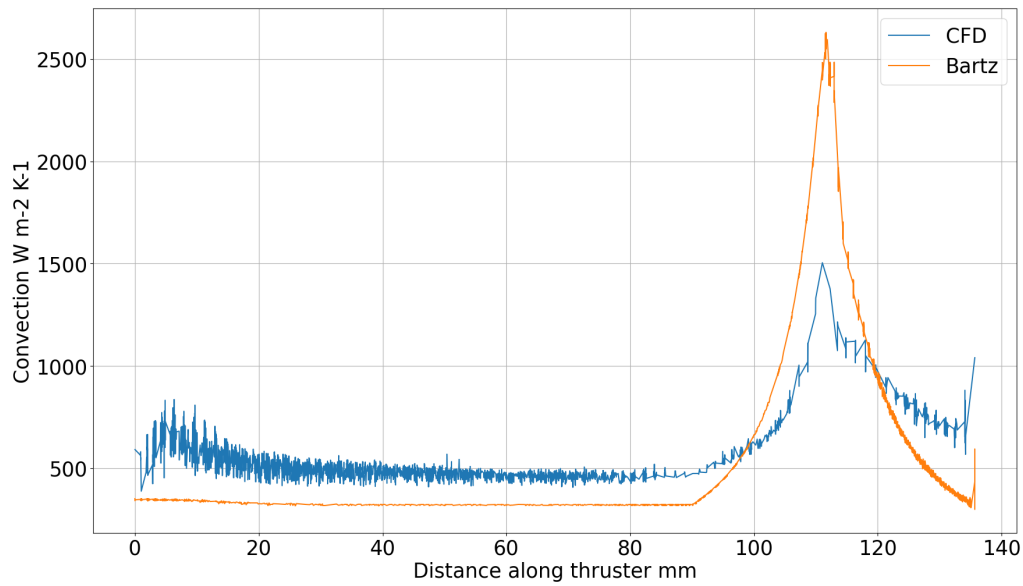


**Figure 4.8:** Convection Coefficient comparison between CFD results and Bartz-based calculations

Looking at Figure 4.8 and Figure 4.7, it can be seen that there is a large discrepancy between the theoretical Bartz values and the CFD-based results. The nature of the curve however is very much present, with peak convection occurring at the throat. Simply following the nature of the curve verifies the CFD inputs into the FEA.



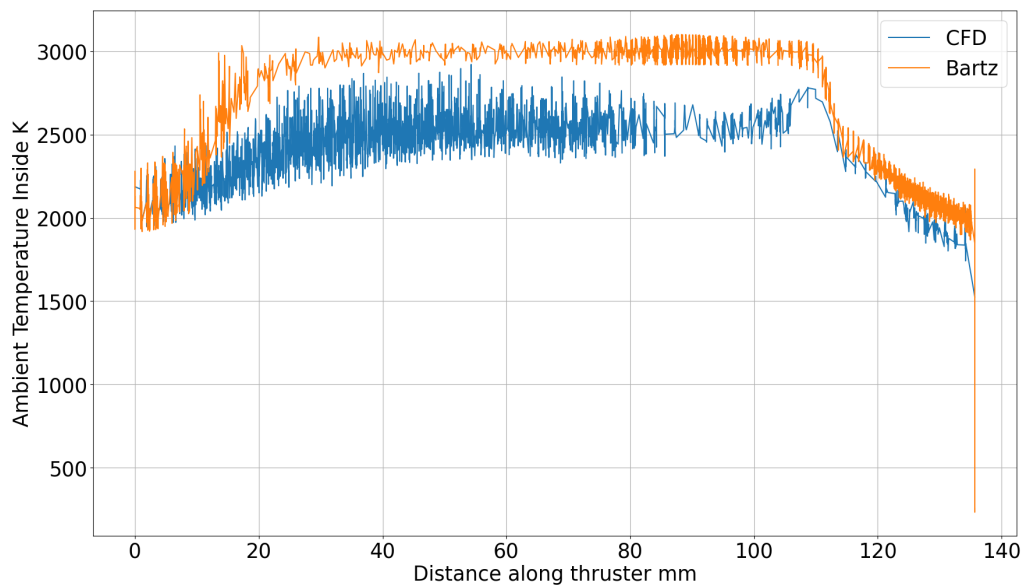**Figure 4.9:** Near Wall Temperature comparison between CFD results and Bartz-based calculations

First, it must be noted in Figure 4.9, that the Bartz temperature was obtained directly from the steady state CFD flow temperature assuming adiabatic wall conditions. Again, the CFD which assumed adiabatic wall conditions were used and its flow values were probed along the thruster to calculate the convection coefficient. The aforementioned was done since combustion was being captured at the beginning of the chamber, and it was desired to see if this combustion would also be captured when applying Bartz. Taking the maximum values, there is a difference of 75% concerning the actual CFD value. While this seems high it is within the order of magnitude of discrepancies when referring to studies that compared CFD with Bartz. One source, Design and Estimation of HTC in CD Nozzle using Bartz's Equation, had a difference of 34%. [31] Another source, a Comparison of empirical correlations for the estimation of conjugate heat transfer in a thrust chamber, had a much larger discrepancy in the order of 69%.[19] While these sources show the CFD having much lower convection than the one determined by Bartz, a source was found, Development of Heat Transfer Correlations for LOX/CH4 Thrust Chambers, which had much better correlation and had the Bartz formula underestimate compared to the CFD.[4] The aforementioned paper also discussed the calibration of the Bartz relation to further increase its validity, this was however not done in this thesis as the CFD results will be taken as input into the simulation. In Figure 4.8, it can be seen that due to taking the $k$, $Pr$, and $c_p$ as varying, a very slight bump in the very beginning of the chamber is seen, perhaps confirming that the progression of combustion does affect convection. Thus confirming the more pronounced effect that is seen by the actual CFD. Additionally, the peaks in the convection coefficient also align, including the locations where it rises and drops. One thing to note is the sharp rise from the chamber to the throat with Bartz, but the more gradual increase in convection seen with the CFD results. This kink is expected to be an artefact of the way the convection is calculated using the Bartz relation. In Figure 4.9, the temperature in the chamber for Bartz is much higher than that of the CFD. Both the CFD and Bartz however show a decrease trend for the near wall temperature at and after the throat region. Additionally, the same trend of an increasing temperature right at the beginning of the chamber is seen due to the progression of combustion.



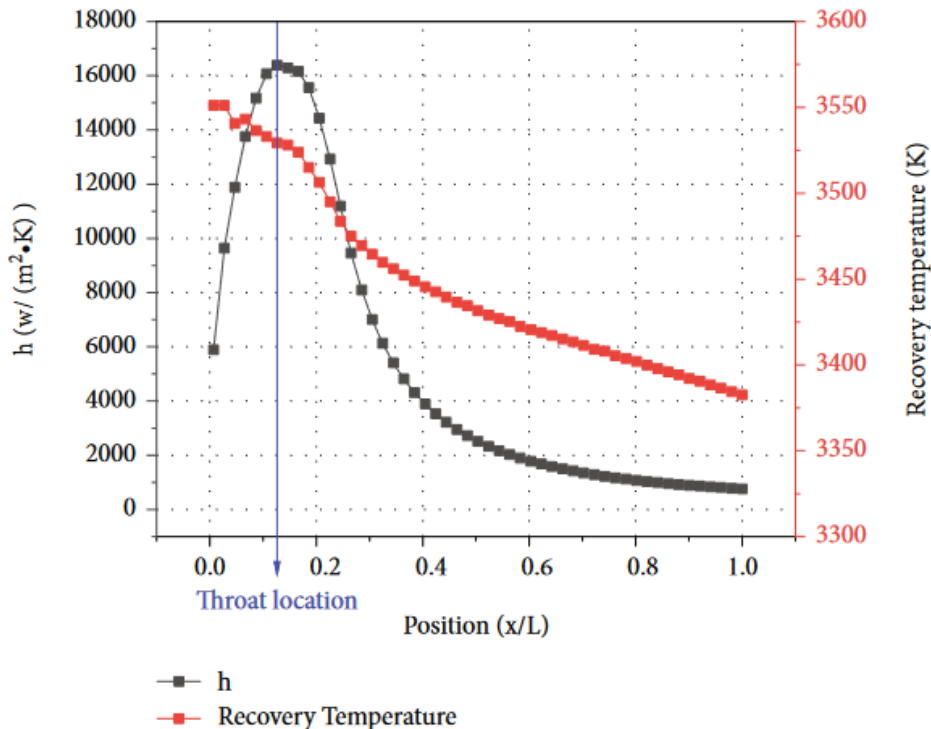**Figure 4.10:** Convection and recovery temperature taken from a paper on thermo-structural FEA.[67]

Figure 4.10 shows a very good correlation between the behaviour of the convection and recovery temperature to the ones obtained from CFD and Bartz. This serves as a way to verify the input thermal loadings that will be used in the simulations in terms of expected parameter behaviour over the nozzle.

Although a direct numerical comparison from a literature source was not found, the decrease in convection and recovery temperature in the divergent section and the peak convection seen at the throat are both good signs that the input loading conditions exhibit the correct behaviour.

### 4.3.2. Structural Loads

The structural loads experienced by the thruster are two, the thermal stresses due to the thermal expansion of the materials, obtained from thermal analysis, and the pressure loading. The pressure loading is obtained for the CFD results and the pressure values are adjusted to the nearest 1e-2 mm to facilitate the pasting of information into ANSYS reliably. The pressure load applied on the inside of the thruster is given below.
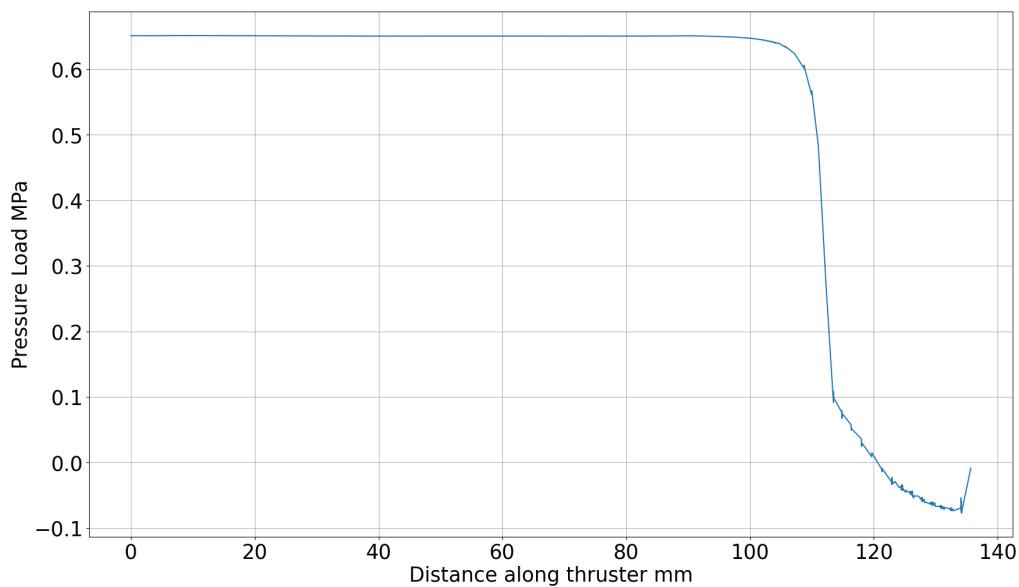


**Figure 4.11:** Pressure load obtained from CFD results file and simplified to the nearest 1e-2 mm

From Figure 4.11 it can be seen that the pressure drops below zero while the fluid is in the divergent section of the nozzle. This is because of the way the CFD simulation is formulated where the ambient temperature is set to that of sea level, thus the pressure values obtained are the net pressure force that occurs in the thruster since the CFD assumes the thruster is operating on the ground. Essentially, when the pressure drops below zero, this indicates that the static pressure in the divergent section of the nozzle is lower than the ambient pressure, but not negative in value. Thus, the pressure differential is what is applied to the inside of the thruster when running structural simulations. This is also the reason convection to air is taken, although it is not present when operating in space. The decision made here was to ensure that the structural outputs were aligned with the CFD conditions and assumptions, hence the lack of a vacuum thruster operation case.

A simple verification of the pressure will also be done using the nature of the curve. An FEA source which provides a figure for the pressure progression throughout the nozzle section will be used as a reference. The pressure before the nozzle, in this case sections A and B will be assumed to be held at constant pressure, the chamber pressure. This is done below.

(b) Structural boundary conditions

**Figure 4.12:** Nozzle Pressure taken from a paper on thermo-structural FEA.[67]

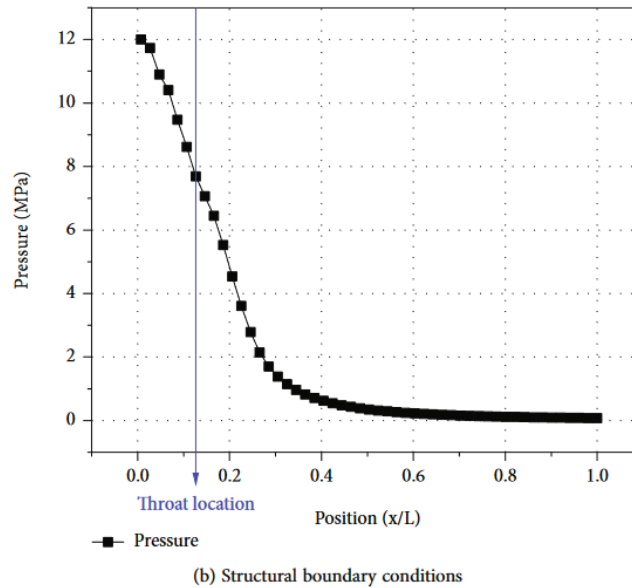Figure 4.12 shows a similar behaviour of decreasing when inside the nozzle. Before the nozzle is reached, in Figure 4.11, and the fluid is travelling along the combustion chamber, the pressure is constant and at its highest value. Whilst direct numerical comparisons cannot be drawn, given that a paper doing similar thermo-structural FEA of a thruster also has inputs that exhibit similar behaviour to the one used in this thesis, this verifies the pressure input that will be used for simulations, Figure 4.11.

## 4.4. Simple and Complex Thruster Model

This section will discuss the simple and complex thruster models that were devised to model the thruster, including why such distinction and necessity for the models was made. First, however, the assumptions that were made for running the simulation and concerning the model will be listed. It must be noted that these are assumptions made based not only on simplifying the problem but also on taking into account the computational capabilities of the computer used for this thesis. For reference, the computer used has 40 GB DDR5 RAM at 4800 MHz with an i9-12900H clocked to 4 GHz. The aforementioned RAM is effectively 30 GB allocated for ANSYS calculations, given the background system operations that need to be done. Additionally, any time frames for simulations will be given for these pieces of hardware. The assumptions for simulations and modelling;

- The surfaces of the thruster are perfectly smooth and no material imperfections are causing unwanted stress concentrations
- The entire thruster will be assumed to be made as one entire piece
- Unidentified thruster schematic measurements for local curvatures will be assumed to be in the range of 1 to 5 mm.
- The CFD loading applied is constant from the time of 0 to 10 seconds of operational time
- The CFD pressure loading is perfectly perpendicular to the inside surface contour of the thruster
- The emissivity of the material will be assumed to be a constant 0.8 throughout the entire thruster temperature range, from room temperature to 2500 degrees Celsius
- The thruster's ambient temperature is assumed to be 295.15 K, thus the spacecraft/test bench to which the thruster will be attached during operation/testing will also be assumed to be at 295.15 degrees Kelvin.
- The convection coefficient of the thruster is a constant 5 $Wm^{-2}K^{-1}$ in air.
- The thruster is assumed to be completely within the linear regime of the material when under operation

- Non-linear contacts can only be taken when working with the complex model to better capture thruster behaviour in certain areas.
- The material is assumed to be perfectly isotropic and the data between two data points is extrapolated linearly.
- The thruster does not experience damping effects where energy is dissipated due to internal thruster mechanisms such as internal friction
- The thruster produces a consistent thrust force in a certain direction and is unaffected by the changing operating conditions of the thruster itself due to changing thruster geometry such as expansion. This also implies a uni-directional modelling approach where there is no iteration to check the convergence of a changing thruster geometry and its effects on the CFD and thrust produced.
- The applied tabular loadings for convection, near wall temperature, and pressure will be simplified to 1e-2 mm to facilitate the copying and pasting of the information into ANSYS without causing crashes. This means that between each data point of example 90.01 and 90.02 mm, the relation is linear as read by the ANSYS program.

## 4.4.1. Process Flow and 3D model

To better understand how the information and inputs will be used to simulate the thruster operation, a process flow will be outlined. This flow will be used as a step-by-step guide on how to create the model, mesh it, input the material and loading conditions and finally obtain the results. The explanations given and descriptions will be in chronological order. This order is what was used to perform the simulation and will also be used to explain the models. Ideally, one can recreate the FEA simulations by following along the steps outlined in this section and progressing from subsection to the next in the order written. The entire ANSYS process flow from creating the model to obtaining the final results is shown in the figure below, Figure 4.13.
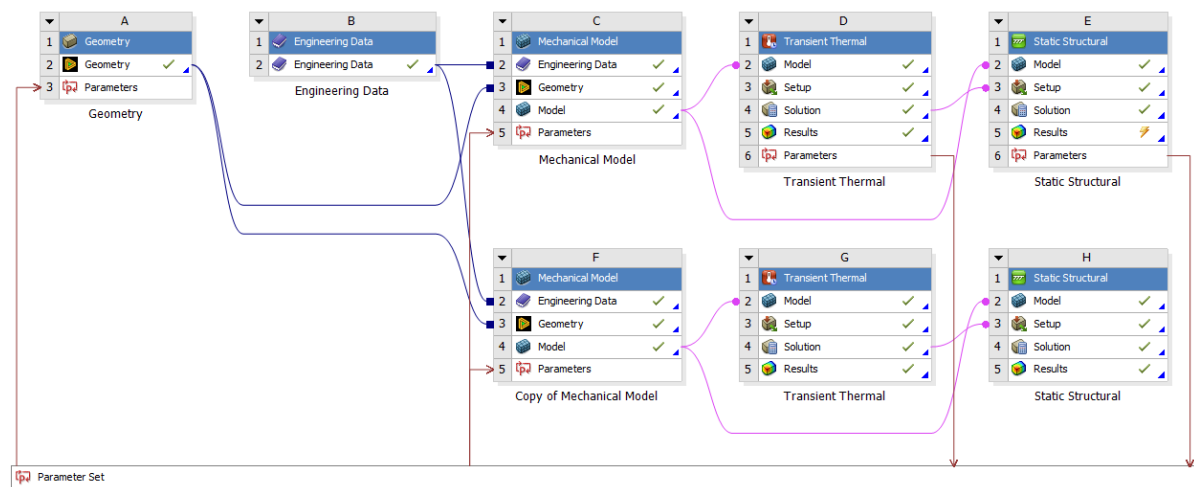


**Figure 4.13:** ANSYS process flow

The figure above and its block labels will be used to describe the entire creation and flow of the simulations. The steps outlined are given below, in the order that they were done in practice, in addition to justifications when needed.

1. Creating the model in **Block A**. The model is created using a design modeller to allow for sketches to be edited afterwards and to select specific parameters for optimizations, the "Parameter Set" red bar at the bottom. Both the complex model and Simple Model parts are all made here.
2. Next, the material properties are inputted in Engineering Data in **Block B**. It is important to ensure this step is done correctly before any actual meshing is done. This is because any changes to Engineering data will have all blocks after they need to be refreshed, thus resulting in a large time loss.

3. Next is **Block C**, the mechanical model block. Since the simple model is created first, the meshing for the simple model is done first in **Block C**. At this step, the named selection for the surfaces is also created to facilitate selecting the faces on which loads will be applied and outputs read from in later blocks.

4. **Block D** is done next. The transient thermal model must be set up and results obtained, before going into the structural model. The information generated in this block will be imported into the next block directly through the workbench by dragging and dropping the solution tab to the setup tab in **Block E**.

5. **Block E**, the static structural block, is always at the end of any branch in the ANSYS workbench blocks. At this step, the stresses and deformations are probed. One important step in this block is that while the model and temperature inputs are already created, the pressure and support inputs are still yet to be created. The pressure inputs can be imported, but that is a beta feature in ANSYS, thus importing them via a table was preferred.

6. Another branch starts with **Block F**, this branch is exclusively for the complex model. In **Block F**, the additional modelled parts for the complex model are *not* suppressed. The contacts and additional complexities will be defined, in addition to any changes to meshing that are needed because of the addition of an extra-modelled body.

7. **Block G** is addressed next and is set up exactly as in **block D**.

8. **Block H** comes last and is where the complex model adds many more complexities into the process. The contacts created in the previous section are imported but must be rechecked to ensure that the update done by ANSYS saw no errors and the results from previous sections were imported cleanly. This is important for the complex model because of the many additional complexities added in **Block F**.

9. Once all the blocks have been passed through, and the models created have been deemed to suffice in accuracy and computational time, the iterative *Parameter Set* for iterations can be set up by selecting all parameters that are to be probed and changed in blocks A to E. Take note that the block specified only points to the simple model branch due to the much more expensive computation cost of the complex model branch making it not feasible to iterate over using the ANSYS workbench.

Most of the blocks can be consolidated into each other, a prime example being the mechanical model and transient thermal blocks. the main reason it was proffered to create as many blocks as possible is to contain potential errors and prevent them from potentially "contaminating" other blocks. This also allowed for errors to be located easily, as ANSYS would always label the block as the source of error and stop the FEA simulation in its tracks. With this many blocks, error detection was more easily facilitated, error turnover and correction were done quicker, and surrounding simulation elements were unaffected.

## 4.4.2. Simple Thruster Model

The simple thruster model only has the thruster itself modelled with the flange, that would be mounted in actual usage, fixed in position. The simple model is fully linear, with no geometric, contact or material non-linearities expected or modelled. Due to how ANSYS meshes a geometrical body that revolves, a slice was made between the flange and the chamber body. This was done to facilitate a consistent mesh that is fully HEX20 elements when changing the thruster dimensions and looking for an optimum. The consequences of this choice are that the option *shared topology* would then have to be activated in ANSYS design modeller, which in the absence of can automatically generate bonded contacts that will affect the results, albeit to a very small degree. Bonded contacts were nonetheless attempted to be avoided since it was simple to do. The shared topology section in the ANSYS mechanical user guide and the forums was also used to confirm the validity of such a decision. Furthermore, named selections were used to make it easier to check that the specified faces are selected for load application for the thermal and structural simulations and to facilitate probing areas for data. The schematic of the thruster that was used to create the model is provided below. The first thruster model that will be used will have a uniform thickness of 4 mm, the maximum allowed.

Figure A.5 is used to create the models for the thruster which will be used in the simulations. Take note that there are missing dimensions in the provided engineering drawing, these missing dimensions

had to be guessed and estimated by scaling or other means. Additionally, the 6 tubular sections, where probes would be placed, are not included in the actual model.
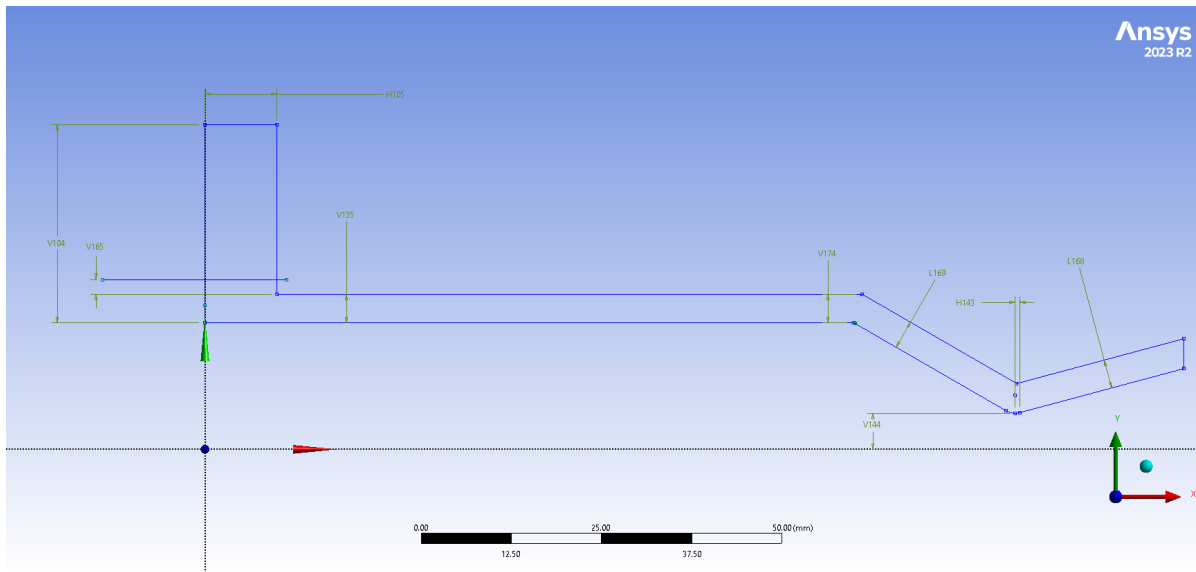


**Figure 4.14:** Side view of thruster sketch with uniform 4 mm thickness

The figure above, Figure 4.14, has labels for each of the constraints. These constraints can be changed and used for the optimization done to find the thruster best suited for in-space applications. The parameter dimensions used for the 4 uniform-thickness, base thrusters are given in the table below. 4 mm is chosen as that is the maximum thickness given for this thesis, this is although 5 mm thickness is specified in Figure A.5.

**Table 4.2:** The constraints and their values as used in design modeller

| Dimension | Value (mm) |
| --- | --- |
| H105 | 10 |
| H143 | 0.65 |
| H2 | 90 |
| L168 | 4 |
| L169 | 4 |
| V104 | 27.5 |
| V135 | 4 |
| V144 | 5.0 |
| V165 | 2 |
| V174 | 4 |

Table 4.2 shows the dimensions used to create the thruster profile. One additional dimension is the holes on the flange for the bolts which were constructed as hole cut-outs by design modeller, hence they were not seen here. The boltholes have a radius of 5.125 mm each and there are 6 of them equally distances on the flange at a radius of 34.75 mm from the axis of symmetry of the thruster. Do take note that the edges in the sketch are all sharp and that is fixed using the blend tool in the design modeller along the outside of the thruster, excluding the flange. The flange is excluded as that part cannot be altered based on the results of this study, thus it has not been altered in any way. A full profile of the thruster is given below to show the curvature and what they were chosen as. Afterwards, the named selections will also be shown, which will be used for applying loads.
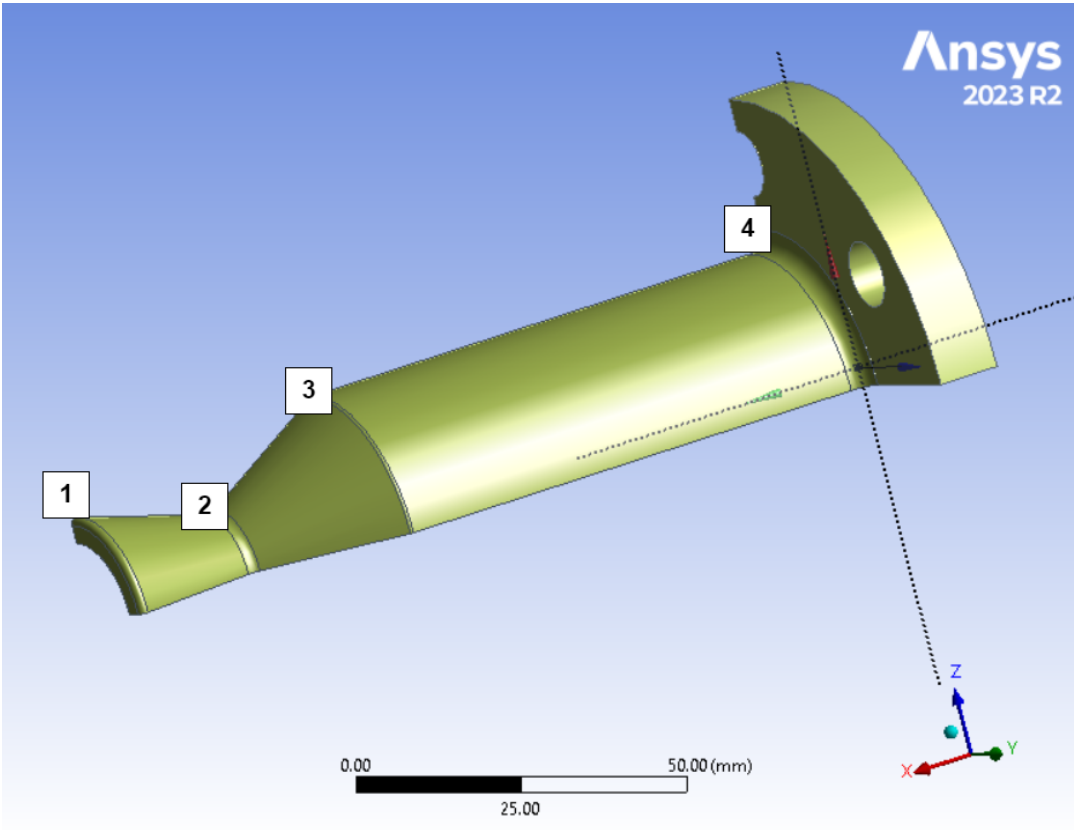
**Figure 4.15:** Diagram showing the sharp edges that were blended

The following blend values were used for each of the labelled curves in Figure 4.15, starting from 1 to 4: 1 mm, 2.5 mm, 1 mm, and 3 mm. Blends 1, 2, and 3 were chosen based on the estimations from the schematic. Blend 4 was subjected to change based on expectations that there would be high stress occurring right at the flange end. It was increased from 2 mm to 3 mm in anticipation of stress concentrations due to the combinations of loads and the fixed flange support that is expected to occur. This amount to increase the radius of curvature was done The exact consequences of this decision will be seen later.
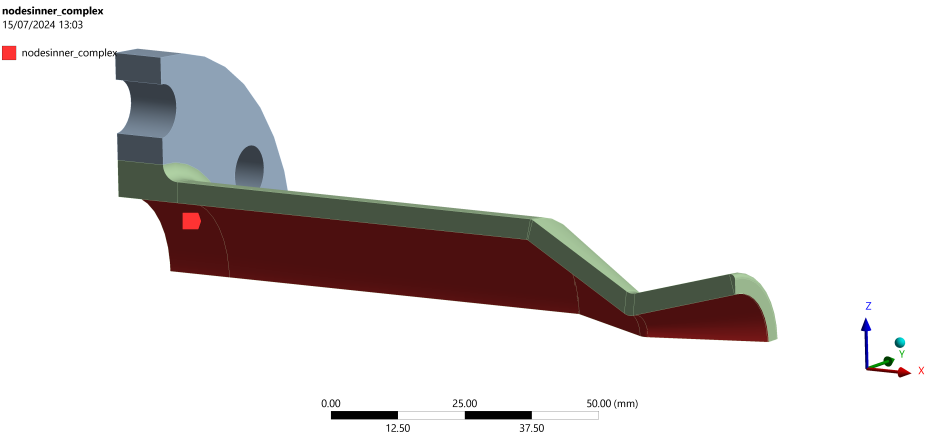


**Figure 4.16:** Inner surface selection for thruster load application and data probing

Figure 4.16 has 7 surfaces which are selected. The surfaces are given as a named selection to allow for parameter optimization to automatically be able to detect the same surfaces if there are changes made in a block that is upstream. This is important as downstream information, which yields the results,

gets greatly affected if a surface is missing and no longer loaded after geometry updates.
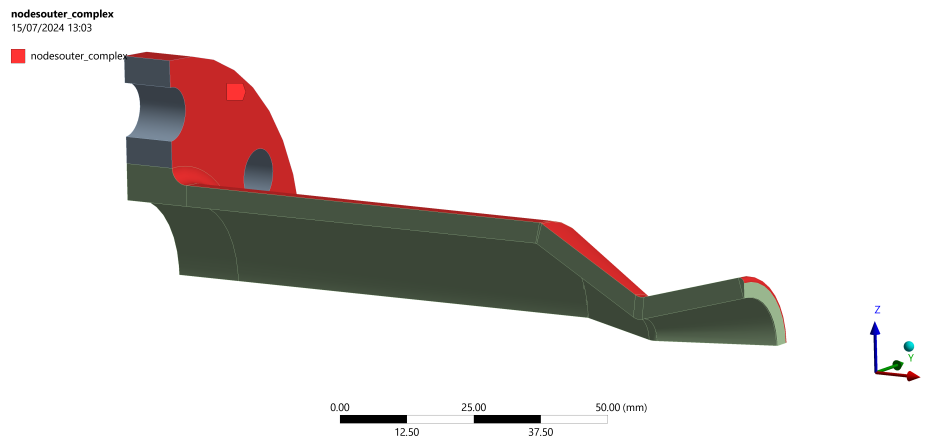


**Figure 4.17:** Outer surface selection for thruster load application

Figure 4.16 and Figure 4.17 show the areas from the loads that will be applied on the thruster. Every time a loading condition is added, one of the above-named selections is chosen as the surface on which the load is applied. The only surface not shown here is the fixed support surface, which is the back of the thruster flange.

Before running the simulations for thermal and structural using the simple thruster model, it is important to know what to expect. Given the fixed support that will be placed on the flange a stress singularity is expected to occur due to the restrictions in the deformation of one face of the HEX20 elements, greatly amplifying the stress as the mesh gets finer. The effects of the fixed support will dampen out the further down the thruster in the axial direction. Regarding the analysis settings, the following can be said:

- Transient Thermal

    - Initial temperature: 295.15 K
    - Convection and radiation ambient temperatures of 295.15 K
    - Analysis Settings: 1 Step, Step End Time 10 s, Initial Time step of 0.1 s, minimum time step of 1e-2 s, maximum time step of 1 s.
    - Heat Convergence: Yes
    - Store Results at All-Time Points

- Static Structural

    - Initial temperature (zero thermal expansion temperature): 295.15 K
    - Large Deformations: Off
    - Analysis Settings: 1 Step, Step End Time 10 s, Initial Time step of 0.1 s, minimum time step of 1e-3 s, maximum time step of 1 s.
    - Pressure Load: applied perpendicular to the surface

The ANSYS user guide goes through all the default program settings, and most have been left to the default program controlled. The reason large deformations are explicitly turned off, rather than left to be "program controlled" like many of the other default options, is to ensure that the program always selects "Off". Heat convergence is turned on since the transient thermal simulation may at times show divergent behaviour if the inputs are not set up correctly, therefore this was turned on to check the behaviour of the program and to kill it in the case that it keeps diverging for long periods. Finally, as was seen previously, only a fourth of the model is seen, this is because 2 axes of symmetry were chosen to be used, which is also why a fourth of the model is displayed in Figure 4.17 and Figure 4.16. The effects of using the symmetry axis are minimal, and it was checked to ensure that the difference is below 1% when compared to the full model. When it comes to axes of symmetry, it can be seen that

a rotational axis of symmetry can be seen. This would reduce the model size to a sixth. Effectively, instead of reducing the computational cost by 4 times, the computational cost could be reduced by 6 times. However, the reason it was not used is that it is not supported for iterations since the information between the mechanical model, and the thermal and structural model has to be connected through the ANSYS blocks in the workbench. The use of such cylindrical symmetry through these blocks is not supported yet by ANSYS. It also says in the ANSYS mechanical user guide that part bodies and interior connections do not support cyclic symmetry.

Next, four different meshes were made for the model. The meshes are as follows: uniform 1.5 mm, 1 mm, 0.75 mm and a custom mesh that locally refines areas where stresses may increase under loading. The meshes are tested if a consistent HEX20 mesh is attached to them, and also they are used for the mesh convergence study that will be done later. The reason the custom mesh is preferred and used in this section will be made clear during the mesh convergence study when all meshes are compared with each other. The custom mesh is shown below in Figure 4.18.
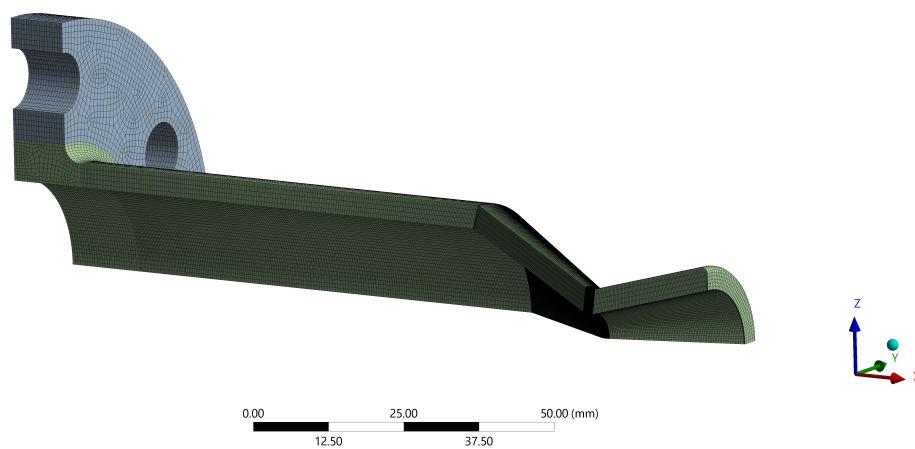


**Figure 4.18:** Custom mesh refined at local areas of expected stress concentrations given the different thickness configurations

In Figure 4.18, the mesh can be seen to heavily be refined in the convergent and throat sections. This was because it is expected that these regions would have the most significant stresses in the nozzle section, thus sufficient mesh elements were desired.
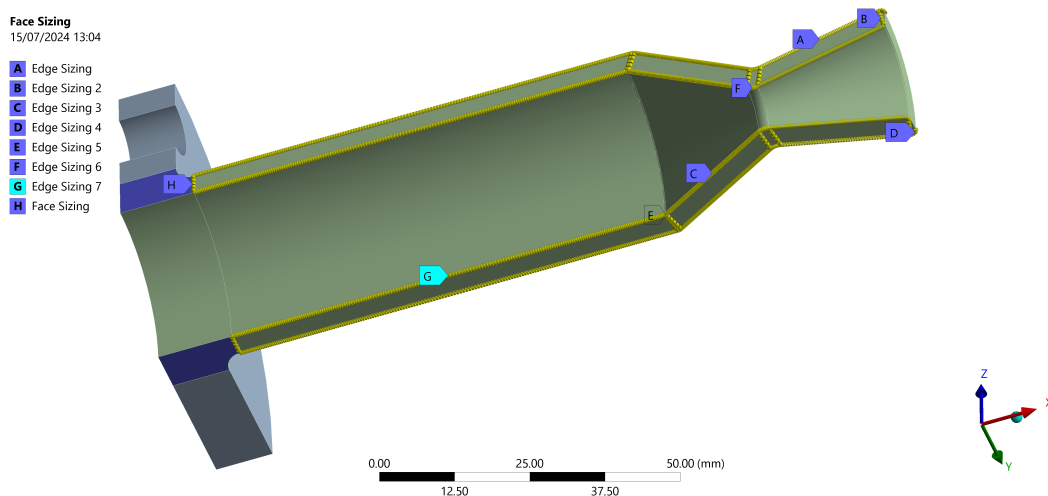


**Figure 4.19:** Custom mesh Parameters and sizing definitions

The labels seen in Figure 4.19 are used as references for the custom mesh. In order, the custom mesh parameters are as follows:

- **A:** 4 edges, 80 divisions
- **B:** 12 edges, 5 divisions
- **C:** 4 edges, 300 divisions
- **D:** 2 edges, 4 divisions
- **E:** 4 edges, 7 divisions
- **F:** 4 edges, 50 divisions
- **G:** 4 edges, 200 divisions, bias type 3 (focus on both ends), bias factor 2.0
- **H:** 2 faces, 0.5 mm sizing

With 4 meshes, many data points can be generated. The specific mesh used to display the results for the uniform 4 mm thruster is the specific mesh last seen. Starting with the transient thermal results, once the internal thermal convection load is applied on the inside of the thruster shown in Figure 4.16 and the radiation and convection loads are applied on the outside surface as shown in Figure 4.17. The final temperature of the thruster at the end of the 10 seconds of operation is shown below.
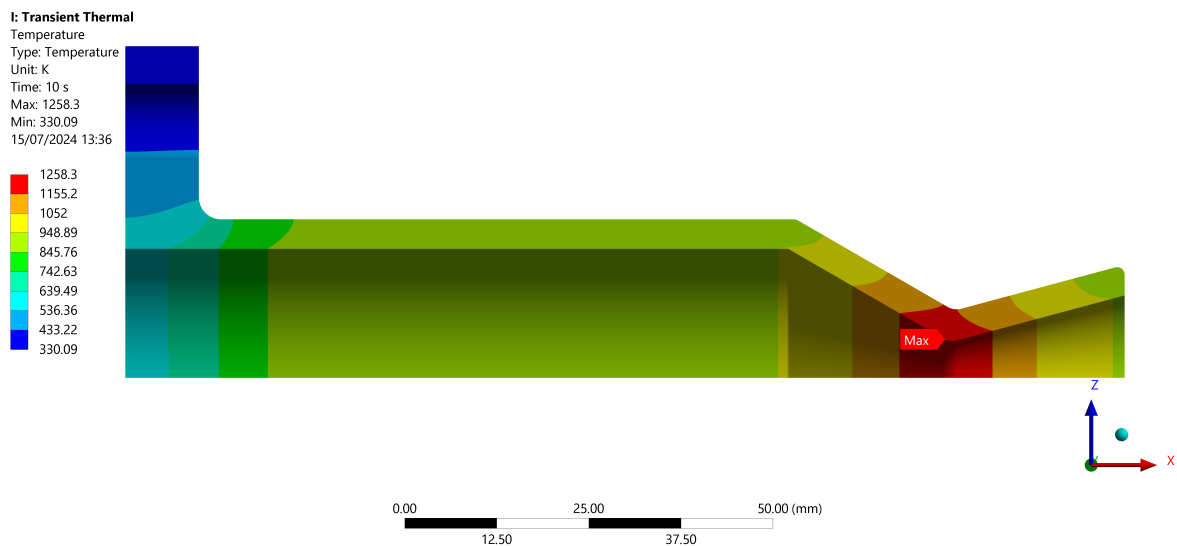


**Figure 4.20:** Thruster Temperature profile at end of thrusting at 10 seconds

From the above figure, Figure 4.20, it can be seen that for a 4 mm thick thruster, a maximum temperature of 1258.3 K is reached at the convergent section of the throat. The location is in line with what is expected based on the results from other papers seen in the literature review. Additionally, ANSYS also determined 16 time steps to be used for transient thermal. The probed areas for data are also given below, Figure 4.21, with the main difference being that the outer surface for probed values does not include the flange itself, but rather starts for the curve edge. The reason is that, as mentioned previously, the actual flange behaviour is not affected by the results of this study because it is outside its scope. Given the expectations of high stresses due to the fixed support and stress concentration due to the sharp edges, the flange is omitted when probing for values. Given that the flange section is omitted, the outer probed section will start from an axial distance of 10 mm, not 0 mm like inside the thruster. This fact can be used to easily distinguish between values probed from the outer and inner surfaces in plots.
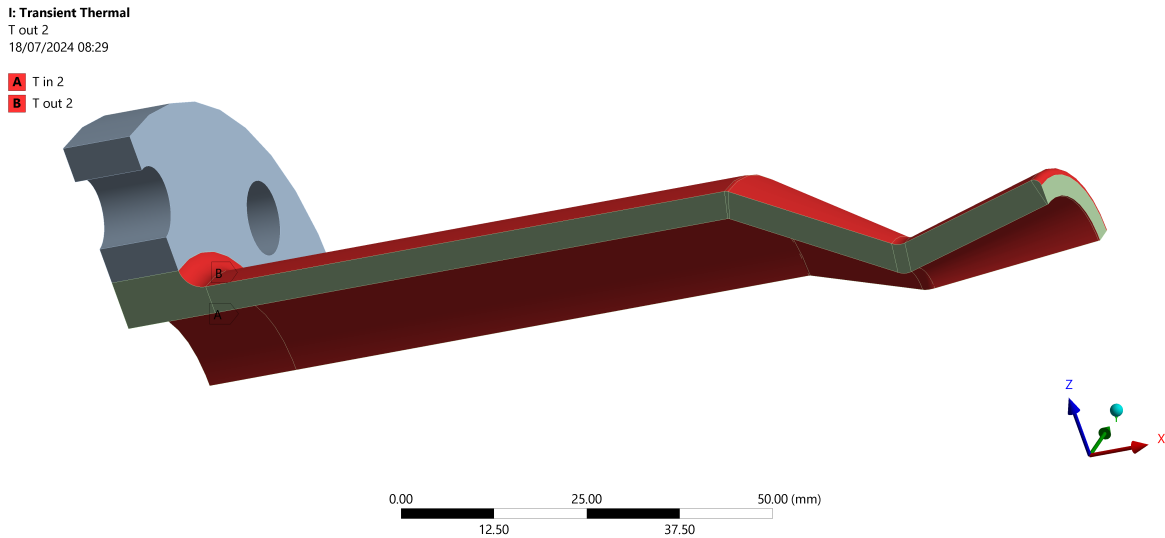
**I: Transient Thermal**
T out 2
18/07/2024 08:29

**A** T in 2
**B** T out 2

0.00            25.00            50.00 (mm)
      12.50            37.50

**Figure 4.21:** B shows the probed surfaces on the outside, and A shows the probed surfaces on the inside. Notice how the flange is not included in the outer surface probed areas.

The maximum temperature on the inside and outside the thruster for each of these 16-time steps is given and discussed below.
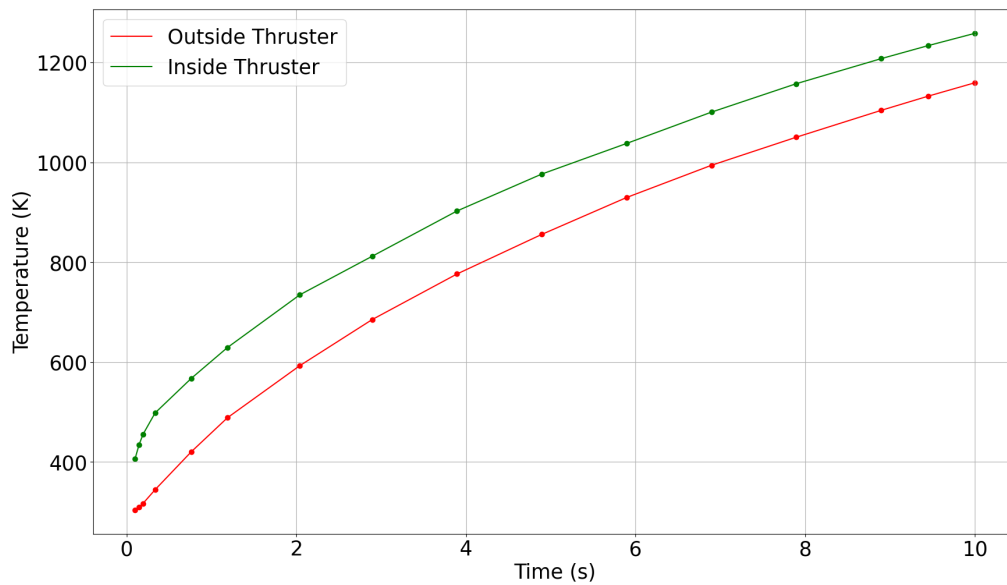
**Figure 4.22:** Inside and Outside Temperature over time for the simple model

The table with the results, Table A.2, is plotted on Figure 4.22 to show the rate at which this increases. It can be seen that the temperature increases rapidly at the beginning and the rate of increase starts to decrease as time progresses, which explains why the software takes more data points at the beginning of the thrusting with smaller time steps compared to near the end where the time step is maxed to 1 second. Additionally, the graph also shows a consistent increase in temperature both on the inside and outside the thruster.

Next up, the stresses experienced by the thruster are to be calculated. Since this is the first test for the

model, more time can be taken to ensure accurate simulations. Instead of using automatic time steps in ANSYS, the time steps from the transient thermal analysis will be manually applied to the steady-state structural simulation exactly as in Table A.2. This allows for a comparison to ensure ANSYS's automatic time stepping falls within an acceptable range. This step is necessary because there is no automatic way to transfer time steps from the thermal to the structural analysis. The structural loading conditions and constraints are shown below in Figure 4.23. The body temperature load is imported by ANSYS and explicitly said to import all time-based results.
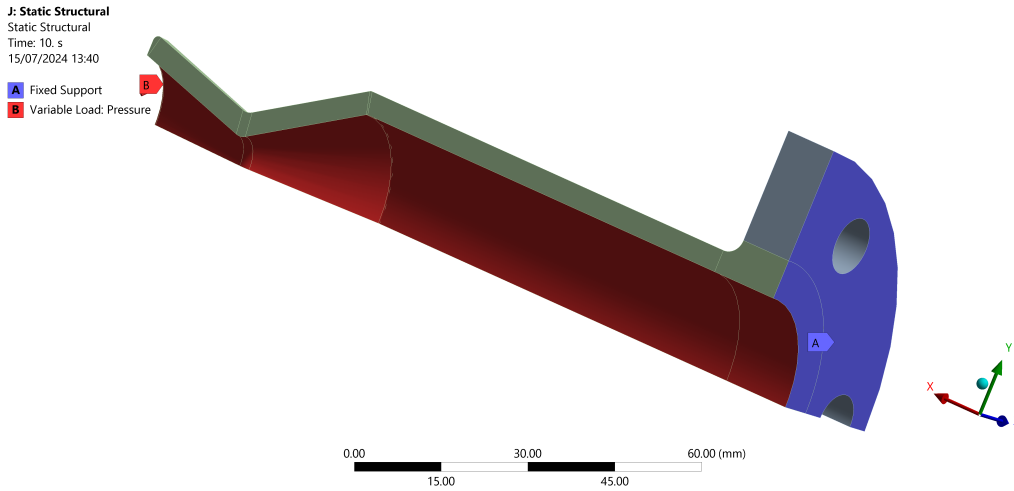


**Figure 4.23:** Fixed Support placed on flange and pressure loading on inside of thruster. This is only to be used for simple structural simulations

With the loading conditions shown above, the simulation is run and the stress at the final time step of 10 seconds during operation is shown below.
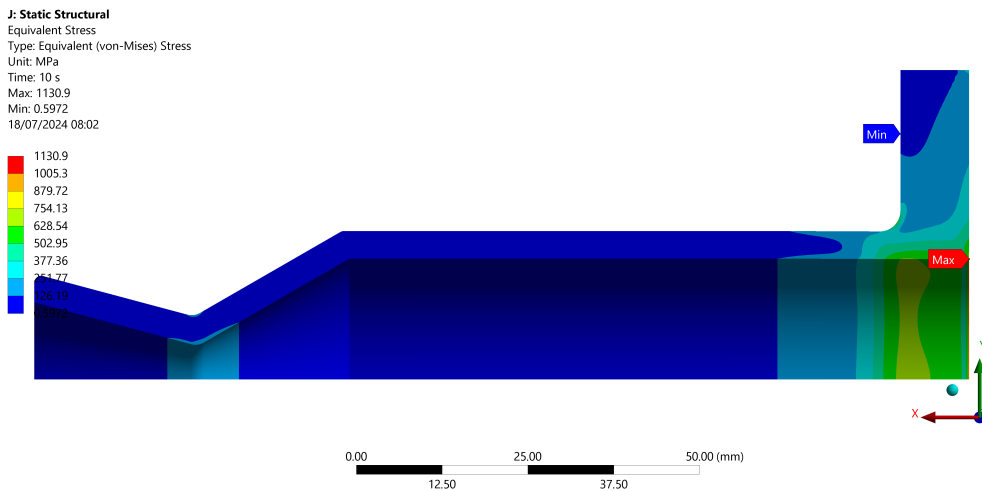


**Figure 4.24:** Stress at end of 10-second operation

From Figure 4.24, it's evident that stress singularities occur as expected due to the fixed support constraints applied to the model. The stresses near the support are significantly higher than in other parts of the thruster, including the expected peak stress in the nozzle's convergent sections near the throat. This outcome was anticipated, as the fixed support prevents deformation in one axis for the HEX20 elements, greatly amplifying stresses—an artefact of FEA simulations, not reflective of real conditions. Since these stresses exceed the material's yield stress, it's crucial to investigate whether this area is a critical stress region requiring further design. To better illustrate stress development over time, a graph of maximum stress at each of the 16 time steps is shown below.
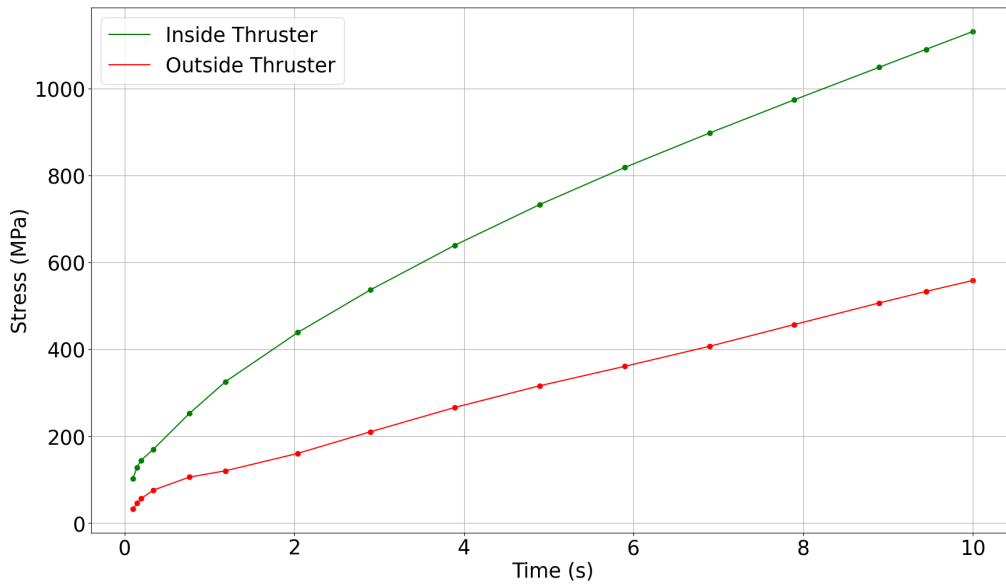
**Figure 4.25:** Inside and Outside Stress over time for the simple model

As shown in the stress versus time graph, Figure 4.25, stress consistently increases until the 10-second mark. The stress singularities from the fixed support are so high that they may obscure other critical areas, such as the nozzle's convergent section, as noted in the literature review. Probing for other high-stress regions reveals that the nozzle experiences the highest stress during the initial operation stages when temperature is rising and has not yet dissipated, leading to significant thermal stresses. An image below illustrates this early stress peak in the thruster.



**Figure 4.26:** Stress peak that occurs earlier at 2.04 seconds in the nozzle

Figure 4.26 only probes section C of the thruster. This same section is what is probed for maximum values of stress over time in the next figure.

**Figure 4.27:** Stress peak graph probing only the nozzle section. Note that this is the inside section of the nozzle only, as that is where the stresses are always highest in the 4 mm uniform thickness case.

In Figure 4.26 and Figure 4.27, it can be seen that a maximal stress of 206.89 MPa at 2.04 seconds is 12.3 % higher than the stress of 18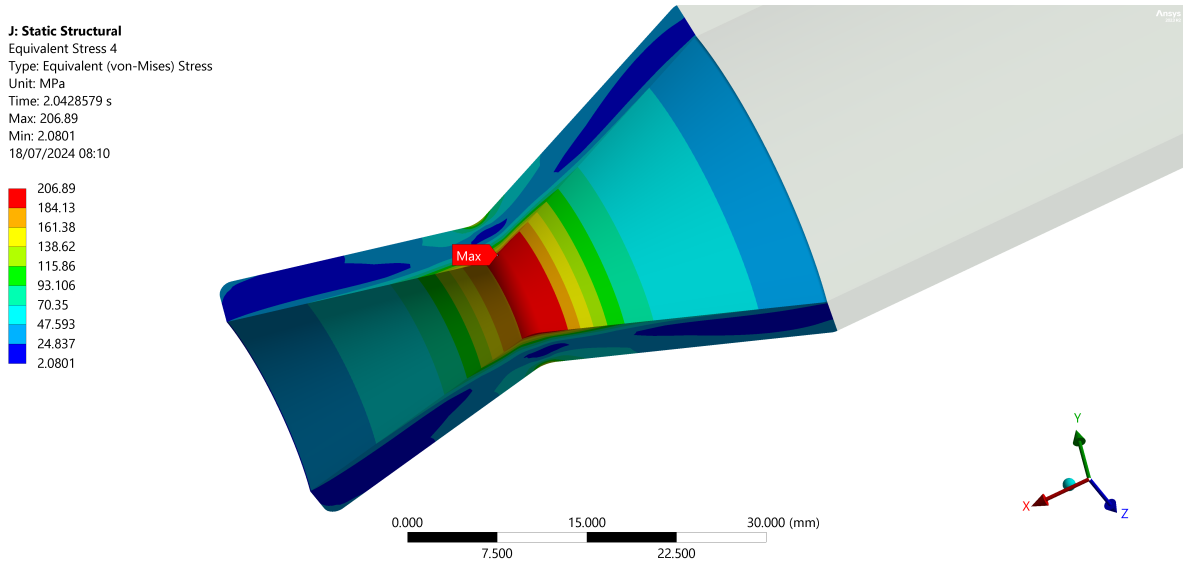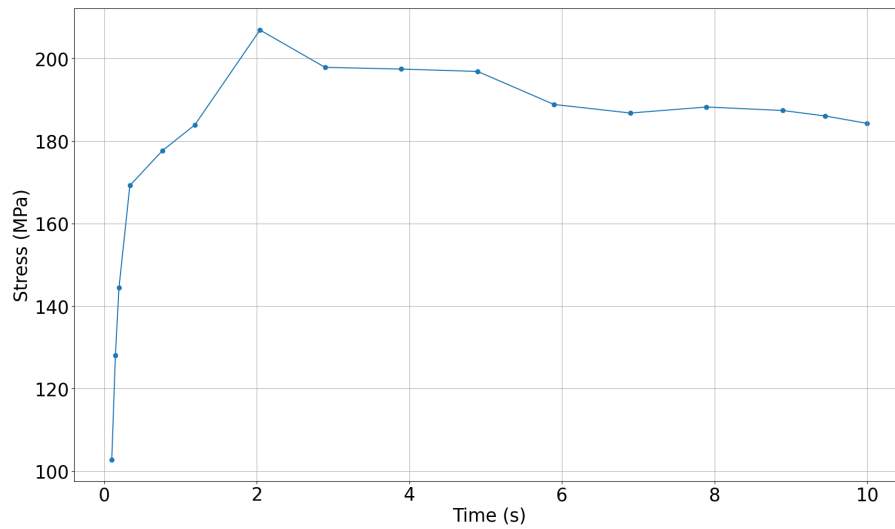4.27 MPa seen at the end of the operation at a time of 10 seconds. The image below shows the same nozzle section but taken at the final operation time of 10 seconds, where a stress ring on the outer side of the nozzle throat is shown.
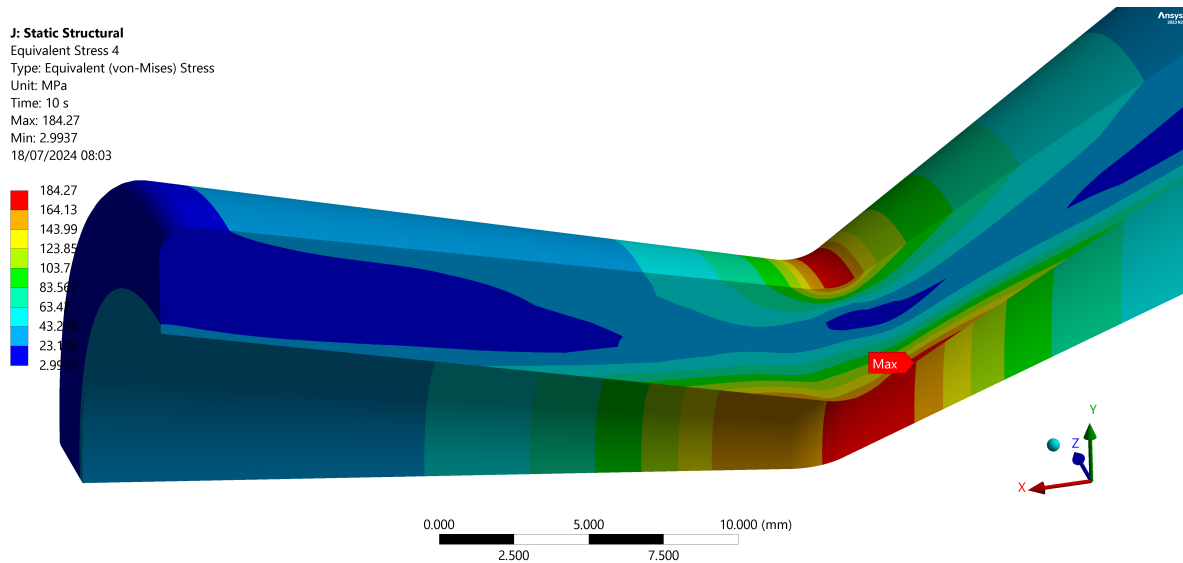


**Figure 4.28:** Stress ring that occurs outside nozzle throat as the operation progresses

Figure 4.28 shows a stress ring that wraps around the outside surface of the throat. Although the stress in the inside convergent section is still higher, the stresses on the outer ring may exceed those observed on the inside of the nozzle. Such an observation is taken note of as of this point, as it may come into play when analysing the optimum design of the thruster. As of now, the stress ring was investigated to be due to the curved edge that was chosen to be 2.5 mm, in the case that a thinner thruster design is seen as the best option in mass, the stress ring effects may be amplified. To mitigate this, the optimum design may require a larger curvature to be in place of the 2.5 mm. This is also a reason why Figure 4.27 does not differentiate between the inside and outside of the nozzle, as the inside of the nozzle always

contains the highest observed stresses in the entire nozzle. If there is a case where the aforementioned is not true, then a distinction will be made between the inner and outer surfaces of the nozzle section.

As mentioned previously, the highest peak is not guaranteed to occur at the same time step for every single thruster configuration, as the thickness varies from one point to another. Therefore, this necessitates the confirmation that the setting setup for automatic time steps to facilitate fast iterations has been set up correctly on ANSYS and captures this maximal stress peak that is subject to occur at other times for each configuration. The below image shows the same thruster nozzle section when the analysis setting uses automatic time steps with a minimum and maximum of 1e-3 s and 1 s respectively.
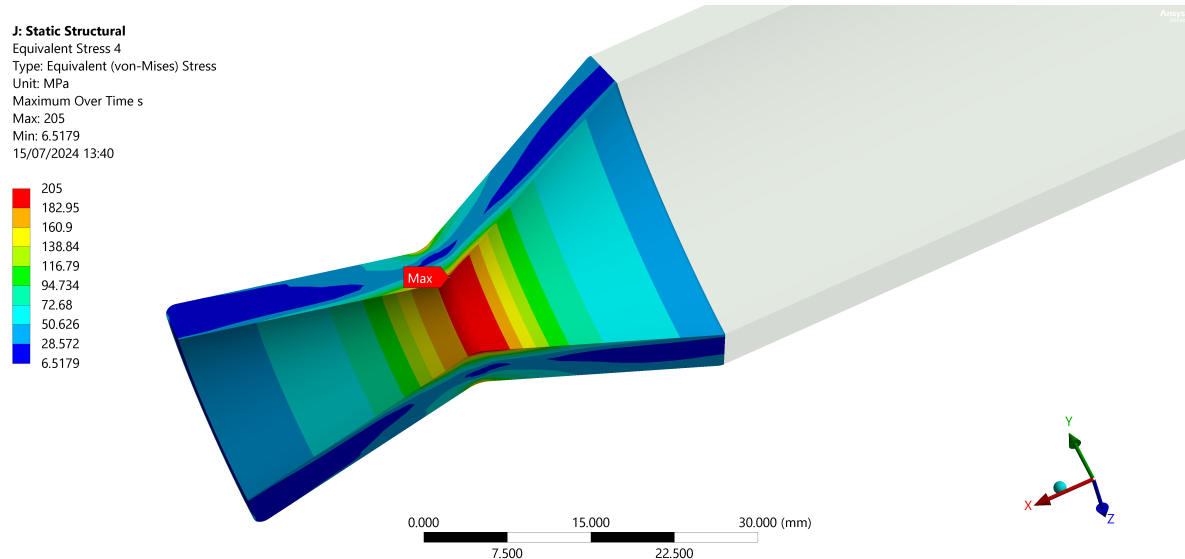


**Figure 4.29:** Stress peak that occurs earlier using automatic time steps occurs at 2.4 seconds in the nozzle instead of 2.04 seconds

It can be seen from the image above, Figure 4.29 (and Table A.3), that the automatic time step is sufficient and the difference in stress results captured if 0.91 % concerning the method that is more hands-on and uses exact the exact time steps. One thing to note is the discrepancy between the time at which the maximum stress is encountered. While the exact time step showed the maximum stress occurs at 2.04 seconds, the ANSYS auto time step method showed a maximum stress at 2.4 seconds. This shows that the final chosen design will opt for the manual time step input analysis chosen to ensure that the highest stress peaks are adequately captured.

This difference of 0.91% is small and sufficient to continue the analysis from this step onwards using the ANSYS auto time step. It is also faster and still gives a good enough indication as to the stresses to be expected in the nozzle. The use of automatic time steps removes the need to manually adjust the time steps every iteration, significantly reducing the time needed to run multiple concurrent simulations.

An additional element to take note of is that static structural was used rather than transient structural for the analysis. This is because the inherent difference between static structural and transient structural is that Large Deflections are turned on and damping effects are on. One transient analysis test was performed with these settings on and the difference was seen to be very minimal in terms of absolute stress values and where they were experienced compared to the exact time step static structural method. Also, the computational cost of these settings is extremely high while yielding very similar results, thus static structural with large defections and damping effects was preferred to save time while also yielding a very good result that can be used for iterative purposes to obtain the best thruster thickness design.
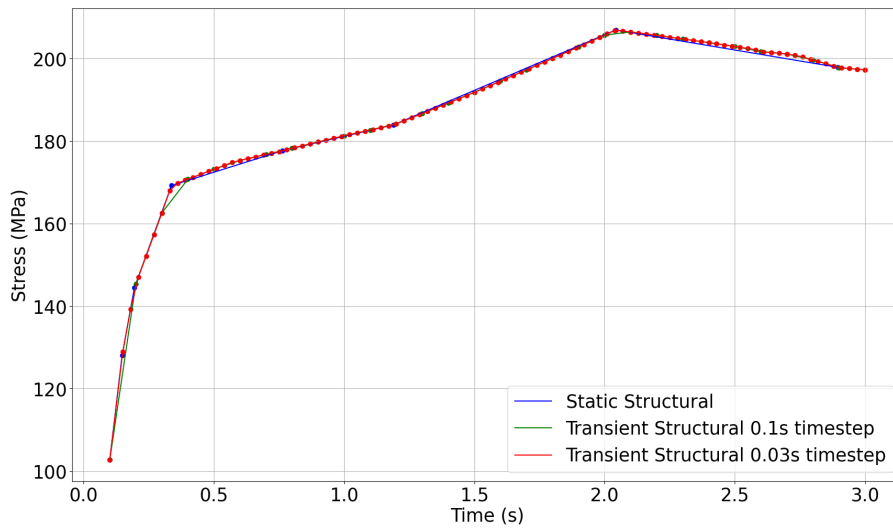
**Figure 4.30:** Maximum stress over time in the nozzle, comparing both test transient simulation

Figure 4.30 shows that the test transient simulations yielded very similar results to the static simulations. There were two transient structural simulations here, the coarse at 0.1 second time steps and fine at 0.03 second time steps. Both took 1.5 and 6 hours respectively to simulate up to 3 seconds. The main difference is that there are more data points between the different time steps. The peak stress, however, in its absolute value remains the same, and so does the general behaviour of the curve.
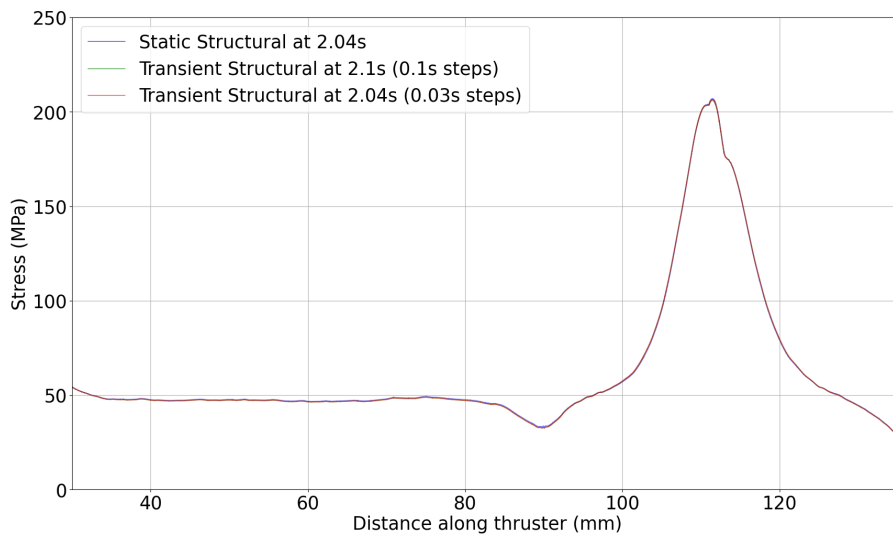


**Figure 4.31:** Stress contours of all transient and static simulations

When plotting the contours of all the different simulations; at 2.04 seconds for static structural, 2.1 seconds for coarse transient structural and 2.04 for fine transient structural. The stress contours almost exactly align with each other, as seen in Figure 4.31. While it can be expected that more detail may be shown if even smaller time steps are given to the transient thermal and structural simulations, it was too computationally expensive and risky towards the computer to maintain such high computational loads for long periods, thus this was not done.

Gives that there is a stress singularity that is caused by the constraints on the simple model, the stresses are high enough that they can be attributed to being due to the constraints and therefore not experienced during actual operations. This, however, needs to be verified and looked into to confirm the theory, thus necessitating a more complex model specifically created to look more into the region near the fixed support. This is covered in the next section.

### 4.4.3. Complex thruster model

The complex model contains a back plate which simulates the plate, spacecraft, or fixture that the thruster would be attached to through the boltholes on the thruster flange. It must be reiterated that the point of creating the complex model is to further investigate the locations of high stress that are susceptible to the fixed flange constraints. The complex model will aim to simulate the bolting of the flange to the back plate and see how it affects high-stress locations, the goal is to effectively fix the back plate of the assembly rather than the thruster and use bolts as a way to fix the thruster in place, thereby relieving the stresses seen previously in the simple mode. Since there are now many more open variables that can affect the results, additional assumptions will have to be made. These assumptions would take into account the computational cost and accuracy desired. The complex model has more additional assumptions that are needed. Based on preliminary results and simple analysis that was done with fully modelled bolts, pretension, contact non-linearities and looking at similar case studies on the internet which attempted to model bolts, it was determined that it is best to start simple and add complexities slowly. One of the highly recommended ways to model bolts preliminarily, given the high lack of detail on how the thruster would be attached, is to use simple beams in ANSYS as bolts. This method will be done in this section first and if the stresses are sufficiently addressed, then more complex models will further deal with given the results seen. The additional assumptions for the complex model are stated below:

- It is assumed that there is no bolt pretension when modelling the bolts. This is done such as to allow for a "worst-case" approach to modelling
- A back plate for thruster attachment will be modelled. This back plate and the bolt will both be assumed to be made out of the standard *structural steel* material in ANSYS.
- The boundary condition between the back plate and the thruster flange is modelled as a non-linear frictionless contact defined by "adjust to touch" to minimize the clipping of bodies into each other.
- Given the limited capabilities of the computer and the time restrictions, bolts will be modelled as beams, therefore effectively not modelling the stiffness of bolt heads, but exclusively the shaft. The reasoning behind this assumption will be explained in more detail in the complex model section.

It must be noted that the above assumptions for the creation and modelling of the complex model were made taking into account that the following information was not available; no experimental data is provided to confirm that the stress concentration artefacts are due to modelling, no specifics were given on the types of bolts used, no specification was given on the material of the bolts or back plate, no information is known on bolt pretension requirements, and no information was given on the exact expected behaviour between UHTCMC and steel in terms of contact modelling. ANSYS beam bolts are modelled as cylindrical tubes put through the holes in the flange and the corresponding one in the back plate. The cylindrical beams are set to be made of structural steel with a radius equal to that of the size of the holes on the thruster flange, as seen in Figure 4.33. Below are the simulation settings defined for the complex model.

- Mechanical Model

    - Frictionless asymmetric contact behaviour between steel back plate and UHTCMC flange, with Interface Treatment set to "Adjust to Touch". The contact surfaces are shown in Figure 4.32
    - 3 x Circular Beams created sticking 5 mm out on both ends, with a radius of 5.125 mm connected to areas of larger radius of 8 mm. Behaviour is set to deformable. This can be seen in Figure 4.33.
    - Only 1 axis of symmetry is chosen with 3 complete boltholes present in the model.

– A back plate and the 3 bolts added are all made of the standard structural steel material
provided by ANSYS by default. Steel was chosen as opposed to aluminium given it can
better withstand higher temperatures.

- Transient Thermal

    – Set to the same as the simple model

- Static Structural

    – Set to the same as the simple model

To be clear, the fact that transient thermal and static structural simulations are set to the same analysis
setting as the simple model does not mean that there will not be any changes when it comes to other
aspects of these simulations. Both simulations are downstream of the mechanical model block, and
thus any changes made in the mechanical block will directly affect these simulations. The extent of
this effect will thus be discussed to justify the usage of the complex model to obtain more tangible and
usable results.



(a) Contact Body
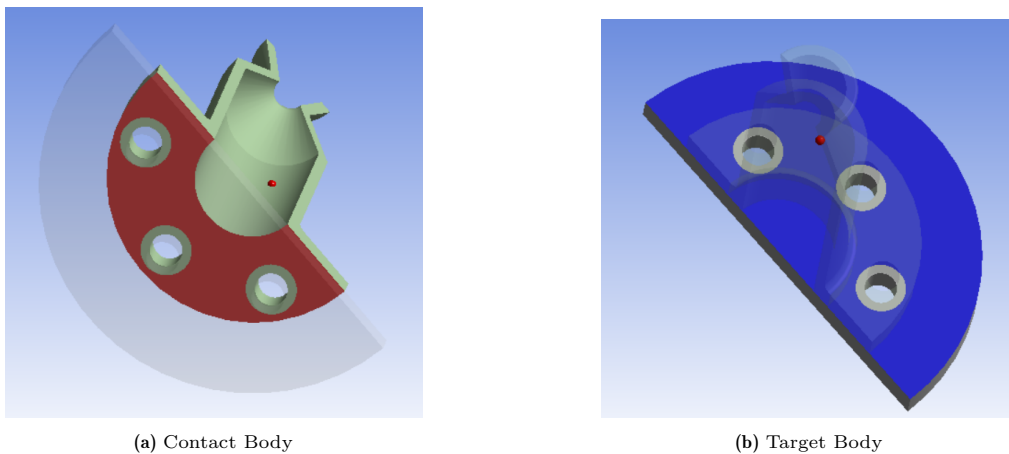


(b) Target Body

**Figure 4.32:** The contact and target body set up for contact surfaces.

Figure 4.32 show contacts set using asymmetric contact behaviour between the back plate and the
flange in the complex model. Note that the 8 mm effective bolt area that will be used to create beam
elements is not part of the contact selection.
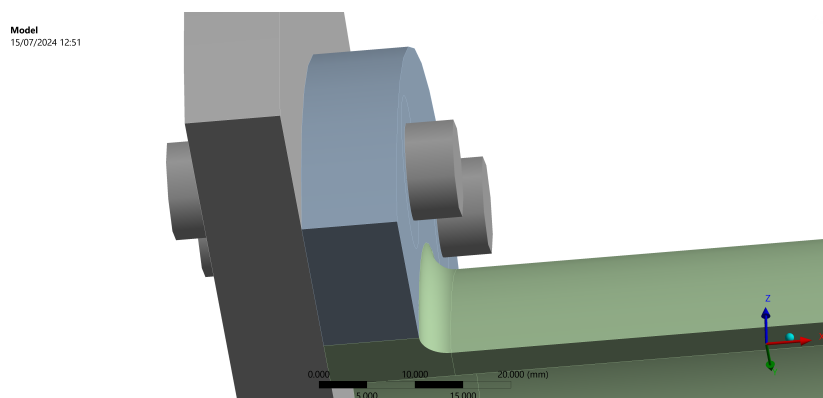


**Figure 4.33:** Close up on the beam method used in ANSYS to simulate bolts

The main changes made are in the mechanical model part, the block that feeds information into the
thermal and structural solutions. The 8 mm effective bolt influence was taken as an initial guess,
including the bolt sticking out 5 mm out of both ends. The aforementioned can be seen in the figure

above, Figure 4.33. The 1 axis of symmetry is a necessary step that was taken, this is because when taking 2 axes of symmetry, a bolthole would be split in half. The beam modelled however would still be complete, not halved at the cut hole. Thus, additional stiffness and stress concentration occur at that specific region. Therefore, it was opted to run the simulations for complex models with a half model to avoid such situations. The mesh used for the analysis is set up the same way as in the simple model-specific mesh. Additional complexity was added to the process of mesh generation, which was to first create the mesh for the back plate and then the thruster. This was done to avoid errors in ANSYS when optimization iterations are done.
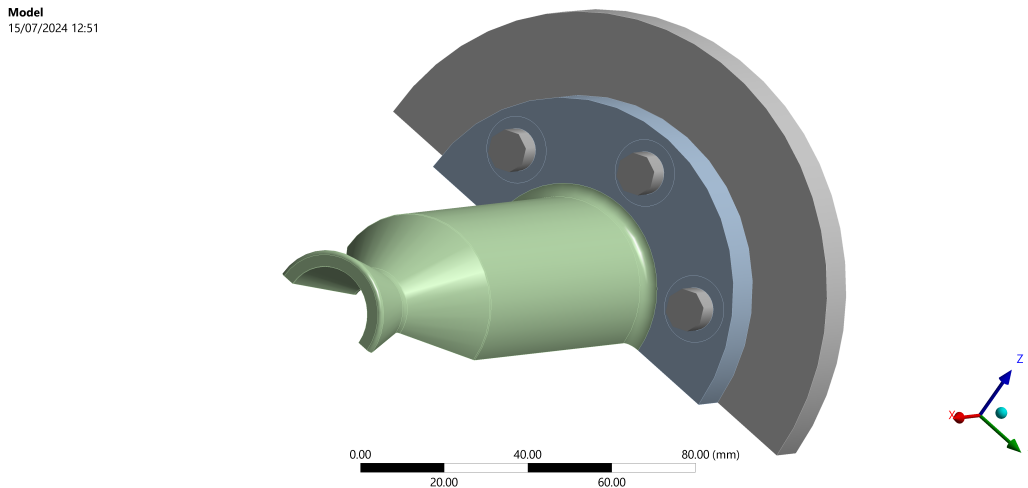


**Figure 4.34:** Full view of the complex model with 1 axis of symmetry and beam elements

Figure 4.34 shows the full model. Take note that the thermal boundary conditions are set up the same and the emissivity or heat loss due to the back plate or the beams is not taken into account directly by the addition of any radiation or convection inputs. This is because the back plate aims to relieve stress and to investigate the areas of high stress caused by a fixed flange, not to relieve any temperature. It must be said however that a slight drop in temperature due to the presence of material is expected in areas close to the added back plate. The final time of 10 seconds for thermal is shown below.
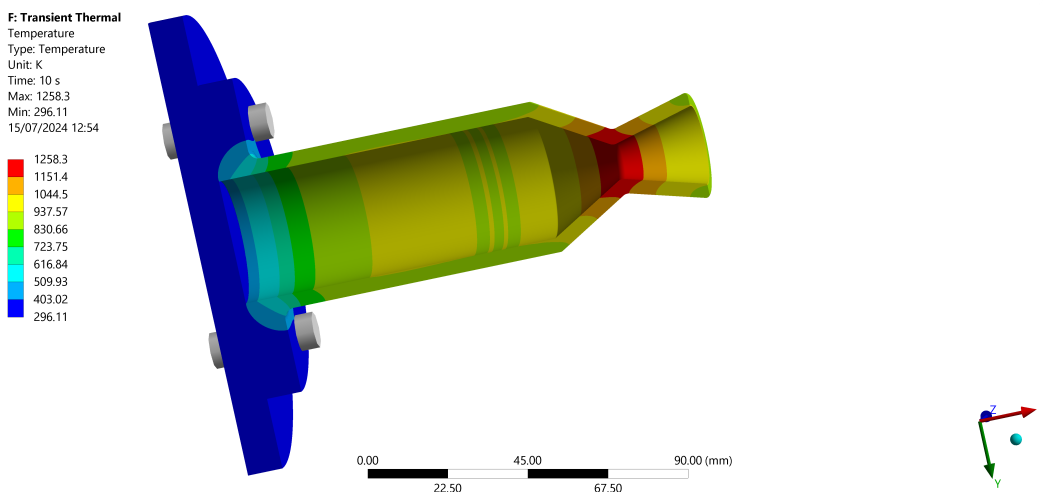


**Figure 4.35:** Complex model temperature profile at end of 10 seconds operation

Figure 4.35 shows very close similarities to the simple model temperature at 10 seconds, Figure 4.20. The maximum temperature shows a difference of 0.0011% compared to the simple model. The probed areas in the complex model are the same as the simple model, as seen in Figure 4.21, for consistency. The table below shows the thruster temps on the inside and outside walls of the thruster.
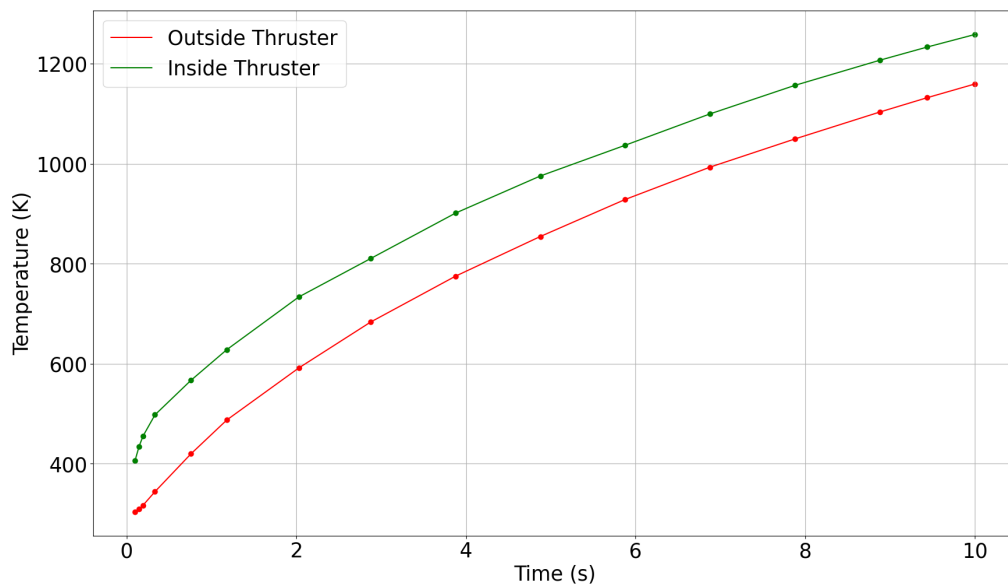
**Figure 4.36:** Inside and Outside Temperature over time for the complex model

The behaviour of the graph seen in, Figure 4.36, is similar to that of the simple model. Table A.4 also shows a consistent increase, like the simple model, Table A.2. To obtain more insight, the graphs would be overlaid onto each other to see where exactly the complex model and simple model have deviations. Such a graph for the inside and outside of the thruster is shown below.
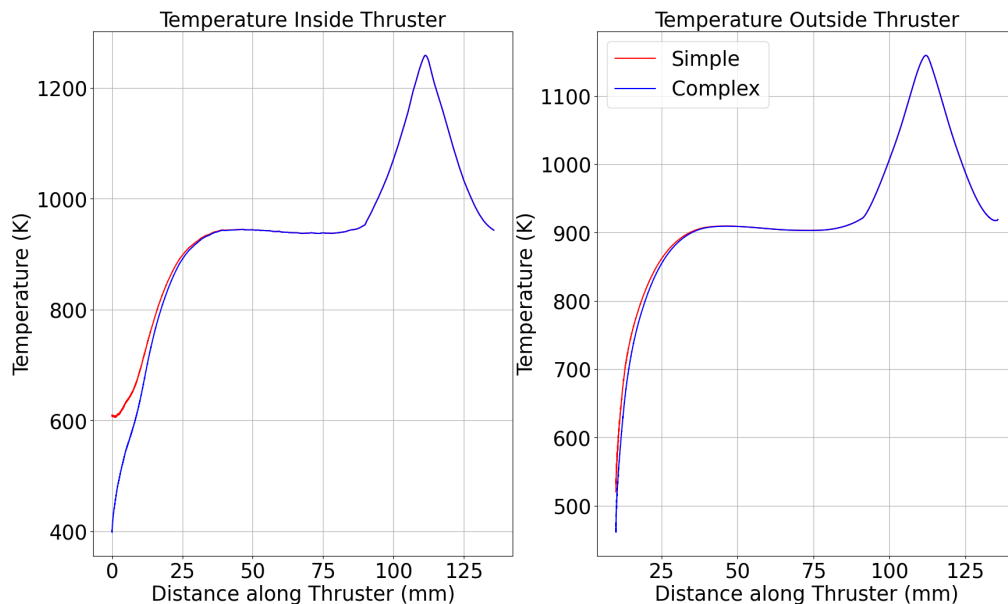


**Figure 4.37:** Simple versus Complex temperature distribution along the nozzle. The Simple model is in red and the Complex model is in blue

As seen from the figure above, Figure 4.37, the temperature is mostly coinciding for the complex and simple model, except for near the beginning and closer to the back plate. Specifically, for the inner and

outer measurements, the temperatures of the complex model are within 2% of those in the sample after 18.7 mm for both the inside and outside temperature measurements. As expected, the temperature in the complex model is slightly lower, most likely due to the added material which would conduct heat and therefore cause the temperature at the probed areas to decrease. The next step is to perform the structural analysis using the complex model. The figure below shows the new fixed support that was placed instead of the fixed support on the flange.
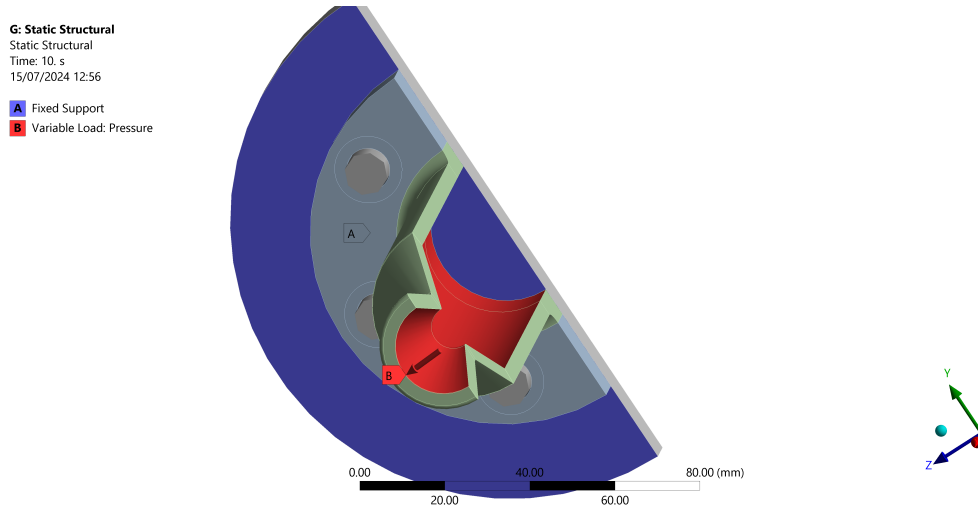


**Figure 4.38:** Adjusted Support on the back plate instead of flange for the new complex model used in the structural simulation

With the new support chosen as in the above figure, Figure 4.38, the simulation is then run with exact time steps obtained from the transient thermal simulation. The exact time steps are used since it is preferred to not assume that the auto time step would still be able to capture any phenomena that occur due to the modification made in the complex model. The results of the complex model are shown below at a time of 10 seconds.
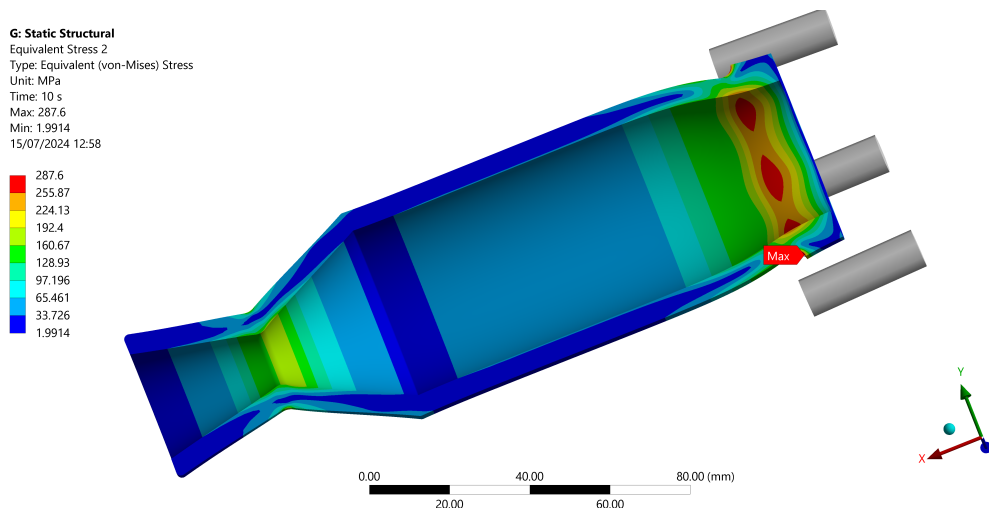


**Figure 4.39:** Complex model stress at 10 seconds for only the thruster, excluding the flange

It can be seen from Figure 4.39, that the high stresses seen near the flange have been greatly reduced. So much so that they are now below the fracture strength of the UHTCMC material. Similarly to the simple model, however, the stresses near the flange are still greater than those experienced at the nozzle. However, looking closer at the stress over the whole thruster, there is a local stress peak occurring well before the 10-second mark is reached.
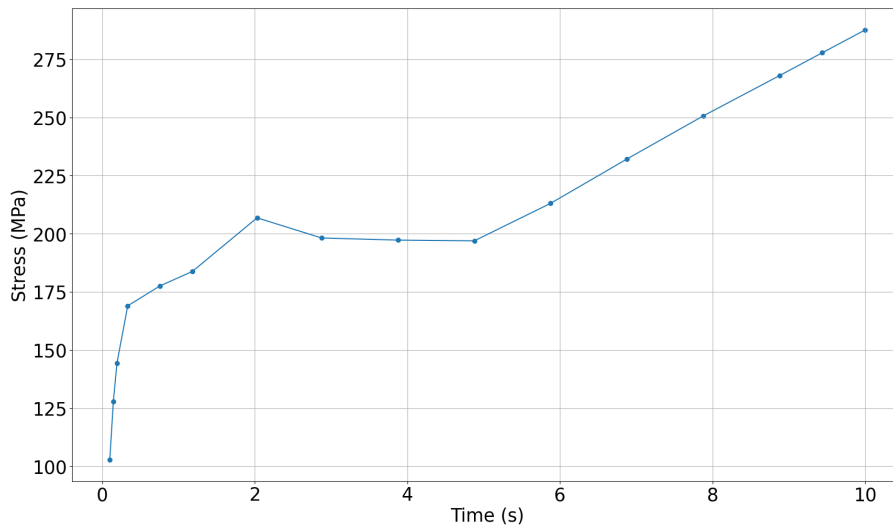
**Figure 4.40:** Complex model stress for only the thruster, excluding the flange

From Figure 4.40 it is seen that this peak is more pronounced due to the much lower stress magnitude difference from the stresses near the flange. This local stress peak is probed, and it can be seen, that similarly to the simple model, it occurs in the nozzle inside the convergent section. The inside and outside probed surfaces of the thruster model are used to observe some interesting things that occur, as seen in the figure below.
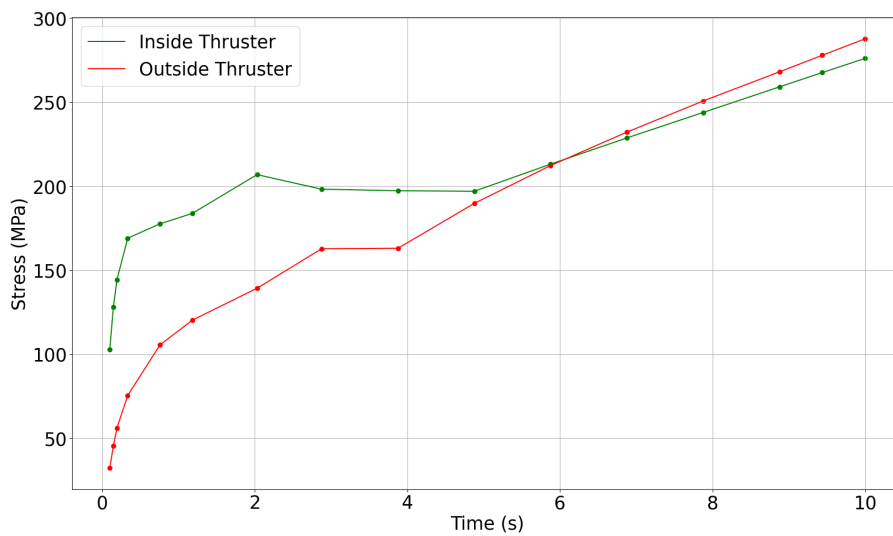


**Figure 4.41:** Inside and Outside Stress over time for the complex model

Figure 4.41 offers valuable insights into the previously observed stress peak. Initially, for the first 5 seconds, the thruster behaves as expected, with stress increasing to a peak before gradually decreasing due to a more uniform thermal load distribution. This pattern matches observations from literature, where the highest stresses occur in the nozzle's convergent section shortly after thrusting begins but well before it ends. However, after 5 seconds, stress begins to rise again, now dominated by the flange rather than the nozzle. By 6 seconds, the highest stress is observed at the outer curved section of the

flange (with a 3 mm curvature), and this remains the case until the end of the operation. The crossing of the red and green lines indicates potential stress concentrations at the flange during actual operation. This finding suggests that more complex models, with fewer free variables, are needed to confirm these results. The complex model succeeded in reducing the high peak stresses seen in the simple model and highlighted other critical areas beyond the nozzle's convergent section.
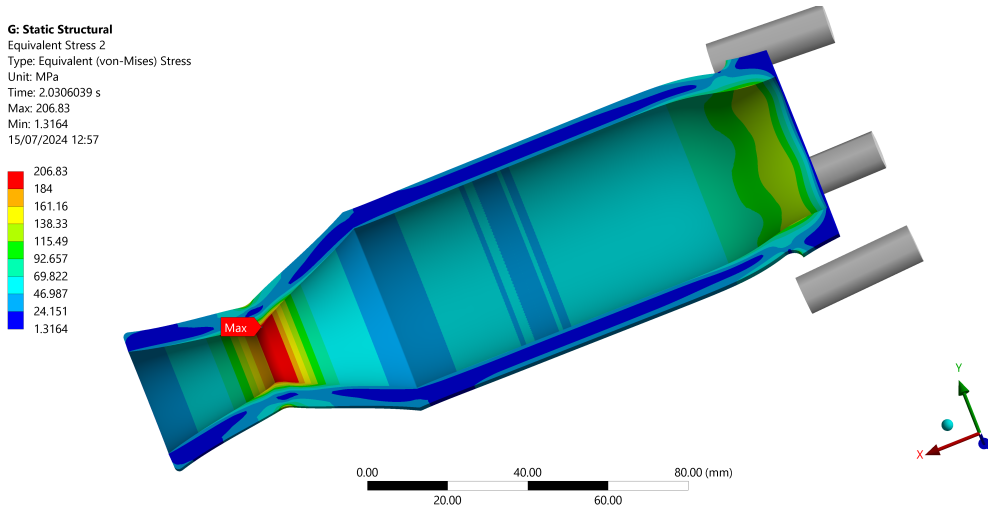


**Figure 4.42:** Stress peak that occurred earlier in the nozzle showed in the full thruster model, given the less pronounced stress effects previously seen in the simple model

Figure 4.42 has the beam elements shown but not the flange. This is to illustrate the slight stress oscillations observed in pale yellow near the beams. The oscillations are due to the localised stiffness of the beams. This effect may lead to further stress concentration as the beam which aims to secure the thruster in place, has the side effect of inducing stress concentrations. This also illustrates why a very complex connective model may not be in the best interest. A very complex model would need many assumptions which directly affect this flange area and may relieve or even induce stresses that cannot be justified as there is no experimental data to refer to.
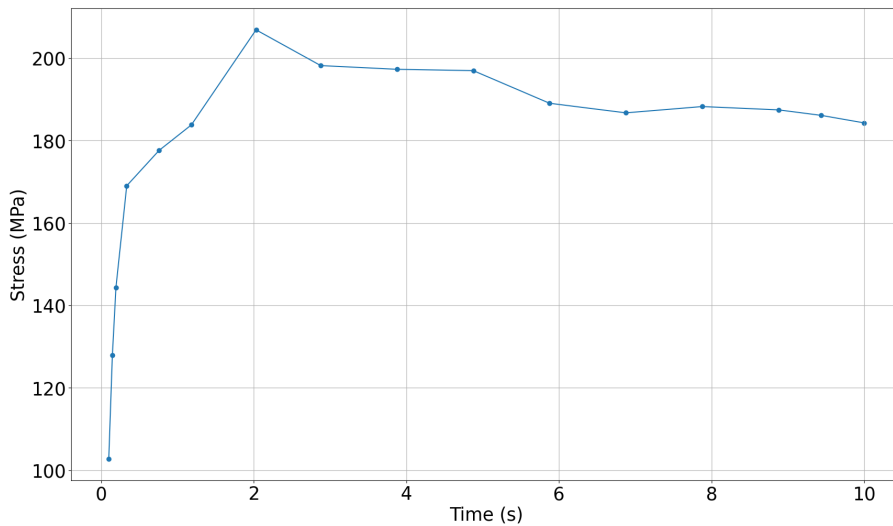


**Figure 4.43:** Complex model stress for only the thruster nozzle. Similarly to the simple model counterpart, this is the inside section of the nozzle only, where the stresses are always highest in the 4 mm uniform thickness case.

Figure 4.42 and Figure 4.43 show a stress peak of 206.83 MPa, which is similar to that of the simple model and has a minimal difference of 0.027% compared to the simple model stress of 206.89 MPa. Table A.5 shows the inside stress in the nozzle only, as stated previously, if the outer stress ring is seen to be significant to cause higher stresses on the outside than inside the nozzle, this will be explicitly mentioned. This indicates that the stresses at the nozzle, far away, from the modification region of the flange and the back plate are looking to have a good correlation and are not affected much. Below is a figure which shows the maximum stress over time inside and outside for just the nozzle section. Since the same faces and areas are probed for stress and temperature, analysis can be done to investigate the differences caused by the modifications more thoroughly when it comes to stresses experienced by the thruster. This can be seen in the graph below.
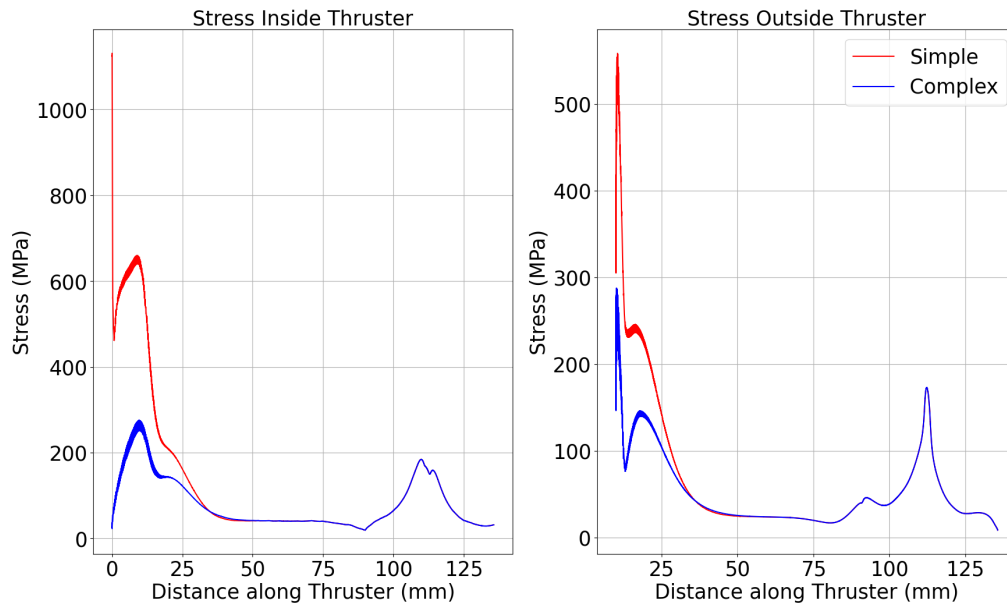


**Figure 4.44:** Simple versus Complex Stress distribution along the nozzle. The Simple model is in red and the Complex model is in blue

Figure 4.44 displays stress along the thruster length at 10 seconds, with stresses on the y-axis and distance on the x-axis, starting from the chamber. The graph highlights the impact of complex model decisions. Notably, the largest stress differences between the simple and complex models occur near the flange on the thruster's interior. Beyond 34.0 mm (inside) and 34.8 mm (outside), this difference drops to less than 2%, indicating that flange stress concentrations have minimal impact beyond a certain point. The complex model reveals two distinct stress peaks: one in the nozzle's convergent section and another at the 3 mm curved flange section. This additional detail was missed in the simple model, though a small peak around 11 mm on the inside stress curve hinted at surface curvature stress concentrations. The identification of a stress concentration at the flange corner, where the 3 mm curvature was chosen based on preliminary simulations, highlights a critical area. While the stress at this point may decrease in a more complex bolted thruster model, exploring that scenario is beyond the scope of this thesis due to the numerous variables and assumptions required, which could undermine the validity of the results.

The next step is to see whether the fracture strength of the material is exceeded or not. To do this, since the fracture strength of the UHTCMC is seen to be temperature dependent, the fracture strength at every location on the inside and outside the thruster can be plotted using linear interpolation for the fracture strength with temperature. The graph which adds fracture strength of the material over the complex model stresses along the thruster is given below.
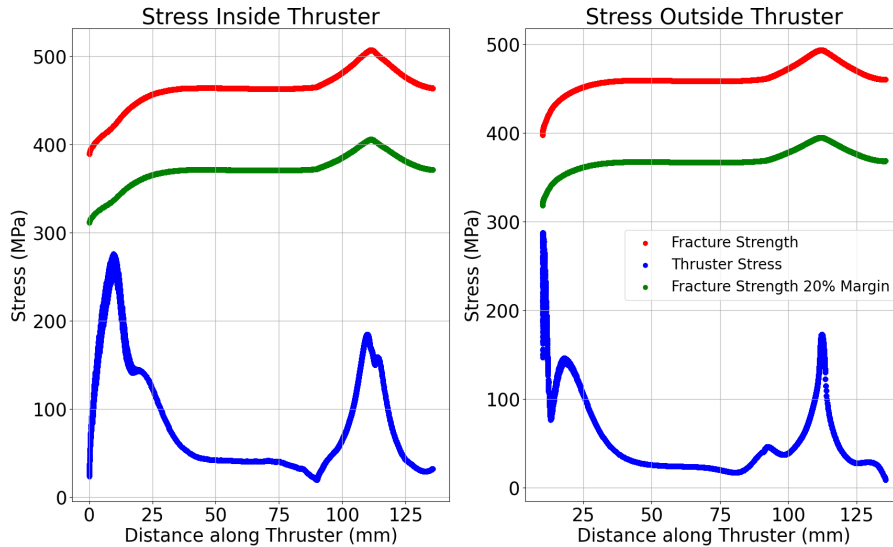
**Figure 4.45:** Fracture Strength and Stress along the Thruster for the complex model at 10 seconds The red line is the fracture strength, the green line is the fracture strength with 20% margin, and the blue line is the stress

From Figure 4.45 shows that the stress in the thruster, when the complex model is used, does not exceed the fracture strength of the material where the stresses are highest near the flange. This is a good sign as it shows that adding some small model complexities, to alleviate the stress and create a more real-world representative model, confirmed that the thruster design is viable and will not have a high likelihood of fracture under operating conditions.
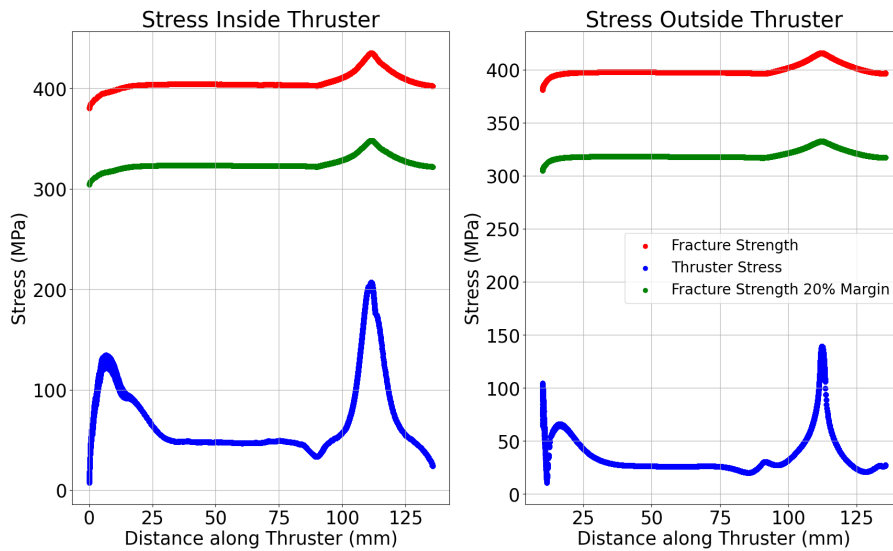


**Figure 4.46:** Fracture Strength and Stress along the Thruster for the complex model at 2.03 seconds.

Figure 4.46 shows the earlier 2.03 peak stress that occurs in the nozzle earlier in operation. Both graphs show that the stresses in the thruster do not exceed the fracture strength of the material. The thruster has a 4 mm thickness near the flange, which prompted further investigation to determine if thinner configurations could exceed the material's fracture strength. Preliminary simulations revealed that thrusters with less than 4 mm thickness near the flange would indeed surpass the fracture strength. This finding is crucial, as it limits the thruster's design options, requiring a minimum 4 mm thickness at the

chamber's start to ensure structural integrity. Although a more complex model could potentially reduce stresses and show that thinner sections might be safe, the numerous unknowns related to the thruster's mounting and assembly introduce too many assumptions, potentially compromising the accuracy of the simulation results. Therefore, the safest approach moving forward is to maintain a consistent 4 mm thickness near the flange to ensure the thruster can withstand operational loads.
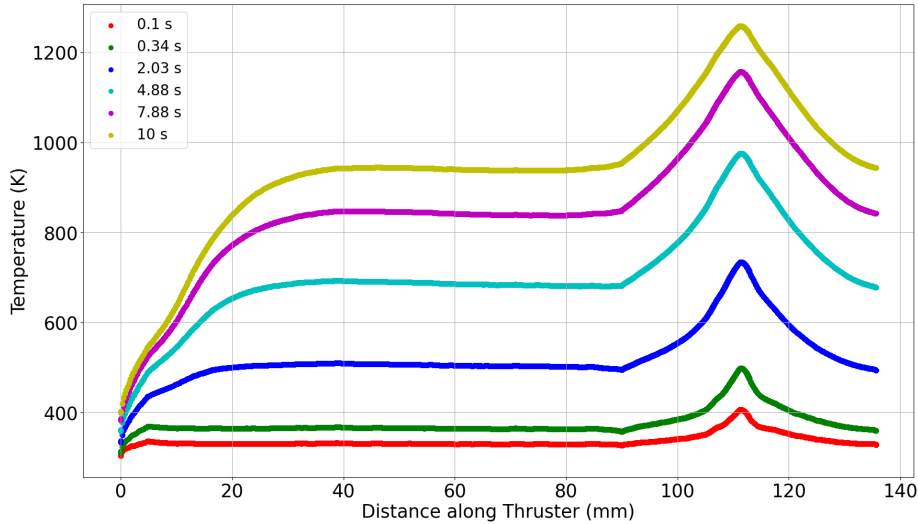


**Figure 4.47:** Thruster Temperature Contour over different time steps

Figure 4.47 shows the nozzle experiences the highest and steadily increasing temperatures with time. The temperature contours shift upward over time, with the rate of increase slowing after 4.88 seconds. The contours converge closer together near the flange, likely due to this area being farther from the highest convection point, the throat, requiring more time for the temperature to change. The temperature gradient near the beginning steepens over time, indicating a more pronounced temperature difference near the flange and around 30 mm along the thruster.



**Figure 4.48:** Thruster Stress Contour over different time steps

Figure 4.48 shows that the stresses at the flange, axial distance of less than 30 mm in general, experience a rise in stress the longer the thruster is in operation. The highest stress is of course reached at a time of 10 seconds. The peak stress in the areas aft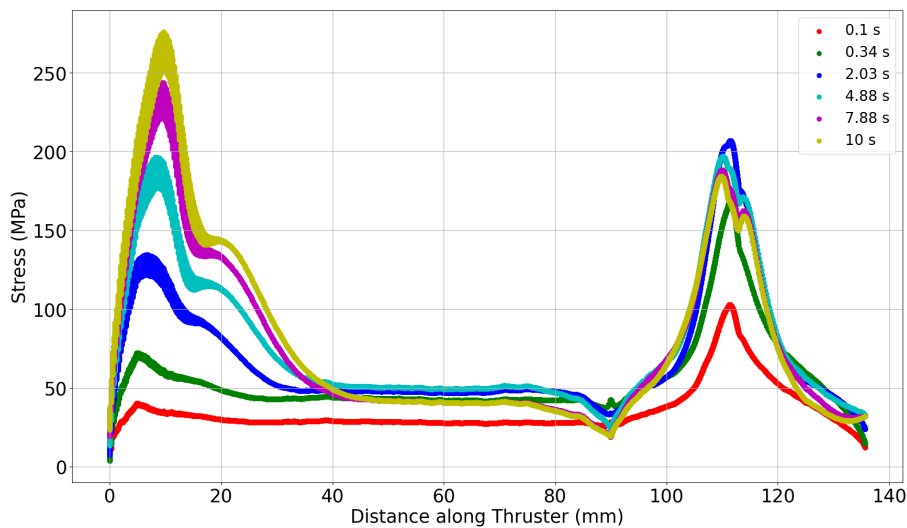er 30 mm is in the nozzle, of course as stated previously. It can be seen that from time steps of 0.1 to 2.03, the stress rises at a very fast rate, after which the stress decreases at a much lower rate from 2.04 to the final time step of 10 seconds. Such rapid rise in stress before reaching a peak and decreasing may be likely due to thermal effects where the temperature difference is very high between outside and inside the nozzle section.

## 4.5. Verification

The verification done for the simple and complex models are of 3 main ones. These are listed below, including the reason as to why they are deemed necessary.

- **Mesh Convergence:** Ensuring that the mesh used adequately captures the stresses and that stress values do not vary much as a result of finer meshes is necessary to ensure the results do not show less stress than expected.
- **Uniform and Consistent Hex20 Elements:** Since many configurations of nozzles are to be simulated, a consistent mesh across all of them is necessary for fairness.
- **Symmetry Checks:** Since 2 axes of symmetry are used in the simple model and complex model, the symmetry set up for the quarter and half models needs to be verified to ensure that the results do not vary from the full model counterpart.

### 4.5.1. Mesh Convergence

Many different meshes were made for the mesh convergence study to be done on the 4 mm uniform thickness thruster. The meshes devised for the mesh convergence analysis are 4 in total, as listed below.

- **Uniform 1.5 mm mesh:**  This was chosen as an upper limit for element size
- **Uniform 1 mm mesh:**  Chosen as a baseline
- **Uniform 0.75 mm mesh:**  This is based on what the laptop running the simulations can handle in terms of the smallest mesh size and obtaining results within a reasonable time frame
- **Custom Specific mesh:**  The custom mesh is the one that has been used up until this point for all previous analysis

Below is a compilation of images and graphs for all the above-mentioned meshes. Figure 4.49, Figure 4.50, and Figure 4.51 show how much better the hex20 quadratic mesh elements can follow the specific contour of the convergent and divergent section, including better capturing the small curvatures of 1 mm at the convergent section beginning and the divergent section curved lip. Since simulating a thinner thruster, would mean that the number of elements would decrease given the same global setting, the effect would be that fewer elements are present in the thinner nozzle sections, therefore allowing for the possibility of inadequate meshes being used in the analysis.

Therefore, this necessitates being able to control the mesh to an extent as to give all the different configurations an equal chance to be chosen as the optimum. Since the dimensions near the flange of the thruster will not change at 4 mm start the start of the chamber, V125 seen in Figure 4.14 and 3 m curve set for area 4 in Figure 4.15, the nozzle mesh will have to be controlled thoroughly. That is why the custom mesh goes to many lengths to increase the number of elements in the nozzle and specify every single edge division in anticipation of unforeseen stress concentration that may occur when a thinner nozzle is simulated.
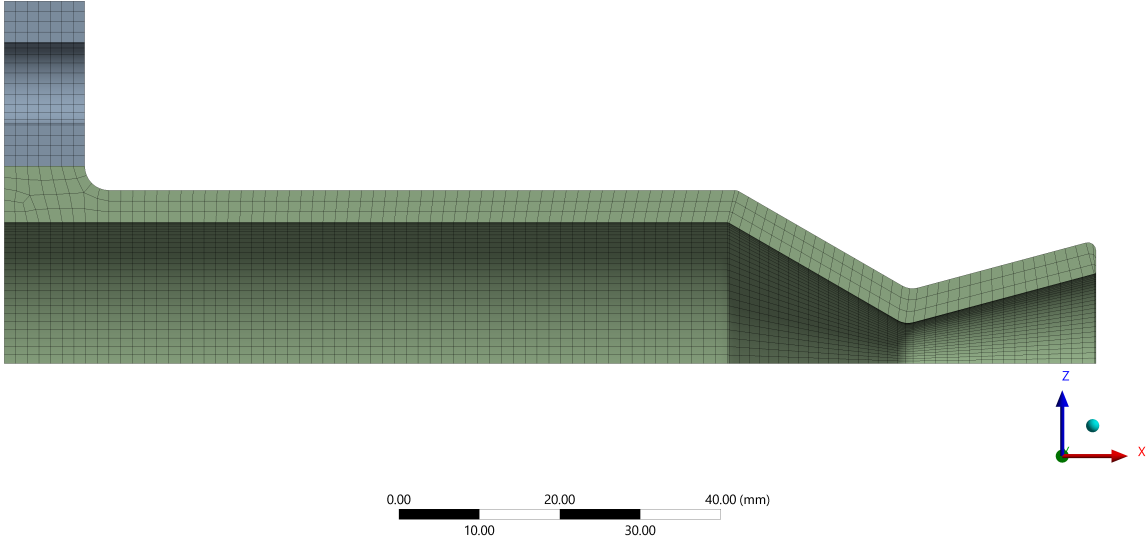
**Figure 4.49:** 1.5 mm Thruster Mesh

Figure 4.49 shows a very uniform mesh, with 3 mesh elements being created along the thickness of the thruster. Looking at the mesh metrics, Figure A.1, it can be seen that although the aspect ratios look favourable, the mesh skewness sees a majority of the elements to be below 0.2. This is most likely due to the convergent and divergent sections of the nozzle. Additionally, the mesh metrics in the complex model are only better because of the addition of meshing an entire backplate, thus the perceived increase in mesh quality may not translate to better results in the nozzle area.
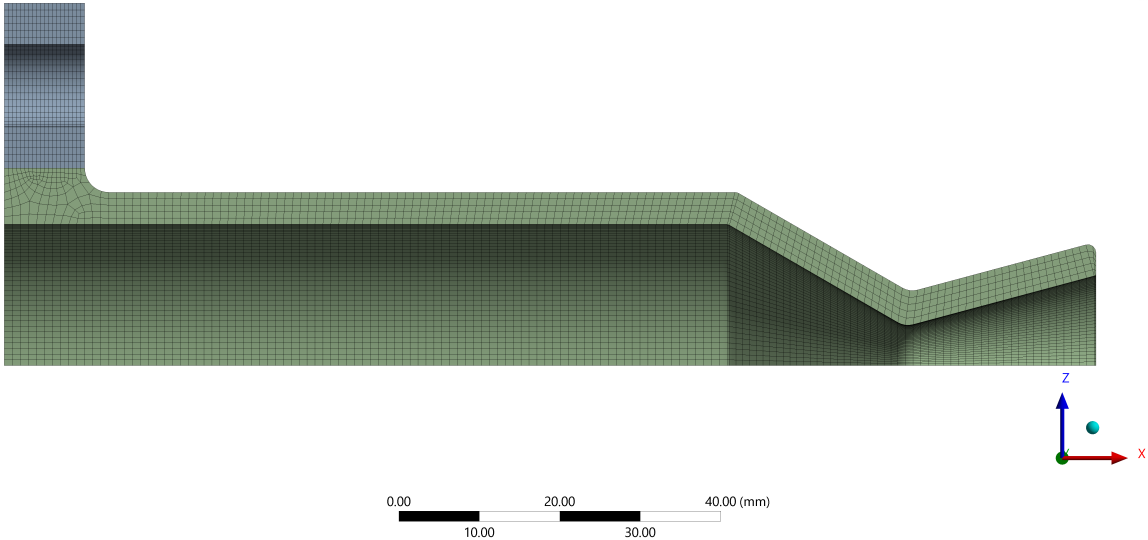


**Figure 4.50:** 1 mm Thruster Mesh

Figure 4.50 shows a better mesh created compared to the previous 1.5 mm mesh, with 5 mesh elements along the thickness of the thruster. The observations regarding Figure A.2 mostly remain the same, with the exception that the skewness now looks more favourable given that there are an overwhelming majority of elements in the chamber and flange section of the thruster compared to just the nozzle.
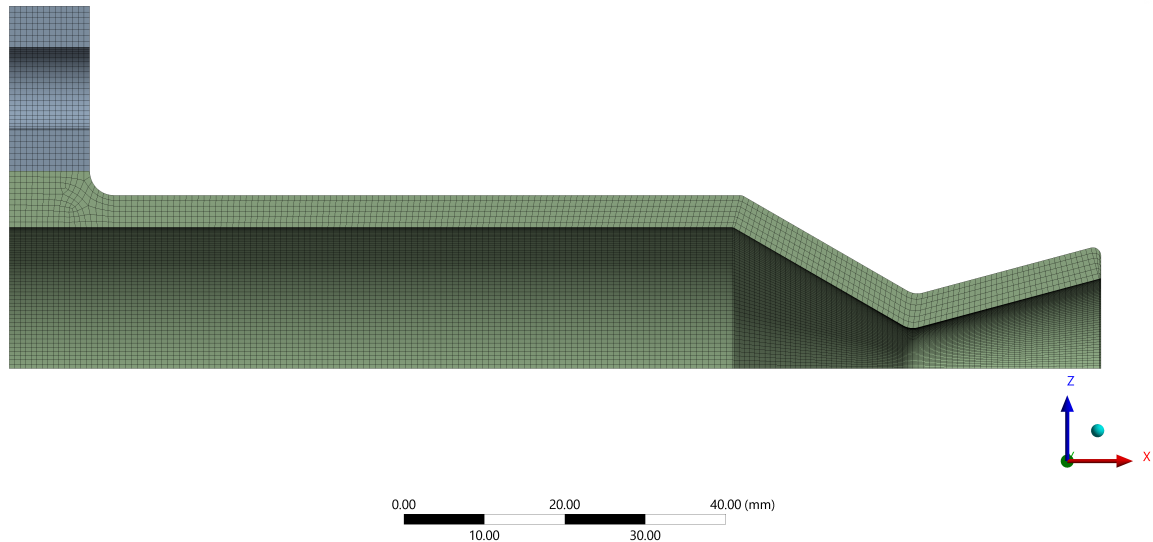
**Figure 4.51:** 0.75 mm Thruster Mesh

From the most coarse to refined uniform mesh, it can be seen that Figure A.1c, Figure A.2c, and Figure A.3c show improved mesh metrics with the peak for near perfect aspect ratio becoming more pronounced. The element skewness shows a similar trend in Figure A.1a, Figure A.2a, and Figure A.3a though it leaves much to be desired in terms of having a very pronounced peak for near zero skewness. Probing for the more skewed elements that are of skewness 0.10 to 0.20, they are mostly within the convergent and divergent section of the nozzle. Though a more refined model is desired, it was unable to be done given the resources available, most importantly the laptop memory. An additional observation is that when using the complex model, Figure A.1d, Figure A.2d, Figure A.3d, Figure A.1b, Figure A.2b, and Figure A.3b all show improved metrics, although this is only because of the additional backplate that is modelled, this does not reflect a better mesh quality in the regions near the nozzle. The backplate, due to it being a highly uniform model, only serves to amplify the peaks at a skewness of 0 and aspect ratio of 1 with very minimal increases in mesh quality and results in regions where it is very important such as the nozzle. Therefore, a custom mesh is opted to be used, using the 1 m uniform mesh as its base. The mesh seen in Figure 4.18 has the below aspect ratio and quality metrics for the simple and complex mesh.

Figure A.4 shows an interesting observation due to the custom mesh. The figures show that a secondary peak is seen due to the heavy refinements made in the convergent section of the nozzle to the throat. The divergent section also has modifications, though not to as severe of a degree as the convergent section or throat area. All the above meshes were used to run simulations again, with exact time steps chosen, and the data can be superimposed to see how the meshes perform concerning one another. The reason the exact time steps were used, although it may be more manually involved is to keep the playing field level for the uniform 1.5, 1 and 0.75 mm meshes compared to the custom mesh, where the exact time step was used when actual data analysis is involved. Figures are given below which will be used to compare meshes. When looking more closely at the local areas where refinement was made, the values probed from that section can be used to see why a custom mesh was preferred, despite the mesh metrics favouring uniform models.

**Figure 4.52:** Meshes Compared for Temperature and Stress Data in the Simple Model, on the inside and outside the thruster at the time step of 10 seconds

Comparing meshes using contours shows how meshes behave in very localised areas. The "Stress Inside Thruster" subfigure in Figure 4.52 shows signs of the stress singularity at the fixed support where there is a singular node that causes stresses to rise upwards of 1000 MPa. Additionally, all meshes show a thin stress band between 0 to 10 mm most likely of the oscillatory stress behaviour due to the lack of material in the dedicated bolt holes and the presence of beam elements. This highlights the flange section when it comes to stresses in that region.



**Figure 4.53:** Meshes Compared for Temperature and Stress Data in the Complex Model, on the indie ad outside the thruster at the time step of 10 seconds

Figure 4.52 and Figure 4.53 show that far away from the flange, the results show very similar progression of stress and temperature as we progress further along the nozzle. Near the flange, in the simple model, due to the fixed support limiting the deformation of the fixed face of the HEX20 element, the stresses get larger as the meh becomes more refined. This is simply an artefact of FEA that is to be dealt with and taken into account. Such an artefact is called a stress singularity, where mesh refinement also increases the stresses further and further until infinity. This is less pronounced in the outside thruster stress in the complex model between meshes because the flange is not directly fixed, but it is fixed through the back plate and connecting beams. Since the figures are taken at a time step of 10 seconds, where the maximal stresses are seen near the flange, more specifically at the 3 mm curved flange edge section, as seen in the complex model and area 4 in Figure 4.15. The temperature graphs for all 8 meshes show a very good correlation, this only further solidifies that the main area of focus for convergence should be looking more into the stresses.

**Table 4.3:** Percentage Differences of maximum values at a time step of 10 seconds compared to the custom mesh complex model results

|  | 1.5 Simple | 1 Simple | 0.75 Simple | Custom Simple | 1.5 Complex | 1 Complex | 0.75 Complex |
|---|---|---|---|---|---|---|---|
| T in | -0.33 | -0.02 | 0.11 | 0 | -0.033 | -0.02 | 0.11 |
| T out | -0.33 | 0 | 0.09 | 0 | -0.35 | 0 | 0.09 |
| S in | 190.7 | 228.98 | 270.3 | 309.78 | -2.8 | 1.18 | 0.083 |
| S out | 80.49 | 86.11 | 94.94 | 94.08 | -2.53 | 0.12 | 1.1 |

Table 4.3 shows that all temperature graphs show a maximum difference of less than 1% compared to the custom mesh complex model's maximum recorded value at 10 seconds. The stresses on the other hand show variability. Although there are extreme differences between the simple and complex models, the main focus is on the values of the complex model. The highest percentage difference is 2.8% due to the most course 1.5 mm mesh used in the complex model. Since this is less than 5% this is deemed as acceptable and the mesh has converged in this case for meshes of 1 mm and finer.
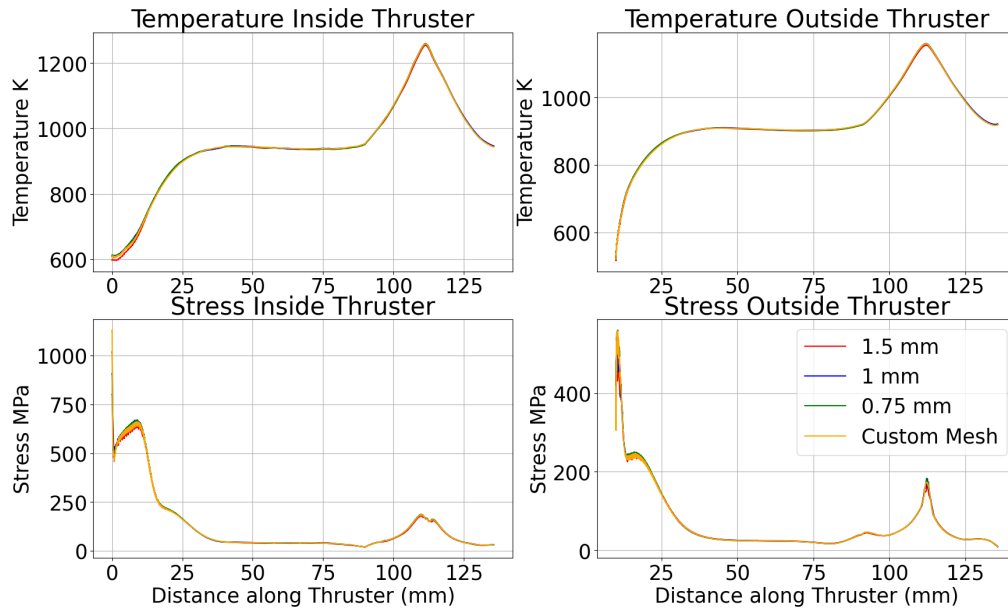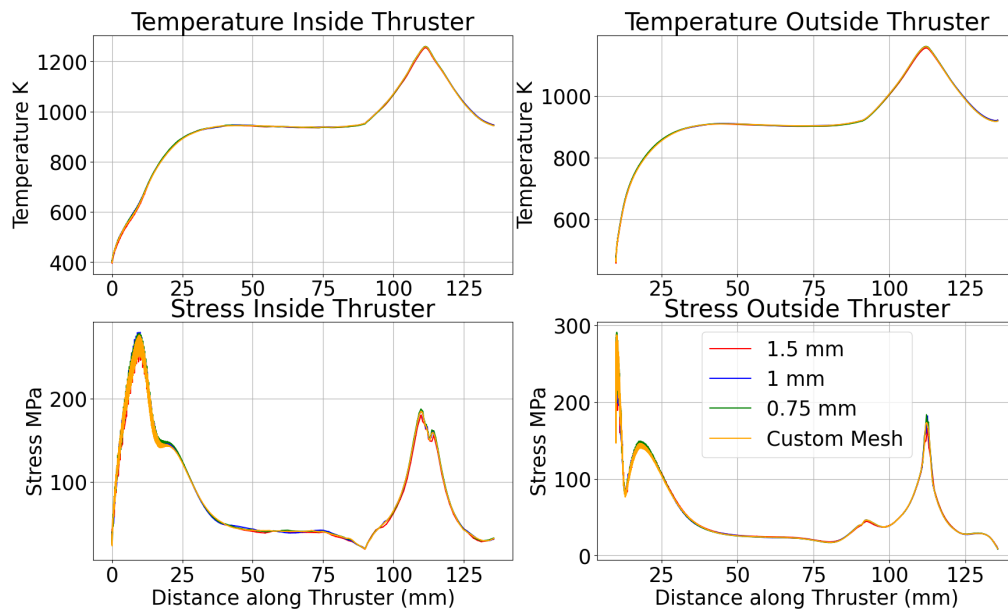


**Figure 4.54:** Meshes Compared for Temperature and Stress Data in the Simple Model, on the inside and outside the thruster at the time step of maximum nozzle stress.

The simple model convergence at peak nozzle stress on the outside of the thruster starts to show gaps and issues in the mesh when looking at Figure 4.54. While the rest of the thruster as a whole shows good

overlap, the absolute highest stress at the nozzle throat section shows great uncertainty. This is due to the meshes no longer being sufficient when trying to capture stress concentration due to geometrical effects at extreme conditions.
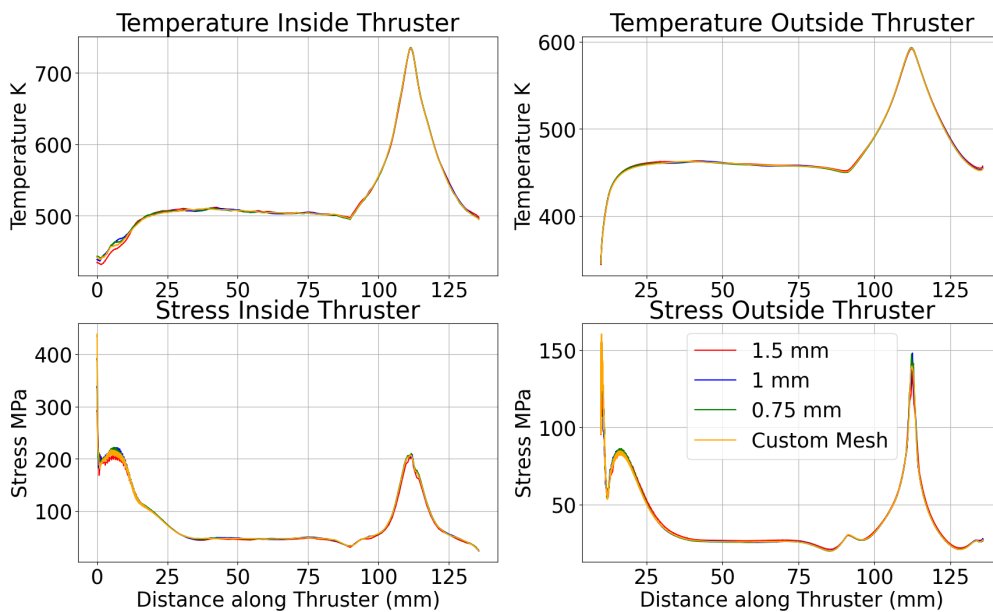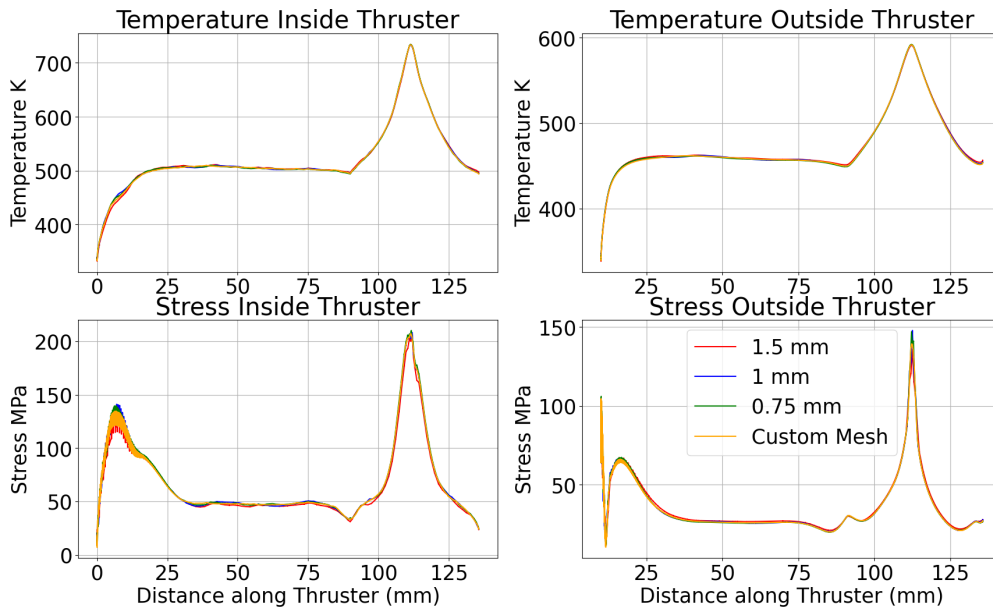


**Figure 4.55:** Meshes Compared for Temperature and Stress Data in the Complex Model, on the indie ad outside the thruster at the time step of maximum nozzle stress.

Figure 4.54 and Figure 4.55 have an interesting observation near the peak of the nozzle stresses. Since the stresses are higher, the difference between each mesh is also much higher.

**Table 4.4:** Percentage Differences of maximum values at time step of peak stress in the nozzle compared to the custom mesh complex model results

|         | 1.5 Simple | 1 Simple | 0.75 Simple | Custom Simple | 1.5 Complex | 1 Complex | 0.75 Complex |
|---------|------------|----------|-------------|---------------|-------------|-----------|--------------|
| T in    | 0.24       | 0.12     | 0.28        | 0.17          | 0.11        | -0.04     | 0.1          |
| T out   | 0.09       | 0.17     | 0.33        | 0.23          | -0.11       | -0.04     | 0.1          |
| S in    | 41.3       | 63.73    | 90.07       | 112.04        | -0.27       | 0.71      | 1.64         |
| S out   | 9.84       | 14       | 12.78       | 15.22         | -2.57       | 6.1       | 5.53         |

Although the meshes all show a very good correlation with each other, Table 4.4 shows a different story. Yet again, all the maximum temperature values are within 1% of each other for all meshes. When it comes to the stresses, the percentage differences are much lower overall when looking at the simple model meshes. The aforementioned is most likely because the temperatures are not able to build up very quickly within 3 seconds of the thruster operating near the flange, thus resulting in less stress singularity peak magnitudes. When looking at the percentage difference between the custom mesh and complex model maximum values and the other meshes, the outside mesh has a difference of 6.1 and 5.53 % from the 1 mm uniform and 0.75 mm uniform mesh respectively. The location of this maximal stress is the stress ring right around the throat area on the outside of the thruster. This difference is greater than 5% and suggests but does not show signs of constant increase due to mesh refinement as the 0.75 mm finer mesh, shows a smaller percentage difference compared to the 1 mm mesh. To look more into this specific area, another custom mesh is used, which is based on the 0.75 mm uniform mesh, but with local refinements made into just the throat area, setting the throat edges to divisions in the size of 0.2 mm. This additional mesh is coloured cyan and shown below at the peak nozzle stress time step.
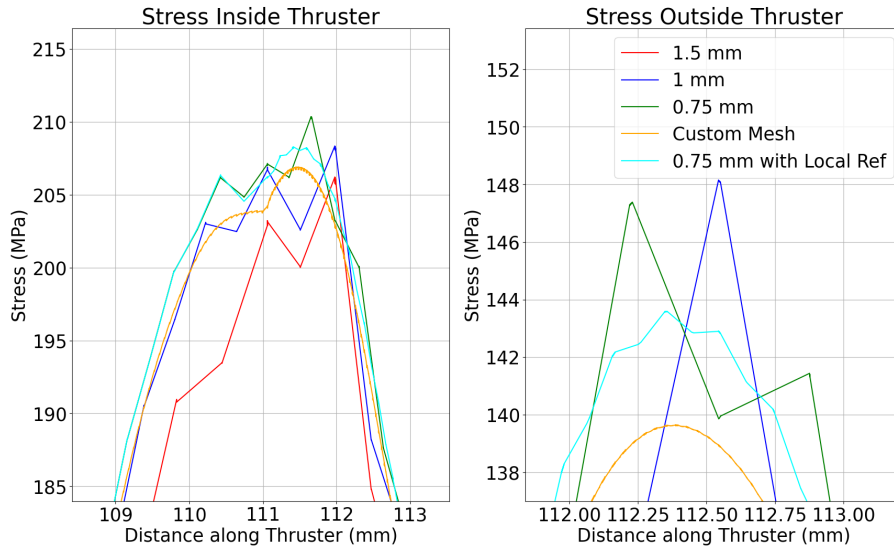
**Figure 4.56:** Zoom in on the Nozzle peak stresses time for the Simple Model with the addition of another Mesh for comparison purposes

Figure 4.56 shows that all uniform meshes from 1.5 mm to 0.75 mm have very erratic and non-smooth stress behaviour near the throat region. The custom mesh shows a very smooth curve due to the high number of elements that were used for refinement. The cyan, 0.75 mm with local throat mesh refinement, shows a smoother curve compared to just the uniform 0.75 mm mesh.

**Table 4.5:** Percentage Differences of maximum values at a time step of 2.03 seconds for the 0.75 mesh with local refinements made at the nozzle outer edge compared to the custom mesh for the simple model

|       | 0.75 mm mesh with Local Throat Refinement |
| ----- | ----------------------------------------- |
| S out | 3.11                                      |
| S in  | 0.7                                       |

Table 4.5 shows that the percentage difference in the outside stress is now 3.11 % from 5.53%, less than 5% difference. This additional mesh serves as to reason why the custom mesh was created in the first place, using the insight gained from the 3 uniform meshes and manually checking the effects of individual local mesh refinements. The custom mesh is used for the following reasons.

- The custom mesh employs heavy mesh refinements at the beginning convergent section of the nozzle to the end of the divergent section of the nozzle to ensure the results and plots generated are smooth and do not show erratic behaviour
- The custom mesh allows for all thruster thickness configurations to have a similar number of elements and mesh quality due to the direct control over most of the edges in the model
- The custom mesh focuses on mesh refinements near the throat due to the anticipation that stress concentrations on the outside of the throat may be larger than the stresses observed on the inside of the throat as thinner thruster thicknesses are simulated in those regions. Other geometrical complexities when varying the thruster thickness requiring finer meshing would also be captured this way.

Common mesh metrics like element aspect ratio, skewness, and others are important, but they may not necessarily guarantee good solution accuracy. What was seen here is that a mesh with good metrics might still perform poorly if it doesn't capture the physics of the problem accurately in the regions of interest. A critical feature of the geometry is the throat and convergent section, where

stresses are expected to be the highest. The better "looking" meshes did not have sufficient elements to capture enough detail of how the stress progresses in specific areas. Thus, a custom mesh was made through extensive trial and error to capture enough information and also be usable for every thruster configuration, no matter how thin the thickness becomes. This custom mesh is made due to the limitations of the hardware and memory, given more powerful hardware, a very refined uniform mesh, less than 0.2 mm, may very well replace such custom mesh. The aggressiveness of the custom mesh aims to first be as robust as possible when applied to all the different thruster configurations before being as computationally cheap as possible. This is a direct explanation as to why the curve is aggressively smooth with high-stress alleviation. The custom mesh aims to work in most server cases of a very thin thruster, thus an even higher chance of a stress concentration due to geometry and more mesh refinement potentially needed.

### 4.5.2. Uniform Elements HEX20
Initially, it was seen that a full thruster model with no cut made between the chamber and the flange, which is then rejoined later in the design model, was unable to create a uniform HEX20 mesh. The mesh created was instead triangular quadratic elements and at times a mix of wedge, quadrilateral and triangular elements. Such mesh inconsistency may result in stresses that are considered not yet converged given the element qualities for the specific thruster design. Therefore, two main things were done to ensure that the meshes generated all possess a similar number of elements, element types, and cuts where necessary. The changes done to the models to ensure that are listed below.

- A cut made between the flange and the chamber body, blue and green sections of the model respectively, as seen in Figure 4.18.
- Mesh generation order specified to facilitate HEX20 meshes being made
- Most edges explicitly split into predetermined divisions

The aforementioned changes always resulted in the mesh generated having HEX20 quadratic elements all around. It must be stated that the method used to verify this was the case was manual. Since there were an initial 9 configurations to be used preliminarily and the number of configurations would only increase in the case that it is deemed necessary, all 9 were manually checked to see if their mesh would generate a uniform HEX20 mesh given the same meshing order and conditions. Do note that the order in which the mesh is generated is extremely important, the flange section was generated first, followed by the rest of the thruster, doing the opposite would yield ANSYS errors in meshing. The same meshing order and conditions were employed in the complex model. The addition of the back plate in the complex model had no impact on meshing failure or success.

### 4.5.3. Symmetry checks
Symmetry checks were done on the simple model with the full, half and quarter models. It was seen that the difference was less than 1% compared to the full model for the models with symmetry implemented, this was true for both deflection and stresses. The main essence of this verification came into play for the complex model. Looking at Figure 4.18, it is clear that there is a bolthole that is cut in half and not connected, and since the beam elements are complete and cannot be cut in half, as seen in Figure 4.33, some complications will occur. When running simulations for the complex model at quarter model size, the full beam was present at the hole that was cut in half, which caused higher stresses to be seen. More specifically, the corners of the half-cut hole saw much higher stresses, most likely due to the interaction between the full bolt model and the half bolthole. When simulating the full model and half model, where no partial holes are present, the same observation was not found. Thus the decision was made to only use quarter-model symmetry with simple models, and half-model symmetry with complex models, where there are no partial holes.

## 4.6. Validation
When it comes to validation procedures available, the lack of experimental data means that it will not be possible to make direct comparisons with real-world tests. Therefore, validation will be limited to analytical means to determine whether the results obtained are by observations seen in other thruster simulations and stress measurements. An additional validation step to analytical comparisons is a

sensitivity analysis that will be done on the 4 mm thick nozzle. The sensitivity analysis will aim to show just how much variance can be expected in the case that the stiffness of the material is lower than expected due to manufacturing difficulties or if convection from the inside fluid is higher than expected.

## 4.6.1. Stresses and their Locations

To adequately assess whether the stresses' concentration location seen during the simulations results, Figure 4.28, figures from other papers which also show stress concentrations can be used for comparison. Below is a compilation of 3 papers, taken from sources previously seen in the Table 2.2. These figures will be used to conclude the validity of the results obtained.
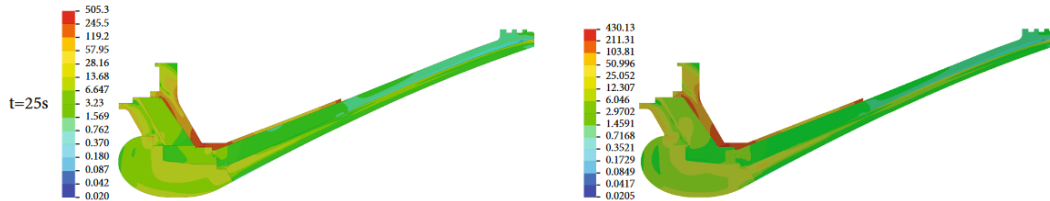


**Figure 4.57:** Fluid flow is from left to right. It can be seen that there is a stress concentration at the sharp edges outside the nozzle. The right figure is the traditional model and the left figure is the non-linear model. [67]
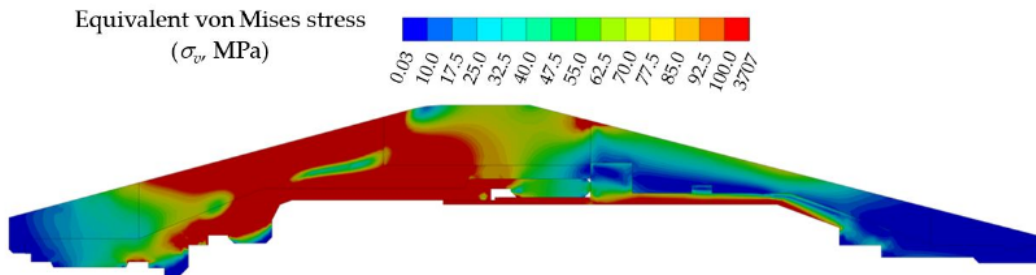


**Figure 4.58:** Fluid flow is from left to right in the above nozzle. The stress can be seen to be highest near the throat [71]
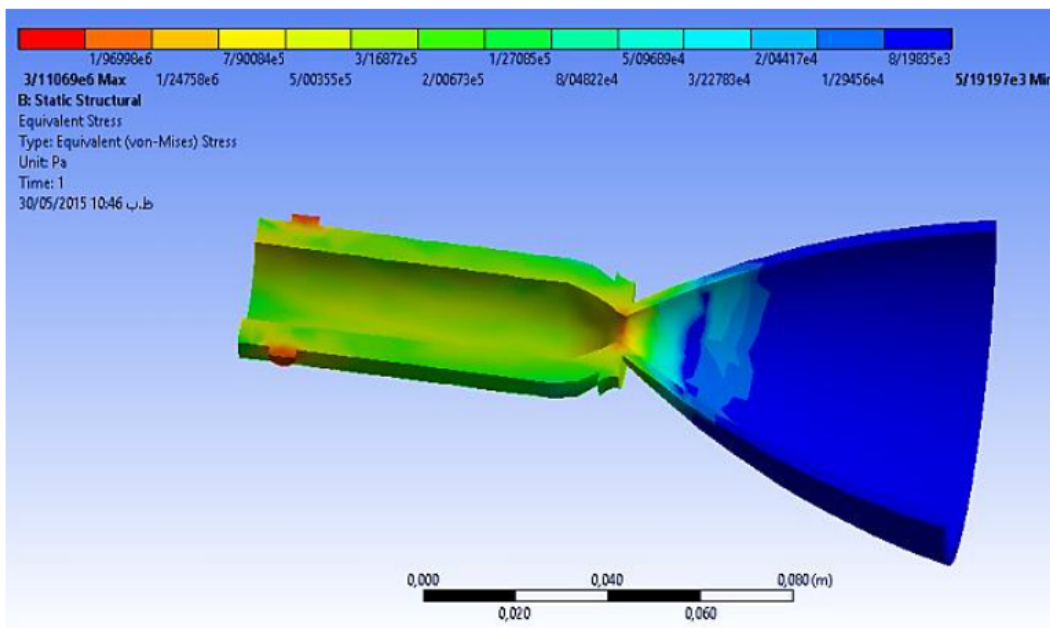


**Figure 4.59:** Nozzle Stress of a thruster operating in a vacuum. [58]

From Figure 4.59, a full 3D FEA of a nozzle is shown, with stress concentrations coloured bright orange to red at the nozzle. The stress location aligns with the stress location found in the simulations. Figure 4.58 shows a more detailed 2D side view of the stresses in the nozzle. The figure shows the make pattern of the highest stresses being at the convergent section of the nozzle, right before the throat. Additionally, an interesting observation is that there are also high stresses seen on the outside of the nozzle section. This thin red line can be an indication that the stress ring that was observed in the simulations done in this thesis is also valid, as they do exist in other similar nozzle simulations. Finally, Figure 4.57 also shows a sharp rise in stress right at the outside section of the nozzle throat, where there is a sharp change in geometry. The aforementioned also leads to the conclusion that fining a stress ring on the outer surface at the throat can be due to geometrical factors that would need to be taken into account since the change in geometry Figure 4.57 is a sharp angle that has not been rounded. Additionally, while not clear immediately, the throat area for the nozzle has a light green to yellow colour, showing signs of higher stress at the inside of the throat and the convergent section. A final source from a thesis also stated that the maximal location of axial tension is at the throat or in the converging section immediately before the throat.[69]

### 4.6.2. Temperature and Stresses Over Time

A thesis on Thermo-Structural Analysis of a Rocket Engine Thrust Chamber was found to produce graphs similar to those created for the complex model.[69] The thesis does its analysis on a 2D thruster chamber with the nozzle throat estimated to be located around 67 mm. The figures from the thesis are provided below and can be used to compare their behaviour and results seen in the thesis with the results provided previously for the 4 uniform thickness complex thruster model.
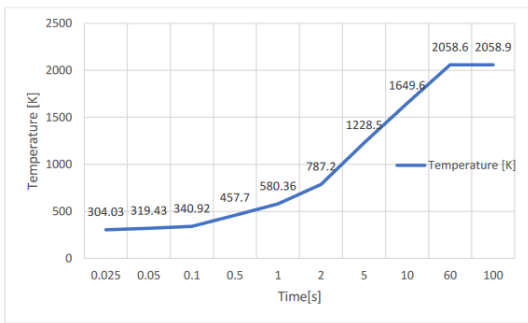
(a) Temperature Profile
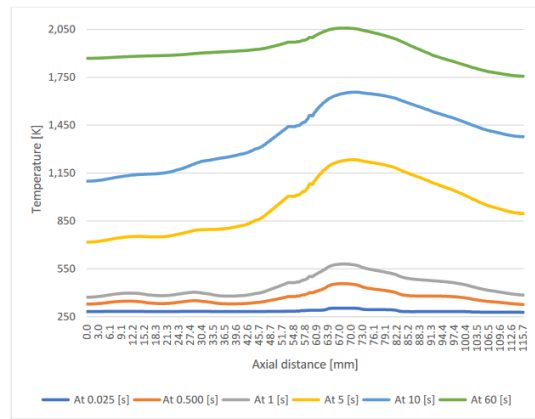
(b) Temperature as a function of time.
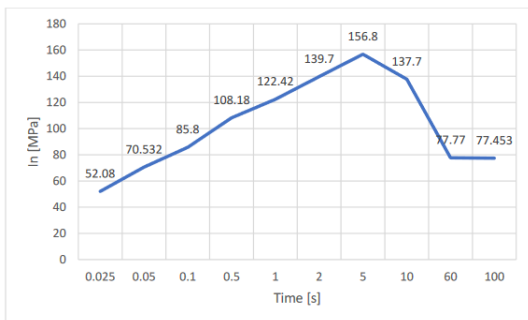
(c) Von-Mises Stress profile.
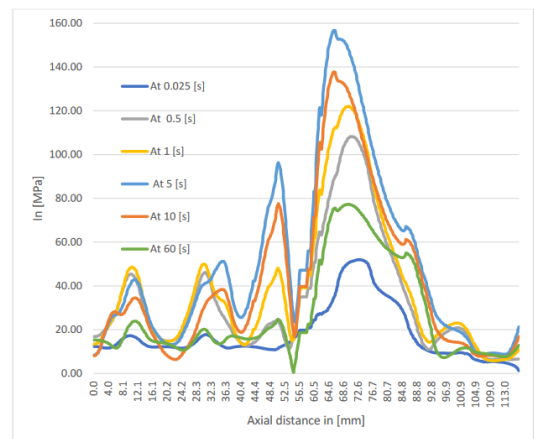
(d) Von-Mises Stress as a function of time.

**Figure 4.60:** Thruster temperature and stresses and their profiles over time from a thesis source [69]

Figure 4.60a and Figure 4.60c show similar behaviour to Figure 4.36 and Figure 4.43, respectively. For temperature, there is a continuous increase and for stress, there is a peak that occurs before the final time of 60 seconds at 5 seconds, similarly in this report at a time of 2.03 seconds, there is a peak that occurs before the final operation time of 10 seconds.[69] Additionally, Figure 4.60b and Figure 4.60d also show similar behaviour as found before in Figure 4.47 and Figure 4.48. Do take note that the throat section is near 67 mm in the source obtained from the paper. To take validation a step further, multiple sources which provided similar metrics as those generated previously for the complex model were compiled and used. The graphs from these sources will be overlaid over each other and the graphs from this report. Furthermore, they will be normalised to allow legibility and facilitate further discussions. The main way that the validation will be done for the model is by examining the nature of the curve obtained from other sources and comparing the with that obtained from the complex model results. the reason the nature of the curve is chosen is that there are many different types of thrusters working under varying operating conditions, in different environments, using different propellants and fuel combinations, operating for different durations and purposes, made of many different sizes and materials. Accounting for all the aforementioned factors, looking for a paper that has very close smarties to the complex model used, the material used, and is made with the same purpose in mind, orbit control and manoeuvre, is not likely to be found. This becomes even more difficult when it becomes clear that not all papers provide similar metrics to measure thruster stress and would rather state the location of maximum stresses. Therefore, the papers that provided graphs of temperature and stress contours that were legible and able to be used were targeted. The sources used and found for validation analysis are provided below, with references and their name tags that were also used in the legends in the figures.

- **Source 1:** Coupled Thermo-Structural Analysis Model of Solid Rocket Motor Nozzle considering the Variation of Friction Coefficient under Operating Conditions. [67]
- **Source 2:** Thermo-Structural Analysis of a Rocket Engine Thrust Chamber [69]
- **Source 3:** Effects of thermal and pressure loads on structural deformation of liquid oxygen/methane engine combustion chamber [25]
- **Source 4:** Design Optimization of A Conventional Rocket Nozzle Using Coupled Thermo-Structural Analysis [52]
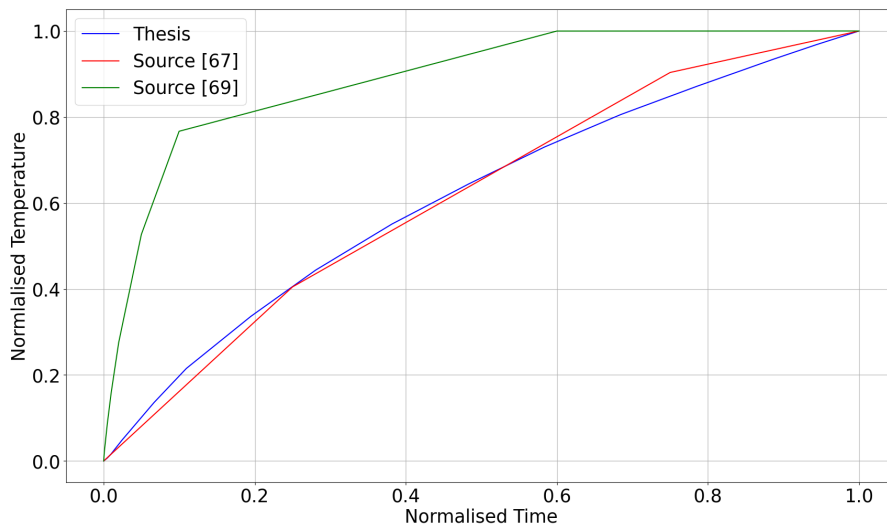


**Figure 4.61:** Temperature over time for various sources compared with this paper's results

As can be seen from Figure 4.61, the data points obtained from sources [67] and [69] both showed that as the thruster is during its burn phase or under nominal operating conditions, the temperature continues to rise until the end of the operation time when it is at its maximum. The main point to

take away from this figure specifically is that the data obtained from the complex model aligns with the other sources; temperature rises consistently until it reaches the peak at the end of its operation. Next, the stress over time can be looked into.
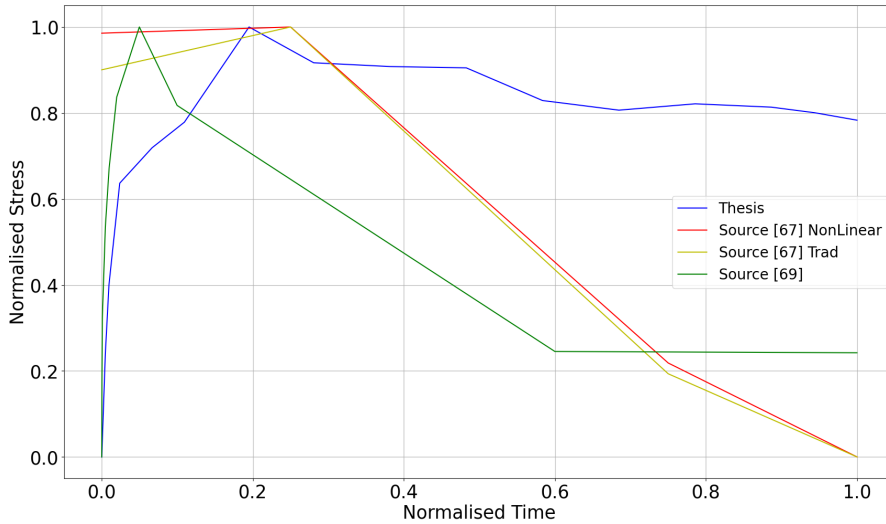


**Figure 4.62:** Stress over time for various sources compared with this paper's results

Figure 4.62 confirms the earlier observation from the complex model that maximum stress in the nozzle occurs shortly after startup, well before the end of the operating time. Both the Nonlinear and traditional models show similar curve behaviours. Source [69] highlights the rapid stress rise before it peaks and then decreases as the thruster continues to operate. This validates the curve patterns for stress and temperature over time, showing that maximum temperature is reached at the end of operation, while maximum stress occurs early on. The different rates of stress and temperature changes are likely due to the source thruster operating for longer periods, reaching a steady state with lower stresses compared to the findings in this thesis. Next, the temperature contours will be discussed.
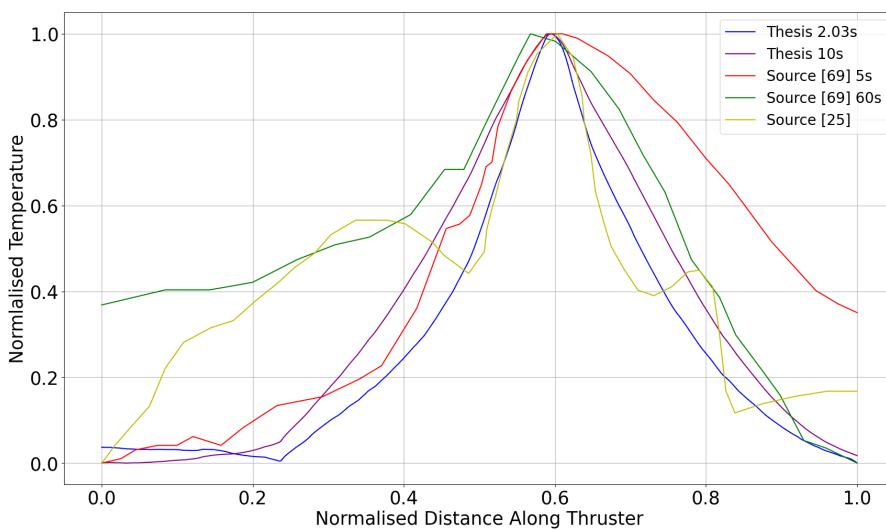


**Figure 4.63:** Temperature Contours for various sources compared with this paper's results

Figure 4.63 shows each line accompanied by a dashed line indicating the location of peak temperature. All the graphs in the above figure have their peak stress occur or in very close proximity to the throat region, this aligns very well with the complex model results, the blue and purple line. The complex model shows that temperature rises in the chamber, peaks at the throat, and then decreases. Such curve behaviour is the same as seen in source [69], where temperature rises, albeit slowly, until the peak temperature is reached at the throat region. After the peak temperature is reached in the throat, the temperature drops further away from the throat. Source [25], the yellow line, also shows similar behaviour. Another observation from this figure is that the location of peak temperature slightly changes over time. This can be seen by comparing the green and red graphs of source [69]. Such behaviour of slightly changing maximum temperature location is also present in the complex thruster model, though it is less pronounced as the maximum temperature location at 2.03 seconds and 1 second are very close to each other. Such similarities in behaviour are a good indication that the results obtained from the complex model are in line with what is expected to occur and what other papers can simulate. Next, the stress contours are taken a closer look at.
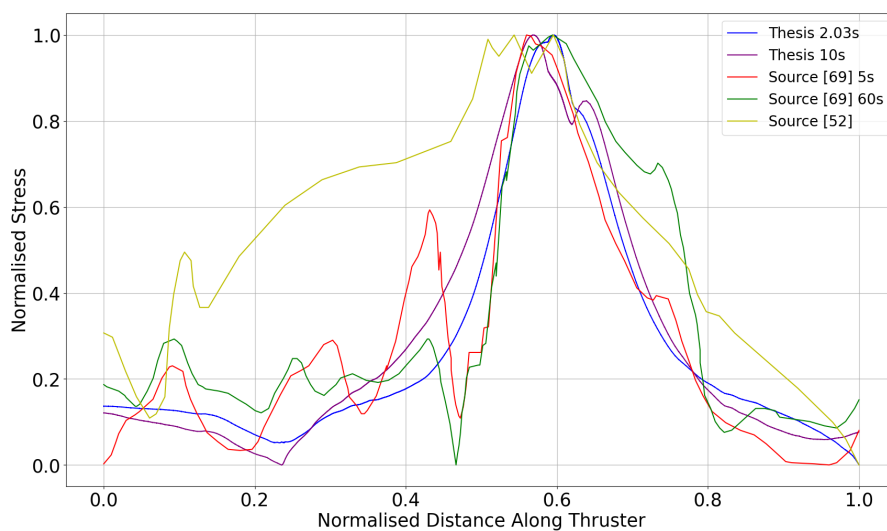


**Figure 4.64:** Stress Contours for various sources compared with this paper's results

Similarly to the temperature contours figure, Figure 4.64 also has the dashed lines to show where the peak stress occurs in the thruster. All the dashed lines in the figure indicating peak stress location coincide with the location of the throat region, or the convergent section very close to the throat region in the nozzle. Source [69], the green and red lines, show that as one progresses down to the throat region, the stresses are more or less rising erratically due to the geometry of the nozzle in this area. Once the peak stress is reached in the throat, the stresses then start to decrease. The same can be said for source [52], the yellow line, where travelling down the nozzle shows a rise in stress until it peaks in the throat and then starts to decrease as one moves further along towards the exit of the nozzle. An interesting observation is that the rates of increase and decrease in stress for all the figures are relatively close to each other near their respective throat, and therefore peak stress, regions. A final observation is that the location of peak stress, while still near the throat, slightly changes over time. This can be seen in source [69] for time steps 5 and 60 seconds and additionally in the complex model results, where the peak nozzle stress at the throat is slightly shifted as time progresses. Do take note that the complex model stress contour for 10 seconds has been cut off to exclude the flange stresses for clarity. This will not affect the previously discussed points, as the flange was not included in the papers which did FEA above.

To summarise, the following can be said about this validation section:

- For the Temperature over Time plot, Sources [67] and [69] both show a good correlation with the complex model results. Temperature increases until it reaches its peak at the end of operation.

- For the Stress over Time plot, Sources [67] and [69] both show that there is a peak stress that occurs well before the final operating time and close to the initial burn time of the thruster. This behaviour is also found in the complex model results.
- For the Temperature Contours, sources [69] and [25] prove that the complex model results of peak temperature at the nozzle throat section are valid as it is an observation seen in their plots as well. Additionally, the slight shift in the location of peak temperature seen in source [69] was also seen in the complex model results.
- For the Stress Contours, source [69] and [52] aligned well with the complex model results. Yet again, the peak stresses for all lines occur close to the throat region. It was also seen that the slight shift in the position of maximum stress at the throat region over time was also present in source [69] and the complex model stress contours.
- Given the different purposes the thrusters were designed for, including operation time this may lead to discrepancies when comparing them to the thesis model.

### 4.6.3. Sensitivity Analysis

The sensitivity analysis will evaluate the effects of a further 20% decrease in Young's Modulus and a 20% increase in the convection coefficient. These changes will be individually assessed against previous results to determine their impact. The Young's Modulus is being reduced by an additional 20% (for a total reduction of 40%) to account for potential discrepancies between the expected and actual properties of the produced UHTCMC material. In the material section, the UHTCMC Young's Modulus was calculated using a formula from a paper that also manufactured the UHTCMC[80], making it a reliable reference. The paper reported a Young's Modulus of 322 GPa experimentally and 349 GPa using their formula, an 8.39% difference, which is acceptable. However, UHTCMCs can vary significantly in manufacturing, potentially resulting in lower stiffness than expected. Another study found ZrB2 with 10 vol% SiC and 40 vol% milled carbon fibre had a Young's Modulus of 181 GPa parallel to the fibres and 81 GPa perpendicular[50], highlighting this variability. To account for this, an additional 20% reduction in Young's Modulus is applied, bringing the total reduction to 40%, for the sensitivity analysis.

The analysis also considers a 20% increase in the CFD convection coefficient to assess its impact on the thruster, given the significant difference between the calculated Bartz and CFD results. The figures show the results, with E20 (green) representing the 20% decrease in stiffness, C20 (blue) representing the 20% increase in convection, and the standard FEA (red).
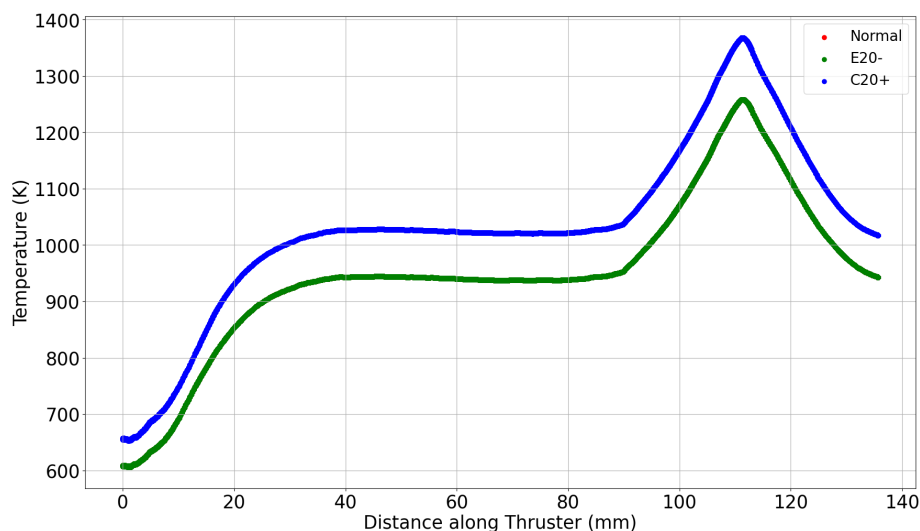


**Figure 4.65:** Inside Temperature Sensitivity Analysis Plots

Figure 4.65 has the E20- and Normal graphs coincide. This is because when it comes to thermal

simulations, the stiffness of the material is not taken into consideration to determine how the material absorbs and dissipates energy. While the Normal red graph is not seen, it is simply overlapped by the green E20- graph.
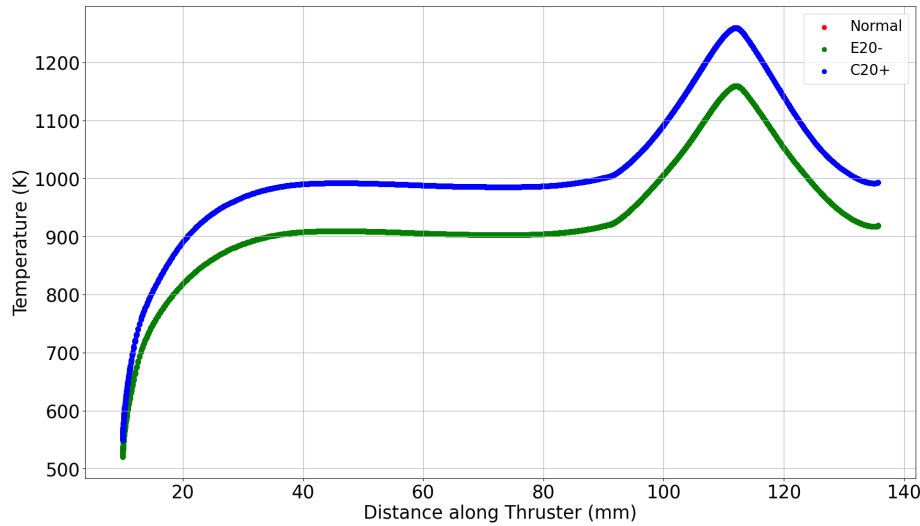


**Figure 4.66:** Outside Temperature Sensitivity Analysis Plots

Like in Figure 4.65, Figure 4.66 also has the E20- and the Normal graphs coincide. Convection in general, curve C20+, causes a shift in the temperature contours upwards compared to the normal, red, contour. The lines converge to each other in Figure 4.66 near the flange, the closer we get to 10 mm along the thruster in the axial direction.
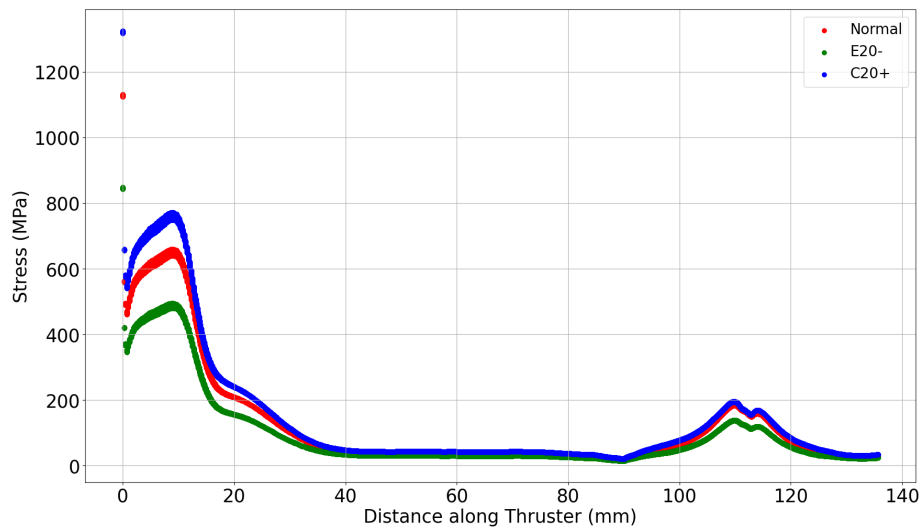


**Figure 4.67:** Inside Stress Sensitivity Analysis Plots

Since the simple model is used to investigate the sensitivity of the model to the other cases, distinct points are seen on the y-axis. Because the very first element is restricted directly where values are probed, the effects of the different cases are most pronounced on these elements. The fact that these

points are ordered from highest expected stress to lowest ( C20+ to Normal to E20-) serves as a
verification that the model behaves as expected under these loadings and material properties.



**Figure 4.68:** Outside Stress Sensitivity Analysis Plots

In Figure 4.67 and Figure 4.68 show that stresses increase in the following order E20-, green, to Normal,
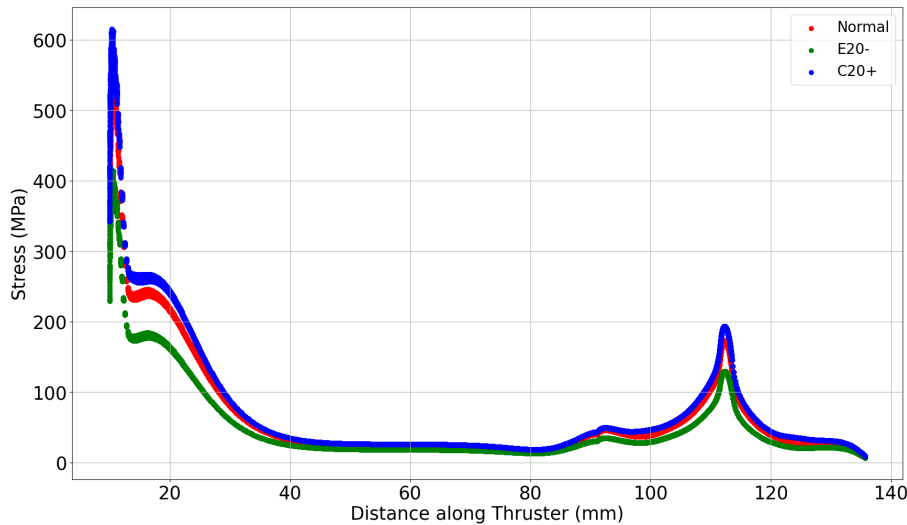red, and the highest, C20+, blue. Do take note that the drop in stresses from E20- is larger than the
rise in stresses in C20+ in absolute magnitude.

**Table 4.6:** Percentage difference of adjusted material properties and convection inputs compared to the standard FEA in
red

|                        | Green - E20 | Blue - C20 |
| ---------------------- | ----------- | ---------- |
| Inside Temperature     | 0 %         | 8.69 %     |
| Outside Temperature    | 0 %         | 8.64 %     |
| Inside Stress          | -24.99 %    | 17.14 %    |
| Outside Stress         | -25.81 %    | 10.29 %    |
| Nozzle Inside Stress   | -25.18 %    | 5.86 %     |
| Nozzle Outside Stress  | -25.04 %    | 11.82 %    |

Table 4.6 shows that there is no difference in peak temperature measurements between the standard
and the E20 FEA. The contours also overlapped for the E20 and standard FEA as seen in Figure 4.65
and Figure 4.66. Convection affects these temperatures, showing an increase of nearly 9% for the peak
temperatures. The temperature graphs also show the contours of temperatures have been shifted up.
This does make sense, as an increase in convection means that the temperatures rise faster. The "shifted
up" observation does not apply near the flange on the outside wall, seen in Figure 4.66 near 10 to 20
mm. The stress peaks do show a rather large difference. Table 4.6 shows that a decrease in stiffness
by 20% leads to a decrease in stresses by nearly 25%. This is in line with what is expected, as a lower
stiffness comes at the cost of higher deformation and lower stresses. The C20 graphs for convection show
the highest peak stress increase of 17.14% on the inside of the thruster. But since the simple model
is used for the sensitivity analysis instead of the complex model, probing for just the nozzle section of
the thruster shows an increase of only 11.82% in stress on the outside of the nozzle, and 5.86% on the
inside. The outside of the nozzle increases in stress by 20.4 MPa and the inside by 10.8 MPa. This
shows signs that the outside of the nozzle, where the stress ring is, may become more crucial if it is
seen that the convection is higher than anticipated. It must be noted that the reason why the complex
model was not used to run simulations for sensitivity is because of how computationally expensive it

is. Since the most important aspect is to analyse the effects in the nozzle, the simple model is enough, as the complex model deals mainly with flange complexities. Only one complex model was run for the increase in convection case since it showed an increase in stresses. it was found that the stress at the flange is 340.3 MPa, an increase of 18.3 % compared to the complex model of 286.7 MPa. The new stress contour for the complex model and 20% higher convection can be seen below.
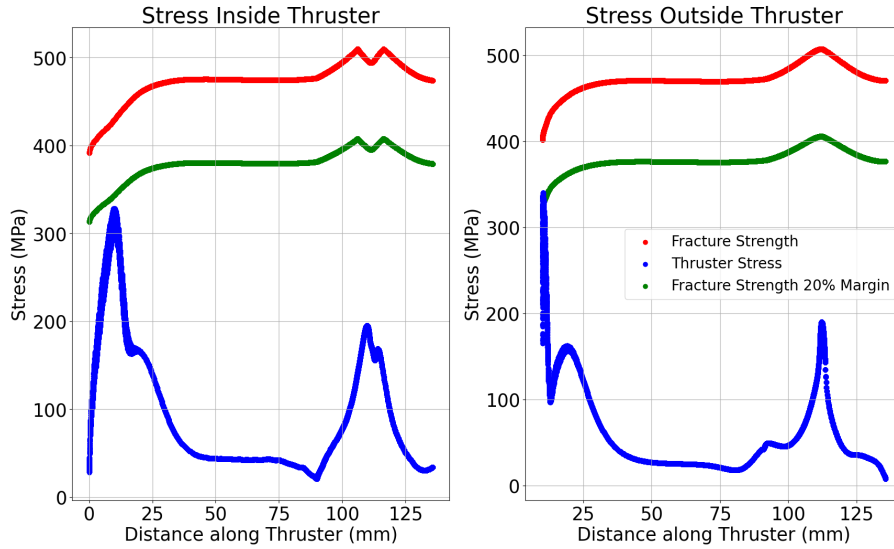


**Figure 4.69:** Stress Contour for Thruster under C20 conditions at 10 seconds operation time

Figure 4.69 shows that the outer area of the thruster just barely exceeds the fracture strength margin line. This is highly likely to be due to the 3 mm curved edge at the flange causing higher stress concentrations. Here, a geometrical stress concentration, while still not exceeding the absolute flexural strength limit in red, still exceeds the material margin after 10 seconds of operation. Though operating for 10 seconds is very unlikely in practice for such a thruster class, if deemed necessary, then the thruster may very well fracture given higher-than-expected convection.
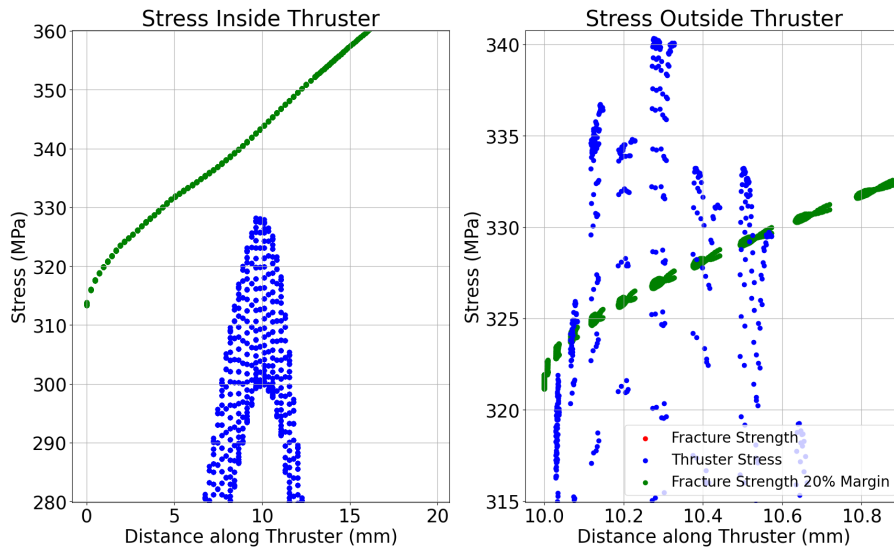


**Figure 4.70:** Zoom In on areas where Stress gets close to Green margin for a complex model under C20 conditions

Figure 4.70 shows a zoom-in figure over that specific region, where a lot of variability can be seen in the points taken, but still it shows signs that the thruster has a good chance of exceeding the fracture strength of the outside curved flange section connecting to the outer thruster chamber body.

The sensitivity analysis thus concludes that the effects of a decrease in Young's Modulus are not critical if material manufacturing results in less-than-optimal material properties. An increase in the convection coefficient by 20% also saw the resilience of the thruster when it came to the nozzle section stresses, as there is still a lot of room before the green margin line will be reached by the nozzle peak stress under more thermal load. The only critical area is the thruster flange, as mentioned previously, there is a lot of uncertainty around. Therefore, at this stage, it is further confirmation that to ensure the optimum chosen design will be feasible the highest allowed thickness of material will be taken in that area, 4 millimetres. Taking this higher thickness reduces the risk of potential thermal stress cracks occurring at the rounded flange edge, in favour of reliability at the cost of a higher thruster mass. Additionally as mentioned previously as well, a more complex model, knowing more about the mounting of the thruster, may show even lower stresses observed at the flange. But as the aforementioned is only an educated guess, the safest route is to assume the worst and take the maximum allowed thickness at the flange rounded edge, area 4 in Figure 4.15 and parameter V135 in Table 4.2 set to 4 mm for all iterations.

# 5

# Results and Discussion

With the models verified and validated, they can then be finally used to iterate over all possible thruster configurations to find the optimum design, this is done in section 5.1. Sections B and C are then discussed, named the nozzle, in section 5.2. The flange, section A, is then discussed in section 5.3. Then, sections A, B, and C, are combined and the whole thruster is discussed in section 5.4. Finally, the applicability of this optimum thruster will be discussed in section 5.5.

## 5.1. Optimization

Before starting the actual simulations on all possible thruster configurations, it is important to understand what parameters are being varied and which are held constant. All the relevant parameters are given in Table 4.2. Due to the high-stress concentrations near the flange, V135 is set to a constant 4 mm throughout all the iterations to ensure that no matter which thruster configuration is chosen, it can withstand the stresses under operation near the flange. The following parameters can be altered to have either 2, 3 or 4 mm values: L168, L169, and V174 for the divergent section thickness, the convergent sections, and the beginning of the nozzle thickness. It must be noted that the parameters V174 and L169 will always be equal to each other, such as to maintain a constant thickness along the convergent section of the nozzle. Since the minimum and maximum thickness of the thruster are 2 and 4 mm respectively, the values can be varied between them. To start with, an additional 3 mm thick option will be given for the thruster thickness of a section, this makes the total number of 9 possible combinations. These combinations are given in Table 5.1. It must be noted that thicknesses that are 2.5 mm or 3.5 mm are also possible, however, the decision to include such options will be made once it is deemed necessary after the results of this smaller dataset are calculated. This serves to reduce the total number of combinations for the first batch of runs from 25 to 9 possible thickness combinations.

**Table 5.1:** Compilation of all possible configurations simulated

| Configuration | Convergent Thickness (mm) | Divergent Thickness (mm) |
| --- | --- | --- |
| C1 | 4 | 4 |
| C2 | 4 | 3 |
| C3 | 4 | 2 |
| C4 | 3 | 4 |
| C5 | 3 | 3 |
| C6 | 3 | 2 |
| C7 | 2 | 4 |
| C8 | 2 | 3 |
| C9 | 2 | 2 |

Thinner configurations decrease the maximum stress observed, seen in Table A.1. A pattern of decreasi stress with thickness is also observed in a paper, Thermal–Solid Interaction Study of Serpentine Nozzle and Analysis on Structural Response Law.[70] The paper does a study on aero-engines as opposed to

engines designed to work in space, but since they are also performing a thermo-structural analysis, they observed that the maximum stress increased with thickness increasing from 1 mm to 4 mm. Additionally, the paper also observed a decreasing temperature with increasing thickness, which is also seen in Table A.1 for the different configurations and iterations. Also, the variation in the number of mesh elements is at most 607, much less than 1% of the total number of elements in the model, this shows that the custom mesh is doing its task of controlling the mesh quality across all thruster configurations.
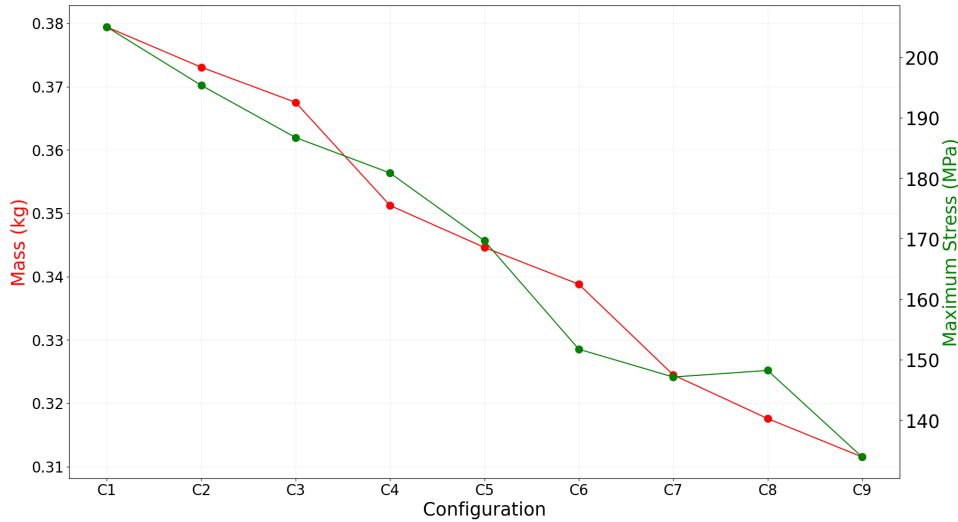


**Figure 5.1:** Mass and Maximum Stress of different configurations

Figure 5.1 shows that stress decreases as the configuration's mass decreases. This is because the mass reduction occurs in critical areas, particularly sections B and C of the nozzle, which become thinner. As the nozzle thins, the temperature difference across the material lessens, leading to reduced thermal stresses. Thus, there is a direct correlation between mass and stress, with lower mass corresponding to reduced nozzle thickness and thermal stresses.
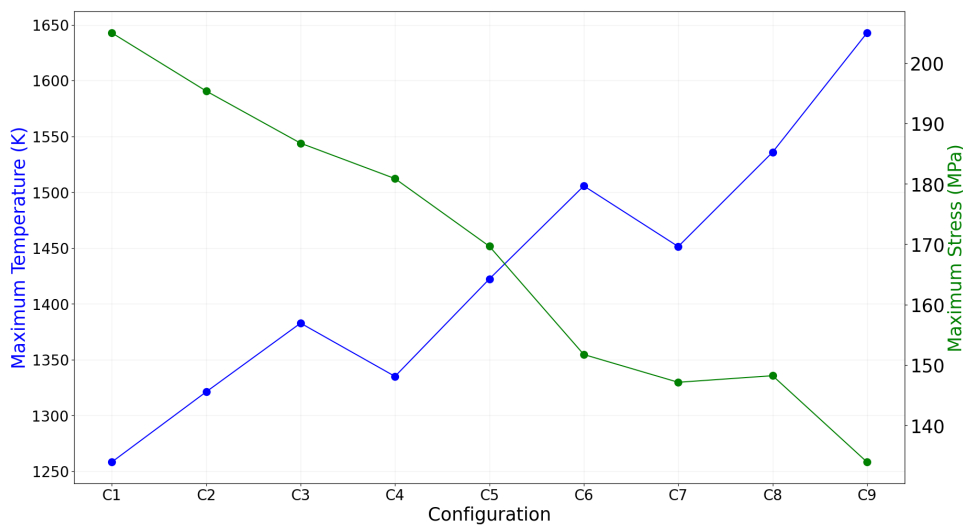


**Figure 5.2:** Maximum Temperature and Maximum Stress of different configurations

Figure 5.2 shows that as the stresses observed in the nozzle decrease, the temperatures increase. Since a decrease in maximum stress is a direct effect of the decrease in mass, a decrease in thickness can be used to explain why temperature rises for lower mass configurations. With a thinner nozzle, the energy from convective heat transfer is more easily absorbed as there is less material to share this energy with. Thus with less material comes less weight but also a higher temperature as less material takes less energy to heat up by a single degree. Both the aforementioned plots demonstrate a trade-off that can occur between configurations, generally speaking, as the thruster nozzle section becomes thinner, the stresses decrease but the temperature increases. This means that there is a possibility of choosing the optimum based on lower stresses or lower temperatures. In this case, since the highest temperature seen is 1642.7 Kelvin, and the UHTCMC material used is expected to comfortably be able to withstand 1800 degrees Kelvin, it is determined that temperature will not be a determining factor when it comes to selecting an optimum design. The UHTCMC material is expected to be very durable at high temperatures with little to no erosion seen in tests where UHTCMC is exposed to very high temperatures such as those seen in reentry, this was discussed in the literature previously [57][33]. The next criteria would then naturally be stress and mass. Since configuration 9 boasts the lowest stress and the lowest mass, 0.31 kg, it is therefore the optimum design.
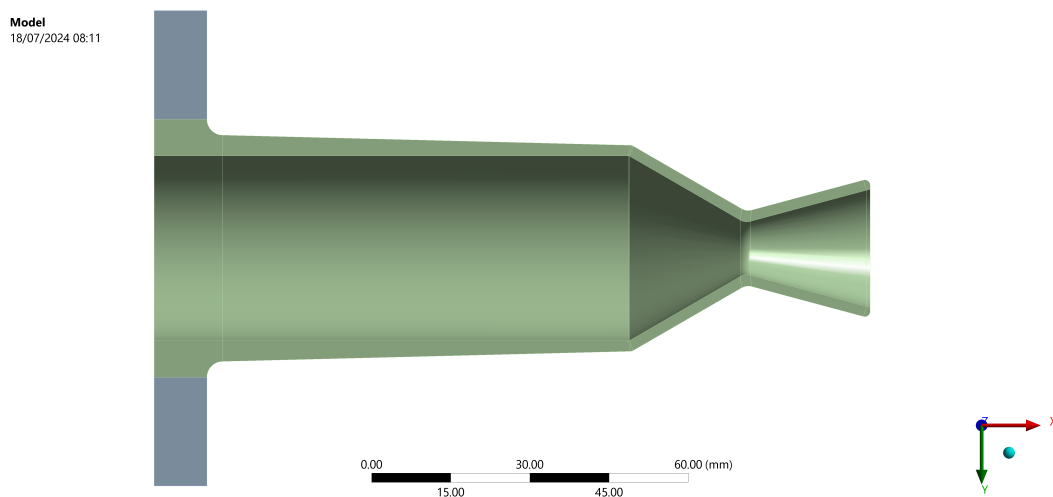


**Figure 5.3:** Optimum Thruster Configuration Side View

The best design is shown in the figure above, Figure 5.3, with a thickness of 2 mm around the entire nozzle. Do take note that the thickness from the flange to the start of the convergent section linearly decreases from 4 mm to 2 mm. Such geometric complexity will have to be addressed when it comes to manufacturing considerations, especially when attempting to 3D print such geometry. From here on, all further results and discussion will refer directly to this optimum thruster design chosen.

## 5.2. Optimum Chamber and Nozzle

Once the optimum design is chosen based on the iterations run on the simple model, the thermo-structural analysis of the design will be done on the complex model. With this in mind, the simulations will be done by using the exact time step method, where the time step found in transient thermal will be exactly copied into the static structural simulations settings. Additionally, the complex model will have only 1 axis of symmetry to account for the fact that the beam elements cannot be split in half in partially cut boltholes.

Additionally, there will be an additional analysis done in this case for strain, which was not previously covered, for the final design. The thermal strain of the thruster will also be shown and used to facilitate discussion. The thermal analysis is discussed first, followed by the structural analysis.

The thermo-structural analysis will focus on covering only sections B and C, in Figure 3.1, for the

structural analysis. The structural analysis would benefit greatly from excluding the flange section, as many reports for literature do not cover the attachment of the thruster. Since thruster attachment in the complex model is done explicitly in this thesis, it is also covered in a separate section. In thermal and structural analysis, the specific connections made between the flange and the back plate have very little effect on the nozzle past a certain distance as seen previously.

## 5.2.1. Thermal

The thermal analysis results of the optimum design will be discussed. The settings for thermal analysis are identical to those discussed in the previous chapter, as seen in section 4.4 for the complex model. A figure showing the temperature distribution simulation results in the thruster is shown below.
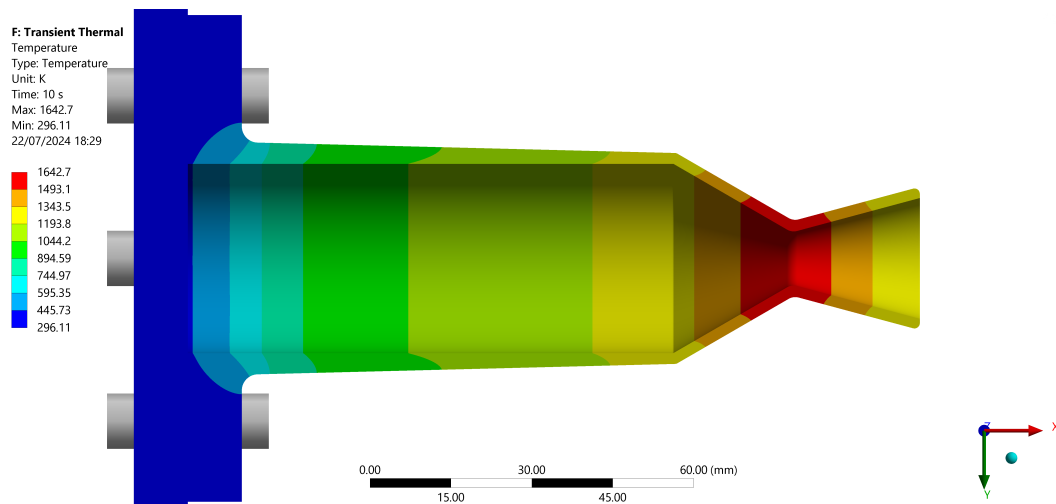


**Figure 5.4:** Temperature of the whole thruster

As can be seen in Figure 5.4, the higher temperatures are concentrated on the throat region, where convection coefficients and near-wall temperatures are highest. It can be seen that further away from the throat, the temperatures drop rapidly from the peak of 1642.7 kelvin, at an axial distance of 113 mm, at the end of the operation time, 10 seconds.
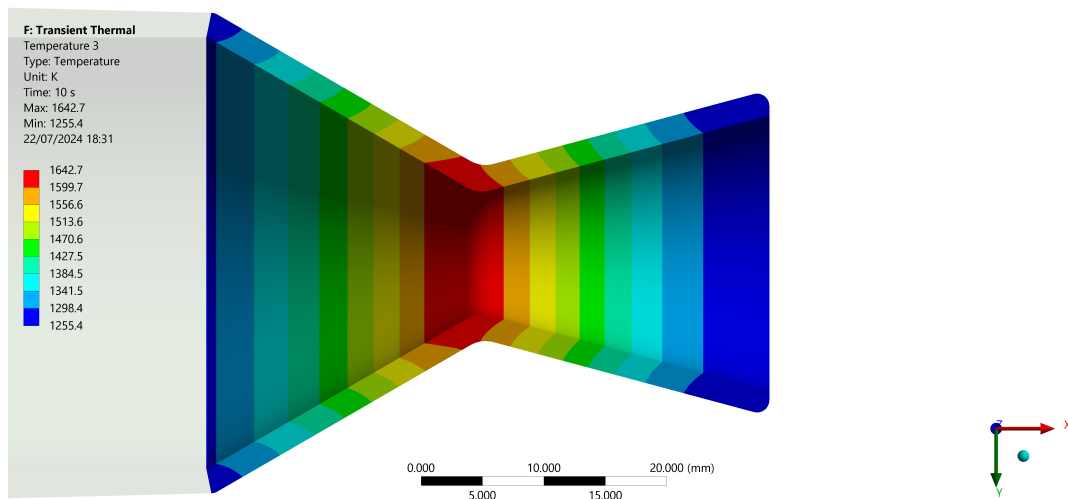


**Figure 5.5:** Temperature of the Nozzle at 10 seconds

A zoom-in to just the temperatures in the nozzle section, section C, shows more temperature contours in Figure 5.5. These contours further show the pronounced effect that the temperature at the throat and convergent section spikes very rapidly near the throat and the further away from the throat one

moves, the more temperature drops. The temperature drop can also be seen to be nearly 400 degrees in the short distance of around 23 mm.
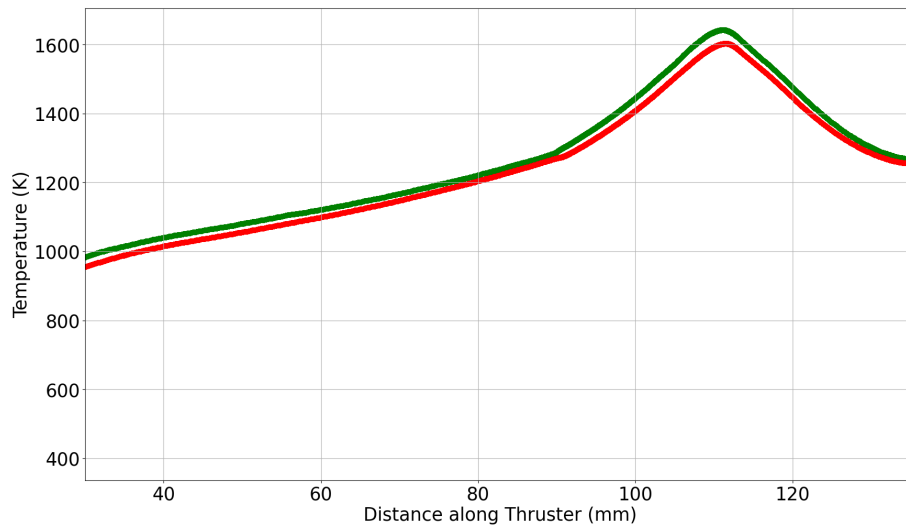


**Figure 5.6:** Temperature Contours of sections B and C at the end of operation

Figure 5.6 plots the inside and outside temperature contours of sections B and C at the end operating time of 10 seconds. The same trend of peak temperatures is seen in the throat. Additionally, the rate of increase and decrease in temperature is highest in the convergent and divergent sections, respectively. The temperature rate of the decrease can then be seen to decrease more or less linearly from the start of the convergent section to 30 mm.
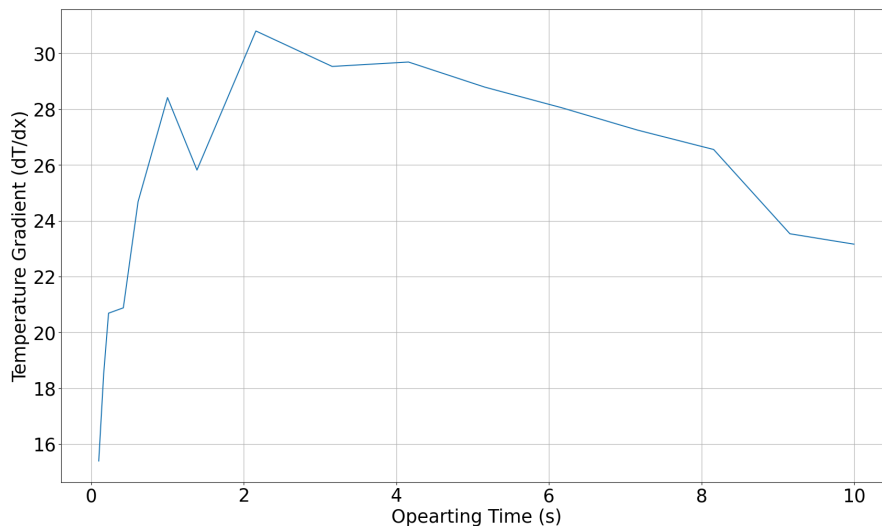


**Figure 5.7:** Maximum temperature gradient axially for sections B and C

In Figure 5.7, the highest thermal gradient is seen to occur at 2.16 seconds after operation. This can serve as a very preliminary indication as to when the highest thermal stresses are expected to occur in the nozzle. Thermal stresses are expected to be much more prevalent in a nozzle compared to

mechanical stresses, the peak time obtained here is thus used as an indicator. This peak time will be used to further investigate sections B and C.
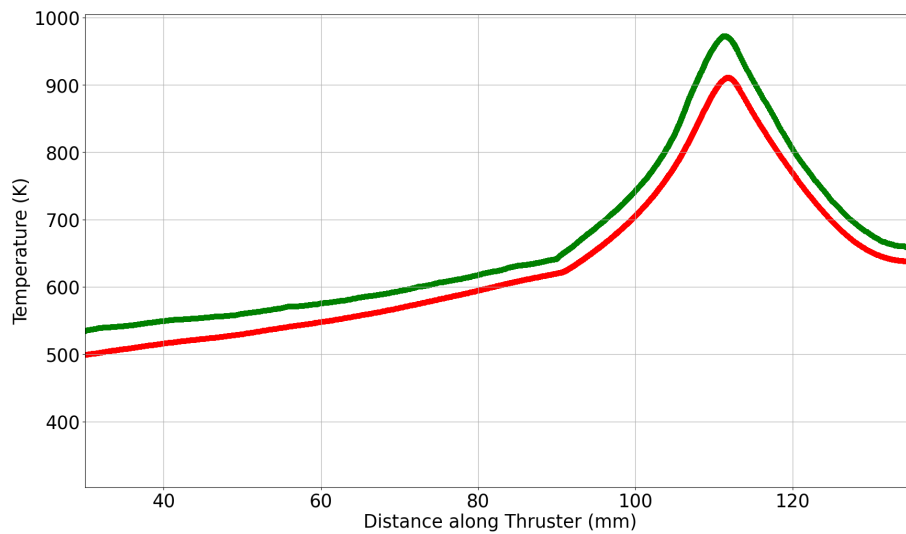


**Figure 5.8:** Temperature Contours of sections B and C at the time of peak thermal gradient

In the figure above, Figure 5.8 shows a higher temperature difference between the inside and outside of the thruster. This likely occurs because, during the early stages of the transient phase, the inside heats up rapidly, while the outer side, reliant on conduction, hasn't had enough time to catch up. This may also explain the growing temperature difference in the chamber section, where the linear thickness varies from 4 mm at the flange to 2 mm from the flange to the convergent section.
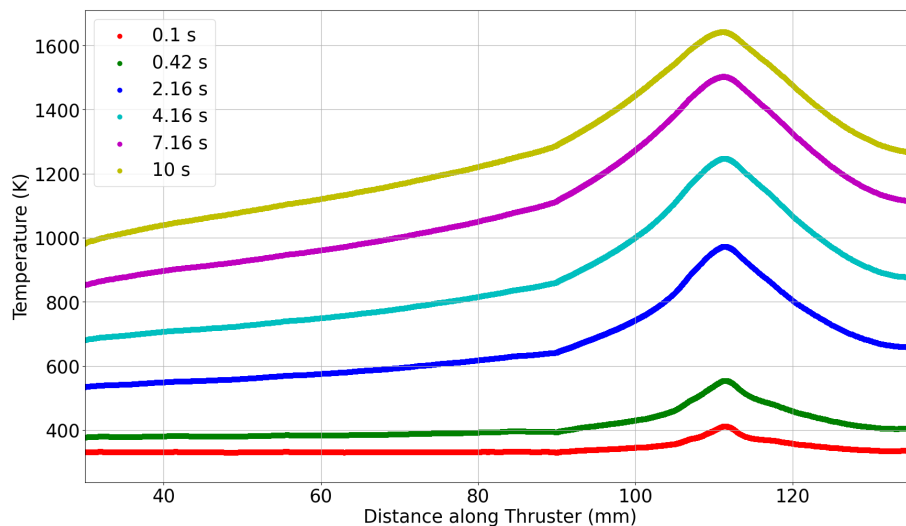


**Figure 5.9:** Sections B and C temperature contours at 6 time steps

The figure above, Figure 5.9 shows the variation of temperature contours over time from 0.1 seconds to 10 seconds. Do take note that the slope of the rise in temperature over distance, specifically that from 30 to 90 mm in the thruster chamber, increases as time progresses, showing that the temperature difference from the beginning of the chamber and to the start of the convergent section rises over time.
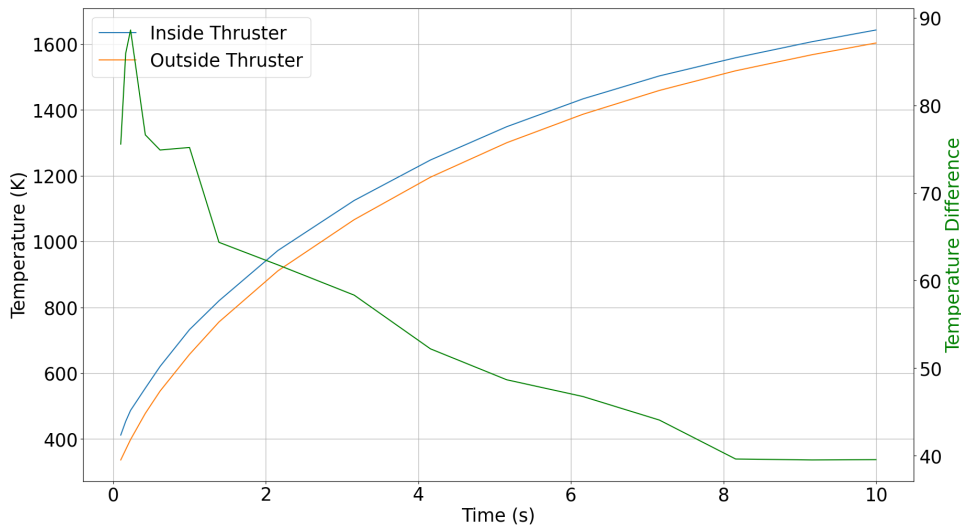
**Figure 5.10:** Maximum temperature over time in sections B and C. Temperature is on the left y-axis and temperature difference is on the right y-axis (Green plot)

Figure 5.10 shows how the maximum temperatures on the inside and outside of the thruster change over time, with the largest temperature differences occurring early on. By the end of the operation, the temperature difference at the throat is minimal. Table A.7 provides these numbers. Compared to Table A.4, showing the temperatures for the 4 mm uniform thickness thruster configuration, the absolute temperature difference between the inside and outside is much less, which points towards lower thermal stress. This serves as just an indication of how thickness can be related to temperature and stress, taking into account decreasing Young's modulus with higher temperatures.

### 5.2.2. Structural

With transient thermal simulations completed, the static structural simulation is performed next. The static structural simulations will focus on the results obtained in areas B and C in Figure 3.1.
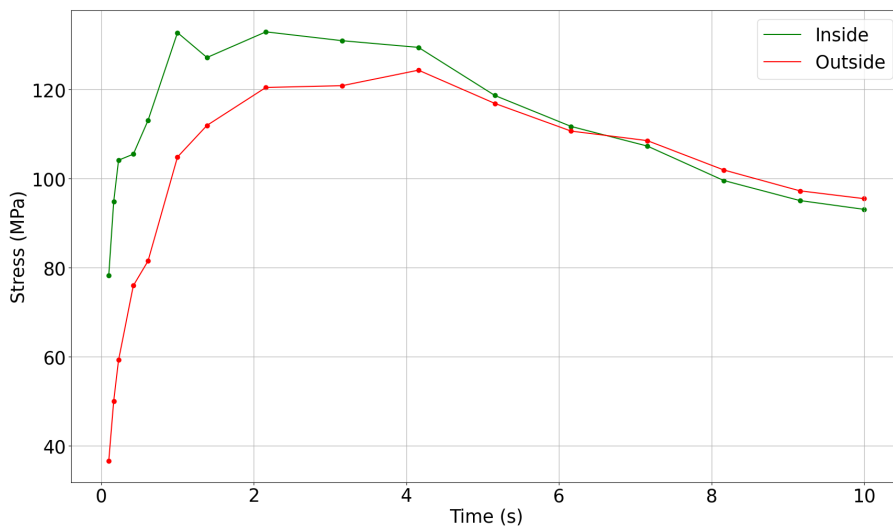


**Figure 5.11:** Maximum Stress over time for the inside and outside of sections B and C

Figure 5.11 shows a local stress peak that occurs at around 1 second. This peak stress occurs in the inside nozzle section C at the throat. The figure then shows a slight drop in peak stress before it continues to rise again until the absolute peak stress at 2.16 seconds. After 6.62 seconds, the stresses on the outside of the thruster overtake those on the inside because of the stress concentrations due to geometry on the outside of the throat. This is due to the thinner thruster thickness of 2 mm, which would amplify the stress concentration ring on the outside of the throat. A potential way to reduce this stress concentration ring is to increase the curvature radius in area 2 of Figure 4.15.
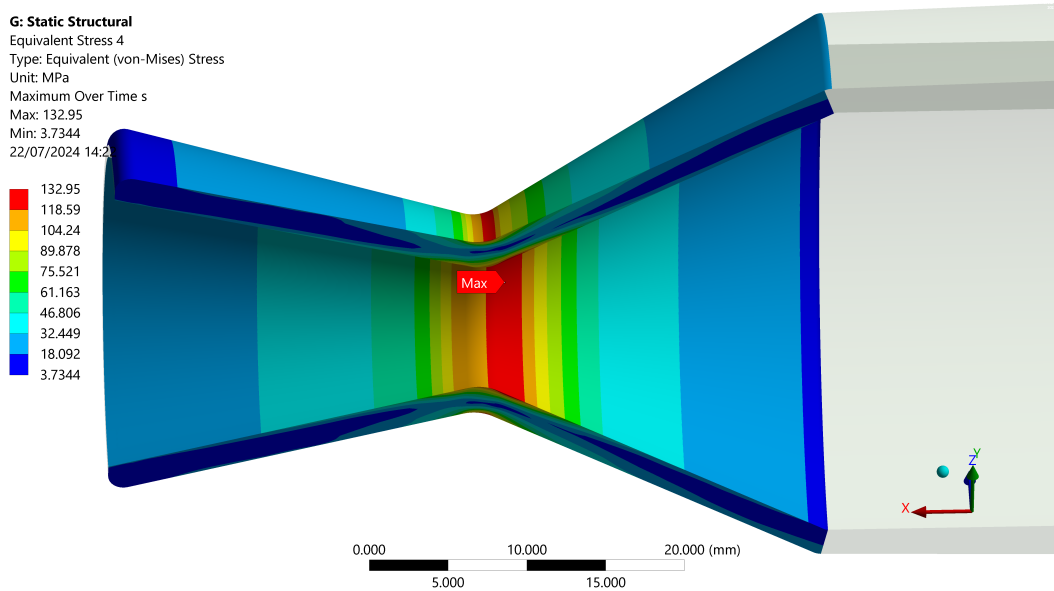


**Figure 5.12:** Zoom into the nozzle throat section

Zooming into just the nozzle section, as seen in Figure 5.12, the maximum stress is the convergent section near the throat with the addition of a stress concentration ring around the throat on the outside. A graph of the peak stress over time for just the nozzle section is plotted below.
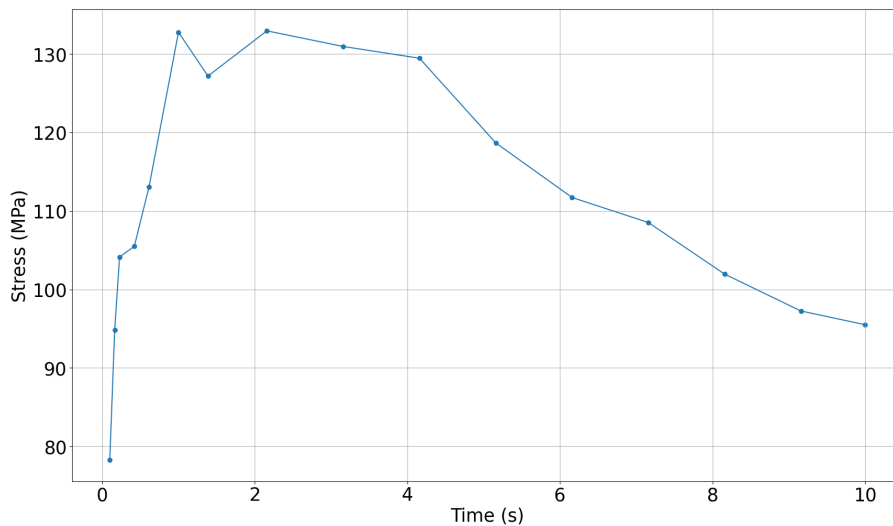


**Figure 5.13:** Maximum absolute nozzle stress over time

Figure 5.13 shows that the peak stress in the thruster is 132.95 MPa at 2.16 seconds, with an earlier

peak of 132.77 MPa at 1 second. Such an observation is critical, as it also shows that there is further room for improvement to investigate the secondary peak that occurs at 1 second. After the highest peak is reached at 2.16 seconds, the stresses continuously keep on decreasing. Table A.6 shows the results that were used for discussion and generating some of the graphs for maximum stress over time in the nozzle and whole thruster.
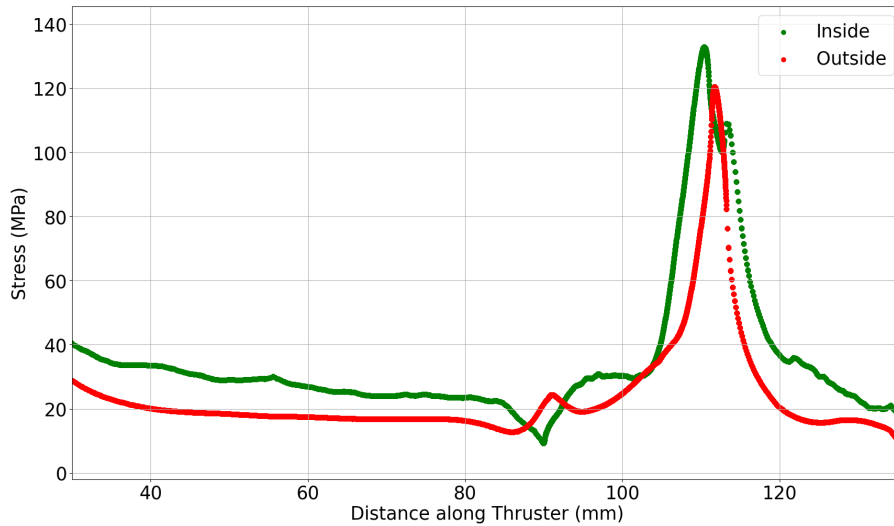


**Figure 5.14:** Nozzle stress contour at peak nozzle stress of 2.16 seconds

Figure 5.14 shows the stress contour at the time when peak stresses occur in the nozzle section. It can be seen that the inside stresses dominate throughout the nozzle section except for the stress ring on the outside that occurs a small distance further behind the nozzle. The stress ring, while still not having the highest global stress, still has a peak at the throat section which is higher on the outside than inside of the thruster at that axial position. The secondary local peak and dip in the outside and inside stress contours occur right when the convergent section of the nozzle starts, at 90 mm along the thruster.
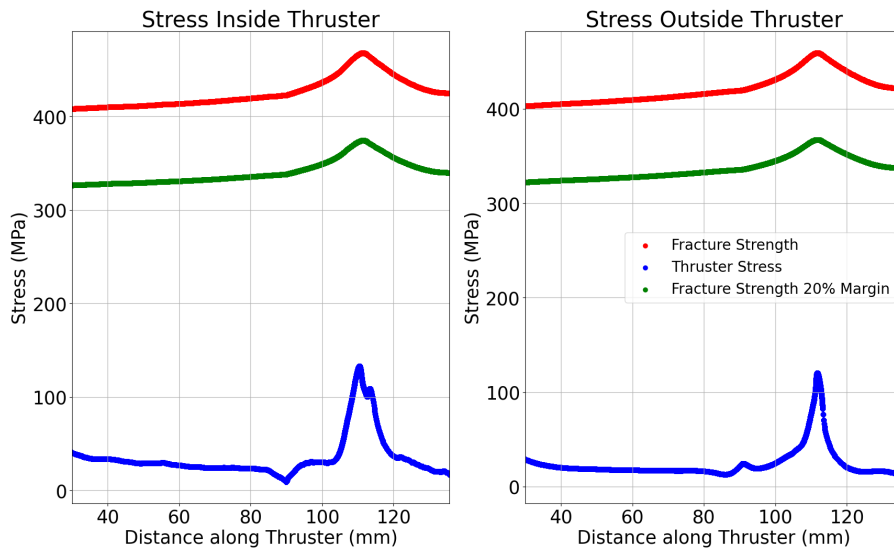


**Figure 5.15:** Nozzle stress contour versus stress margin at peak nozzle stress of 2.16 seconds

Figure 5.15 shows that the stress contour at the nozzle stress time is well below the fracture strength limit. Additionally, as the temperature of the nozzle has not risen over the region where the material fracture strength starts to deteriorate, the fracture strength of the material also experiences a rise near the nozzle throat section, this serves to give an additional margin of stress as opposed to the material behaviour showing deterioration given any temperature rise.
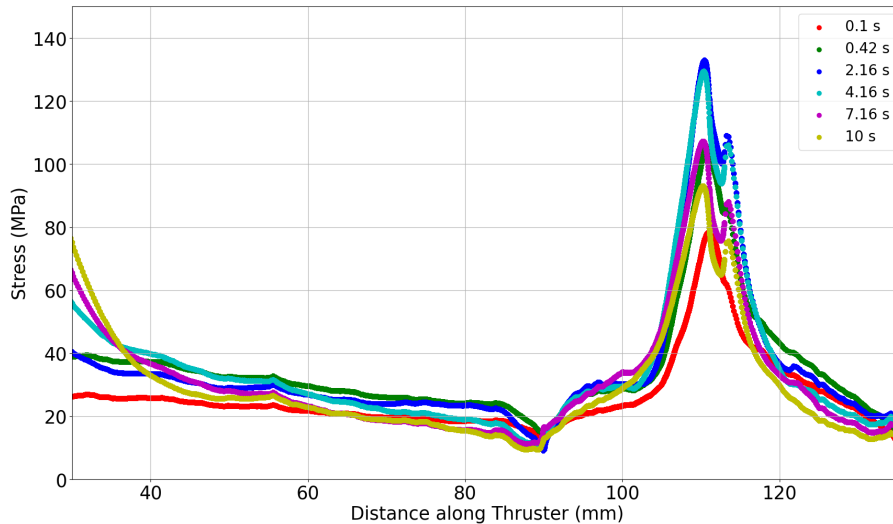


**Figure 5.16:** Stress contours over time for sections B and C

Figure 5.16 illustrates the expected stress behaviour, with stress contours increasing over time until reaching a peak. In the nozzle section, the highest stress, indicated by a dark blue contour, occurs at 2.16 seconds. Due to the nozzle's thinness, thermal energy transfers quickly, leading to a rapid peak in stress. Even with a maximum thrusting time of 10 seconds, the stress levels decrease slowly and remain higher than those at 0.1 seconds.
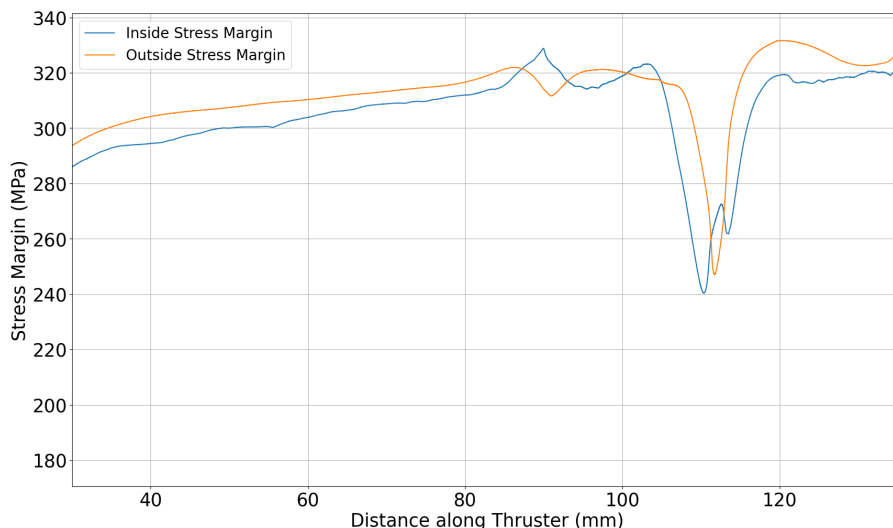


**Figure 5.17:** Nozzle Stress Margin at 2.16 seconds

Figure 5.17 shows that the stress margin is lowest inside the nozzle at 2.16 seconds due to higher

temperatures and increased fracture strength degradation. Although the margin is lower at 90 and 112 mm on the outside (the start of section C and the outer stress ring), the inner surface still has the lowest margin overall just upstream of the throat.
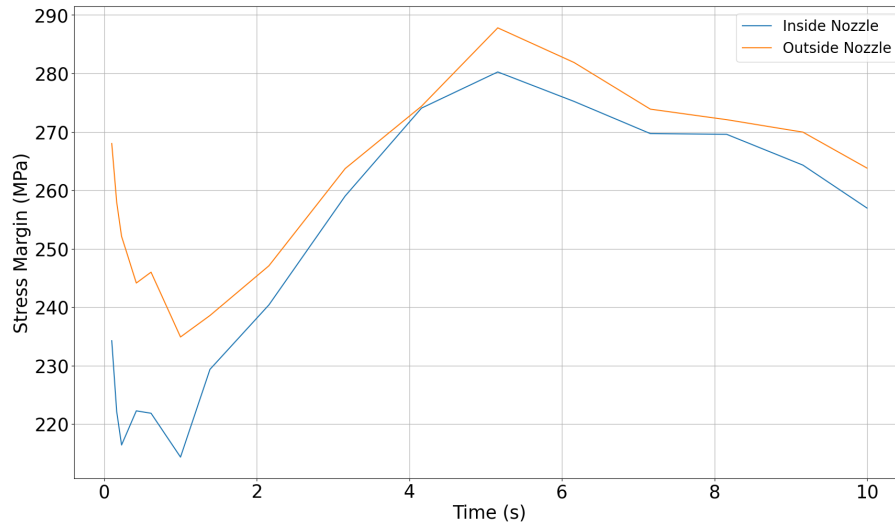


**Figure 5.18:** Inside Nozzle Stress Margin over 10 seconds

Figure 5.18 shows that the nozzle's most critical period is at 1 second, where the stress margin is lowest. Additionally, the stress margin inside the thruster is consistently lower than on the outside, even though the outer stress ring may experience higher stresses after 6.62 seconds of continuous thrust.

## 5.2.3. Strain

Strain is examined because it serves as an indicator of stress behaviour, helping to determine whether thermal or mechanical stresses are more dominant and critical in specific regions. Therefore, the total thermal and total equivalent strains for sections B and C will be analyzed and discussed.
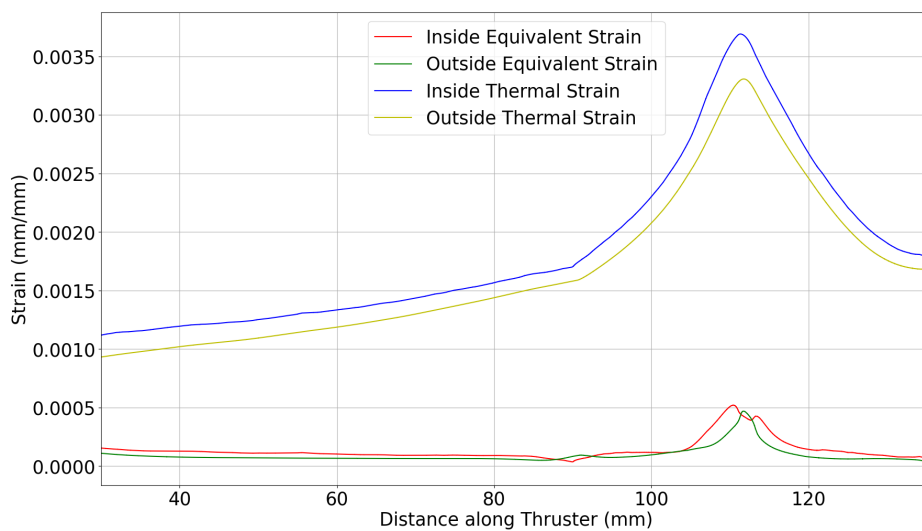


**Figure 5.19:** Strains for sections B and C at peak stress time of 2.16 seconds

Figure 5.19 shows that the equivalent strain of the material is always lower than the thermal strain at peak stress. Both curves mirror the patterns seen in the temperature and stress curves, with the thermal strain following Figure 5.8 and the equivalent stress following Figure 5.14. The higher thermal strain indicates significant thermal expansion resisted by the nozzle, confirming that thermal stress is the primary source of stress. Though not all thermal strain is translated to stress, a significant amount is expected to result in thermal stress.
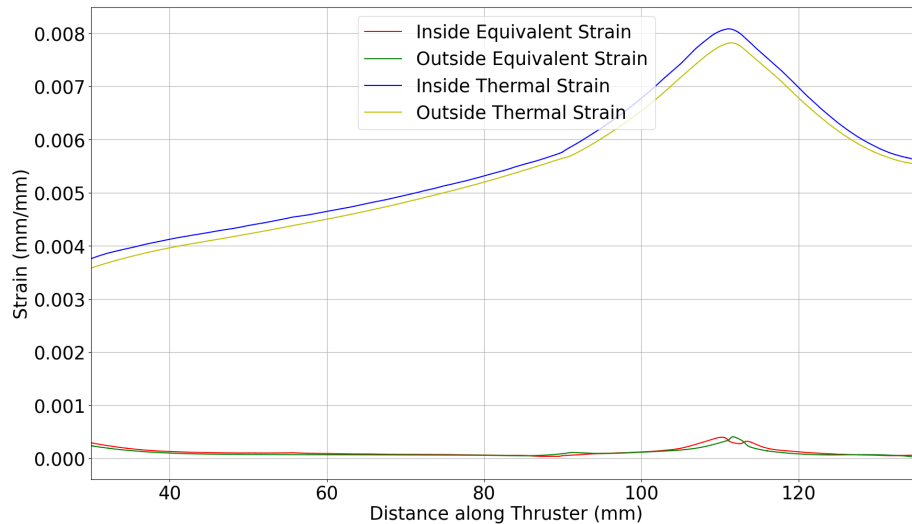


**Figure 5.20:** Strains for sections B and C at 10 seconds

Again, in figure Figure 5.20, the thermal strain is higher than the equivalent strain, which indicates that the material's deformation due to temperature changes is greater than from other sources, in this case, the pressure load. This suggests that some of the thermal expansion is being counteracted, likely by stresses or constraints that limit the material's ability to expand. And again, the major source of stress is thermal. The outer stress ring at the throat has higher stresses, most likely due to the relatively sharp transition from convergent to divergent section, thermal stresses are still very dominant overall, though it is much more difficult to observe. The next section will highlight where the thermal strain is lower than that of the equivalent, where such geometrical considerations are more pronounced. The gap between the equivalent and thermal strain increases from 2.16 seconds to 10 seconds, but the stresses, as was seen, decrease. This could be likely due to the material properties of the UHTCMC, where a higher temperature reduces the Young's modulus, effectively reducing the material's resistance to expansion under a constant load. Many compounding effects make it difficult to separate each effect and pinpoint a cause fully.

Taking into consideration that higher peak stress at the stress ring was not seen whatsoever in the 4 mm base thruster is a testament to how a thinner nozzle can amplify geometrical stress concentrations. A fix, if desired would be to increase the curvature of the stress ring section by one or two millimeters. This will of course be limited by manufacturing capabilities when this thruster is made.

### 5.2.4. Nozzle Operational Damage

The operation aspects of the thruster are discussed in this section. Key damage mechanisms likely include oxidation, erosion, ablation, and thermal shock gradients due to the thruster's short 10-second operation before cooling. These issues stem from high-temperature fluid flow within the thruster. Note that the analysis here is theoretical; actual testing is needed for accurate long-term performance data. However, it provides insights into potential failure points, their causes, and mitigation strategies. First, thermal shocks will be discussed.

As was seen previously, the temperature rises from room temperature to 1642.7 degrees Kelvin within 10 seconds of operation at the nozzle throat. Such rapid rise in temperature is corroborated by high thermal stresses and damage. The figure below can be used to further investigate this.
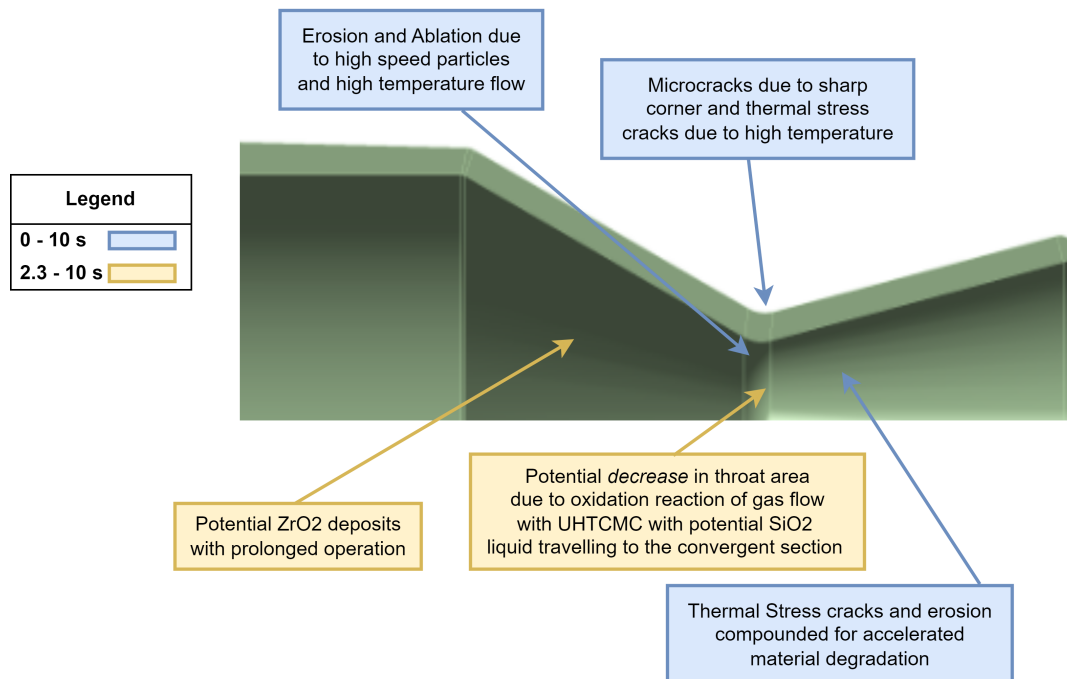


**Figure 5.21:** Damage mechanisms in the throat concerning time

From the literature review, it was found that thermal shocks would lead to thermal stress cracks. These thermal stress cracks would likely occur on the inside convergent section of the nozzle, near the throat, where the stresses are also highest. Given that there is still quite a large margin before the fracture strength and stress contour in the throat section coincide, the stress cracks are expected to grow slowly over time. Figure 5.21 shows that thermal stress cracks and cracks due to erosion and ablation are the primary concerns when operating in the range of 0 to 10 seconds. In the very rare case that operation would exceed 2.3 seconds, oxidation would then be an effect that would need to be taken into account. However since such thrusters would most likely be used for thrusts in the range of 0 to 3 seconds, it is not expected that any oxidation would occur.

The actual combustion reactions are in reality expected to occur to a high degree in the middle section of the thruster, and the high-speed flow to get up to speed in the later section of the thruster. With this in mind, erosion, ablation, and oxidation effects which depend on the actual high-speed flow not found in the chamber due to the no-changing cross-section area will be likely concentrated in the nozzle section of the thruster, where the flow reaches the supersonic speeds and is carrying the by-products of combustion.

Knowing that oxidation, ablation, and erosion are more likely to occur in the nozzle, specifically in the throat area, the effects of these phenomena compounded with thermal stress cracks can be discussed. Given the high-speed flow in the nozzle, erosion, and ablation are both likely to cause the removal of material in the throat section of the nozzle, where these phenomena are most concentrated. The combination of high temperature in the throat section and possible flow particles made of combustion products would collide with the inner wall of the nozzle divergent section. Since the temperature in the nozzle throat section is very high, thermal stress cracks would occur thereafter each operation. These cracks would grow over time with each operation cycle and the growth rate would increase since erosion is also playing a part in increasing the rate at which these cracks would grow. This cycle of cracks forming due to thermal cycling and growing right after due to erosion would keep on occurring until the thruster eventually fails. It is expected that the crack growth rate will increase over time in this case.

Since the erosion depends on the size of particles and the by-products of combustion, its rate would have to be identified experimentally.

Oxidation is a difficult phenomenon to determine since it involves investigating the fluid-structure interaction that occurs at high operating temperatures. A source was found however that investigated oxidation effects in a test, Propulsion tests on ultra-high-temperature ceramic matrix composites for reusable rocket nozzles. [57] This paper will be mainly used to determine the oxidation effects that may be of consideration for the optimum thruster design. The paper states that temperatures in the wall ranged between 1600K and 1900K, a. The optimum thruster design observes temperatures that reach the lower end of this range, 1643K. Although the UHTCMC used in the paper is a long fibre based on 10 vol% SiC in the UHTC, the reaction that occurs at these high temperatures can be assumed to be the same since the reactants are the same. Based on the paper results, it can be said that the optimum design will have oxidation effects, occurring as soon as 2.3 seconds after operation. The oxidation may be very light as it is given that the pressures are not very high, 6 bar in the chamber, with 9.5 bar used to estimate the oxidation products in the paper. The expected oxidation procedure, although likely different for the optimum thruster in reality, is outlined below.

1. From 995.15 K - 1295.15K: Fibres and boride matrix are oxidised, forming ZrO2 and Br2O3.
2. At 1495.15K: SiO2 oxidation occurs, forming ZrO2-SiO2 scale, which supposedly protects up to temperatures of 1995.15K.
3. The liquid SiO2 layer, with enough pressure from the flow will be moved upstream

The effects of oxidation are that the new oxidized layer that forms, has lower thermal conductivity, specific heat, and thermal emissivity properties. The paper shows that the temperatures will therefore increase when the thruster is refired. This may have the added effect of increasing thermal stresses with the next firing sequence. This will however have to be verified experimentally given the different combustion conditions and different UHTCMC compositions for the optimum thruster.

The causes and effects are summarized in the table below. The causes were not directly linked to the effects as there is still not enough information on the flow and structure interaction, constituents of the flow, and the internal material morphology. The last point is attributed to the lack of understanding of how exactly the interface between a singular chopped carbon fibre would interact with the surrounding UHTC when a crack comes close to the vicinity of such a boundary. Such information and detail are outside the scope of this thesis, but is important to understand how the rate of crack growth would be affected at these critical interfaces. The most that can be said therefore is the location of cracks and their effects.

**Table 5.2:** Summary of Damage over time for optimum thruster

| Damage | Description |
|---|---|
| Throat Ablation - Very minimal if any | • Effect mostly in the nozzle throat section<br>• Increase in throat diameter, decrease in pressure curve and decrease in thrust.<br>• Compounded effect with other damage mechanism lead to lower life cycle with damage accumulation |
| Thermal Stress Cracks - moderate to severe | • Effect in the nozzle throat convergent section and the outer stress ring around the throat.<br>• Compounded effect in the nozzle convergent section with erosion and ablation. |

**Table 5.2 continued from previous page**

| Damage | Description |
|---|---|
| Erosion - Very minimal if any | <ul><li>Decrease chamber pressure and thrust</li><li>Damage accumulation over time can result in accelerated crack growth.</li></ul> |
| Oxidation - Moderate | <ul><li>To occur as soon as 2.3 seconds when temperatures are high enough and in the nozzle section</li><li>Decrease throat area and increase in pressure of inner walls.</li></ul> |

Overall, the thruster is expected to be greatly resistant towards all damage mechanisms. This makes sense as it is the whole reason behind the research and development of UHTCMC, high durability and performance. Oxidation will require actual testing to be sure of its effect over the long term. The information provided on oxidation for the optimum thruster is at best educated guesses given the lack of testing data.

### Crack Growth and Damage Effects

Damage mechanisms and crack growth are difficult topics to cover when it comes to materials such as UHTCMC. As was seen in the literature review, much is still unknown about the exact material morphology, which can change based on the manufacturing process and material composition. Thus, no exact crack growth can be determined for this material and subsequently measuring material life also becomes much more complex. A discussion can still be had on how the crack would progress through the material and fibre in the UHTCMC. The figure below can be used for this.
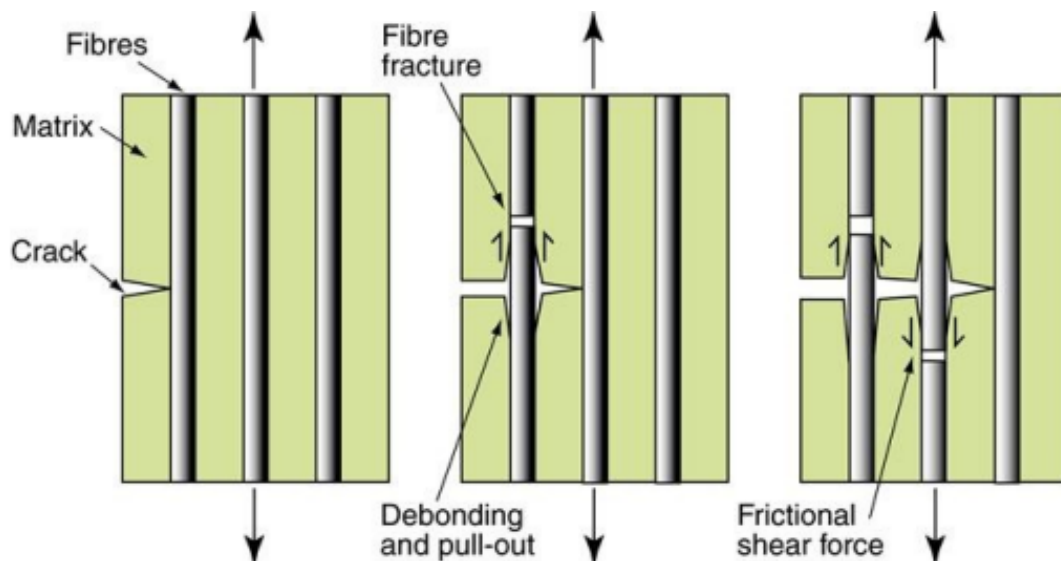


**Figure 5.22:** Crack growth behaviour expected taken from Materials Book [2]

Figure 5.22 shows how the crack growth is expected to progress throughout the UHTCMC as the crack approaches the individual fibres. The material book states that such material with fibres has higher fracture toughness, due to the fibres bridging the gaps and remaining intact. This allows for many cracks to form, thereby increasing the energy dissipation. Even as the fibre breaks, fibre pulls out dissipated energy via friction. [2]This therefore contribute to the fracture strength. Do note that the aforementioned information is expected to apply mostly to traditional composite material where the matrix is weaker than the fibre. Nevertheless, the fact that fibres are expected to positively contribute

towards fracture toughness is to be expected in the UHTCMC material. Additionally, one of the main reasons UHTCs and CMCs are combined to form UHTCMC is so that the combined material retains the high erosion/ablation/oxidation resistance of the UHTC and the higher fracture strength and specific weight of the CMC. [85]

$$F = \dot{m}v_e + (p_e - p_a)A_e \tag{5.1}$$

$$\dot{m} = \frac{\Gamma p_c A^*}{\sqrt{RT_c}} \tag{5.2}$$

$$v_e = \sqrt{\frac{2\gamma}{\gamma - 1}RT_c[1 - (\frac{p_e}{p_c})^{\frac{\gamma-1}{\gamma}}]} \tag{5.3}$$

Assuming a total operational time of 10 minutes, taking an ablation rate that is assumed to 1.05 $\mu m s^{-1}$ and 3.07 $g m^{-2} s^{-1}$,[38] a total of ablation of 0.63 mm. Since ablation is mostly concentrated in the throat region, this can lead to an increase in the throat area by 26.8%. Using ideal thrusts theory in Equation 5.1, Equation 5.3, and Equation 5.2, although it can be said that the thrust would increase by 26.8% because of the positive correlation between throat area and trust, the fact that ablation causes a decrease in thrust must mean that the effect of a decrease in pressure and temperature in the chamber is much more significant. The numbers above are however a worst-case scenario as the ablation rate provided here is under a temperature of 2500 degrees Celsius. This temperature is more than 1100 degrees higher than the highest temperature seen in the optimum thruster in the extremely unlikely case that it is decided to operate the thruster for the whole 10 seconds. In reality, given that the thruster may only operate in bursts of less than 3 seconds, the temperature difference is in practice more than 1650 degrees. With such a huge temperature difference when it comes to ablation rates, it can confidently be said that the current optimum thruster would not experience any measure ablation rates due to the low temperatures and relatively high pressures, compared to the low-pressure extreme ablation environment stated in the $C^3HARME$ project.

### Damage Prevention
Ideally, the thruster would be tested experimentally first to determine its failure mechanisms and the extent of damage endured. Once the extent of damage has been identified, then a decision can be made on how to best protect the nozzle. Table 2.4 summarizes the techniques that can be used to identify damage on the thruster in practice. Since there is no experimental thruster data to base protection decisions over, the expected damage mechanisms discussed previously will be used instead.

Before beginning, since the nozzle material is UHTCMC, which is specifically designed for its high endurance and performance compared to traditional material, it is highly unlikely that any additional protection measure will be necessary for this nozzle. Therefore, no additional coatings will be used to protect the nozzle, as this would defeat the purpose of creating it completely out of UHTCMC. Instead, indirect ways of decreasing the damage will be used, and methods that involve operation time and changing the operating conditions of the thruster are outlined.

It is extremely rare and very unlikely that an operation would need a consistent 100 N thruster for 10 seconds for such a thruster. Such a thruster that is used for orbit maintenance and attitude control will be fired for milliseconds to at most 3 seconds in practice. This does not give the thruster enough time to reach very high temperatures. Therefore, the risk of erosion, ablation and even thermal stress cracks developing enough over time to cause serious damage is also very low. But in the case that it is seen as still critical, operations could be split. An operation that would provide a total of 100 Nm, 100 N thrust in 1 second, can be split into 2 or more bursts adding up to the same impulse. This would reduce the maximum temperatures seen, thermal expansion, and even the maximum stresses seen, thereby primarily targeting a reduction in thermal stress cracks.

Another way to reduce the risk is to alter the thruster operating conditions to decrease the thermal and structural loads. This can be done by altering the propellant and oxidizer mixture ratio, which will result in a decrease in chamber pressure and thruster, as discussed in the literature review previously.

If the goal is to primarily deliver a certain amount of impulse, then a lower thrust will mean a longer required operating time for a given impulse. Such measures however would not be sufficient in the case of action, time being of great importance given that the manoeuvre would have to be performed very quickly.

## 5.3. Optimum Flange

The flange section of the thruster is essentially the connecting piece of the thruster to a body. Since it was previously shown that the flange model has very little impact on the stresses seen in the nozzle section and most of the chamber section when comparing the simple and complex models, the analysis for the nozzle and the flange can be split. This chapter will look more in-depth in the flange section and perform similar stress analysis, as well as investigate potential damage over time. Thermal analysis will not be covered as that was done in the previous chapter and the addition of the flange connection complication has a very minimal effect on thermal transient simulations and their results.

### 5.3.1. Thermal

As seen in the modelling chapter, the flange itself is far from the points of highest convection thus making it more shielded from the rapid temperature rise effects seen in the nozzle section. The temperature contours are used to build up a basis from which stress discussion can be facilitated. Though there is minimal to discuss when compared to the base 4mm uniform thruster, observations are still made.
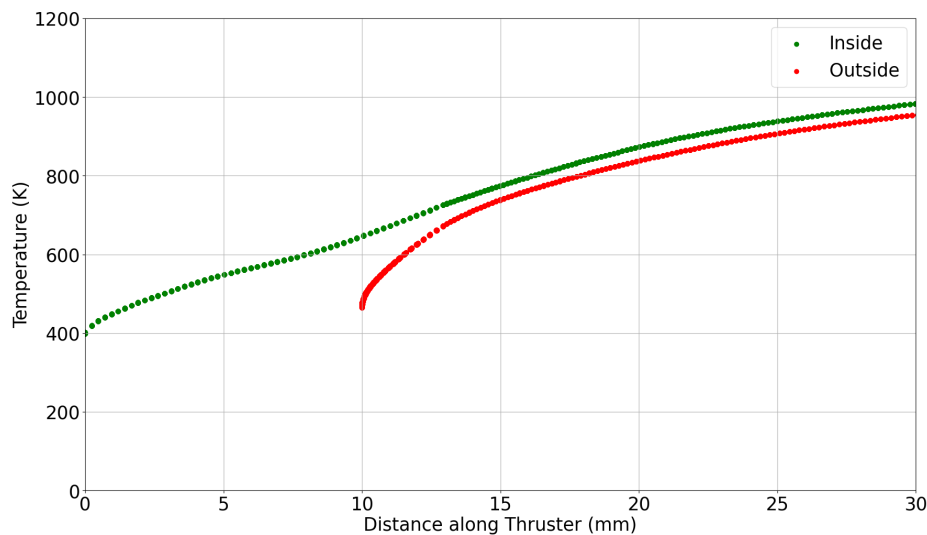


**Figure 5.23:** Temperature contour for the inside and outside of the flange section, section A

Looking at Figure 5.23, from 10 mm to roughly 13 mm, the temperature of the outside surface starts to converge from that of the inner surface. All whilst the temperature of the inner surface is always higher than the outer due to the direct exposure to the combustion gases. This divergence is attributed to the curve section being physically further away from the inner surface of the flange. This curved section directly correlates to the 3mm curved blend that connects the flange to the chamber body. This can be seen to show a greater temperature difference at that specific axial distance, but one must also remember that there is more material due to the 3 mm curved edge at that axial distance as well.
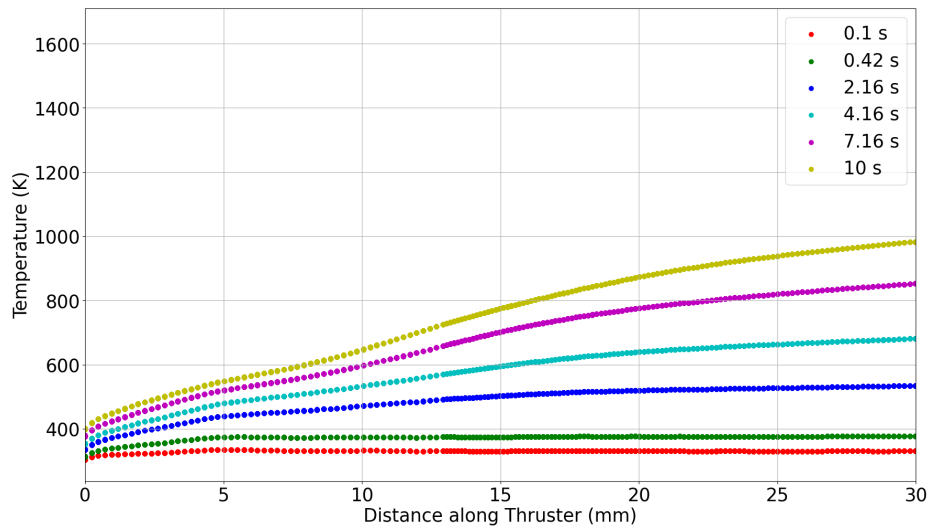
**Figure 5.24:** Temperature contours for section A inner surface over time

Figure 5.24 show that as expected the temperature contours show progressively higher temperatures with time. The temperature contours converge to one another closer to 0 mm as the highest convection location, the nozzle, is further downstream. This physically makes sense as it takes time for energy to move upstream the nozzle walls and the sections furthest away would take the longest.

## 5.3.2. Structural

The structural analysis of the flange section is purposefully separated from the nozzle and most of the chamber section because of the many added complexities that were introduced in the complex model. The complex model focused heavily on relieving stresses in the flange section by more accurately modelling the flange connection to a surface or body. A similar stress analysis to that seen on the nozzle is performed for the flange.
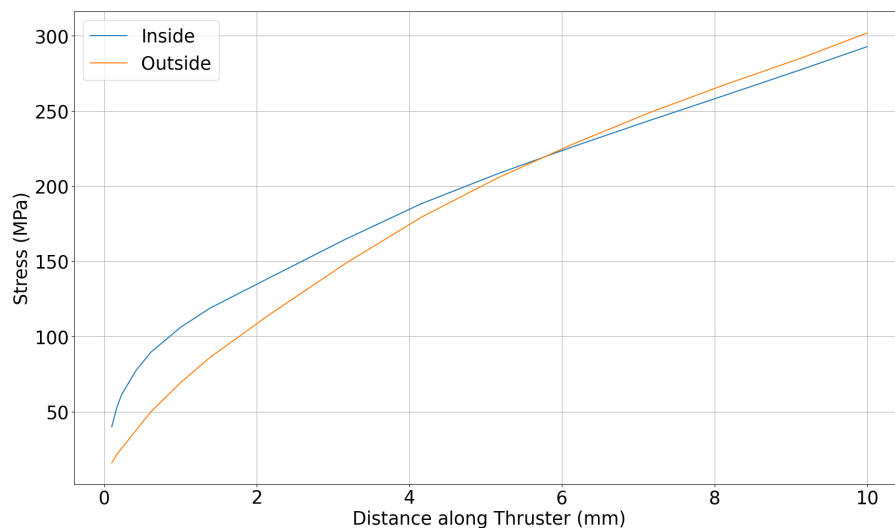


**Figure 5.25:** Max stresses at the flange for inside and outside the thruster

from Figure 5.25, the stresses in the flange show a consistent increase over time. The stress at the flange on the inside, the very beginning of the chamber, is highest until 5.77 seconds, after which the stresses at the curved edges on the outside of the chamber become more dominant.
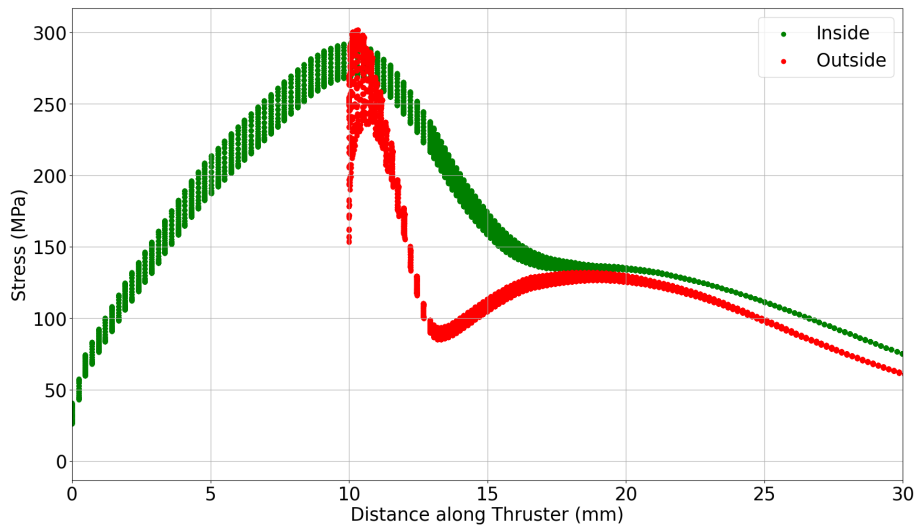


**Figure 5.26:** Stress contour at 10 seconds for the flange section

Figure 5.26 shows the stress contour at the end of 10 seconds of operational time. It can be seen that the stresses in the flange section are much higher than those observed in the nozzle and chamber sections.
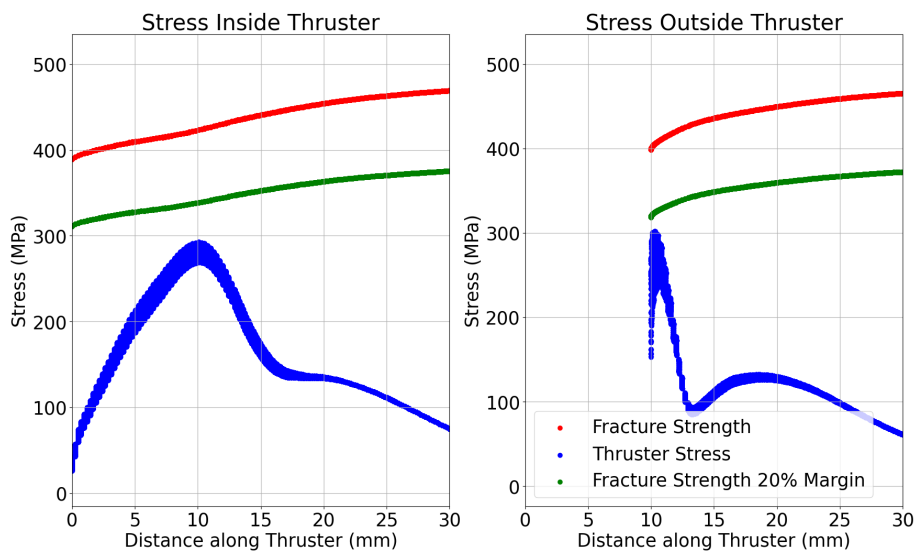


**Figure 5.27:** Stress contour and flexural strength limit at 10 seconds. The inside of the flange is on the left and the outside is on the right

Figure 5.27 shows that the stresses observed in the thruster are always within the fracture strength margin of the material and will not suddenly fracture when operating under these conditions. The stress is however extremely high, giving very good reason to believe that operating for extended periods, though very unlikely, may lead to sudden fractures. A figure to show the stress margin over time concerning the flange stresses is given below.
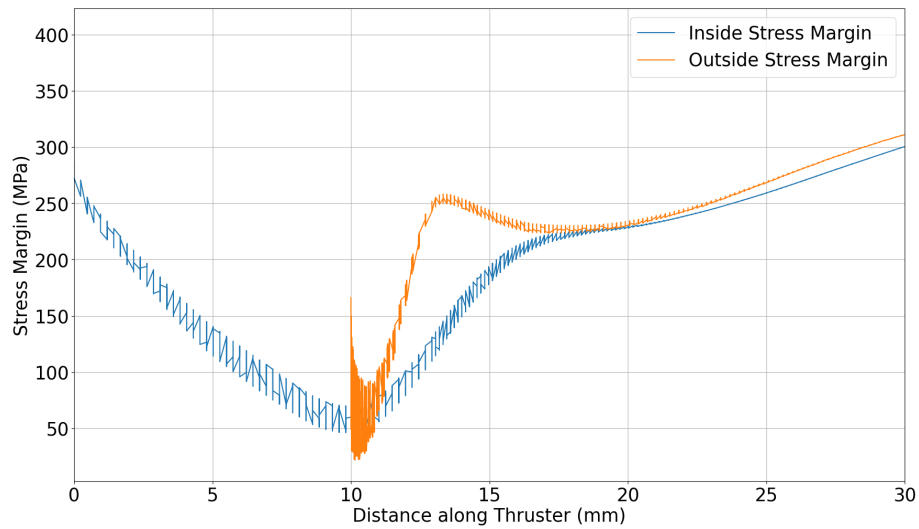
**Figure 5.28:** Stress Margin of the flange at 10 seconds

Figure 5.28 shows the stress margin, again it must be noted that the stress margin finds the amount of buffer stress based on axial position. Since temperature varies along the axial potion of the nozzle, the flexural strength does as well. Yet as opposed to the results seen in the nozzle section, the outer flange surface margin dips below that of the inner surface at the curved 3 mm edge section.
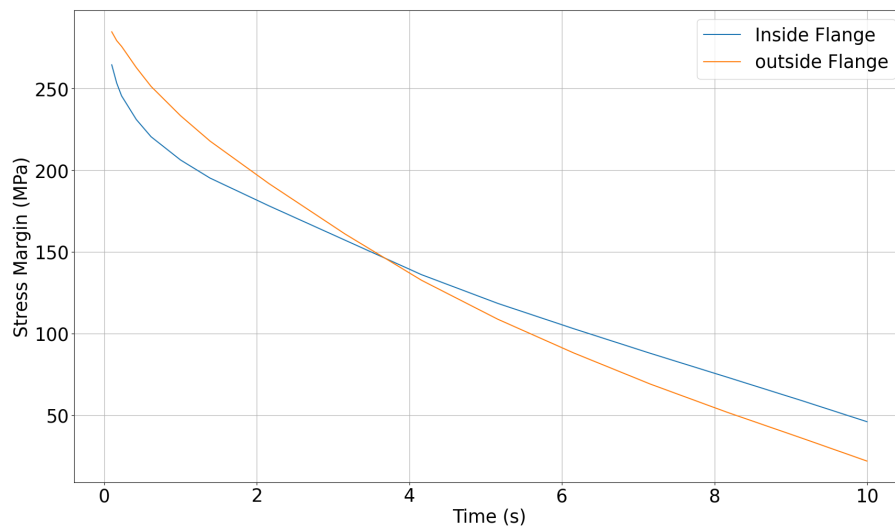


**Figure 5.29:** Stress Margin throughout operation for the flange

Figure 5.29 shows that with material degradation over time, the stress margin outside the nozzle drops below that inside after 3.68 seconds. This suggests that although outer stresses are lower than inner stresses between 3.68 and 5.77 seconds, the outer stresses become more critical for continuous operation beyond 3.68 seconds.
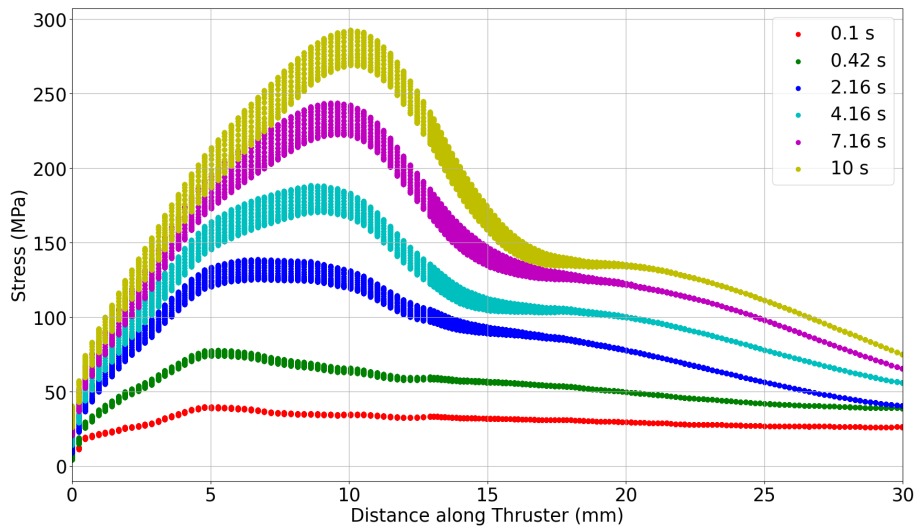
**Figure 5.30:** Stress contour of the inside at the flange over time

Figure 5.30 shows how the stress contour at the flange continuously increases over time and the peak stress shifts more forward as time progresses. Another observation is that the stress contours are not perfect thin lines, rather they are bands of stress. This band of stress occurs because the surface is being probed for stress values and there are multiple nodes with the same axial position. This can be interpreted as a stress uncertainty, however, this is most likely due to the beam elements causing oscillatory stresses because of localised additional stiffness in proximity to the bolt locations.
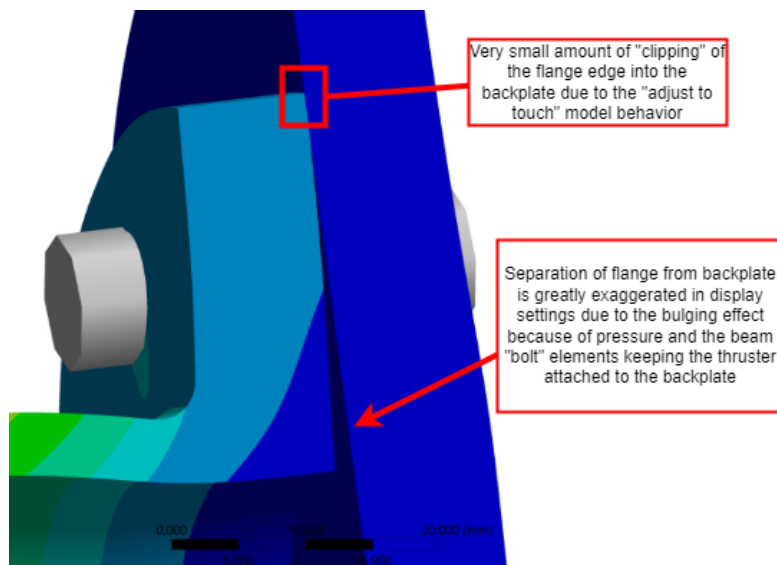


**Figure 5.31:** Zoom in on the Adjust to touch effect on the model

Figure 5.31 shows a close-up of the contact area between the back plate and the flange. The enabled "adjust to touch" parameter caused minor clipping between the flange edge and the back plate, which is acceptable due to its minimal size. The lower flange does not adhere to the back plate, a detail exaggerated in the figure. The flange is likely to experience thermal stress cracks because of operation, as other damage mechanisms are unlikely to have an effect here. While a more complex model might show lower stresses, this assumption cannot be confirmed without sufficient data. With this in mind, if the thruster would fail exclusively due to the repeated thermal shock loads, then failure would occur

sooner with prolonged operation in this region given the high stresses in this model.

### 5.3.3. Strain

Strain near the flange is a more critical factor as it will distinguish more clearly between thermal and mechanical-based stresses. This is mostly because the temperature rise in this region is not so much as to have great differences between the thermal and equivalent strains in all regions.
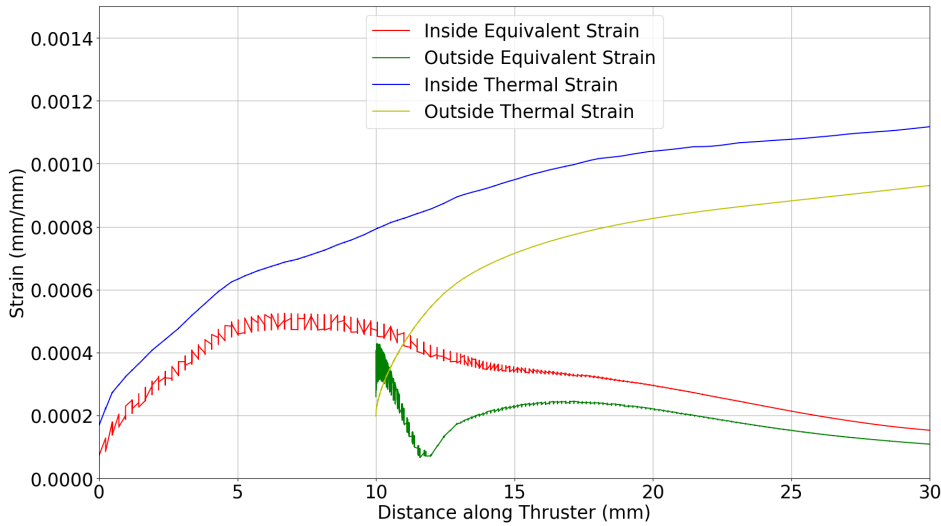


**Figure 5.32:** Strains for section A at peak stress time of 2.16 seconds

Figure 5.32 shows that the equivalent strain is always lower than that of the thermal strain for the inner surface of the flange. The outer surface however shows that the equivalent strain is higher than the thermal strain. This section is the 3 mm curved edge section of the flange on the outside. The higher equivalent strain here symbolised that thermal effects are not accounting for all the stresses seen here, rather there are other factors at play. The 3 mm curve is expected to be too sharp thus introducing geometrical stress concentration in that region. In essence, pinching the the thruster at that region. This region likely has compressive stresses that arise from this pinching.
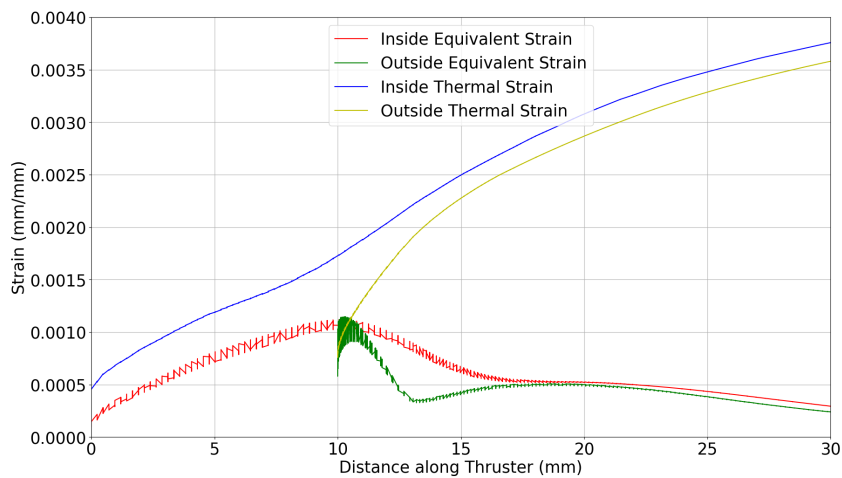


**Figure 5.33:** Strains for section A at 10 seconds

Figure 5.33 show similar behaviour as at 2.16 seconds. the geometrical stress concentration due to the relatively sharp curved edge is still present and pronounced enough on the inside. This can serve indication that to reduce stresses in this region, a less sharp edge can instead be used, perhaps increased by 1 to 2 mm in curvature. This would only serve as a way to keep absolute stress lower than that seen on the inside of the flange.

In regards to stress margin, it may not eliminate it but simply postpone it to occur later than 3.68 seconds. Once testing has been done, operational parameters are duly fixed, and a decision can be made as to whether this flange section should even be addressed. If it should, a slight adjustment to the design can be made with minimal effort.

### 5.3.4. Flange Damage over Time

The flange also experiences different levels of damage over time, with the flange being particularly susceptible to prolonged operation, based on the obtained results. The main damage that will be endured by the flange section is thermal stress cracks and cracks caused by repeated cyclic operation and fatigue over time.
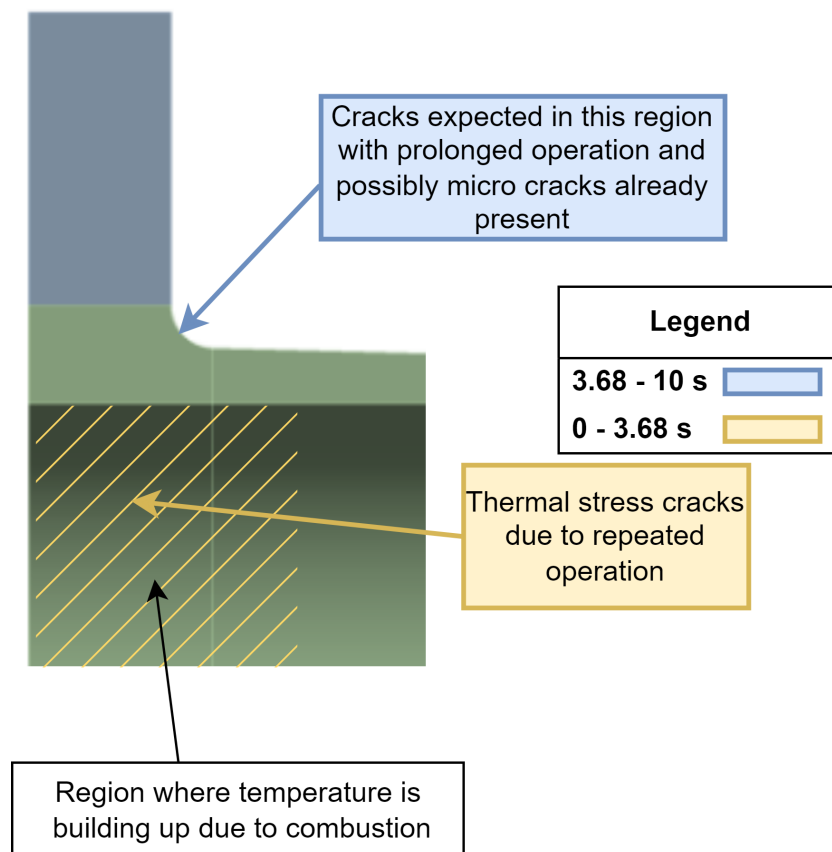


**Figure 5.34:** Flange Operation Effects. The time frames represent which area would experience more damage based on the operation duration that is chosen for a thrusting cycle.

Figure 5.34 shows the main two locations of expected failure given prolonged thruster operation. 3.68 seconds is the cut-off point where the likelihood of the outside curved edge failing starts to become more significant than that of the inside curve. Oxidation is not expected to occur as the temperature does not exceed 985K at 30 mm at 10 seconds at the flange section, assuming oxidation only begins at 995 K as seen in the previous section for the damage in sections B and C.
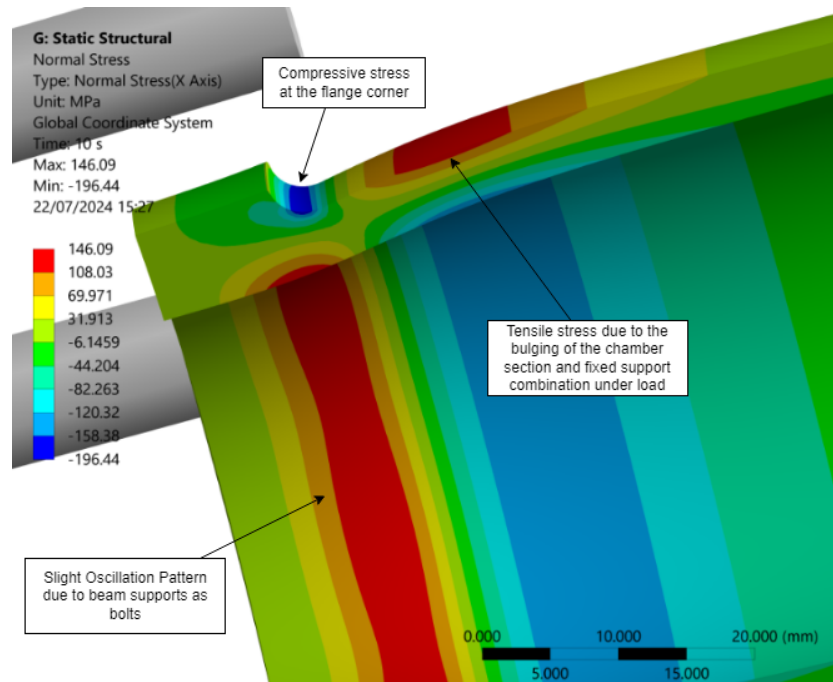
**Figure 5.35:** Zoom in on Flange behaviour during simulations

The figure above, Figure 5.35 shows that the stress cracks on the outer side are not the only considerations, as the indie of the thruster chamber surface is also subject to high thermal stresses and therefore stress cracks. This entire region of the thruster, from 0 to 30 mm is very likely to experience failure due to thermal shocks only and be the primary reason the thruster would fail in operation. The reason other effects such as erosion, oxidation, and ablation are not of concern in this region is that the propellants and oxidiser are still reacting in the chamber and the high-speed flow which generated the thruster has not been fully formed yet in this section which can be considered as the beginning of the thruster chamber, shaded yellow in Figure 5.21.

If the operating time then exceeds 5.77 seconds, the stresses on the outside of the thruster are greater than those on the inside of the thruster, seen in Figure 5.25. This higher stress occurs due to a stress ring at the flange to thruster chamber curved surface connection, the blue compressive stress region in Figure 5.35. But again, since the stress margin is what is critical to damage degradation, the stress ring on the outside of the thruster becomes the critical region after just 3.68 seconds of operation.

## 5.4. Optimum Thruster

The thruster as a whole is now discussed. This aims to connect sections B and C, the nozzle, to section A, the flange. With all sections now combined, the overall effect on the thruster can be discussed. This will essentially aim to draw a connection between critical locations in the thruster and times when they are critical. This section also aims to highlight section B which acts as a connection between the most extreme zones where very high temperatures or stresses are seen, sections A and C.

### 5.4.1. Thermal

The temperature contours of the inner and outer surfaces of the whole thruster are used to facilitate discussion. The flange section, which gets thicker is to have a direct effect on the temperature slope. Since linear variation in thickness occurs only in sections A and B, then this slope is expected to be higher than that compared to a 4 mm uniform thickness base thruster.
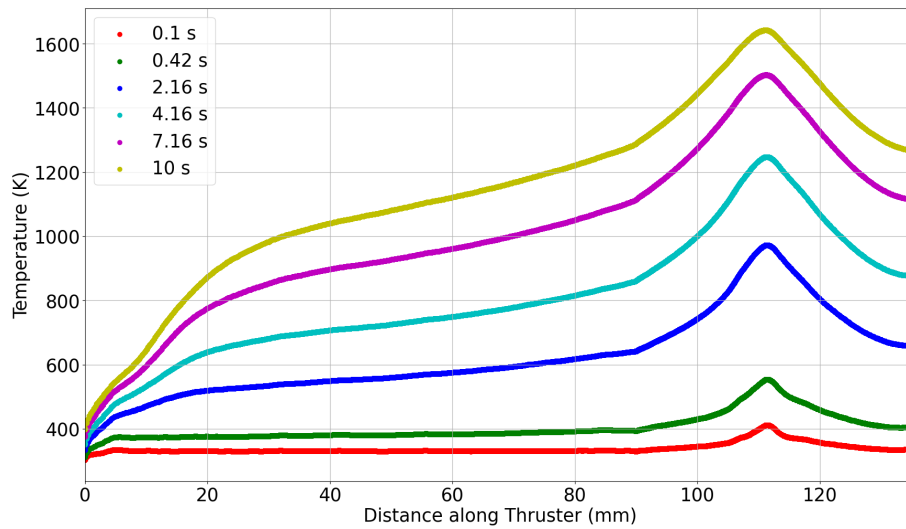
**Figure 5.36:** Temperature contours of the inner surface for the whole thruster

Figure 5.36 shows the surface exposed to combustion gases. The chamber walls transfer heat from the high-energy nozzle walls of section C to areas with lower convection. The temperature slope likely depends on wall thickness. Thicker walls, approaching 0 mm, need more time to heat up, making the temperature slope steeper. The slight kink around 10 mm likely results from energy having more difficulty heating the material, as it transfers to the bulk of the flange, the blue area in Figure 5.34, rather than just a few mm across in thickness.
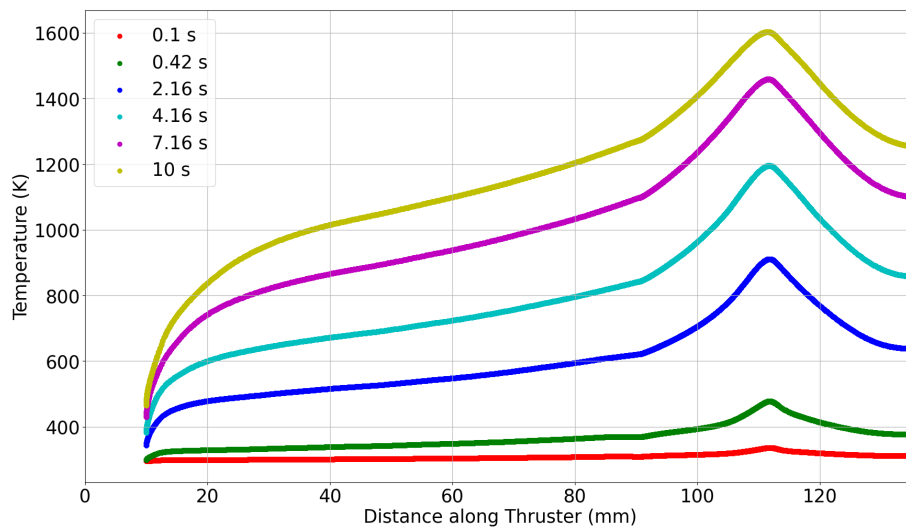


**Figure 5.37:** Temperature contours of the outer surface for the whole thruster

Figure 5.37 has lower temperatures at every single axial position compared to the previous graph. A temperature gradient graph reveals more insight into temperature behaviour over time, as seen below.
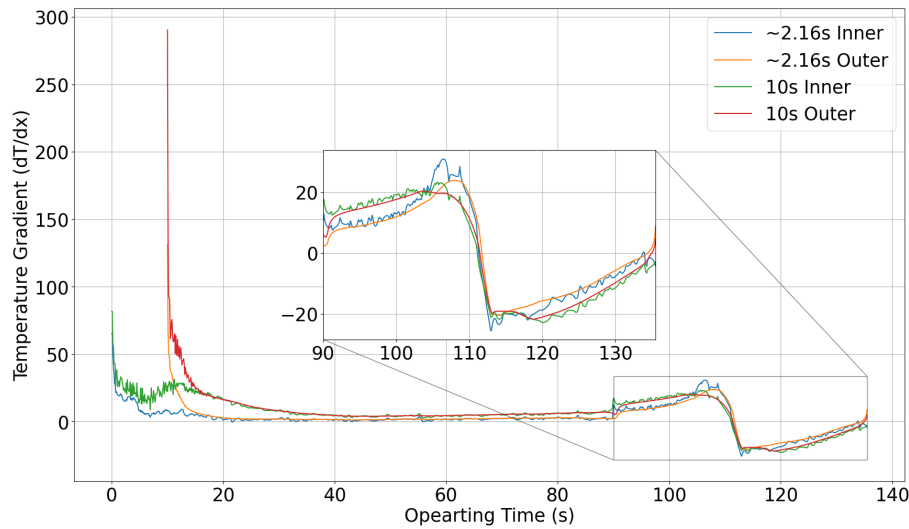
**Figure 5.38:** Temperature Gradient Contour for the inner and outer surface at 2.16 and 10 seconds.

Figure 5.38 shows that the temperature gradient near the flange drops more sharply at 2.16 seconds compared to 10 seconds, indicating less temperature progression early in operation. At 10 seconds, the gradient is higher throughout section B, confirming the increasing slope seen in the temperature contours. The zoomed-in view reveals that the peak temperature gradient in the convergent section is lower at 10 seconds than at 2.16 seconds. This occurs because thermal energy has not fully dissipated through the nozzle, resulting in a higher peak gradient at 2.16 seconds and a lower average gradient as thermal energy transfers from section B to section C. This trend aligns with physical expectations.

## 5.4.2. Structural
The peak stress throughout the nozzle over time is investigated in this subsection. This combines the stress in sections A, B, and C to see which sections experience higher stresses at a point in time.
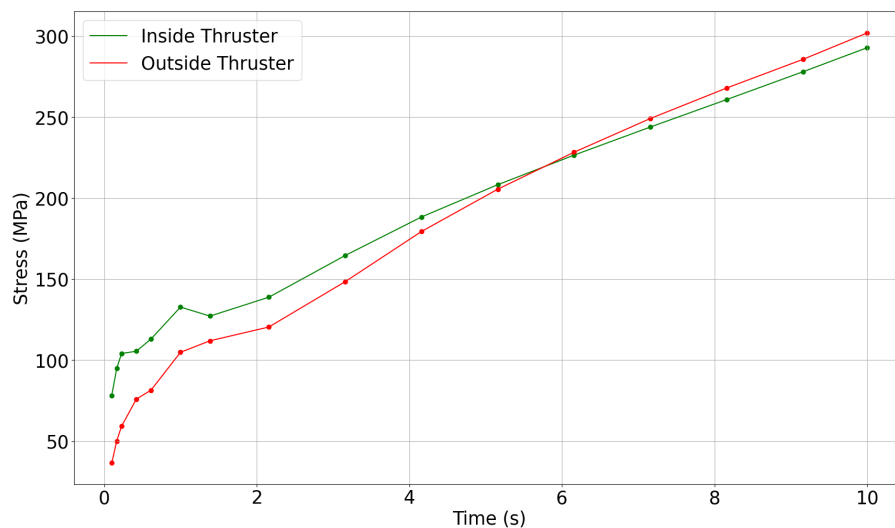


**Figure 5.39:** Maximum Stress over the entire thruster throughout operation

Taking Figure 5.39, it can be seen that the flange stress overtakes the nozzle stresses at 2.16 seconds of burn time, though 2.16 seconds is when the nozzle stress is at maximum. The flange stresses on the inside are already higher at 1.84 seconds. The red line also shows that the stress on the outer side of the flange at the 3 mm curvature is the highest stress that will be seen by the thruster.
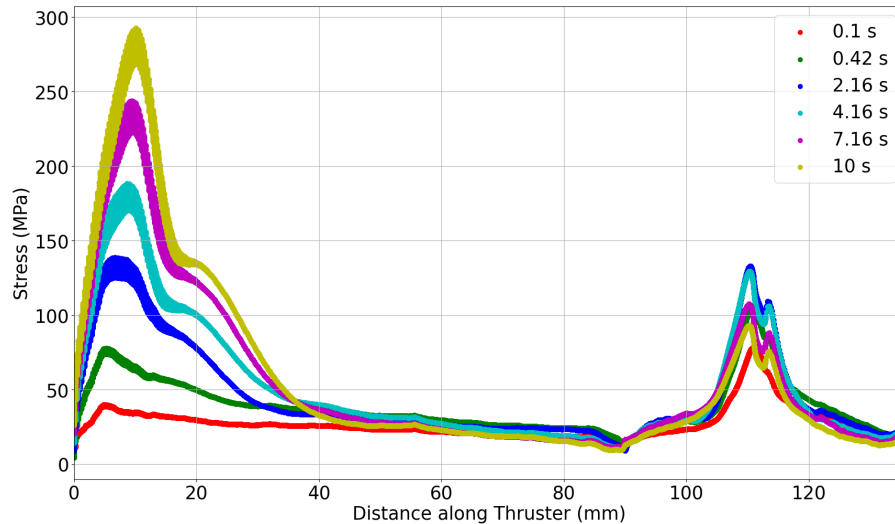


**Figure 5.40:** Stress contours of the inner surface for the whole thruster

Figure 5.40 highlights how quickly the inner surface stresses near the flange develop compared to the nozzle stresses. Where the blue line, 2.16 seconds, which represents the peak stress in the nozzle is already contested by the absolute stresses closer to the flange. This further highlights the importance of adequate modelling of the flange connecting section.
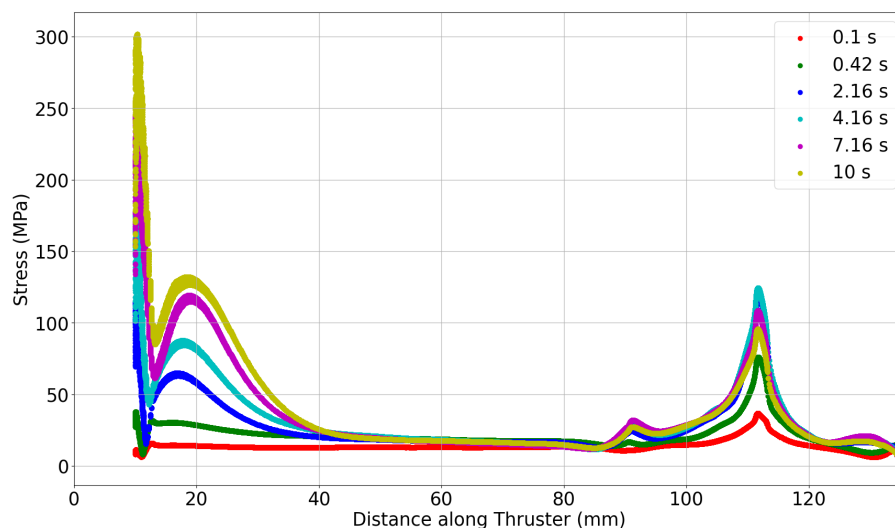


**Figure 5.41:** Stress contours of the outer surface for the whole thruster

Figure 5.41 shows that flange stresses increase more slowly than outer nozzle stresses. The sharp peak near 10 mm results from the 3 mm curved edge. More detailed data on the thruster's attachment

would refine this analysis. Currently, the attachment used likely overestimates stresses but is adequate for assessing immediate fracture risks. Though stresses are expected to be lower, it is uncertain by how much due to various factors, limiting the analysis to evaluating immediate fracture potential. A diagram showing the progression of stress through the entire thruster is given in Figure 5.42. This can be used to visualise the rapid stress rise in the nozzle compared to the flange at different time steps from those in contour graphs.
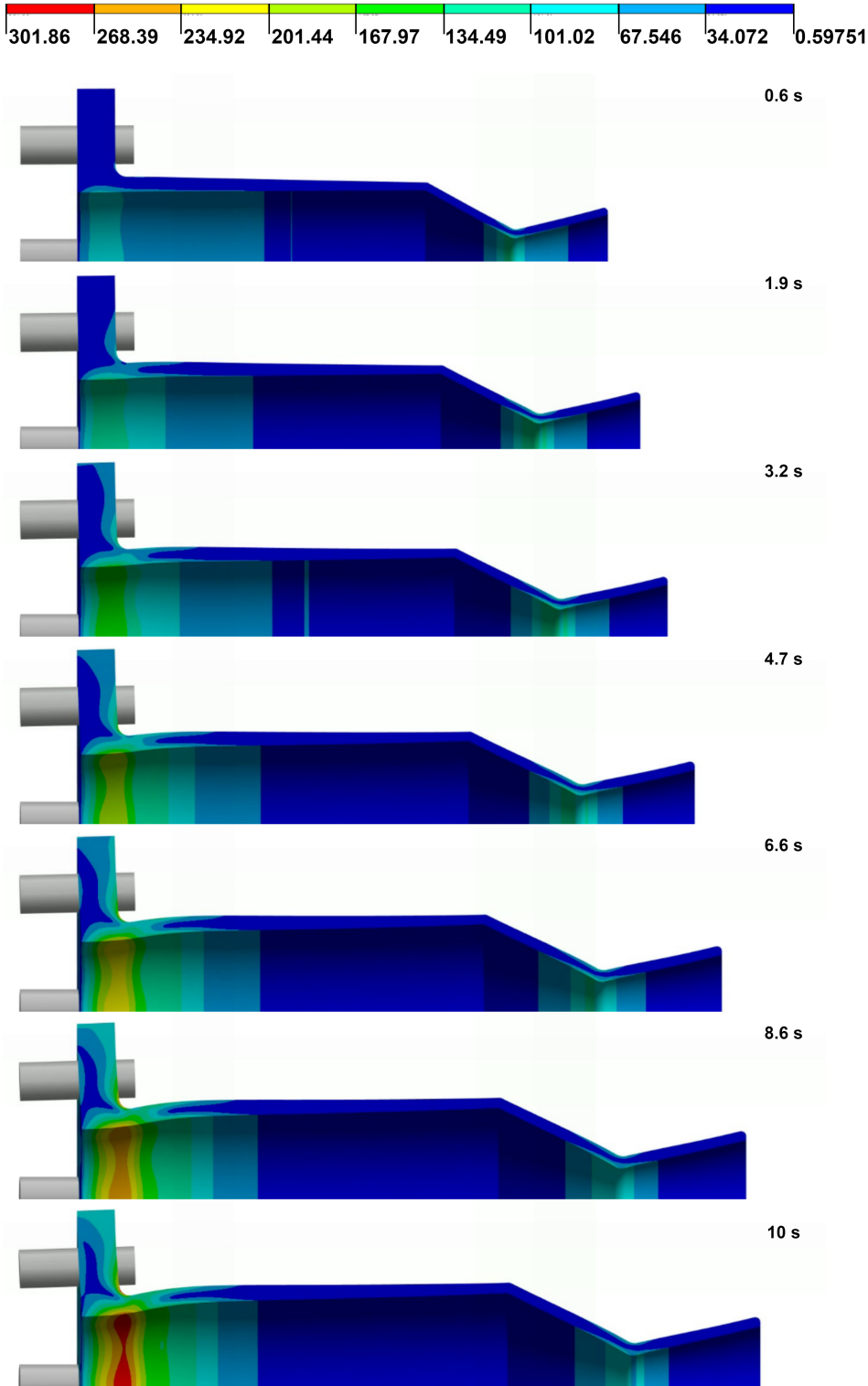


**Figure 5.42:** Snapshots of Stress progression through the thruster during Operation, the stress is given in MPa

### 5.4.3. Strain

The strains of all the sections are combined and the deflection of the thruster will also be discussed.
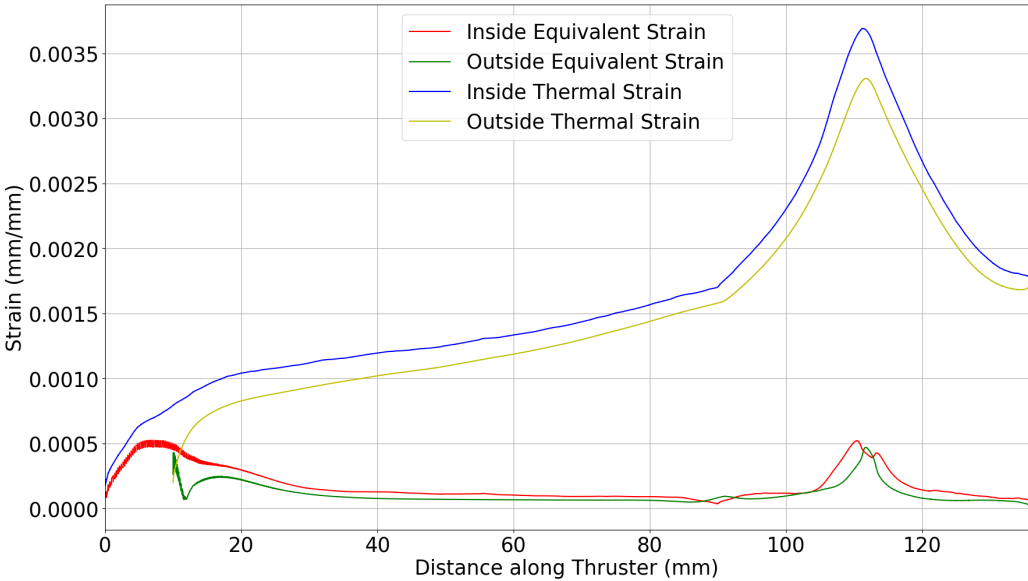


**Figure 5.43:** Strains for the whole thruster at peak stress time of 2.16 seconds

Thermal strain can be seen to be more consequential closer to the throat in Figure 5.43. Where the flange may have geometry acting in a more critical role in determining where stresses originate from, this only applies close to 10 mm.
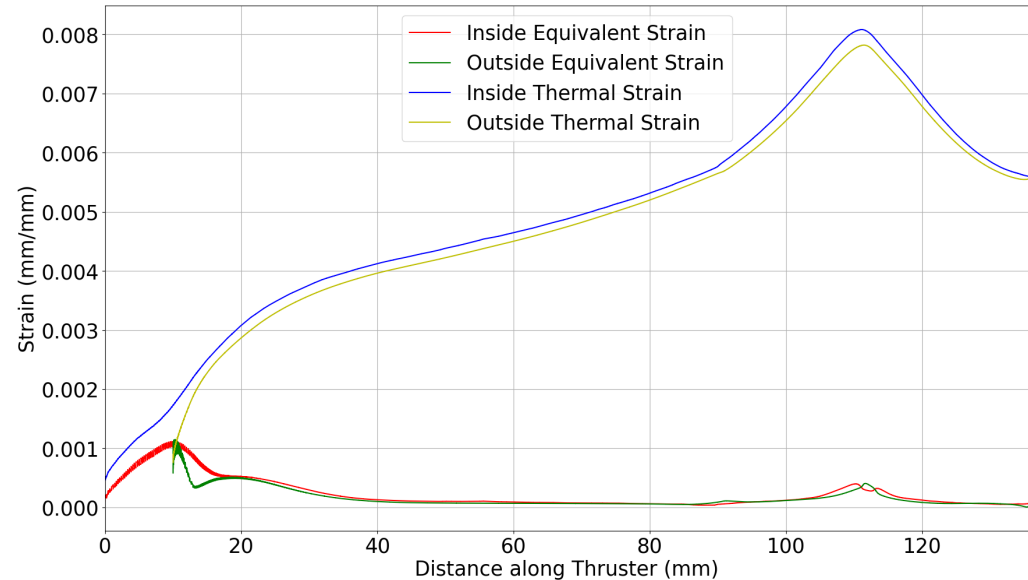


**Figure 5.44:** Strains for the whole thruster at 10 seconds

Figure 5.44 shows that with the prolonged operation, at 10 seconds, the peak nozzle thermal strain

becomes nearly 16 times higher than that of the equivalent strain compared to the factor of about 7 times greater at the throat while the flange section has a factor of nearly 2 times, in Figure 5.43. Yet again, though the stresses decrease, it is expected that this larger gap is due to the dr op in the material Young's modulus with the much higher temperatures seen at 10 seconds. A lower Young's modulus makes it easier for the material to deform, thus a lower thermal stress, but a much higher thermal strain would mean that Young's modulus degrades much faster than the thermal strain increase, eventually leading to a lower thermal stress at 10 seconds. In Figure 5.44, the flange section strain also sees an increase to nearly 3.5 times. The increase is less than that of the nozzle presumably again due to a combination of the temperatures not rising as fast in section A compared to section C and a lower degradtaion in material Young's modulus as well.



(a) Defection in X direction



(b) Radial Deflection
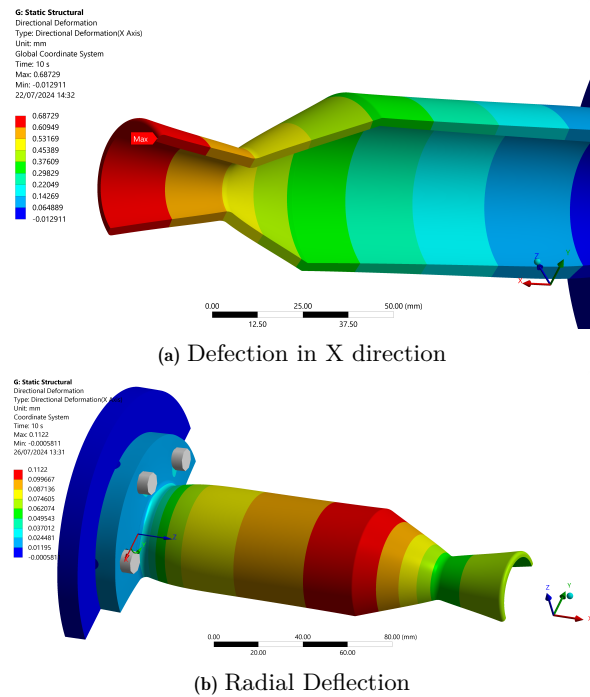
**Figure 5.45:** Optimum Design Deflection at 10s

Figure 5.45a shows the as-expected deformation that occurs in the axial direction. The deformation at the end of 10 seconds is 0.68729 mm at the thruster exit. Given the total thruster length of 135.72 mm, this is a 0.51% increase in the thruster length. The deflection perpendicular to the x-axis also shows expected behaviour, the highest deflection is at the very start of the convergent section.

The aforementioned can be attributed partially to the fact that the pressure is highest in the thruster chamber until the start of the convergent section and then starts to decrease. So this higher pressure normal to the surface at the convergent section causes deformations to be seen as highest there. The y deflection is also higher, slightly more downstream the flange 3 mm curved section, This can cause to justify why the axial stress figure sen earlier, Figure 5.35, may show compressive stresses and tensile stresses due to the pinching effect observed at the flange.

Additionally, the deformations are largely due to the thermal strain causing the thruster to expand thermally. Hence the difficulty in trying to determine exactly how much of the thermal strain results in thermal expansion and how much of this thermal expansion is restricted which leads to thermal stresses. Though this is ratio may not be given, it is still well understood that thermal stresses are the main source contributor to the total stresses experienced by a thruster during operation.

### 5.4.4. Damage

Although stresses are critical in determining critical locations and damage degradation over time, the absolute stress is not what is most important in this case, but rather the stress margin given the flexural strength dependence on temperature. Figure 5.46 shows the stress margin at 4 of the most critical locations in the thruster.
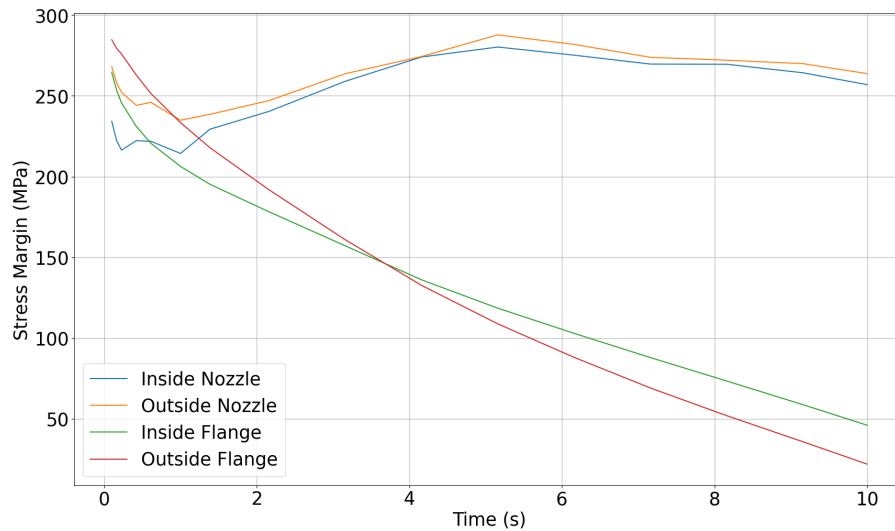


**Figure 5.46:** The stress margins for all 4 locations of interest in the thruster

It must be noted that the location of these stress cracks and which ones would lead to failure varies heavily on the operating time. After 2.16 seconds, the stress cracks that occurred at the flange will be greater according to the higher absolute stresses seen at the flange. But in reality, since the degradation rather depends on the stress margin and not the absolute magnitude of the stress, the flange becomes the more critical area after just 0.59 seconds of operation. Essentially, if failure occurs due to thermal stress cracks, below 0.59 seconds operation time, failure would occur in the nozzle convergent section near the throat, until 3.68 seconds, failure would occur on the inside of the thruster near at 0 to 30 mm axial position, and after 3.68 seconds, the outer stress ring around the flange section is where thermal stress cracks would be most prevalent and failure would occur.

Since it is highly expected that the thruster would operate for very short bursts, in a few tenths of a second to less than 3 seconds, the nozzle section is the most critical region. Though after 0.59 seconds the inside of the thruster may experience more degradation, operations greater than 0.59 seconds may be seen as few in between for this class of thruster and what it is made for. An operation greater than 3.68 seconds is extremely unlikely to occur and may happen just once in the entire lifespan of a thruster for a very special situation. Figure 5.46 can be used to give the most critical damage that would occur given the time frame that a thruster is used continuously. Based on the most preferred thrust duration throughout the whole thruster lifetime, the list below provides the most critical damage to expect over time.

- **0 s – 0.59 s**: The most critical damage, in this case, would occur in the inside nozzle converge section near the throat. Effects such as ablation and erosion would be present, though very minimal. Over time, if failure would occur it would be due to the inside convergent section material properties deteriorating due to the thermal cycling over the thruster's operational life

- **0.59 s - 3.68 s**: If failure would occur, it would be due to thermal stress cracks over repeated cyclic loading that occur on the inside of the thruster very close to the flange, at roughly 10 mm in axial position.

- **3.68 s - 10 s**: Continuous operation in this time frame would cause the outer bend connecting the flange to the chamber body to be the most critical point. Failure is likely to occur due to

the cyclic loading increasing the potentially already present cracks during manufacturing or those created through cyclic thermal loading.
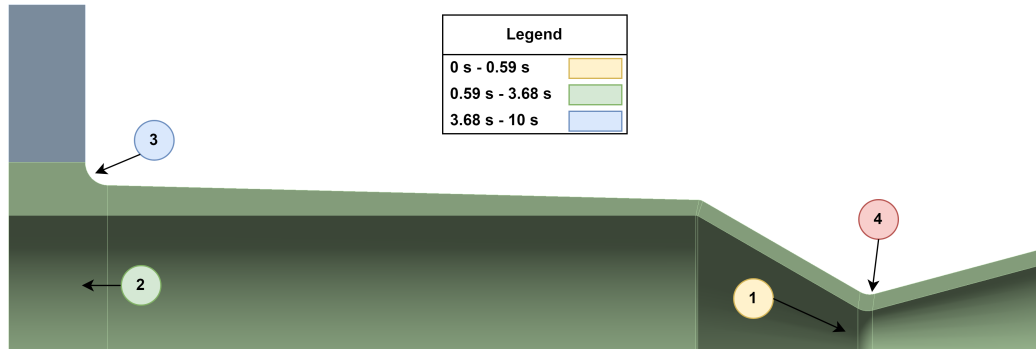


**Figure 5.47:** Based on a thrust duration, the area to withstand the most degradation can be seen in this figure

Figure 5.47 can be used to visually show the areas of interest referred to in the list. If the thruster could be used through a singular range of time frame throughout its entire lifetime, the figure can also be used to say where fracture would first occur. If however, the thruster operating time would vary greatly, then it becomes more difficult to specify which section of the 4 would fracture first. in the figure, the red-coloured area 4 is not in the legend because it will never be the location to fracture first.

## 5.5. Thruster Applicability

A 100 N class thruster of this size and weight is mainly used in orbit control manoeuvres, attitude control, de-orbiting, in-orbit docking, and orbit maintenance. [78] Since information on propellant consumption and volume and mass of auxiliary propulsion components are unknown, The thruster can be assumed to be able to be integrated into medium-sized spacecraft and larger. The thruster would operate in space and therefore have its extreme operating condition being the shadow of Earth, where the temperature gradient would be highest. In this analysis, however, ground operating conditions were considered, since thruster testing is the first thing that will be done before space testing and verification.

Space Mission Engineering - The New SMAD, can be used to determine what functions the in-space propulsion system is expected to perform and, therefore what the 100-N thruster in this thesis is expected to perform.[78] The SMAD book provides Delta-V ranges for each operation, except for attitude control, where pulse widths are given instead. The Delta-V ranges will be converted to operating times by assuming a 100 kg spacecraft using the below equation.

$$t = \frac{\Delta V \cdot m_{sc}}{F} \tag{5.4}$$

The above equation, Equation 5.4, is used to convert Delta-V to operation time. When it comes to Attitude Control, total impulse and a range of the number of impulses are given. These are used to convert to a range of operation times. If such numbers are not given, then the pulse width is simply used as an indicator of typical operation times for a single cycle or to perform a specific function once.

$$t = \frac{I_t}{F \cdot N_{pulses}} \tag{5.5}$$

With the above equations, the Delta-V and Impulses are converted and a table for the possible thrusting operations, operating times, and damage considerations is provided.

**Table 5.3:** Potential functions, their corresponding thrusting time for upper stage and in space propulsion [78]assuming a 100 kg spacecraft and constant 100 N thrust for operating time calculations

| Propulsion Function | Specific Function | Total Operating Time (s) |
|---|---|---|
| Orbit Raising | Drag Makeup | 60 - 500 s |
| | Re-Entry | 120 - 150 s |
| Orbit Maintenance | Orbit Correction | 15 - 75 s per year |
| | Station Keeping | 3 - 55 s pear year |
| | Survivability \Evasive Manoeuvres | 150 - 4600 s |
| Attitude Control | Acquisition Sun/Earth/Star | 0.005 - 0.05 s |
| | On-Orbit Normal Mode Control with 3-axis Stabilization | 0.01 - 0.25 s pulse width |
| | Precession Control | 0.007 - 0.07 s |
| | Momentum Management | 0.02 - 0.1 s pulse width |
| | 3-axis Control During Delta V | 0.05 - 0.2 s pulse width |

Using Table 5.3, the operational times can be related to the time frames described in the previous subsection, subsection 5.4.4. This was done by placing specific functions in operational time frames exactly as those which describe the most critical damage concerning how long the thruster is continuously operated. Additionally, the damage consideration column assumes the thruster *always* operates within that time frame for thrusting range. This is seen below.

**Table 5.4:** Propulsion Duration, related to in-space propulsion function and damage sustained

| Operational Duration | Specific Function | Damage Considerations |
|---|---|---|
| 0 - 0.59 s | • All *Attitude Control* operations are feasible in this range.<br>• *Station Keeping* and *Orbit Correction* for a total Delta-V of 30.68 m/s every year, assuming 1 burst of 0.59 seconds every week. Assuming *Station Keeping* and *Orbit Correction* to require periodic, not continuous, thrust burns. | Damage is most critical in the inner nozzle near the throat, where thermal cycling can cause material degradation and failure. This is area 1 in Figure 5.47 |

**Table 5.4 continued from previous page**

| Operational Duration | Specific Function | Damage Considerations |
|---|---|---|
| 0.59 - 3.68 s | • *Station Keeping* and *Orbit Correction*, which require more Delta-V than 30.68 m/s in a single year to perform assuming weekly pulses.<br>• *Drag Makeup* done weekly with thrust bursts of 3.68 seconds for a 1 year amounting to 191.36 s. This is 0.3 to 2.6 years worth of *Drag Makeup* assuming a weekly burst. | Failure would occur due to thermal stress cracks from repeated cyclic loading near the thruster's inside flange, approximately 10 mm in the axial position. This is area 2 in Figure 5.47 |
| 3.68 - 10 s | • *Re-Entry* and *Survivability/ Evasive Manoeuvres.* Both operations require a lot of impulse in a relatively short period, also putting the most strain on the thruster. | Continuous operation would make the outer bend near the flange the most critical point, with failure likely increasing from cyclic loading worsening potentially existing cracks. This is area 3 in Figure 5.47 |

The above table, Table 5.4, can be compared with the list created in subsection 5.4.4. Based on the type of operation that is desired to be performed, the expected time frame or thrust duration for a single cycle can be estimated. This time frame can then be used to determine which section of the thruster would experience the most degradation for a given operation.

# 6

# Conclusions and Recommendations

This chapter will aim to conclude and summarize all the answers to the research questions devised for this thesis. the conclusion section, section 6.1, will answer the research questions and give a definitive critical damage area and method for each operating time range. Additionally, these operating times can be related to actual functions that are expected to be performed by an in-space thruster. This would thereby allow one to determine what type of damage to expected based on the propulsion function chosen to be performed. Finally, recommendations for future iterations and improvements that can be made upon the work in this thesis can be discussed in section 6.2.

## 6.1. Conclusion

The answers to the Research question and the sub-question will be addressed directly in this section. The sub-questions answers are provided below.

- **Question 1.1:** Based on similar FEA simulations, interior convection from CFD to Bartz was taken and outer surface radiation and convection were also inputted. Ground Operation was taken as the CFD results referred to the ground operating case, and the first test a thruster will go through may very well be in ambient condition on the ground. The thermal loads experienced by the thruster in this thesis were convection from the combustion gases on the inner surface of the thruster which peaked at $1500\ Wm-2K-1$ at the throat. Additionally, a constant emissivity of 0.8 and convection of 5 $Wm-2K-1$ was taken to characterise heat loss to the surrounding environment when operating on Ground conditions.

- **Question 1.2:** The structural loads on the thruster were of two sources, pressure from the combustion gases, which was imported from the CFD and taken to be the differential between the environment pressure and the combustion gases, thus the mechanical pressure load acting on the thruster interior. Additionally, thermal expansion loads taken during the transient thermal case are also inputted. A steel back plate and beam elements were used to attach the thruster flange and restrict movement to relieve stresses arising from the direct fixing of the flange, stresses identified as stress singularities.

- **Question 1.3:** The 100 N thruster is mainly used for in-space propulsion capabilities. The main categories are Orbit Control, Orbit Maintenance and Attitude Control. The thruster is much more suited for Attitude Control and limited Orbit Maintenance as discussed in subsection 5.4.4, because these lower duration operations put less stress on the thruster thus increasing the number of cycles to failure. Operating in the shadow of the earth is expected to cause larger thermal stress shocks, thus lower cycles, it is undetermined how much the effect is due to a lack of morphological analysis on this specific UHTCMC composition.

- **Question 2.1:** The temperatures peak at the throat where the highest temperature is 1643 K at 10 seconds on the inner surface. Stresses in the Nozzle peak at 2.16 seconds on the inner surface at peak stress of 133 MPa. The inner and outer surfaces at the flange both peak at 10 seconds at 292 MPa and 302 MPa respectively. From 0 to 1.84 seconds, the stress at the inner nozzle throat is highest, from 1.84 to 5.77 seconds, the inner flange surface has the highest stress, and from 5.77 to 10 seconds, the outer flange bend experiences the highest stress.

- **Question 2.2:** The thruster elongates in the x direction by 0.51%, 0.69 mm at 10 seconds and in the y direction by 0.11 mm. The y deflection peak occurs at the start of the convergent section. The y deflection also shows the bulging effect near the flange, which causes compressive loads to occur on the outer bend and stress concentration due to the restrictiveness of the geometry.
- **Question 2.3:** The Optimum thickness was found to be the configuration which has a linear tapering thickness from 4 mm to 2 mm at the beginning of the convergent section, section C. Section C then has a uniform thickness of 2 mm. The mass is 0.31 Kg.
- **Question 3.1:** Erosion and ablation, though very limited if any as seen by the results of different papers using UHTCMC of different volume fractions, are expected to occur throughout the entire duration of thrusting. Oxidation effects will need much further investigation given the dependence on material composition, especially as it may occur as soon as 2.3 seconds. Thermal stress cracks are expected to occur on the inner throat surface and outer stress ring. Thermal stress cracks are also expected to occur on the inner surface of the flange and at the outer bend of the flange, where the rapid contraction and expansion, as well as geometrical factors, of the thruster, may cause further degradation in these areas.
- **Question 3.2:** No preventative measures are needed for the thruster. UHTCs are used as protective coatings because of their very good durability and resistance to damage. UHTCMCs have also been seen to combine the properties of UHTCs with CMCs, which provide better fracture toughness and specific weight. Given that the thruster is made entirely of UHTCMC, it is unnecessary to protect it further.
- **Question 3.3:** Damage effects and when they are active refer to the stress margin rather than absolute stress. From 0 to 0.59 seconds, the inner throat surface is at the highest risk of fracture and experiences the most degradation. Operation from 0.59 seconds to 3.68 seconds has the inner surface near the flange to be the most critical. Operation longer than 3.68 up to 10 seconds determines that the outer bend of 3mm at the flange is the most critical area where fracture may occur.

## 6.2. Future Work

There are many ways in which this thesis can be improved upon. This section will aim to outline as many as possible. The recommendations will be ordered from the easiest to perform as long to the most difficult and potentially time-consuming.

The first recommendation is to re-run the simulations with actual material properties that are obtained through testing. The current way material properties were estimated is using formulas and material properties of the UHTCMC constituents. This method can be seen as idealised and does not take into account the manufacturing methods, porosity of the material, or even complications due to the addition of fibres. Since the manufacturing of the material and determining its material properties is not explicitly done in this thesis and instead done by another colleague, waiting until the material has been manufactured, and tested, and its properties measured with statistical significance is a good move. This gives higher confidence in the FEA simulations and results. This does come at the cost of time and money since statistical significance implies many samples being made and tested.

The next recommendation is to obtain more information on how the thruster would be mounted onto a spacecraft or even a test bench. This would need information on the bolts used, surface roughness, and materials. This would also directly entail that more complex models would then be used, such as modelling the bolts as solid objects (head, shaft, etc) and even having frictional contacts between the bolt shaft with the flange holes and the flange with the back plate. This comes at a greater computational cost and a much greater effort to be placed into verifying and validating that the connection has been correctly modelled. An observation that may be seen is that the stresses in the flange section, from 0 to 30 mm, are much less than those seen here in the results.

Another recommendation is to re-run the simulations with better CFD results and have a CFD-FEA feedback loop. When running the initial CFD used in the current FEA, it was found that the specific heat of the walls could not be set to vary with temperature. Trying to set the wall properties to vary with temperature for the CFD could change the convection conditions. Having a feedback loop built

into the CFD and FEA could also improve the results. The wall temperature results found in the FEA could be fed back into the CFD and the simulations rerun. This feedback would result in a convergence in wall temperatures from all the simulations being run. This would come at a great computational cost, since running this feedback loop multiple times until the convergence criteria are met may take days of continuous running.

The final recommendation is to investigate the material morphology of the particular UHTCMC. This is very important when trying to assess crack formation and propagation during operation. Crack formation when in the proximity of the bonding region of carbon fibre and the UHTC and fluid-structure interaction is imperative for understating damage mechanisms and should be investigated in future work. Since the thruster is planned to be 3D printed in the longer run, microcracks and defects can better have their effects on the thruster lifetime described.

# References

[1]  ANSYS. *Stresses in pressure vessels Pre-Analysis and Start-Up — Lesson 2*. URL: `https://courses.ansys.com/index.php/courses/stresses-in-pressure-vessels/lessons/pre-analysis-start-up-lesson-2-9/` (visited on 06/12/2024).

[2]  Micheal Ashby, Hugh Shercliff, and David Cebon. *Material Engineering, Science, Processing and Deisgn*. 3rd ed. Oxford, United Kingdom: Elsevier, 2014.

[3]  D. R. BARTZ. "A Simple Equation for Rapid Estimation of Rocket Nozzle Convective Heat Transfer Coefficients". In: (1957). DOI: `http://arc.aiaa.org|DOI:10.2514/8.12572`.

[4]  B. Betti et al. "Development of Heat Transfer Correlations for LOX/CH4 Thrust Chambers". In: *6th EUROPEAN CONFERENCE FOR AEROSPACE SCIENCES* (2015).

[5]  Jon Binner et al. "Selection, processing, properties and applications of ultra-high temperature ceramic matrix composites, UHTCMCs – a review". In: *International Materials Reviews* 65.7 (Sept. 2019), pp. 389–444. DOI: `10.1080/09506608.2019.1652006`.

[6]  Luca Boccaletto and Jean-Paul Dussauge. "High-Performance Rocket Nozzle Concept". In: *Journal of Propulsion and Power* 26.5 (Sept. 2010), pp. 969–979. DOI: `10.2514/1.48904`.

[7]  Raviteja Boyanapalli et al. "Analysis of Composite De-Laval Nozzle Suitable for Rocket Applications". In: *International Journal of Innovative Technology and Exploring Engineering (IJITEE)* 2 (Apr. 2013).

[8]  A. Brown. "Rocket engine system loads". In: *Synthesis Lectures on Mechanical Engineering* (2022), pp. 131–150. DOI: `10.1007/978-3-031-18207-5_5`.

[9]  Andy Brown. *Structural Dynamics of Rocket Engines*. Jan. 2016.

[10]  Raffaele D'Elia et al. "Experimental analysis of SiC-based refractory concrete in hybrid rocket nozzles". In: *Acta Astronautica* 126 (Sept. 2016), pp. 168–177. DOI: `10.1016/j.actaastro.2016.04.034`.

[11]  Nanosats Database. *Launches with forecasts*. 2024. URL: `https://www.nanosats.eu/` (visited on 03/07/2024).

[12]  Dipesh Dhital et al. "A review of flaws and damage in space launch vehicles: Motors and engines". In: *Journal of Intelligent Material Systems and Structures* 25.5 (July 2013), pp. 524–540. DOI: `10.1177/1045389x13493360`.

[13]  ENGINEER4FREE. *Beam slope and deflection table*. URL: `https://www.engineer4free.com/extras/beam-slope-and-deflection-table` (visited on 07/07/2024).

[14]  Faserverbundwerkstoffe. *Chopped carbon fibre strands 6 mm (Forged carbon)*. URL: `https://www.r-g.de/en/art/21013706` (visited on 08/07/2024).

[15]  Ulrich Gotzig. "Challenges and Economic Benefits of Green Propellants for Satellite Propulsion". In: *7TH EUROPEAN CONFERENCE FOR AERONAUTICS AND SPACE SCIENCES (EUCASS)* (2015).

[16]  Chunfeng HU et al. "Microstructure and properties of ZrB2-SiC and HfB2-SiC composites fabricated by spark plasma sintering (SPS) using TaSi2 as sintering aid". In: *Journal of the Ceramic Society of Japan* 118.1383 (Jan. 2010), pp. 997–1001. DOI: `10.2109/jcersj2.118.997`.

[17]  HyperPhysics. *Linear Expansion*. URL: `http://hyperphysics.phy-astr.gsu.edu/hbase/thermo/thexp.html` (visited on 07/07/2024).

[18]  ANSYS Inc. *ANSYS 2023 R2 Element Reference*. July 2023.

[19]  M Iqbal et al. "Comparison of empirical correlations for the estimation of conjugate heat transfer in a thrust chamber". In: *Life Science Journal* 9 (July 2012).

[20]    Sanvito S. Jain N. "Specific set of recommendation for materials development in WP2 based on micro-models/DFT". In: (2017). URL: https://c3harme.eu/wp-content/uploads/%202018/02/C3_D3.7.pdf.

[21]    Craig A. Kluever. "Spaceflight Mechanics". In: *Encyclopedia of Physical Science and Technology (Third Edition)*. Ed. by Robert A. Meyers. Third Edition. New York: Academic Press, 2003, pp. 507–520. ISBN: 978-0-12-227410-7. DOI: https://doi.org/10.1016/B0-12-227410-5/00892-9. URL: https://www.sciencedirect.com/science/article/pii/B0122274105008929.

[22]    I. Krucińska and T. Stypka. "Direct measurement of the axial poisson's ratio of single carbon fibres". In: *Composites Science and Technology* 41 (1 1991), pp. 1–12. DOI: 10.1016/0266-3538(91)90049-u.

[23]    The University of Lahore. *Thermal Stresses-1 and the osmosis of financial*. URL: https://www.studocu.com/row/document/the-university-of-lahore/civil-engineering/thermal-stresses-1-and-the-osmosis-of-financial/22874126 (visited on 07/07/2024).

[24]    Linda Larsson and Saowanee Suphap. *Fluid Structure Interaction in a Rocket Nozzle*. Jan. 2006.

[25]    D. Liu et al. "Effects of thermal and pressure loads on structural deformation of liquid oxygen/methane engine combustion chamber". In: *Journal of Thermal Science and Technology* 15 (3 2020), JTST0022–JTST0022. DOI: 10.1299/jtst.2020jtst0022.

[26]    Ronald Loehman and Erica Corral. "Ultra High Temperature Ceramics for Hypersonic Vehicle Applications". In: (2006).

[27]    Manab Mallik et al. "Electrical and thermophysical properties of ZrB2 and HfB2 based composites". In: *Journal of the European Ceramic Society* 32.10 (2012), pp. 2545–2555. ISSN: 0955-2219. DOI: https://doi.org/10.1016/j.jeurceramsoc.2012.02.013. URL: https://www.sciencedirect.com/science/article/pii/S0955221912000763.

[28]    MIT. *Combined Conduction and Convection*. URL: https://web.mit.edu/16.unified/www/FALL/thermodynamics/notes/node123.html (visited on 07/07/2024).

[29]    MitsubishiChemical. *Carbon Chopped Fiber and Milled Fiber (Short Fiber)*. URL: https://www.m-chemical.co.jp/carbon-fiber/en/product/mid/ (visited on 06/06/2024).

[30]    E.V. Morozov and J.F.P. Pitot de la Beaujardiere. "Numerical simulation of the dynamic thermostructural response of a composite rocket nozzle throat". In: *Composite Structures* 91.4 (Dec. 2009), pp. 412–420. DOI: 10.1016/j.compstruct.2009.04.006.

[31]    Harish Mugutkar et al. "Design and Estimation of HTC in CD Nozzle using Bartz's Equation". In: *International Journal of Recent Technology and Engineering (IJRTE)* 8.6 (Mar. 2020), pp. 4942–4946. DOI: 10.35940/ijrte.f8960.038620.

[32]    S. Mungiguerra, G.D. Di Martino, and A. Cecere. "Arc-jet wind tunnel characterization of ultra-high-temperature ceramic matrix composites". In: *Corrosion Science* 149 (Apr. 2019), pp. 18–28. DOI: 10.1016/j.corsci.2018.12.039.

[33]    Stefano Mungiguerra et al. "Characterization of novel ceramic composites for rocket nozzles in high-temperature harsh environments". In: *International Journal of Heat and Mass Transfer* 163 (Dec. 2020), p. 120492. DOI: 10.1016/j.ijheatmasstransfer.2020.120492.

[34]    J. Paul Murugan et al. "Thermo-structural Analysis of Solid Rocket Scarfed Nozzle with Composite Ablative Liners for Crew Escape Solid Motor". In: *Advances in Astronautics Science and Technology* 1.1 (Aug. 2018), pp. 87–97. DOI: 10.1007/s42423-018-0020-6.

[35]    NASA. *Cosmic Background Explorer*. 2008. URL: https://lambda.gsfc.nasa.gov/product/cobe/ (visited on 03/11/2024).

[36]    NASA. *State-of-the-Art in Small Spacecraft Propulsion*. 2024. URL: https://www.nasa.gov/smallsat-institute/sst-soa/in-space_propulsion/#4.6.1 (visited on 03/07/2024).

[37]    J.H. Neilson and A. Gilchrist. "An experimental investigation into aspects of erosion in rocket motor tail nozzles". In: *Wear* 11.2 (Feb. 1968), pp. 123–143. DOI: 10.1016/0043-1648(68)90592-9.

[38]    Dewei Ni et al. "Advances in ultra-high temperature ceramics, composites, and coatings". In: *Journal of Advanced Ceramics* 11.1 (Dec. 2021), pp. 1–56. DOI: 10.1007/s40145-021-0550-6.

[39]  BARIŞ NİGAR. *ANALYSIS OF CRACK INITIATION AND PROPAGATION IN SOLID ROCKET MOTOR NOZZLE THROATS*. 2019.

[40]  Jan Östlund. *FLOW PROCESSES IN ROCKET ENGINE NOZZLES WITH FOCUS ON FLOW SEPARATION AND SIDE-LOADS*. 2002.

[41]  Heung-Bae Park and Byong-Whi Lee. "Effect of specimen thickness on fatigue crack growth rate". In: *Nuclear Engineering and Design* 197.1-2 (Apr. 2000), pp. 197–203. DOI: `10.1016/s0029-5493(99)00253-8`.

[42]  M. Patel, V. B. Prasad, and V. Jayaram. "Heat conduction mechanisms in hot pressed zrb2 and zrb2–sic composites". In: *Journal of the European Ceramic Society* 33 (10 2013), pp. 1615–1624. DOI: `10.1016/j.jeurceramsoc.2013.03.006`.

[43]  Manish Patel, V.V. Bhanu Prasad, and Vikram Jayaram. "Heat conduction mechanisms in hot pressed ZrB2 and ZrB2–SiC composites". In: *Journal of the European Ceramic Society* 33.10 (2013), pp. 1615–1624. ISSN: 0955-2219. DOI: `https://doi.org/10.1016/j.jeurceramsoc.2013.03.006`. URL: `https://www.sciencedirect.com/science/article/pii/S0955221913001441`.

[44]  Manish Patel et al. "Strength of hot pressed ZrB2–SiC composite after exposure to high temperatures (1000–1700 °C)". In: *Journal of the European Ceramic Society* 32.16 (Dec. 2012), pp. 4455–4467. DOI: `10.1016/j.jeurceramsoc.2012.06.025`.

[45]  Aniket Patil, Manoj Radle, and Biswadip Shome. "One-Dimensional Solar Heat Load Simulation Model for a Parked Car". In: vol. 2015. Apr. 2015. DOI: `10.4271/2015-01-0356`.

[46]  Dr.ir. Daniel Peeters. *AE4ASM003 – Linear Modelling (incl. F.E.M)*. Sept. 2022.

[47]  C. Pradere and C. Sauder. "Transverse and longitudinal coefficient of thermal expansion of carbon fibers at high temperatures (300–2500K)". In: *Carbon* 46.14 (2008), pp. 1874–1884. ISSN: 0008-6223. DOI: `https://doi.org/10.1016/j.carbon.2008.07.035`. URL: `https://www.sciencedirect.com/science/article/pii/S0008622308003837`.

[48]  C. Pradère et al. "Specific-heat measurement of single metallic, carbon, and ceramic fibers at very high temperature". In: *Review of Scientific Instruments* 76 (6 2005). DOI: `10.1063/1.1927102`.

[49]  C. Pradère et al. "Thermal properties of carbon fibers at very high temperature". In: *Carbon* 47 (3 2009), pp. 737–743. DOI: `10.1016/j.carbon.2008.11.015`.

[50]  T. Reimer et al. "Experimental characterization of fatigue life of ZrB2-SiC based ultra high-temperature ceramic matrix composites". In: *International Journal of Fatigue* 168 (2023), p. 107389. ISSN: 0142-1123. DOI: `https://doi.org/10.1016/j.ijfatigue.2022.107389`. URL: `https://www.sciencedirect.com/science/article/pii/S0142112322006399`.

[51]  Heather F. Riley. *Green Propellants*. 2015. URL: `https://www.nasa.gov/centers-and-facilities/white-sands/green-propellants/` (visited on 03/07/2024).

[52]  M. Dito Saputra and Novi Andria. "Design Optimization of A Conventional Rocket Nozzle Using Coupled Thermo-Structural Analysis". In: *Jurnal Teknologi Dirgantara* 19.6 (Dec. 2021), pp. 157–168. DOI: `http://dx.doi.org/10.30536/j.jtd.2021.v19.a3570`.

[53]  C. Sauder, J. Lamon, and R. Pailler. "Thermomechanical properties of carbon fibres at high temperatures up to 2000 °c". In: *Composites Science and Technology* 62 (4 2002), pp. 499–504. DOI: `10.1016/s0266-3538(01)00140-3`.

[54]  Raffaele Savino et al. "Aero-thermo-chemical characterization of ultra-high-temperature ceramics for aerospace applications". In: *Journal of the European Ceramic Society* 38.8 (2018). Cermodel 2017: Modelling and Simulation Meet Innovation in Ceramics Technology, pp. 2937–2953. ISSN: 0955-2219. DOI: `https://doi.org/10.1016/j.jeurceramsoc.2017.12.043`. URL: `https://www.sciencedirect.com/science/article/pii/S095522191730852X`.

[55]  Bernardo Schneiderman. *The Small/Medium Satellite Launch vehicle Market*. 2023. URL: `https://satellitemarkets.com/small-medium-launch-vehicle-market#:~:text=Smallsats%20represent%2087%25%20of%20spacecraft,remaining%20568%20were%20other%20applications.` (visited on 03/07/2024).

[56]    D. Sciti et al. "Introduction to h2020 project c3harme – next generation ceramic composites for combustion harsh environment and space". In: *Advances in Applied Ceramics* 117 (sup1 2018), s70–s75. DOI: 10.1080/17436753.2018.1509822.

[57]    Diletta Sciti et al. "Propulsion tests on ultra-high-temperature ceramic matrix composites for reusable rocket nozzles". In: *Journal of Advanced Ceramics* 12.7 (July 2023), pp. 1345–1360. DOI: 10.26599/jac.2023.9220759.

[58]    Mazyar Shafaei et al. "Numerical Investigation of Propellant Flow and Finite Element Analysis of Wall Structure for a Bi-propellant Thruster, Compared to Proposed Analytical". In: *International Journal of Mechanical Engineering and Robotics Research.* 5 (Jan. 2016). DOI: 10.18178/ijmerr.5.2.133-137.

[59]    K Shiva Shankar, S Shailesh babu, and A Sai Kumarand Prof. TBS Rao. "Thermo-Structure of Dual-Bell Nozzle". In: *International Journal of Engineering and Innovative Technology (IJEIT)* 4 (11 2015).

[60]    Taro Shimizu, Masatoshi Kodera, and Nobuyuki Tsuboi. "Internal and External Flow of Rocket Nozzle". In: *Journal of the Earth Simulator* 9 (Apr. 2008), pp. 19–26.

[61]    Emilio Sideridis, John Venetis, and Victor Kytopoulos. "The stiffness of short and randomly distributed fiber composites". In: *WSEAS Transactions on Applied and Theoretical Mechanics* 13 (Jan. 2018).

[62]    Robert A. Signorelli and James R. Johnston. *Erosion Resistance and Failure Mechanisms of Several Nozzle Materials in a Small Solid proepllant Rocket Engine.* Feb. 1963.

[63]    Kurt B. Smalley et al. *Flow Separation Side Loads Excitation of Rocket Nozzle FEM.* 2007.

[64]    SolvGe. *Home - About Us.* URL: https://solvge.com/ (visited on 06/12/2024).

[65]    Richard Stadelmann. *Mechanical Properties And Thermal Residual Stresses Of Zrb2-sic Ceramic Composites For Hypersonic Vehicle Applications.* 2013.

[66]    Richard Stadelmann. *ZrB2-SiC Based Ultr ZrB2-SiC Based Ultra High T a High Temperature Ceramic Composites: amic Composites: Mechanical Performance and Measurement and Design of Thermal Residual Stresses for Hypersonic Vehicle Applications.* 2015.

[67]    Lin Sun et al. "Coupled Thermo-Structural Analysis Model of Solid Rocket Motor Nozzle considering the Variation of Friction Coefficient under Operating Conditions". In: *International Journal of Aerospace Engineering* 2022 (Feb. 2022), pp. 1–17. DOI: 10.1155/2022/4608619.

[68]    Das Suprabha et al. "Ultra-High-Temperature Ceramic Coatings ZrC, ZrB2, HfC, and HfB2". In: Dec. 2023, pp. 441–469. ISBN: 978-3-031-40808-3. DOI: 10.1007/978-3-031-40809-0_14.

[69]    Chethan Madhu Suryavanshi. *Thermo-Structural Analysis of a Rocket Engine Thrust Chamber.* Dec. 2018.

[70]    "Thermal–solid interaction study of serpentine nozzle and analysis on structural response law". In: *Journal of Applied Fluid Mechanics* 16 (12 2023). DOI: 10.47176/jafm.16.12.2029.

[71]    Jatuporn Thongsri, Kamonwan Srathonghuam, and Adulyasak Boonpan. "Gas Flow and Ablation of 122 mm Supersonic Rocket Nozzle Investigated by Conjugate Heat Transfer Analysis". In: *Processes* 10.9 (Sept. 2022), p. 1823. DOI: 10.3390/pr10091823.

[72]    FEA Tips. *Linear vs Quadratic FE Elements.* 2024. URL: https://featips.com/2019/03/29/linear-vs-quadratic-fe-elements/ (visited on 04/03/2024).

[73]    FEA Tips. *When to Run Non-Linear FEA?* 2024. URL: https://featips.com/2023/03/08/when-to-run-non-linear-fea/ (visited on 04/05/2024).

[74]    A. D. Vinci et al. "Influence of fibre content on the strength of carbon fibre reinforced hfc/sic composites up to 2100 °c". In: *Journal of the European Ceramic Society* 39 (13 2019), pp. 3594–3603. DOI: 10.1016/j.jeurceramsoc.2019.04.049.

[75]    L. Wang, D. Kong, and J. Liang. "High-temperature tensile strength and fracture behavior of zrb2-sic-graphite composite". In: *International Journal of Applied Ceramic Technology* 14 (1 2016), pp. 31–38. DOI: 10.1111/ijac.12613.

[76] Zhi Wang et al. "Microstructure and thermal shock behavior of ZrB2–SiC–graphite composite". In: *Materials Chemistry and Physics* 113.1 (2009), pp. 338–341. ISSN: 0254-0584. DOI: `https://doi.org/10.1016/j.matchemphys.2008.07.095`. URL: `https://www.sciencedirect.com/science/article/pii/S0254058408005725`.

[77] Bill Webster. *Linear vs Quadratic FE Elements*. 2021. URL: `https://www.fidelisfea.com/post/first-order-vs-second-order-elements-in-fea` (visited on 04/03/2024).

[78] James Richard. Wertz, David F. Everett, and Jeffery John. Puschell. *Space mission engineering : the new SMAD*. eng. Space technology library ; v. 28. Hawthorne, CA: Microcosm Press, 2011. ISBN: 1881883167.

[79] Weihua Xie et al. "Probabilistic Reliability Analysis of Carbon/Carbon Composite Nozzle Cones with Uncertain Parameters". In: *Journal of Spacecraft and Rockets* (Apr. 2019). ISSN: 0022-4650. DOI: `10.2514/1.A34392`.

[80] F. Yang et al. "Analysis of the mechanical properties in short carbon fiber-toughened zrb2—sic ultra-high temperature ceramic". In: *Journal of Composite Materials* 44 (8 2009), pp. 953–961. DOI: `10.1177/0021998309346545`.

[81] Feiyu Yang et al. "Mechanical properties of short carbon fiber reinforced ZrB2–SiC ceramic matrix composites". In: *Materials Letters* 62.17 (2008), pp. 2925–2927. ISSN: 0167-577X. DOI: `https://doi.org/10.1016/j.matlet.2008.01.076`. URL: `https://www.sciencedirect.com/science/article/pii/S0167577X0800116X`.

[82] B.T.C. Zandbergen. *Thermal Rocket Propulsion (version 2.09)*. Sept. 2022.

[83] Shi C. Zhang, Greg E. Hilmas, and William G. Fahrenholtz. "Mechanical properties of sintered ZrB2–SiC ceramics". In: *Journal of the European Ceramic Society* 31.5 (May 2011), pp. 893–901. DOI: `10.1016/j.jeurceramsoc.2010.11.013`.

[84] W. Zhang. "Failure pattern and corresponding mechanism analysis of lre". In: *Failure Characteristics Analysis and Fault Diagnosis for Liquid Rocket Engines* (2016), pp. 11–35. DOI: `10.1007/978-3-662-49254-3_2`.

[85] Luca Zoli et al. "On the thermal shock resistance and mechanical properties of novel unidirectional UHTCMCs for extreme environments". In: *Scientific Reports* 8 (June 2018), p. 9148. DOI: `10.1038/s41598-018-27328-x`.

[86] Ji Zou et al. "High-temperature bending strength, internal friction and stiffness of ZrB2–20vol percent SiC ceramics". In: *Journal of the European Ceramic Society* 32.10 (Aug. 2012), pp. 2519–2527. DOI: `10.1016/j.jeurceramsoc.2012.01.035`.
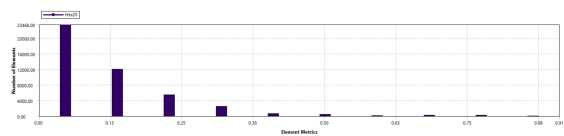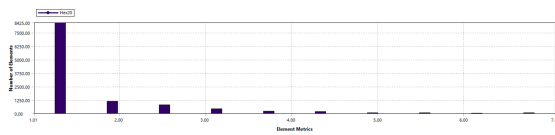
# A

# Appendix A

The appendix contains tables used to create the figures in the report. They can be used to know exactly the numbers seen in the plots. Additionally, all the tables provided here refer to the baseline 4 mm thick thruster and the optimum nozzle. A figure is also present for the progression of stress over time for the optimum thruster.
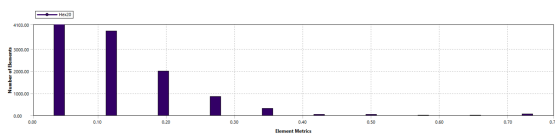


(a) Simple Skewness



(b) Complex Skewness



(c) Simple Aspect Ratio



(d) Complex Aspect Ratio

**Figure A.1:** 1.5 mm Mesh Skewness and Aspect Ratio Metrics for 4 mm uniform thickness thruster



(a) Simple Skewness



(b) Complex Skewness



(c) Simple Aspect Ratio



(d) Complex Aspect Ratio

**Figure A.2:** 1 mm Mesh Skewness and Aspect Ratio Metrics for 4 mm uniform thickness thruster

(a) Simple Skewness

(b) Complex Skewness

(c) Simple Aspect Ratio

(d) Complex Aspect Ratio
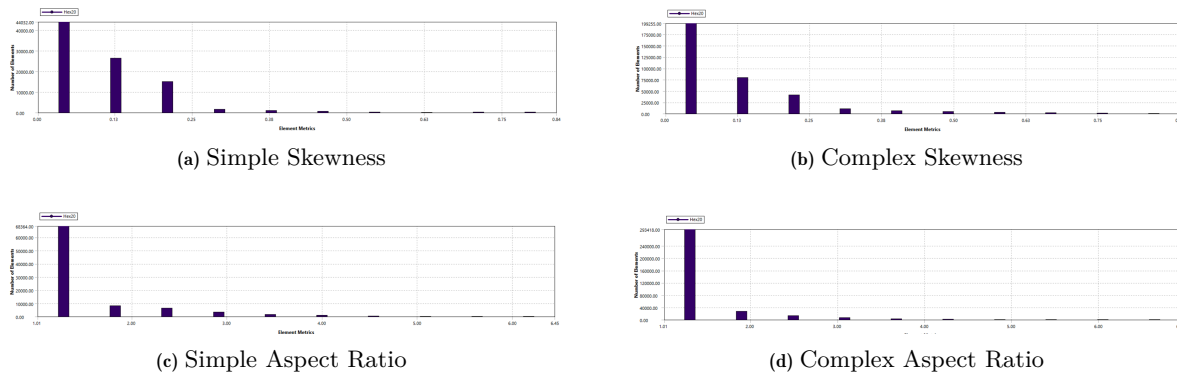
**Figure A.3:** 0.75 mm Mesh Skewness and Aspect Ratio Metrics for 4 mm uniform thickness thruster
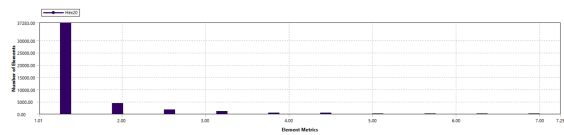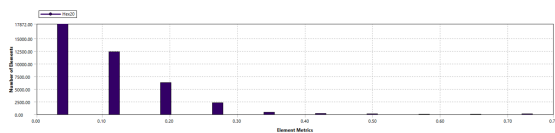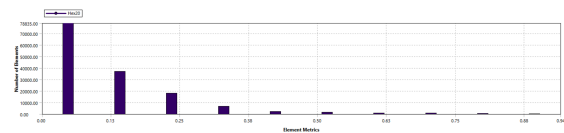


(a) Simple Skewness

(b) Complex Skewness

(c) Simple Aspect Ratio

(d) Complex Aspect Ratio
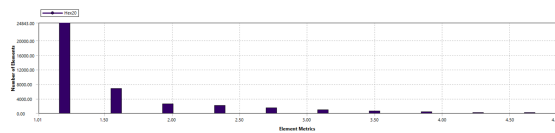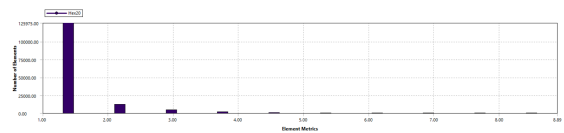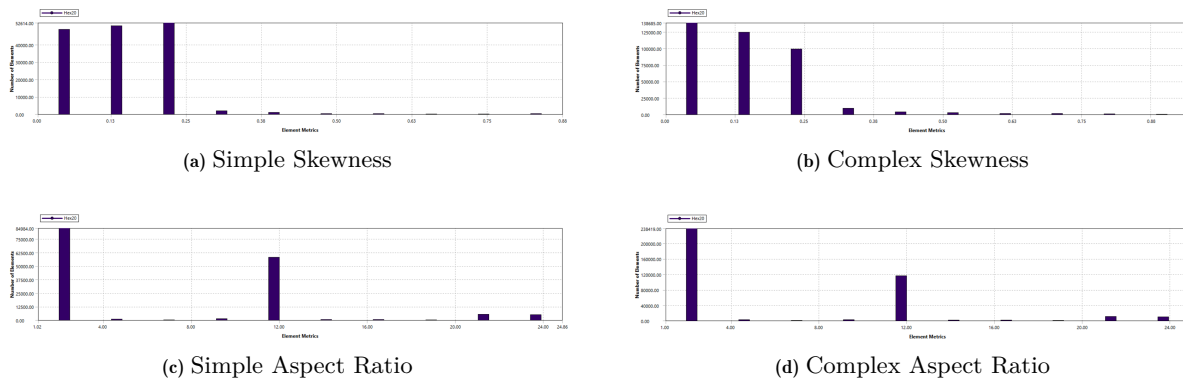
**Figure A.4:** Custom Specific Mesh Skewness and Aspect Ratio Metrics for 4 mm uniform thickness thruster

**Table A.1:** Compilation of performance of all possible configurations simulated

| Configuration | Y Deflection (mm) | X Deflection (mm) | Maximum Temperature (K) | Geometry Mass (kg) | Mesh Elements | Maximum Nozzle Stress (MPa) |
|---|---|---|---|---|---|---|
| C1 | 0.075 | 0.483 | 1258.3 | 0.379 | 155609 | 205.0 |
| C2 | 0.076 | 0.507 | 1321.2 | 0.373 | 156272 | 195.4 |
| C3 | 0.076 | 0.535 | 1382.7 | 0.368 | 156272 | 186.7 |
| C4 | 0.090 | 0.542 | 1335.0 | 0.351 | 155371 | 180.9 |
| C5 | 0.090 | 0.570 | 1422.3 | 0.345 | 155371 | 169.6 |
| C6 | 0.091 | 0.601 | 1505.6 | 0.339 | 155371 | 151.7 |
| C7 | 0.111 | 0.617 | 1451.3 | 0.324 | 155978 | 147.1 |
| C8 | 0.112 | 0.649 | 1535.9 | 0.318 | 155978 | 148.2 |
| C9 | 0.112 | 0.684 | 1642.7 | 0.312 | 155978 | 133.9 |

**Table A.2:** Maximum temperatures on the inside and outside of thruster at all time steps for 4 mm uniform thickness thruster using the simple model

| Time Step (s) | A-Inside Temp (K) | B-Outside Temp (K) |
|---|---|---|
| 0.1 | 405.95 | 303.51 |
| 0.15 | 434.37 | 309.50 |
| 0.19 | 455.54 | 317.13 |
| 0.34 | 498.27 | 344.58 |

Table A.2 continued from previous page

| Time Step (s) | Inside Temp (K) | Outside Temp (K) |
|---|---|---|
| 0.76 | 567.48 | 420.50 |
| 1.19 | 629.24 | 488.67 |
| 2.04 | 734.78 | 592.94 |
| 2.90 | 811.97 | 685.21 |
| 3.90 | 902.64 | 776.51 |
| 4.90 | 976.62 | 855.89 |
| 5.90 | 1037.89 | 929.67 |
| 6.90 | 1100.60 | 994.16 |
| 7.90 | 1157.50 | 1050.38 |
| 8.90 | 1207.64 | 1104.11 |
| 9.45 | 1233.65 | 1132.44 |
| 10 | 1258.30 | 1159.33 |

**Table A.3:** Stress at different time steps for the exact time steps as in transient and auto time steps by ANSYS for 4 mm uniform thickness thruster using the simple model

| Exact Time Steps (s) | Stress (MPa) | Auto Time Steps (s) | Stress (MPa) |
|---|---|---|---|
| 0.1 | 102.73 | 0.1 | 104.26 |
| 0.15 | 128.03 | 0.2 | 146.87 |
| 0.19 | 144.47 | 0.5 | 174.62 |
| 0.34 | 169.20 | 1.4 | 190.54 |
| 0.76 | 177.65 | 2.4 | 205.00 |
| 1.19 | 183.91 | 3.4 | 198.33 |
| 2.04 | 206.89 | 4.4 | 197.34 |
| 2.90 | 197.84 | 5.4 | 193.28 |
| 3.90 | 197.42 | 6.4 | 188.29 |
| 4.90 | 196.85 | 7.4 | 187.84 |
| 5.90 | 188.86 | 8.4 | 188.00 |
| 6.90 | 186.78 | 9.4 | 186.26 |
| 7.90 | 188.23 | 10 | 184.27 |
| 8.90 | 187.39 | | |
| 9.45 | 186.06 | | |
| 10 | 184.27 | | |

**Table A.4:** Maximum temperatures on the inside and outside of thruster at all time steps for the complex model for 4 mm uniform thickness thruster

| Time Step (s) | A-Inside Temp (K) | B-Outside Temp (K) |
|---|---|---|
| 0.1 | 405.95 | 303.51 |
| 0.15 | 434.24 | 309.45 |
| 0.19 | 455.32 | 317.02 |
| 0.34 | 497.90 | 344.29 |
| 0.76 | 566.86 | 419.83 |
| 1.18 | 628.33 | 487.70 |
| 2.03 | 733.56 | 591.59 |
| 2.88 | 810.43 | 683.45 |
| 3.88 | 901.22 | 775.10 |
| 4.88 | 975.48 | 854.48 |
| 5.88 | 1036.91 | 928.48 |
| 6.88 | 1099.58 | 993.13 |

**Table A.4 continued from previous page**

| Time Step (s) | Inside Temp (K) | Outside Temp (K) |
|---|---|---|
| 7.88 | 1156.59 | 1049.43 |
| 8.88 | 1206.82 | 1103.22 |
| 9.44 | 1233.27 | 1132.02 |
| 10 | 1258.31 | 1159.35 |

**Table A.5:** Maximum stress on the inside of thruster at all time steps for the complex model for 4 mm uniform thickness thruster

| Time Step (s) | Stress Inside (MPa) |
|---|---|
| 0.1 | 102.73 |
| 0.15 | 127.93 |
| 0.19 | 144.33 |
| 0.34 | 169.01 |
| 0.76 | 177.58 |
| 1.18 | 183.78 |
| 2.03 | 206.83 |
| 2.88 | 198.16 |
| 3.88 | 197.26 |
| 4.88 | 196.94 |
| 5.88 | 189.02 |
| 6.88 | 186.70 |
| 7.88 | 188.23 |
| 8.88 | 187.42 |
| 9.44 | 186.09 |
| 10 | 184.27 |

**Table A.6:** Maximum Stress on the inside and outside the thruster for the optimum model at all time steps

| Time Step (s) | Nozzle Stress MPa | Inside Stress MPa | Outside Stress MPa |
|---|---|---|---|
| 0.1 | 78.26 | 78.26 | 36.59 |
| 0.16 | 94.82 | 94.82 | 50.05 |
| 0.23 | 104.14 | 104.14 | 59.27 |
| 0.42 | 105.49 | 105.49 | 75.97 |
| 0.61 | 113.08 | 113.08 | 81.52 |
| 1.00 | 132.77 | 132.77 | 104.85 |
| 1.39 | 127.19 | 127.19 | 111.94 |
| 2.16 | 132.95 | 138.85 | 120.47 |
| 3.16 | 130.96 | 164.58 | 148.44 |
| 4.16 | 129.46 | 188.35 | 179.39 |
| 5.16 | 118.67 | 208.26 | 205.49 |
| 6.16 | 111.71 | 226.50 | 228.30 |
| 7.16 | 108.53 | 243.84 | 249.10 |
| 8.16 | 101.95 | 260.78 | 267.91 |
| 9.16 | 97.25 | 277.93 | 285.59 |
| 10 | 95.51 | 292.75 | 301.86 |

**Table A.7:** Maximum temperatures on the inside and outside of the thruster for the optimum model at all time steps

| Time Step (s) | A-Inside Temp (K) | B-Outside Temp (K) |
| --- | --- | --- |
| 0.1 | 411.9 | 336.3 |
| 0.16 | 453.5 | 367.6 |
| 0.23 | 487.0 | 398.4 |
| 0.42 | 554.4 | 477.8 |
| 0.61 | 620.4 | 545.4 |
| 1.00 | 732.4 | 657.2 |
| 1.39 | 819.9 | 755.5 |
| 2.16 | 972.7 | 910.9 |
| 3.16 | 1124.7 | 1066.4 |
| 4.16 | 1247.7 | 1195.5 |
| 5.16 | 1348.9 | 1300.2 |
| 6.16 | 1433.5 | 1386.8 |
| 7.16 | 1503.1 | 1459.0 |
| 8.16 | 1558.4 | 1518.8 |
| 9.16 | 1607.0 | 1567.5 |
| 10 | 1642.7 | 1603.1 |

**Figure A.5:** SolvGe 5mm Nozzle Thruster Engineering Drawing